Development of a polarization modulator for the observation of CMB B-modes in search of primordial gravitational waves with LiteBIRD

September 17, 2021

Kunimoto Komatsu

supervised by
Prof. Hirokazu Ishino

GRADUATE SCHOOL OF NATURAL SCIENCE AND TECHNOLOGY
(DOCTOR'S COURSE)
OKAYAMA UNIVERSITY

Contents

1 Introduction **5**

1.1 Cosmic microwave background . . . 5

  1.1.1 CMB anisotropies . . . 5

1.2 Cosmic inflation . . . 10

1.3 Foreground . . . 13

1.4 LiteBIRD . . . 15

  1.4.1 Detectors . . . 16

  1.4.2 Noise equivalent temperature (NET) . . . 16

1.5 Polarization modulator unit for LiteBIRD low-frequency telescope . . . 21

  1.5.1 Target values of development . . . 22

  1.5.2 Broadband half-wave plate . . . 23

  1.5.3 Sub-wavelength structure . . . 24

  1.5.4 Cryogenic rotation mechanism . . . 24

2 Half-wave plate design **26**

2.1 Introduction . . . 26

2.2 HWP polarimetry . . . 26

  2.2.1 Formalism . . . 26

  2.2.2 Optimization . . . 30

2.3 Results . . . 32

2.4 Discussions . . . 34

  2.4.1 Tolerance analysis . . . 34

  2.4.2 Further optimization for broader frequency coverage . . . 35

  2.4.3 Further design optimization with larger degree of freedoms . . . 36

2.5 Conclusions . . . 38

3 Systematics originated from half-wave plate **39**

3.1 Introduction . . . 39

3.2 Formalism . . . 39

  3.2.1 Spectrum of each sky component . . . 39

  3.2.2 Unit conversion . . . 40

  3.2.3 HWP modulation effect for observed polarization . . . 41

  3.2.4 Model of observed power spectrum . . . 43

3.3 Evaluation method . . . 43

  3.3.1 Analysis flowchart . . . 43

3.4 Results . . . 47

  3.4.1 Elements of matrices . . . 47

  3.4.2 Validation of the methodlogy . . . 47

  3.4.3 Comparison with an ideal HWP . . . 48

3.5 Discussion . . . 53

  3.5.1 Ground calibration . . . 53

  3.5.2 Requirement for calibration of HWP performance . . . 56

  3.5.3 Effect of foreground spectrum change . . . 65

  3.5.4 Future works . . . 65

3.6 Conclusions . . . 65

4 Experimental demonstration **69**
4.1 Modulation efficiency 69
4.2 Demonstration at room temperature 69
4.2.1 Introduction 69
4.2.2 Sample preparation 70
4.2.3 Experiment 72
4.2.4 Results 74
4.2.5 Discussion 78
4.2.6 Conclusions 85
4.3 Demonstration at cryogenic temperatures 87
4.3.1 Introduction 87
4.3.2 Formalism 87
4.3.3 Sample preparation 87
4.3.4 Experiment 90
4.3.5 Results 92
4.3.6 Discussion 96
4.3.7 Conclusions 99

5 Conclusion **101**

6 Future works **103**
6.1 Band-specific requirements 103
6.2 Predicting anti-symmetric design performance with reflection effects 103
6.3 AHWP design optimization specialized for LiteBIRD 104
6.4 Upscaling of measurement setup and PMU 105

A Appendix for Sec. 3 **107**
A.1 Drawing sky maps with *healpy* 107
A.2 Smoothing 107

B Appendix for Sec. 4.3 **109**
B.1 Transmittance measurement for a sapphire plate 109
B.2 Modulation efficiency of a five layer anti-symmetric design AHWP without SWS . . . 110
B.3 Magnetic field measurements of the magnet ring 110

Acknowledgement

First of all, I would like to thank my supervisor, Prof. Hirokazu Ishino. I would also like to thank Prof. Tomotake Matsumura at Kavli IPMU, where I spent most of my time during my master and doctoral courses. Without their continuous and great supports, I would not have been able to achieve the results I shown in this thesis. I would also like to thank Prof. Nobuhiko Katayama for giving me a chance to consider about the design of a new half-wave plate, Dr. Yuki Sakurai for giving me advice about handling the rotation mechanism and a lot of measurements, Dr. Tommaso Ghigna for for giving me advice about the simulation related to systematics effects, Mr. Ryota Takaku for his grateful research on anti-reflective structures and providing them. I want to thank Dr. Samantha Stever who spend a lot of time giving me advice for English every time I write papers (of course, this thesis is also included). I thank students in Ishino lab. and all the people who are involved with me at Kavli IPMU. The chats and discusses with them make me a fulfilling research life. Finally, I would like to thank my family for always supporting me when I am in Okayama, Chiba, and anywhere.

Abstract

The observation of the cosmic microwave background (CMB) has played an important role in modern cosmology. In recent years, measuring polarization of the CMB has generated great interest in the community, and requires enough sensitivity to probe nano-Kelvin fluctuations on top of 3 K CMB itself. This sensitivity would allow for the obervation of primordial B-modes in the inflationary universe. One of the key requirements for such CMB telescopes is to be able to probe large angular scales, where the inflationary signal is the greatest. Correspondingly, instrumental stability is required over long time scales during their scans and the suppression of systematic effects is essential. LiteBIRD is a satellite to probe primordial gravitational waves by detecting cosmological B-modes . LiteBIRD plans to employ a continuously rotating half-wave plate (HWP) as a polarization modulator unit (PMU) for the mitigation of some systematic effects. In this thesis, we report on the development efforts on the PMU of the low frequency telescope (LFT) of the LiteBIRD satellite which covers the frequency range 34-161 GHz. In our developments, we find a new type of the achromatic half-wave plate (AHWP) design has a frequency independent optic axis. We do a simulation to evaluate the impact of this new AHWP design to the oberved CMB polarization. As the reault, we comfirm that the new AHWP design relaxed the requirement for the calibration accuracies of the polarization efficiency and the knowledge for the foreground spectrum than that of the convensional AHWP design which has a frequency dependece of its optic axis. We also demonstrate the AHWP designs and a 1/10 small prototype PMU on room and cryogenic temperature, respectively. From the demonstration, we confirm that the AHWP becomes broadband as designed and identify the source of the frequency contents in the modulated signal of the small PMU.

1 Introduction

1.1 Cosmic microwave background

The Cosmic Microwave Background (CMB) is radiation with a blackbody spectrum of about 3 K observed in all directions of the sky. According to the Big Bang theory, our universe started from a small space and expanded until the present. In the early universe, there was a thermal equilibrium between the photons and the electrons in the primordial plasma, which interacted by scattering. At this time, the universe was opaque because the photons were constantly scattered by electrons. Around 370,000 years after the birth of the universe, its temperature dropped to 3,000 K due to cooling caused by spatial expansion, and electrons were captured by protons to form electrically neutral hydrogen atoms. At the same time, the photons were freed from scattering by electrons, which is called decoupling, and the surface where the decoupling occurred is called the last scattering surface. The light released during the decoupling is still observable and is called the CMB.

The first discovery of CMB was made by A. Penzias and R. Wilson at around 4 GHz in 1965 [52, 17]. The spectrum of the CMB intensity was measured in detail by the Far Infrared Absolute Spectrophotometer (FIRAS) on the COBE satellite, and was confirmed to match the blackbody spectrum at 2.726 ± 0.010 K with an rms accuracy of less than 0.01% [44]. The temperature of the CMB has now been measured to be 2.72548 ± 0.00057K [23].

1.1.1 CMB anisotropies

In addition to FIRAS, the COBE satellite is equipped with two other instruments, one of which, Differential Microwave Radiometers (DMR), has confirmed that while the CMB is almost uniform over the entire sky, there is a temperature anisotropy at the 10^{-5} level [44]. Although the resolution of DMR measurements was 10 degrees, detailed observations are made by the subsequent BOOMERanG balloon-borne missions, WMAP, and Planck satellites [61, 35, 12, 55]. In particular, the Planck satellite observed the anisotropies with a resolution smaller than 10 arcmin and obtained anisotropy maps as shown in Fig. 1. In Fig. 1, the monopole component, which has a blackbody spectrum and is uniform over the entire sky, and the dipole component, which is caused by the movement of the Earth relative to the CMB frame, are removed. The temperature anisotropies shown in the top panel of Fig. 1 correspond to the density of matter in the early universe, and thus the observations provide information about the early universe. In particular, by fitting the power spectrum of the temperature anisotropy with the ΛCDM model, we can obtain information on the composition and age of the universe, the Hubble constant, etc. [55].

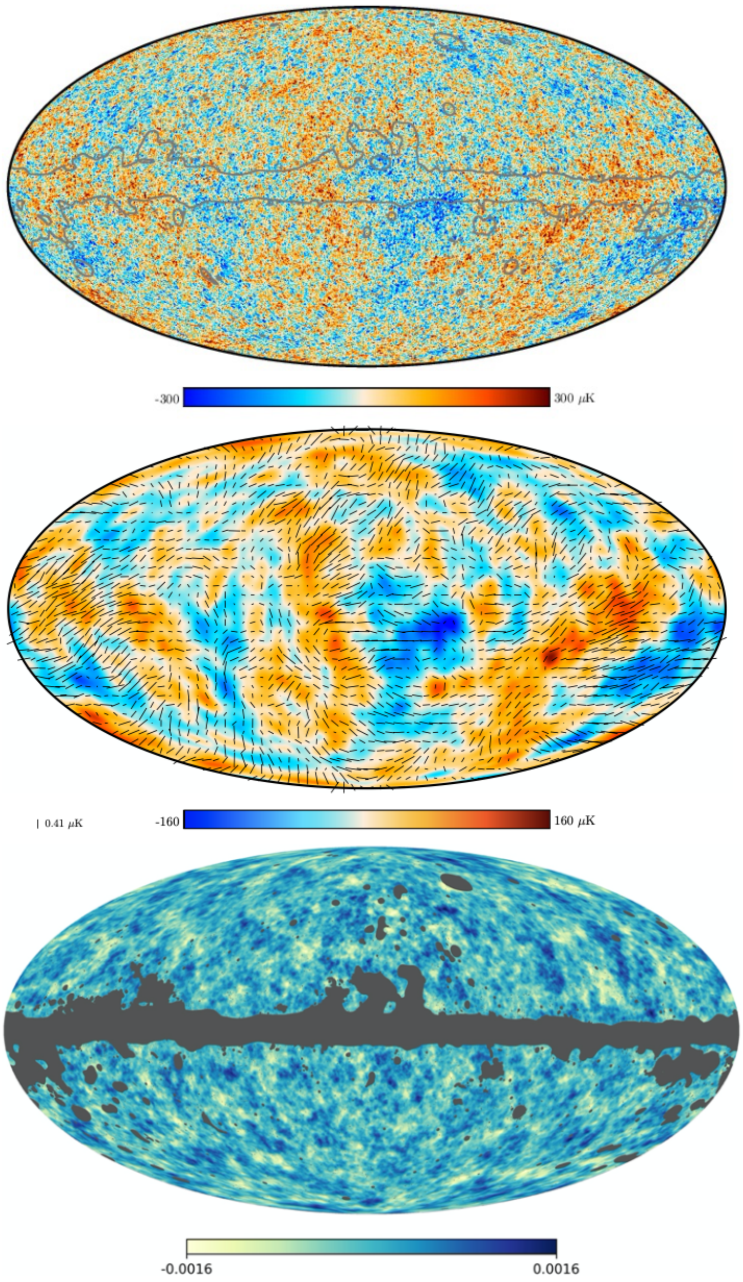

Figure 1: CMB anisotropy maps from the Planck satellite observation. The top panel shows the temperature map. The middle panel shows the polarization map with polarization directions. The bottom panel shows the map of the lensing effect. The gray line and area in the top and bottom panel shows the masked area to remove the large residual of the foreground emission. Image from [55]

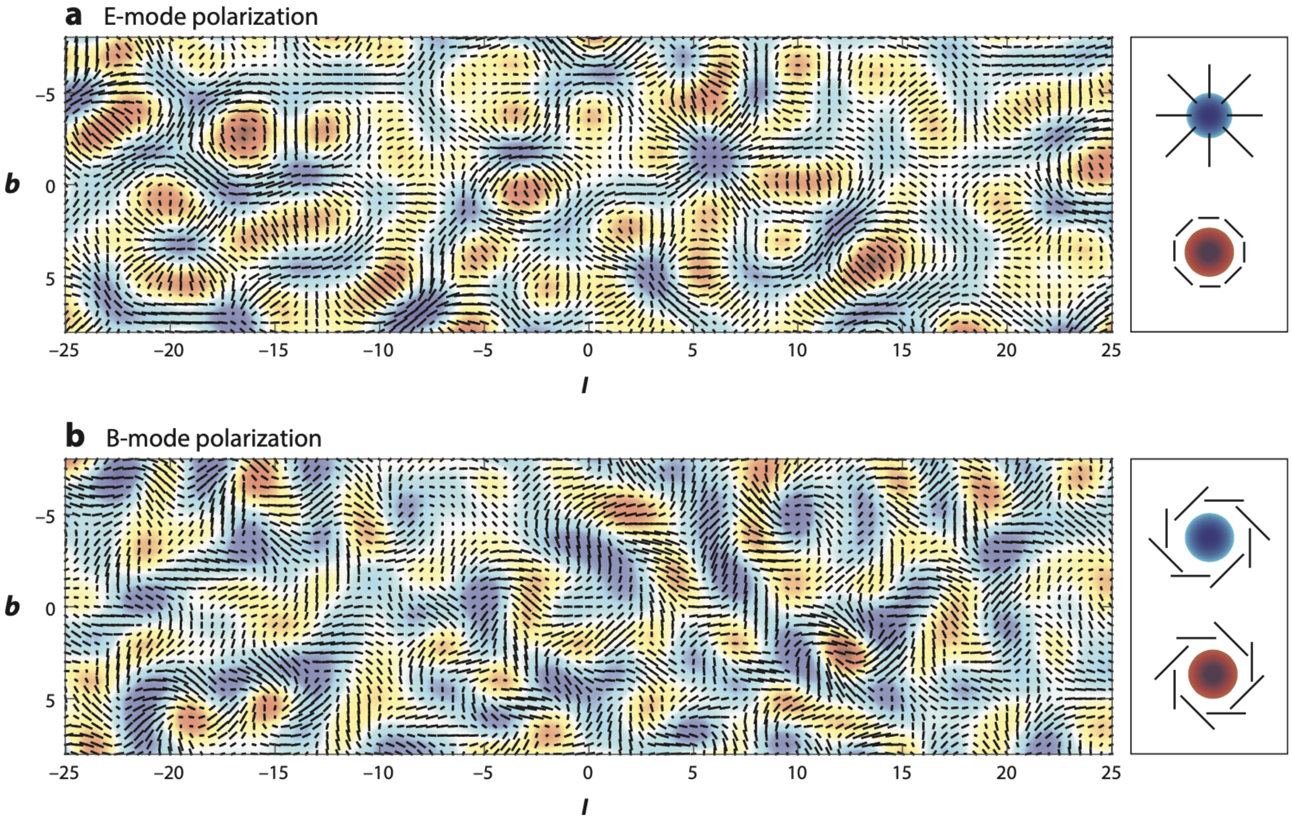

Figure 2: Polarization patterns of E and B-modes. The top and bottom panels show the E and B-mode. The right side of each panel shows the polarization patterns at a hot spot (red) and a cold spots (blue). Image from [36]

Power spectrum The CMB temperature anisotropy, $T(\theta, \phi)$, can be expanded like a Fourier transform using a spherical harmonic function $Y_{\ell m}(\theta, \phi)$, as [78, 5],

$$T(\theta, \phi) = \sum_{\ell=1}^{\infty} \sum_{m=-\ell}^{\ell} a_{\ell m}^{T} Y_{\ell m}(\theta, \phi), \tag{1}$$

where θ and ϕ are positions in spherical coordinates, ℓ represents the angular scale and corresponds to the angle in degrees, ψ, as $\ell = 180/\psi$. Similar to the power spectrum in frequency space in the Fourier transform, the spectrum C_{ℓ}^{TT} on the angular scale of the CMB temperature anisotropy can be defined as,

$$C_{\ell}^{TT} = \frac{1}{2\ell + 1} \sum_{m=-\ell}^{\ell} < a_{\ell m}^{T*} a_{\ell m}^{T} > . \tag{2}$$

We perform a similar expansion and definition of the power spectrum for the anisotropy of CMB polarization. The CMB polarization is observed as Stokes parameters Q and U. These Q and U represent the difference between the power observed at 0 and 90 degrees, and at 45 and 135 degrees, respectively. The values of Q and U change depending on the coordinates defined by the observer (i.e., Q can become U by the coordinate definition). Therefore, we expand the CMB

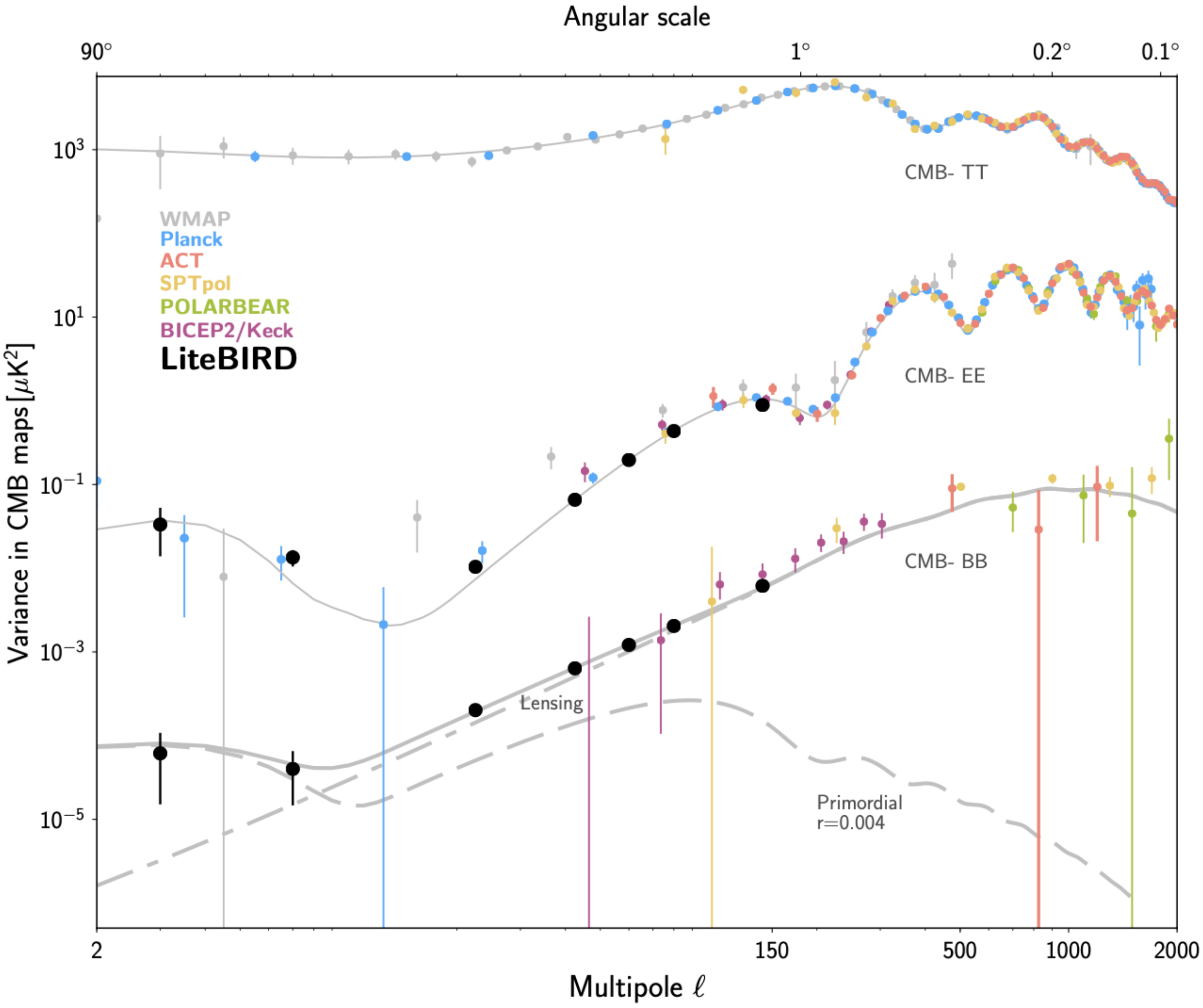

Figure 3: Summary of present measurements of CMB power spectra and expected polarization sensitivity of LiteBIRD. Image from [28]

polarization component using spin-2 spherical harmonics, ${}_{\pm 2}Y_{\ell m}(\theta,\phi)$, as,

$$(Q \pm iU)(\theta,\phi) = \sum_{\ell=1}^{\infty} \sum_{m=-\ell}^{\ell} {}_{\pm 2}a_{\ell m\,\pm 2}Y_{\ell m}(\theta,\phi). \tag{3}$$

From the expansion factors ${}_2a_{\ell m}$ and ${}_{-2}a_{\ell m}$, the coordinate definition-independent expansion factors, $a^E_{\ell m}$ and $a^B_{\ell m}$ can be obtained as,

$$a^E_{\ell m} = -\frac{({}_2a_{\ell m} + {}_{-2}a_{\ell m})}{2}, \tag{4}$$

$$a^B_{\ell m} = i\frac{({}_2a_{\ell m} - {}_{-2}a_{\ell m})}{2}, \tag{5}$$

The polarization patterns expanded by $a^E_{\ell m}$ and $a^B_{\ell m}$ are called E and B-mode polarization, which have radial and swirl polarization patterns on the celestial sphere as Fig 2, respectively. Using $a^E_{\ell m}$

and $a_{\ell m}^{B}$, we can define the power spectrum for the E and B-mode polarization, C_{ℓ}^{EE} and C_{ℓ}^{BB}, as,

$$C_{\ell}^{EE} = \frac{1}{2\ell+1}\sum_{m=-\ell}^{\ell} < a_{\ell m}^{E*} a_{\ell m}^{E} >, \tag{6}$$

$$C_{\ell}^{BB} = \frac{1}{2\ell+1}\sum_{m=-\ell}^{\ell} < a_{\ell m}^{B*} a_{\ell m}^{B} > . \tag{7}$$

CMB polarization CMB polarization is produced by Thomson scattering of radiation from a quadrupole distribution of the photon energy by electrons on the last scattering surface. For example, when there is a photon energy distribution on the last scattering surface as shown in Fig. 4, we observe a polarization with vertical direction. The reason for the presence of electrons on the last scattering surface is that the formation of hydrogen atoms during decoupling is not instantaneous. The main component of CMB polarization is the E-mode due to temperature (density) anisotropy. In addition, there are small E and B-modes caused by primordial gravitational waves and the gravitational lensing effect. Fig. 3 shows a summary of present measurements of CMB power spectra and expected polarization sensitivity of LiteBIRD [28]. From Fig. 3, we see that the temperature anisotropy of the CMB (top line), the E-mode (second line from the top), and the lensing B-mode (bottom line) originated from the lensing effect dominate in high-ℓ, are experimentally well-measured. There are two peaks in the B-mode power spectrum which result from the primordial gravitational waves, which are the primordial B-modes, as the gray dashed line. The peak at $\ell = 100$ is produced by electrons on the last scattering surface. The peak at $\ell = 4$ is produced by electrons which reionized when the stellar radiation formed after the decoupling, and has a larger angular scale due to the expansion of the universe. The primordial B-mode dominates in the low-ℓ region, it has not yet been measured and is hoped to be observed by experiments such as LiteBIRD and CMB-S4 [28, 6].

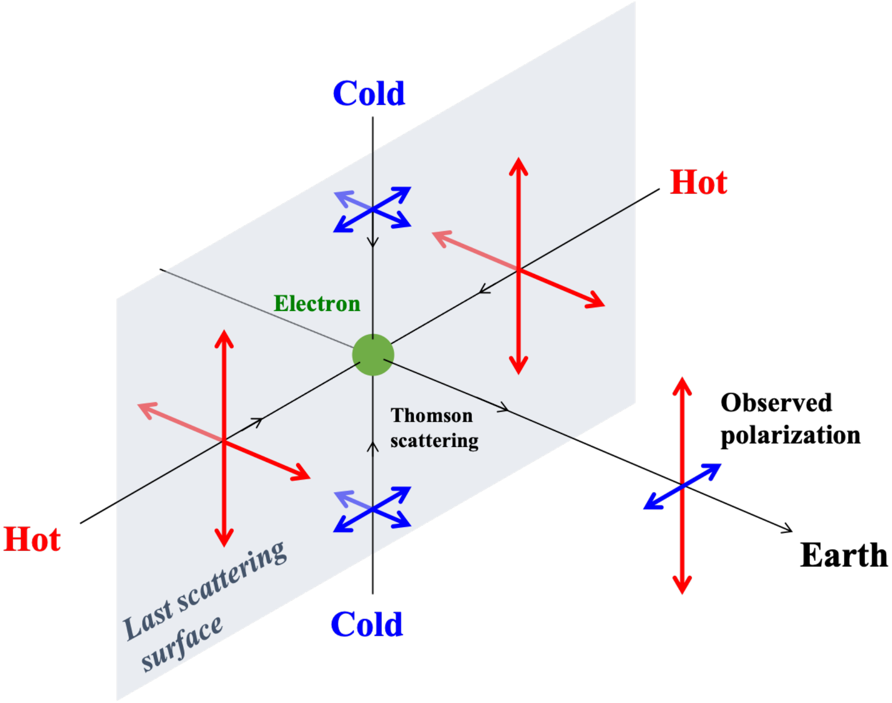

Figure 4: Conceptual sketch the generation of CMB polarization. This sketch shows the case where the lights from hot spots (red) and cold spots (blue) are reflected in the direction of the Earth due to Thomson scattering by an electron.

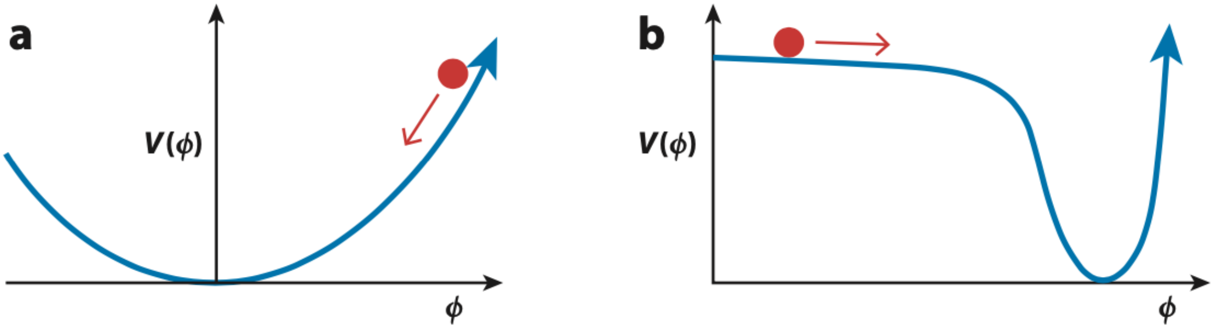

Figure 5: Examples of potential $V(\phi)$. The left panel shows a quadratic potential. The right panel shows a hilltop potential. The inflation is occurred when the scalar field rolls slowly down the potential and ended when the scalar field becomes close to the minimum. Image taken from [36]

1.2 Cosmic inflation

Cosmic inflation is one of the theoretical models that gives rise to the initial conditions of the hot Big Bang of our universe. The inflation means to the exponential space expansion which is occurred earlier than the Big-Bang. The Big Bang theory is experimentally well verified by the existence of the CMB and the fact that its flux has a 3 K blackbody spectrum. However, there are problems that can not be solved by the Big Bang theory alone, such as the flatness problem (the observed curvature close to zero), the horizon problem (the observed CMB isotropy at large angluer scale), and the monopole problem. Cosmic inflation solves these problems and also obtains the seed of large-scale-structure of our universe from the quantum fluctuation. The evolution of the inflaton scalar field, ϕ, is given by the equation of motion and the Friedmann equation [36, 54] with the unit where $c = \hbar = 1$ as,

$$\ddot{\phi} + 3H\dot{\phi} + V'(\phi) = 0, \tag{8}$$

$$H^2 = \frac{1}{3m_{pl}^2}\left[V(\phi) + \frac{\dot{\phi}}{2}\right], \tag{9}$$

where $H = \dot{a}/a$ is the Hubble parameter, a is the scale factor, $m_{pl} = (8\pi G)^{-1/2}$ is the Planck mass, and V is the potential. The subscripts of dots and primes represent derivative with respect to time and ϕ, respectively. The slow-roll parameters, ϵ_V and η_V, are defined as,

$$\epsilon_V \simeq \frac{m_{pl}^2}{2}\left(\frac{V'}{V}\right)^2, \tag{10}$$

$$\eta_V \simeq \frac{m_{pl}^2 V''}{V}. \tag{11}$$

The necessary conditions for the slow-roll are expressed as $\epsilon_V << 1$ and $|\eta_V| << 1$. Fig. 5 shows two examples of the potential $V(\phi)$. On super-Hubble scales, the power spectra of curvature and tensor perturbations can be expanded [54] as,

$$
\begin{aligned}
\mathcal{P}_R(k) &= A_s\left(\frac{k}{k_*}\right)^{n_s-1+\frac{1}{2}dn_s d\ln k\ln(k/k_*)+\ldots}, &(12)\\
\mathcal{P}_t(k) &= A_t\left(\frac{k}{k_*}\right)^{n_t+\frac{1}{2}dn_t d\ln k\ln(k/k_*)+\ldots}, &(13)
\end{aligned}
$$

where k is the comoving wavenumber, A_s and A_t are the scalar and tensor amplitudes, n_s and n_t are the scalar and tensor spectral indices. The subscript asterisk represents the value of the inflation field ϕ_* where the mode $k_* = a_* H_*$ crosses the Hubble radius for the first time. Usually, we use the pivot scale $k_* = 0.05$ Mpc^{-1}. The coefficients at their respective leading orders are expressed by the slow-roll parameters as,

$$
\begin{aligned}
A_s &\approx \frac{V}{24\pi^2 m_{pl}^4 \epsilon_V}, &(14)\\
A_t &\approx \frac{2V}{3\pi^2 m_{pl}^4}, &(15)\\
n_s - 1 &\approx 2\eta_V - 6\epsilon_V, &(16)\\
n_t &\approx -2\epsilon_V. &(17)
\end{aligned}
$$

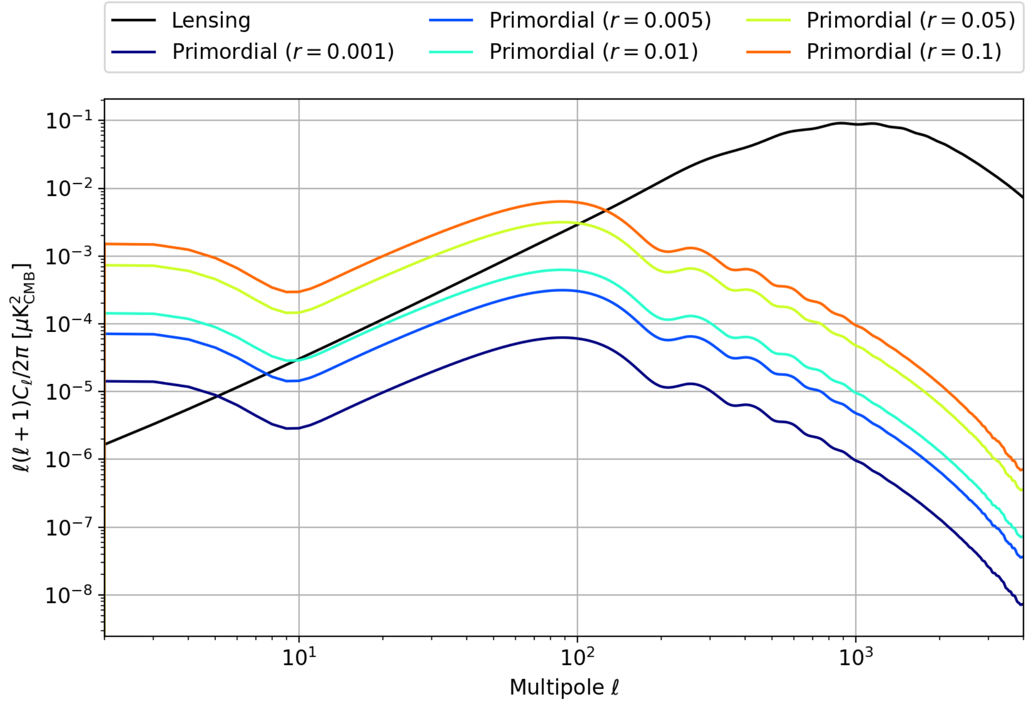

Figure 6: Power spectrum of the lensing B-mode and the primordial B-modes at several r. Each line is calculated using *CAMB* [1].

The rapid expansion of space during inflation, immediately after the beginning of the universe, produced quantum fluctuations in spacetime. Thus, it generated primordial gravitational waves, which imprinted the B-mode polarization in CMB. The strength of the gravitational waves is represented by the tensor-to-scalar ratio, r, defined as,

$$r = \frac{\mathcal{P}_t(k_*)}{\mathcal{P}_R(k_*)} \approx 16\epsilon_V \approx -8n_t. \tag{18}$$

The majority of the single-scalar-field slow-roll inflation models predict the value of $r > 0.01$ [36]. The current upper limit on r is 0.044 [75], and at present many experiments aim to measure it with an accuracy of the order 10^{-3}. The tensor-to-scalar ratio affects the intensity of the primordial B-mode. If r is large, the whole spectrum becomes higher, and if r is low, the whole spectrum becomes lower. Fig. 6 shows the power spectrum of the lensing B-mode and the primordial B-modes at several r. The tensor-to-scalar ratio limit the energy scale of the inflation [56] as,

$$V_* = \frac{3\pi^2 A_s}{2} m_{pl} r < (1.6 \times 10^{16}\ \mathrm{GeV})^4. \tag{19}$$

The tensor-to-scalar ratio and the scalar spectral index give us the constraints for the inflation models in the $n_s - r$ plane. The spectral index is measured as $n_s = 0.9665 \pm 0.0038$ by Planck [55]. Fig. 7 shows the current constraint at the pivot scale $k_* = 0.002\ \mathrm{Mpc}^{-1}$ from Planck, BICEP2/Keck Array, and the measurements of the baryon acoustic oscillation (BAO) scale with the theoretical predictions of selected inflationary models.

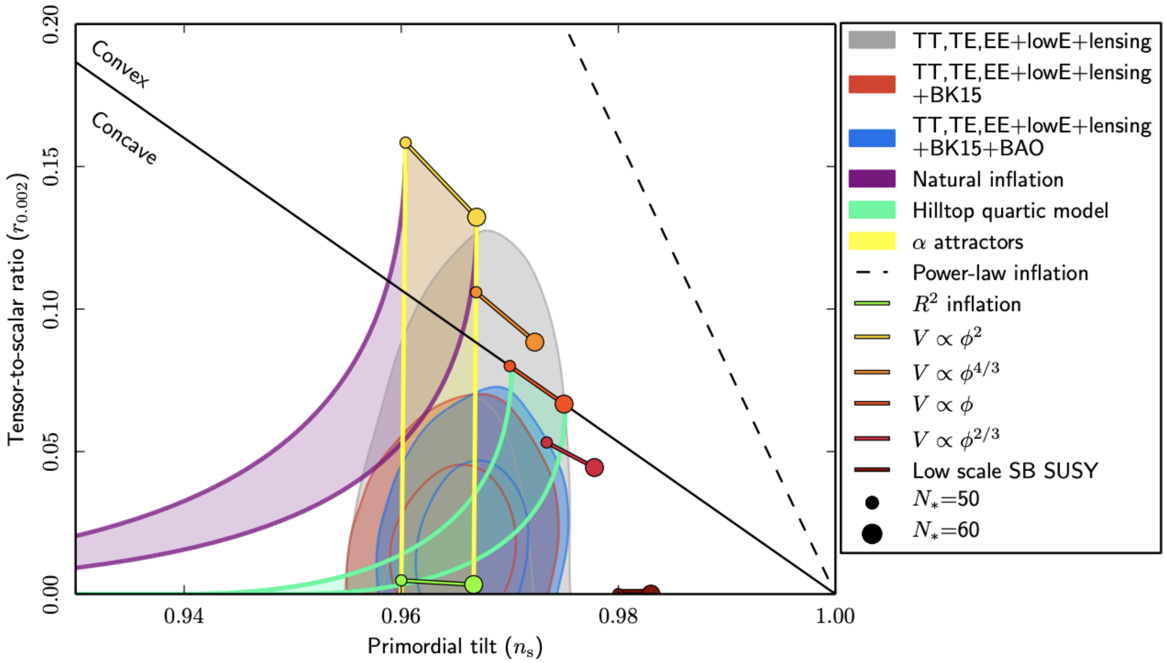

Figure 7: Marginalized joint 68% and 95% CL regions on n_s and r plane obtained from Planck alone and in combination with BK15 or BK15+BAO data. The tensor-to-scalar ratio is at $k = 0.002\ \mathrm{Mpc}^{-1}$. To comparison, the theoretical predictions of selected inflationary models is also shown. They assume $dn_s/d\ln k = 0$ to obtain the marginalized joint regions. Here, the number of e-folds N_* before the end of inflation that is corresponds to the rate of spatial expansion before and after inflation. Image taken from [56].

The observation of primordial B-mode and the measurement of r provides direct proof of inflation and lead to the validation of the model describing the mechanism. The energy scale of inflation is 10^{15} GeV, which is unreachable by ground-based accelerators such as the LHC. Therefore, the verification of the inflation model is important not only for our further knowledge of the early universe, but also for high-energy physics.

1.3 Foreground

The observed sky signal in sub-millimeter wavelength consists of not only the CMB but also foreground emissions originated from astronomical objects (e.g. our galaxy) which exist between a observer and the last scattering surface. Fig. 8 shows the power spectrum of the sub-millimeter sky component. The left and right panels are in temperature and polarization. For temperature, the spinning and thermal dust, free-free, CO (carbon monoxide), and the synchrotron emissions exist as the foregrounds. For polarization, there are only the thermal dust and the synchrotron emissions, and are dominant at higher and lower frequencies reference to about 80 GHz, respectively. The equations of the spectrum of each polarization component including the CMB are shown in Sec. 3.2.1. The polarization of the thermal dust is produced by the orientation of dust particles, which have anisotropic shape and align with the galactic magnetic field. In the case of the synchrotron emission, the polarization is produced by the relativistic electrons which move in a spiral motion in the galactic magnetic field. The polarization direction of the synchrotron emission is tangential to the motion of the electrons. Fig. 9 shows the polarization map at the lowest (30 GHz), central (100 GHz), highest (353 GHz) Planck frequency bands where each polarization sky component is dominated. The CMB anisotropy is uniform for whole sky as shown in Fig. 1, but from the top and bottom panels of Fig. 9, we can see that the thermal dust and synchrotron emissions have strong intensity along the equator of the map. This is due to the galactic plane, which is located at the center of the map and spreads along the equator; thus, our galaxy is the most dominant foreground source. We can see that since CMB dominates only around 80GHz from Fig. 8 and there is no sky area not affected by foregrounds as Fig. 9 demonstrates, it is essential to remove the foregrounds for CMB observation at all frequencies.

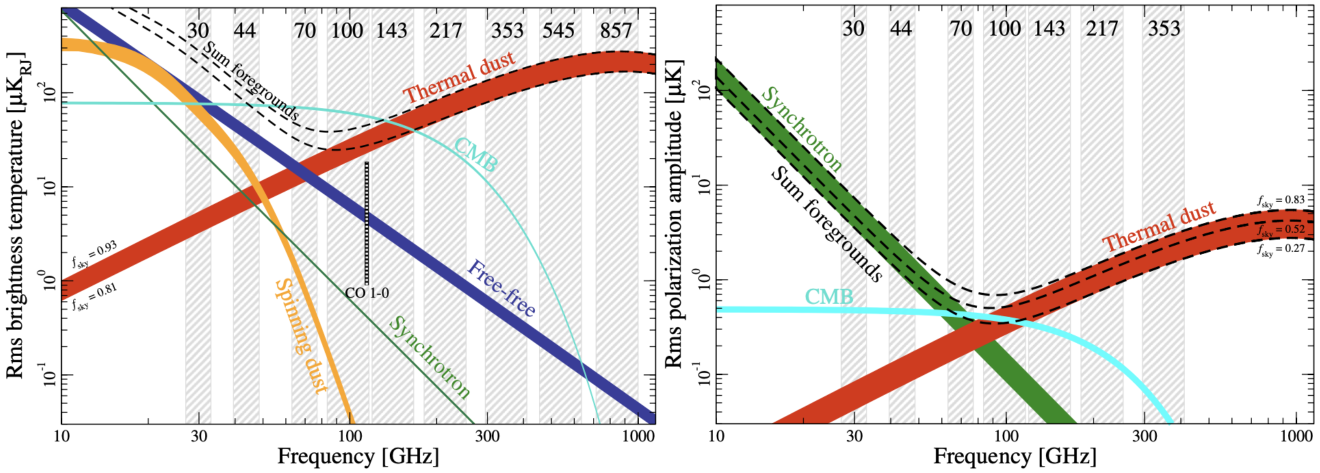

Figure 8: Spectrum of the sub-millimeter sky component. The left panel is in temperature, each component is smoothed to 1 degree. The right panel is in polarization, each component is smoothed to 10 arcmin. The sky coverage of the masks used to obtain the spectrum are expressed as f_{sky}. The gray bands are observation frequency bands of Planck. Image taken from [55]

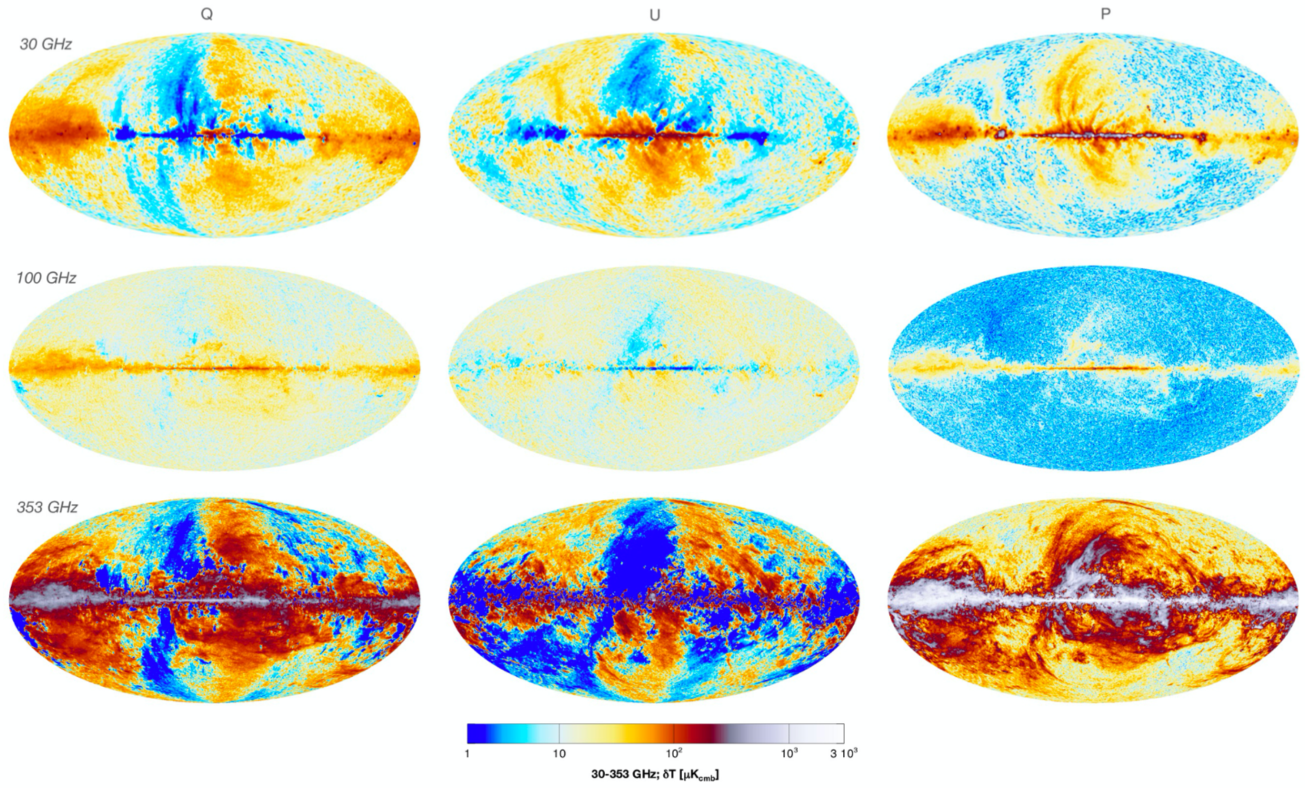

Figure 9: Polarization map from Planck. The maps show the Stokes parameters, Q and U, and the polarization fraction, $P = \sqrt{Q^2 + U^2}$. Planck has seven observation frequency bands for polarization, but in this figure, we only show the lowest (30 GHz), central (100 GHz), highest (353 GHz) frequency bands where each polarization sky component is dominated. Image taken from [55]

1.4 LiteBIRD

LiteBIRD (Lite satellite for the studies of B-mode polarization and Inflation from cosmic background Radiation Detection) is an ISAS/JAXA strategic large-class satellite mission designed to probe primordial B-modes with a target sensitivity of $\delta r < 10^{-3}$ for $2 \leq \ell \leq 200$ [28]. The target sensitivity of LiteBIRD, $\delta r < 10^3$, can verify the well-motivated single-scalar-field slow-roll inflation models and prove that r is less than the Lyth bound, $r > 2 \times 10^{-3}$, even if the primordial gravitational wave is not observed, and rejects most of the inflation models. Fig. 10 shows a conceptual design of the LiteBIRD spacecraft. LiteBIRD cover the frequency range from 34 to 448 GHz by 15 bands using three telescopes: the low frequency telescope (LFT) [66], medium frequency telescope (MFT), and high frequency telescope (HFT) [48]. Each telescope has a large field of view (FoV) in the shape of a rectangle of 18 degrees×9 degees for the LFT and a circle of 18 degrees for the M/HFT. There is no sky area that is free from the Galactic foreground emissions, so it is essential to subtract their contributions. Since the spectrum of each sky element shown in Fig. 8 is different, the foreground can be removed using this spectrum difference when we observe them in a broad range of frequencies. This is why LiteBIRD requires broad band observations. The main specification of LiteBIRD is shown in Fig. 11. LiteBIRD has a total of more than 4,000 superconducting detectors, called Transition Edge Sensors (TES) bolometers on its three telescopes, and it realizes 100 times more sensitivity to polarization than the Planck satellite, which has been the most sensitive to polarization to date.

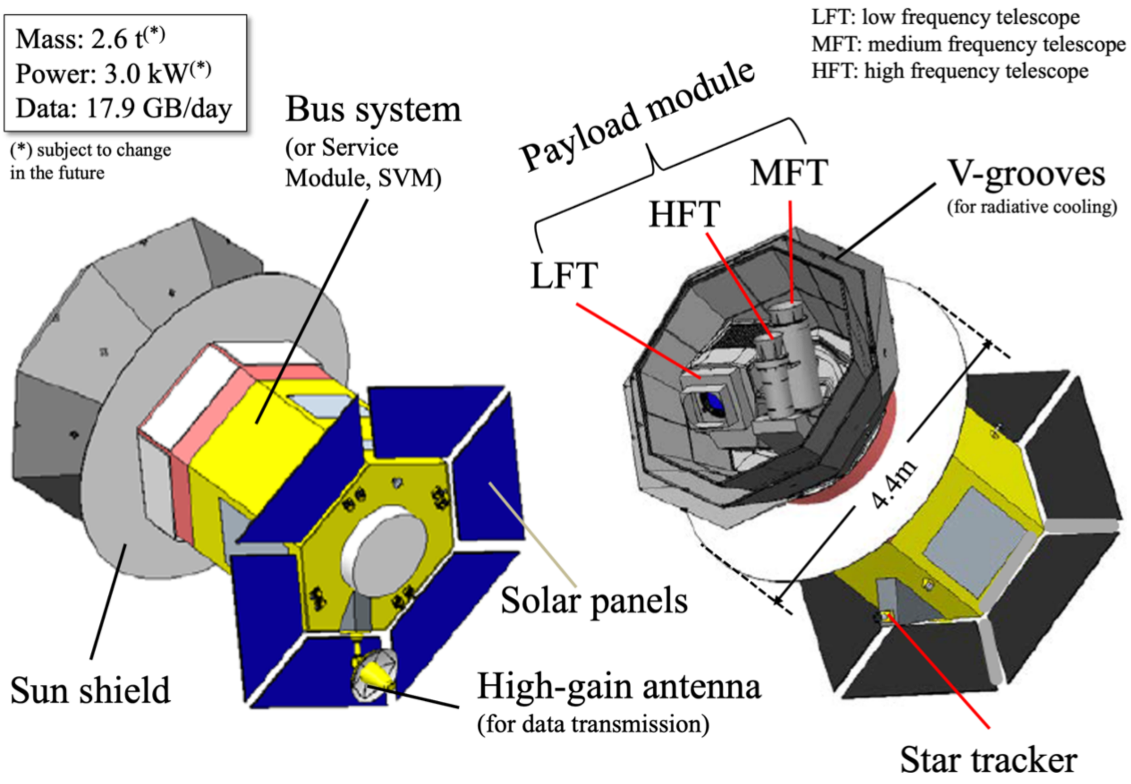

Figure 10: Conceptual design of the LiteBIRD spacecraft. Image from [28]

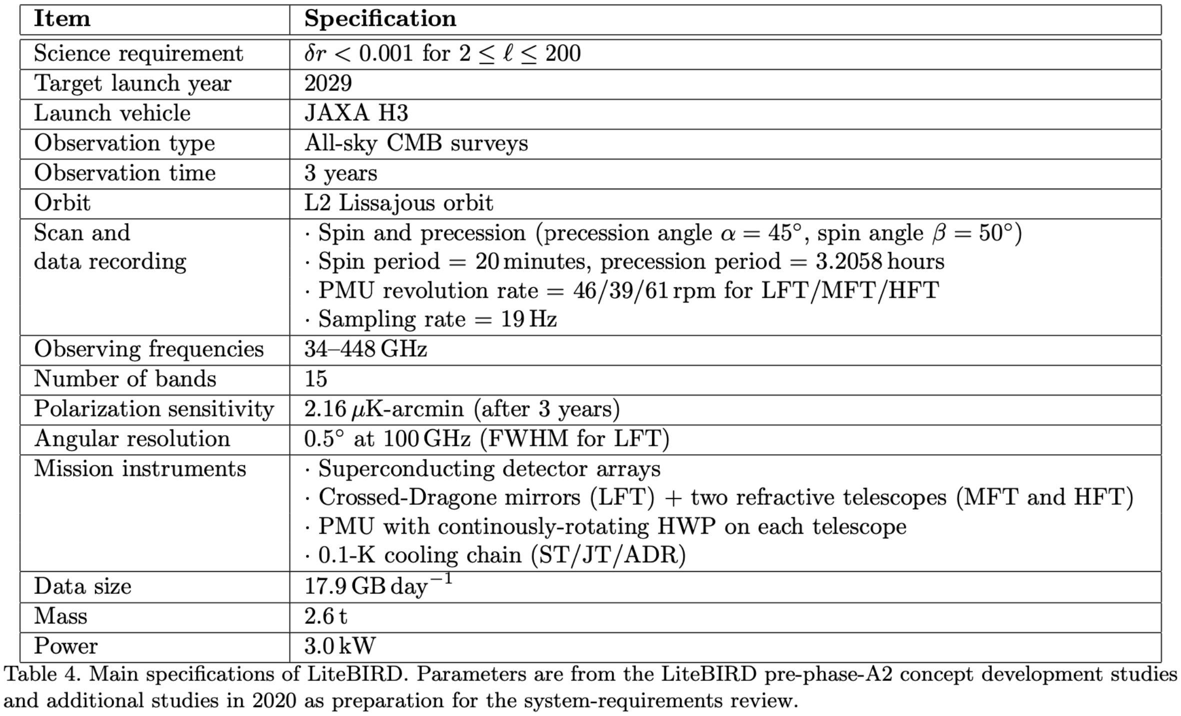

Item	Specification
Science requirement	$\delta r < 0.001$ for $2 \leq \ell \leq 200$
Target launch year	2029
Launch vehicle	JAXA H3
Observation type	All-sky CMB surveys
Observation time	3 years
Orbit	L2 Lissajous orbit
Scan and data recording	· Spin and precession (precession angle $\alpha = 45°$, spin angle $\beta = 50°$) · Spin period = 20 minutes, precession period = 3.2058 hours · PMU revolution rate = 46/39/61 rpm for LFT/MFT/HFT · Sampling rate = 19 Hz
Observing frequencies	34–448 GHz
Number of bands	15
Polarization sensitivity	2.16 μK-arcmin (after 3 years)
Angular resolution	0.5° at 100 GHz (FWHM for LFT)
Mission instruments	· Superconducting detector arrays · Crossed-Dragone mirrors (LFT) + two refractive telescopes (MFT and HFT) · PMU with continously-rotating HWP on each telescope · 0.1-K cooling chain (ST/JT/ADR)
Data size	17.9 GB day^{-1}
Mass	2.6 t
Power	3.0 kW

Table 4. Main specifications of LiteBIRD. Parameters are from the LiteBIRD pre-phase-A2 concept development studies and additional studies in 2020 as preparation for the system-requirements review.

Figure 11: Main specification of LiteBIRD. Image from [28]

1.4.1 Detectors

As mentioned above, LiteBIRD employs TES bolometers at the focal plane of each telescope. A bolometer is a detector that measures the energy of incident radiation, such as electromagnetic waves, through the heat received on a thermistor, a material has a large temperature dependent resistance. Fig. 12 shows the conceptual sketch of a bolometer and the typical resistance of the materials used as a thermistor. The bolometer has slightly higher temperature, $T_{\rm bolo}$, than the thermal bath by a combination of optical loading power, $P_{\rm opt}$, and the thermal power dissipation caused by the electrical bias, $P_{\rm bias}$. When this power balance is broken, a power flow $P_{\rm b}$ between the absorber and the bath through the weak link G occurs. The temperature change of the absorber (e.g. antenna) is detected by the thermistor. The time constant of this thermal power dissipation is defined by the heat capacity value C and the thermal conductance of the weak link G as $\tau = C/G$. A detailed treatment of bolometer theory can be found in [68]. In the case of a TES, a superconductor is used as the thermistor, and $T_{\rm bolo}$ is is moderated by biasing the TES to a point within its superconducting phase transition. Fig. 13 shows two types detector arrays for LiteBIRD. The TES is connected to an antenna coupled with a lenslet for the L/MFT and a horn for the HFT. The typical parameters of the LiteBIRD detectors are $T_{\rm bolo} \sim 160$ mK, $T_{\rm b} \sim 100$ mK, and $\tau \sim 33$ ms [77]. The Focal plane parameters of the 2020 baseline design of LiteBIRD are shown in Fig. 14.

1.4.2 Noise equivalent temperature (NET)

The Noise Equivalent CMB Temperature (NET) shown in Fig. 14 is noise equivalent power (NEP) in CMB temperature units $\rm K_{CMB}$. The NEP is the minimum power when signal-to-noise ratio of an observed signal is equal to 1. Since the NET corresponds to the noise level of observation, a

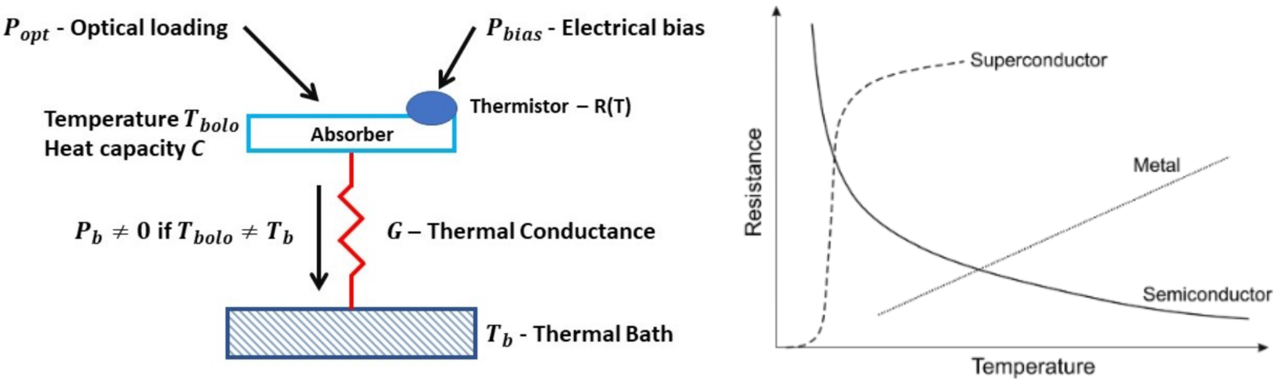

Figure 12: Conceptual sketch of a bolometer and temperature-resistance relation for normal metal, semiconductor-based, or superconducting thermistors. Image from [25]

smaller NET allows us to probe the smaller polarization signal. The noises of modern bolometers, such as TES bolometers, are listed as,

- Photon noise originating from fluctuations in the arrival times of photons at the absorber,
- Thermal carrier noise originating from thermal carrier (phonons) fluctuations in heat flow between the absorber and the bath,
- Johnson-Nyquist noise originating from fluctuations of the electric carriers in the thermistor,
- Readout noise originating from readout systems (e.g. Superconducting Quantum Interference Devices (SQUIDs)),
- External noise originated from outside sources which can be handled independently, such as cosmic rays, vibrations, magnetic fields, and so on.

The total NEP of a detected signal for a detector (bolometer), $\mathrm{NEP_{det}}$, can be written in quadrature sum NEP of each noise as,

$$\mathrm{NEP_{det}} = \sqrt{\mathrm{NEP}_\gamma^2 + \mathrm{NEP}_\mathrm{g}^2 + \mathrm{NEP}_\mathrm{j}^2 + \mathrm{NEP}_\mathrm{read}^2 + \mathrm{NEP}_\mathrm{ext}^2}\ [\mathrm{W}/\sqrt{\mathrm{Hz}}], \tag{20}$$

where NEP_γ, $\mathrm{NEP_g}$, $\mathrm{NEP_j}$, $\mathrm{NEP_{read}}$, and $\mathrm{NEP_{ext}}$ are the NEP of photon noise, thermal carrier noise, Johnson-Nyquist noise, readout noise, and external noise. The conversion from NEP to NET [31] is given by,

$$\mathrm{NET_{det}} = \frac{\mathrm{NEP_{det}}}{\sqrt{2}(\mathrm{dP}/\mathrm{dT_{CMB}})}\ [\mathrm{K_{CMB}}\sqrt{\mathrm{sec}}], \tag{21}$$

where T_CMB is CMB temperature, $\sqrt{2}$ is due to a unit conversion from output bandwidth $1/\sqrt{\mathrm{Hz}}$ to integration time $\sqrt{sec}$. The conversion factor from NEP to NET [31] is defined as,

$$\frac{\mathrm{d}P}{\mathrm{d}T_\mathrm{CMB}} = \int_0^\infty \left[\prod_{i=1}^{N_\mathrm{elem}} \eta_i(\nu) \frac{1}{k_B} \left(\frac{h\nu}{T_\mathrm{CMB} \exp \frac{h\nu}{k_B T_\mathrm{CMB}} - 1}\right)^2 \exp \frac{h\nu}{k_B T_\mathrm{CMB}} g(\nu)\right] \mathrm{d}\nu\ [\mathrm{W/K_{CMB}}], \tag{22}$$

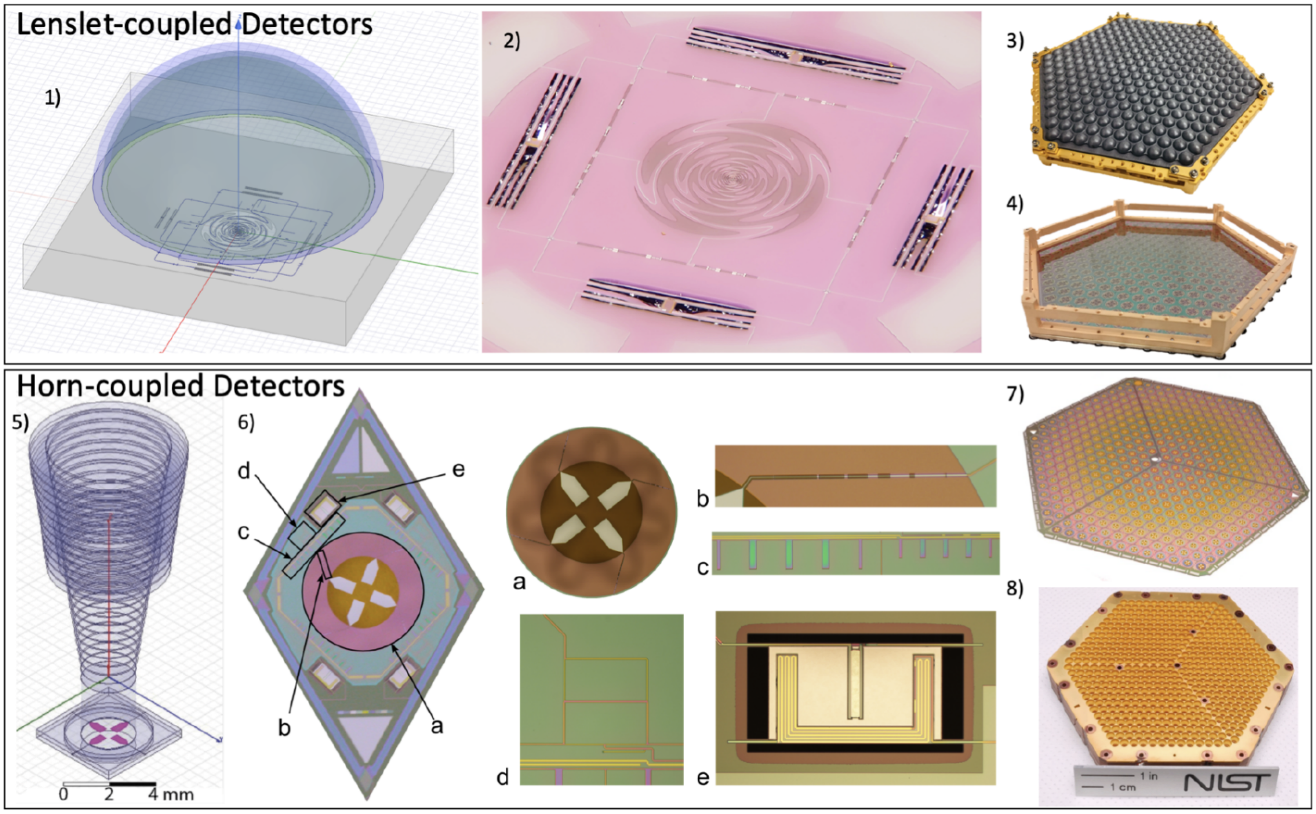

Figure 13: LiteBIRD detector arrays. Upper panel is a detector for the L/MFT focal plane and lower panel is for the HFT focal plane. No.1: Single lenslet-coupled detector. No.2: Photograph of microfabricated sinuous antenna coupled detector. No.3-4: Machined monolithic silicon lenslet array and microfabricated detector array in a gold plated detector holder. No.5: Single horn-coupled detector. No.6: Optical micrograph of detector with labeled components (a: planar orthomode transducer, b: coplanar waveguide to microstrip transition, c: diplexer, d: 180 hybrid, e: TES bolometer). No.7: Photograph of 432 element array of dichroic horn-coupled detectors and mating. No.8: silicon platelet feedhorn array. Image from [77]

where ν is frequency, N_{elem} is the number of optical elements from the sky towards the detector, $\eta_i(\nu)$ is the transmission efficiency of each optical element, h is the Planck constant, k_B is the Boltzmann constant, and $g(\nu)$ is the detector bandpass. The value $\mathrm{NET_{det}}$ is for a single detector and can be converted to a value for the detector array shown in Fig. 14 as,

$$\mathrm{NET_{arr}} = \frac{\mathrm{NET_{det}}}{\sqrt{Y N_{\mathrm{det}}}}\Gamma, \tag{23}$$

where Y is the detector yield rate, N_{det} is the total number of detectors, and the factor $\Gamma \leq 1$ quantifies the degree of correlation of white noise between detector pixels on the focal plane.

In current CMB experiments, $\mathrm{NEP_{det}}$ is limited by photon noise. In this thesis, we report mainly on the optical performance characteristics, such as transmittance and polarization efficiency, of the polarization modulator unit (see next subsection). These performances comprise one of element of $\eta_i(\nu)$ to the size of photon noise and the conversion factor of Eq. 22. For these reasons, we only introduce the formalism of photon noise. The formalism of the other noise can be found in [9, 31, 25]. As mentioned above, photon noise is caused by fluctuations in the arrival times of

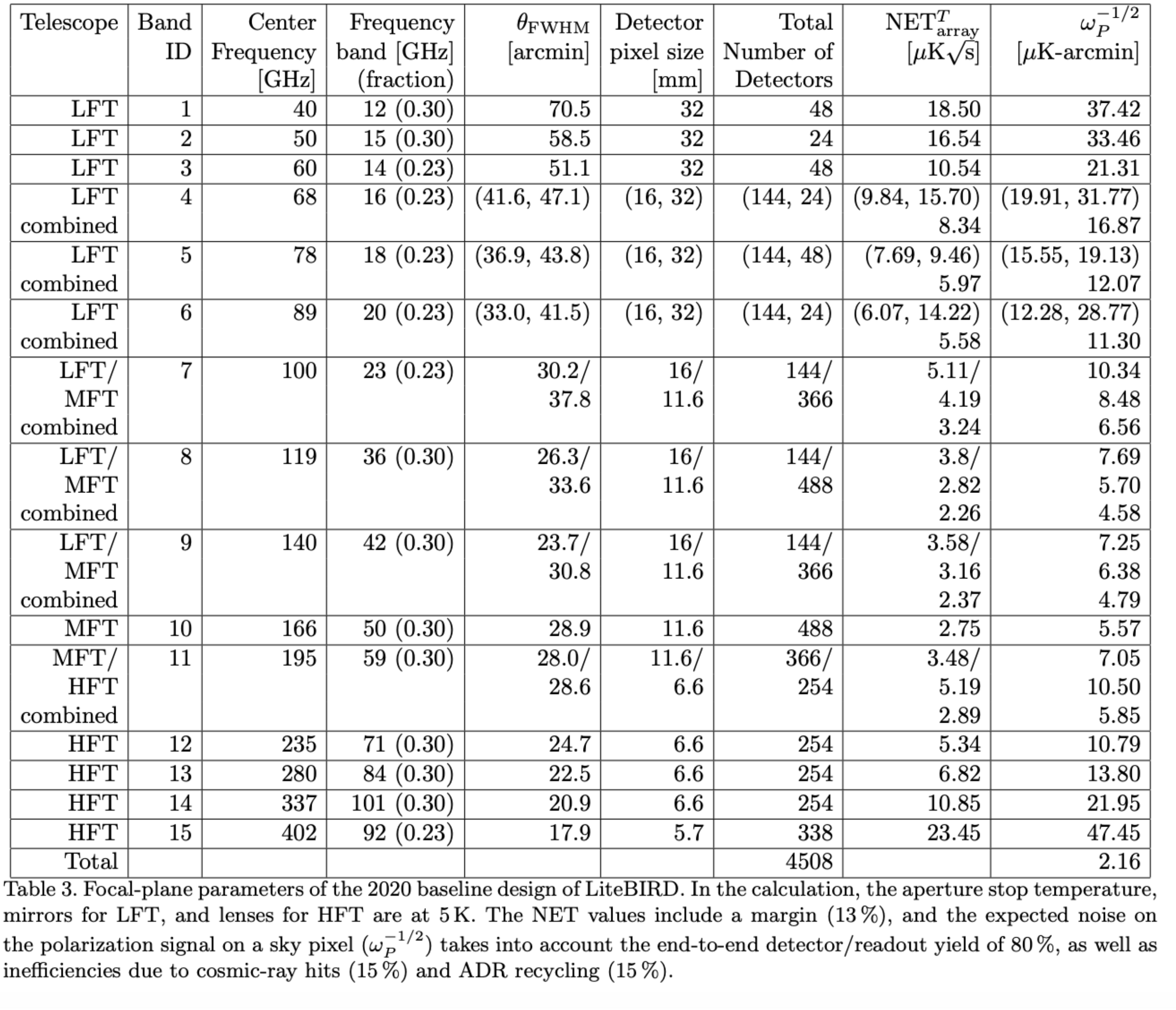

Telescope	Band ID	Center Frequency [GHz]	Frequency band [GHz] (fraction)	θ_{FWHM} [arcmin]	Detector pixel size [mm]	Total Number of Detectors	$\mathrm{NET}^{T}_{\mathrm{array}}$ [$\mu\mathrm{K}\sqrt{\mathrm{s}}$]	$\omega_P^{-1/2}$ [μK-arcmin]
LFT	1	40	12 (0.30)	70.5	32	48	18.50	37.42
LFT	2	50	15 (0.30)	58.5	32	24	16.54	33.46
LFT	3	60	14 (0.23)	51.1	32	48	10.54	21.31
LFT combined	4	68	16 (0.23)	(41.6, 47.1)	(16, 32)	(144, 24)	(9.84, 15.70) 8.34	(19.91, 31.77) 16.87
LFT combined	5	78	18 (0.23)	(36.9, 43.8)	(16, 32)	(144, 48)	(7.69, 9.46) 5.97	(15.55, 19.13) 12.07
LFT combined	6	89	20 (0.23)	(33.0, 41.5)	(16, 32)	(144, 24)	(6.07, 14.22) 5.58	(12.28, 28.77) 11.30
LFT/ MFT combined	7	100	23 (0.23)	30.2/ 37.8	16/ 11.6	144/ 366	5.11/ 4.19 3.24	10.34 8.48 6.56
LFT/ MFT combined	8	119	36 (0.30)	26.3/ 33.6	16/ 11.6	144/ 488	3.8/ 2.82 2.26	7.69 5.70 4.58
LFT/ MFT combined	9	140	42 (0.30)	23.7/ 30.8	16/ 11.6	144/ 366	3.58/ 3.16 2.37	7.25 6.38 4.79
MFT	10	166	50 (0.30)	28.9	11.6	488	2.75	5.57
MFT/ HFT combined	11	195	59 (0.30)	28.0/ 28.6	11.6/ 6.6	366/ 254	3.48/ 5.19 2.89	7.05 10.50 5.85
HFT	12	235	71 (0.30)	24.7	6.6	254	5.34	10.79
HFT	13	280	84 (0.30)	22.5	6.6	254	6.82	13.80
HFT	14	337	101 (0.30)	20.9	6.6	254	10.85	21.95
HFT	15	402	92 (0.23)	17.9	5.7	338	23.45	47.45
Total						4508		2.16

Table 3. Focal-plane parameters of the 2020 baseline design of LiteBIRD. In the calculation, the aperture stop temperature, mirrors for LFT, and lenses for HFT are at 5 K. The NET values include a margin (13 %), and the expected noise on the polarization signal on a sky pixel ($\omega_P^{-1/2}$) takes into account the end-to-end detector/readout yield of 80 %, as well as inefficiencies due to cosmic-ray hits (15 %) and ADR recycling (15 %).

Figure 14: Focal plane parameters of the 2020 baseline design of LiteBIRD. The angle, θ_{FWHM}, is the beam size in full width at half maximum (FWHM). Image from [28].

photons at the absorber. When photons move to a focal plane of the telescope through optical elements from the sky towards the detector, the optical power propagation can be modeled as a one-dimensional chain of blackbody absorbers and emitters in thermal equilibrium. At this time, the optical loading P_{opt} at the detectors is expressed as an analytic integral over the summation of Planck spectra corrected by its frequency-dependent efficiency and emissivity of each optical element [31] as,

$$P_{\mathrm{opt}} = \int_0^\infty \left[\prod_{i=1}^{N_{\mathrm{elem}}} p_i(\nu) \right] g(\nu)\mathrm{d}\nu, \tag{24}$$

where $p_i(\nu)$ is the power spectral density of the i^{th} optical element from the sky towards the focal plane. The power spectral density $p_i(\nu)$ of the i^{th} optical element is written as,

$$p_i(T_i, [\eta_{i+1}(\nu),\ ..., \eta_{N_{elem}}(\nu)], \varepsilon_i(\nu), \delta_i(\nu), T_{\delta,i}, \nu) = \prod_{j=i+1}^{N_{\mathrm{elem}}} \eta_j(\nu)[\varepsilon_i(\nu)S(T_i,\nu) + \delta_i(\nu)S(T_{\delta,i},\nu)], \quad (25)$$

using its blackbody temperature T_i, the transmission efficiency of all optics between it and the focal plane $[\eta_{i+1}(\nu),\ ..., \eta_{N_{elem}}(\nu)]$ (e.g transmittance), its emissivity $\varepsilon_i(\nu)$, its scattering coefficient δ_i (e.g reflectance), the effective temperature by which its scattered power is absorbed $T_{\delta,i}$, and the power spectral density function of the emitted and scattered power from each element $S(T,\nu)$. The power spectrum density function, $S(T,\nu)$, is obtained as the Planck spectral density for a diffraction-limited system as,

$$S(T,\nu) = \frac{h\nu}{\exp\frac{h\nu}{k_B T_{\mathrm{CMB}}} - 1}. \quad (26)$$

The NEP of photon noise is expressed using $p_i(\nu)$ as,

$$\mathrm{NEP}_\gamma = \sqrt{2\int_0^\infty \left[h\nu \sum_{i=1}^{N_{elem}} p_i(\nu) + \left(\sum_{i=1}^{N_{elem}} p_i(\nu)\right)^2\right] g(\nu)\mathrm{d}\nu}. \quad (27)$$

The first term (Poisson term) corresponds to shot noise which is dominated when the photon occupation number, expressed as $S(T,\nu)/h\nu$, is smaller than zero (at high frequency or low temperature). The second term (bunching term) corresponds to wave noise which is dominant when the photon occupation number is larger than zero (at low frequency or high temperature).

1.5 Polarization modulator unit for LiteBIRD low-frequency telescope

Each LiteBIRD telescope employ a continuously rotating broadband half-wave plate (HWP) as a polarization modulator unit (PMU). The PMU is constructed by a broadband HWP and a cryogenic rotation mechanism. The HWP rotates the polarization direction of the incident linearly polarized light by twice the angle of incidence with respect to the optic axis. In other words, the direction of polarized light passing through the continuously-rotating HWP rotates at twice the rotation speed of the HWP. When the power of the rotated polarization is measured with a detector sensitive to a single direction of light, as the power is proportional to the square of the electric field, the polarization component of the incident light can be modulated at a frequency four times the rotational speed of the HWP. This type of modulation system has been employed by EBEX [60], ABS [43], POLARBEAR [59] and is also scheduled to be deployed by POLARBEAR2 [32], LSPE/SWIPE [14], and SO [24]. In this subsection, we introduce only the PMU for LFT, which is the scope of he work reported in this thesis. Fig. 15 shows an overview of the LFT on the left and the PMU on the right. The PMU is located at the aperture of the telescope and is inclined 5 degrees to the optical axis in order to avoid ghosting effects inside the telescope caused by reflections of the HWP. The main systematic effects which are removed by using the PMU originate from the $1/f$ noise in detector response as well as any source of signal differential between two detectors in one pair, other than those measured from a real polarised signal. The polarization is measured as the Stokes parameters Q and U. Without the use of a rotating HWP, measuring Q and U requires pair-differencing (e.g. subtracting the signal of two orthogonal detectors). The difference in properties (e.g. time constant, gain, etc.) between two detectors is a possible source of major systematic effects, and can create leakage from unpolarized light (i.e. temperature) to polarization, thus creating uncertainty in the polarization direction. Since the PMU modulates measured signals by rotating the polarization direction, the PMU solves these systematic effects by measuring the power of all polarization directions using one detector [21]. As mentioned above, tacama B-Mode Search (ABS) uses a continuously-rotating HWP as a PMU. Fig. 16 shows the power spectrum density (PSD) of TES timestreams before and after the demodulation of ABS. The TES timestreams are modulated by a HWP rotated at f_m. The frequency f_{scan} is the telescope scanning frequency. The top and bottom panel show the PSD before and after demodulation. In the red line in the top panel, we can see $1/f$ noise and observed signal below 1 Hz, and a modulated

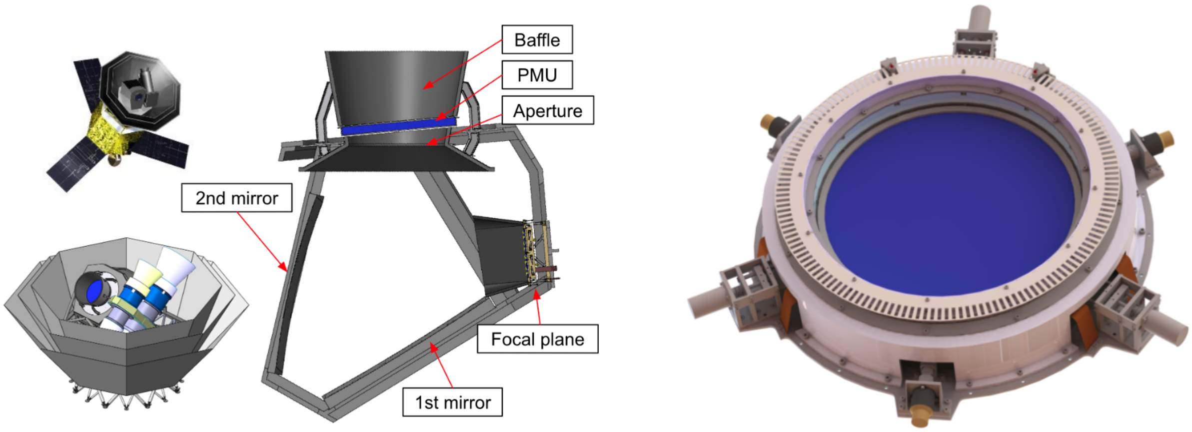

Figure 15: Overview of LFT PMU. An overview of the LFT on the left and the PMU on the right. The HWP is shown as the blue part on the right. Image from [63]

signal around $4f_m$. In the PSD after the demodulation, shown in the bottom panel, we can see that the $1/f$ noise level has been reduced to the level of the white noise.

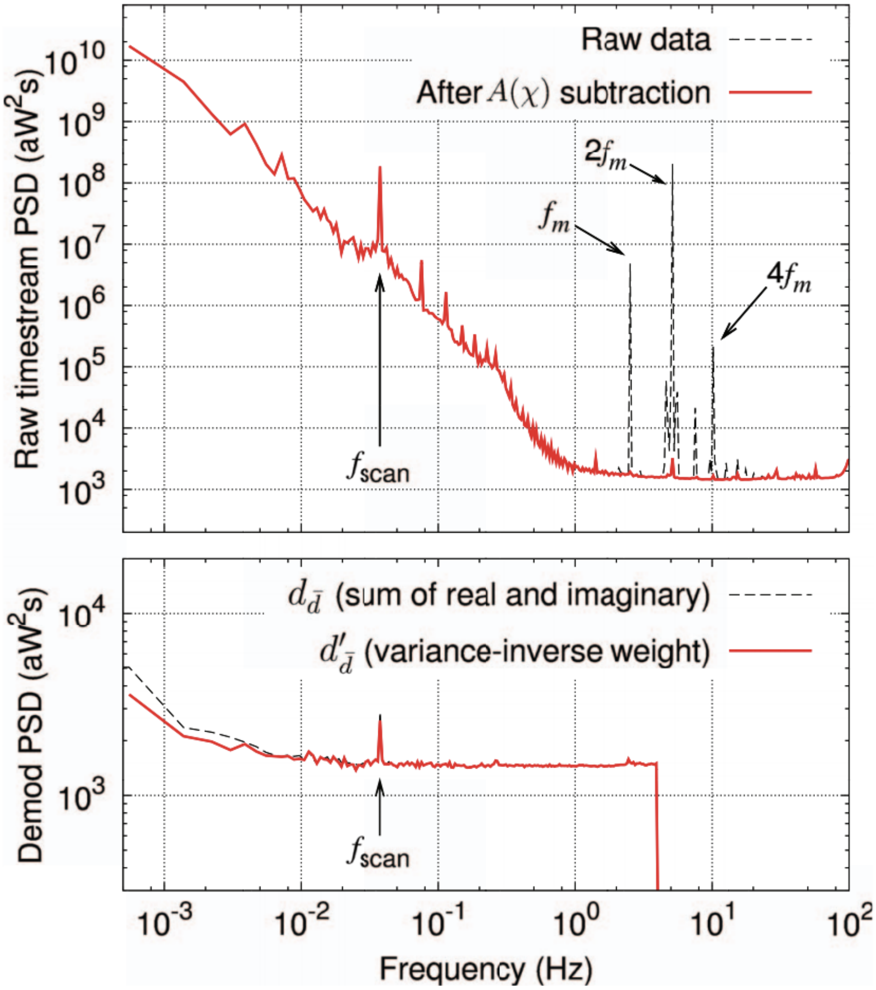

Figure 16: Power spectrum density (PSD) of TES timestreams before and after demodulation of ABS. In the top panel, a dashed line shows the PSD of the raw data and a red line shows the PSD after subtracting spurious modulation signals. The frequency, f_{scan}, is a telescope scan frequency. The frequency, f_m, is the HWP rotation frequency. The bottom panel shows the PSD of TES timestreams after demodulation. Image from [43]

1.5.1 Target values of development

In the development of the PMU for LiteBIRD LFT, we are currently developing a so-called bullet board model (BBM). Each target and achieved value in the BBM for the PMU is summarized in Fig. 17. The current optical area is 330 mm in diameter, which achieves the BBM target of $\leq$ 300 mm. We aim for a diameter of 500 mm, which corresponds to the LFT aperture size in the future work. The target values of transmittance and the polarization efficiency are determined from the sensitivity (noise) calculation shown in Sec. 1.4.2 and each value is the one of $\eta_i(\nu)$ in Eq. 22 and Eq. 25. The sum of transmittance, reflectance, and emissivity is 1. As a result, when transmittance becomes smaller, NET of a detector array becomes higher since $\varepsilon_i(\nu)$ or $\delta_i(\nu)$ of a HWP in NEP$_\gamma$ calculation become higher and $\eta_i(\nu)$ of a HWP in the conversion from NEP becomes smaller. On the other hand, polarization efficiency only affects the conversion from NEP to NET. Polarization efficiency is the efficiency of the modulation of the polarized component and does not affect the unpolarized component. From Fig. 3 or Fig. 8, the observed power from the sky is dominated by the unpolarized (temperature) component. Since NEP$_\gamma$ is calculated by taking the sum of the contributions from each optical element, the unpolarized sky component dominates this calculation. As a result, the polarization efficiency does not contribute to the NEP$_\gamma$ calculation, and NET is simply inversely proportional to the change of the polarization efficiency. The temperature target value is determined from the optical loading calculation in Sec. 1.4.2. The target value of the heat dissipation is determined by the budget assigned from the cooling power of 4 K Joule-Thomson (JT) cooler of LiteBIRD. The rotation frequency is set to a frequency enough larger than the knee frequency of the $1/f$ noise of the instruments. The encoder accuracy target value arises from the tentative polarization angle target value [69]. The mass target value is determined by the satellite system resources and the cooling power of the JT cooler. The mass of the LFT HWP is estimated as ~17 kg for 500 mm diameter scale, meaning that the mass of LFT PMU is limited by the HWP. To estimate the HWP mass, we assume a sapphire density of 3.97g/cm^2 [18] and assume that the HWP is a cylinder with a diameter of 500 mm and a thickness of 5 mm, and that the SWS is a pyramid with a height of $\sim$ 2 mm.

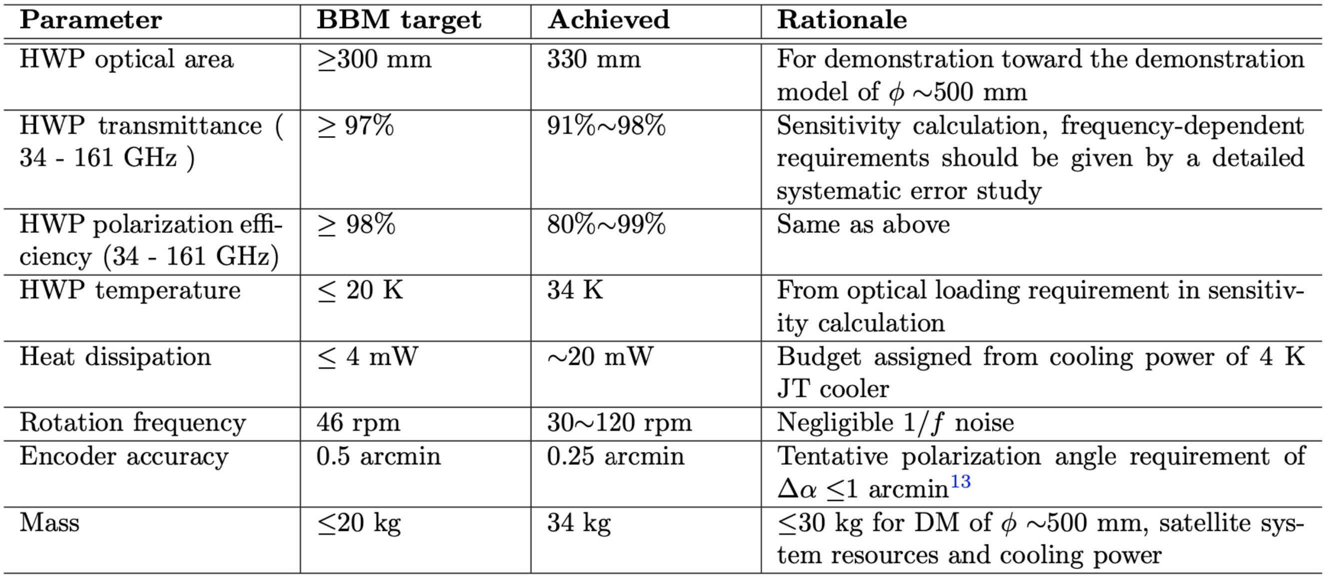

Parameter	**BBM target**	**Achieved**	**Rationale**
HWP optical area	$\geq$300 mm	330 mm	For demonstration toward the demonstration model of ϕ ~500 mm
HWP transmittance (34 - 161 GHz)	$\geq$ 97%	91%~98%	Sensitivity calculation, frequency-dependent requirements should be given by a detailed systematic error study
HWP polarization efficiency (34 - 161 GHz)	$\geq$ 98%	80%~99%	Same as above
HWP temperature	$\leq$ 20 K	34 K	From optical loading requirement in sensitivity calculation
Heat dissipation	$\leq$ 4 mW	~20 mW	Budget assigned from cooling power of 4 K JT cooler
Rotation frequency	46 rpm	30~120 rpm	Negligible $1/f$ noise
Encoder accuracy	0.5 arcmin	0.25 arcmin	Tentative polarization angle requirement of $\Delta\alpha \leq$1 arcmin[13]
Mass	$\leq$20 kg	34 kg	$\leq$30 kg for DM of ϕ ~500 mm, satellite system resources and cooling power

Figure 17: Table of target and achieve value for LFT PMU bullet board model (BBM). Image from [63]

1.5.2 Broadband half-wave plate

The LFT PMU needs to cover a wide bandwidth of 34 to 161 GHz with a single HWP, which requires the development of a broad-band HWP and a broad-band anti-reflective structure described in the next subsection. A common and simple way of producing a HWP is to use a birefringent material, and we will employ this tactic for the LFT HWP. We use sapphire as this birefringent HWP material. Sapphire has superior optical and thermal properties: about 10% difference in the refractive indices between the ordinary and the extraordinary rays [34], a low loss-tangent at millimeter-wave frequency, and a high thermal conductivity, 10^2-10^3 W/K/m, at a temperature of

4 - 10 K [58]. According to M. N. Afsar [8], the variation of the refractive index of sapphire in the frequency range of 60-400 GHz is less than 0.1% for both ordinary and extraordinary rays. A HWP works only at frequencies where the phase difference of the electric field, caused by the plate thickness and the refractive index difference between the orthogonal optic axes, is half-wave (i.e. π). Frequencies which do not satisfy this condition result in the reduction of conversion efficiency from linear to linear polarization states, which leads to the degradation of the polarized sensitivity of a polarimeter. A conventional solution to increase the bandwidth is to use a recipe proposed by Pancharatnam, which employs three wave plates stacked together with specific relative angles among them [50, 51]. In this thesis, we call this type of broadband HWP as Achromatic Half-Wave Plate (AHWP). Further investigations have addressed the extension of this original work to the five and nine layered AHWP [65, 45, 42]. A single layer HWP can achieve about 0.4 of the fractional bandwidth for the polarization efficiency of above 0.9, and an AHWP can generally cover the fractional bandwidth of 1.0, 1.3, 1.4, and 1.5 for 3, 5, 7, and 9 layers, respectively. In the current development of the LFT PMU, our baseline is to use a five layer AHWP. Details of the formalism and the design optimizations are presented in Sec. 2, and experimental validation is presented in Sec. 4. The sapphire plates which comprise the AHWP must be glued together to avoid damage due to vibrations during launch. We are planning to use a sodium silicate solution for this gluing, and details of this work can be found in T. Toda et al. [74].

1.5.3 Sub-wavelength structure

Although sapphire has excellent optical and thermal properties for a HWP, it loses about half of its signal due to reflections caused by its high refractive index ($\approx$3). For this reason, we need to develop a broadband anti-reflection method. We fabricate the Sub-Wavelength Structure (SWS) on the two surfaces of the AHWP in order to achieve broadband anti-reflection (AR) [71, 72]. The SWS AR is composed of periodically-arranged pyramidal structures as shown in the left side of Fig. 18. This technique allows the refractive index to gradually change from air to the sapphire plate, therefore minimizing the reflection at the boundary between the air and HWP. The SWS is a type of biomimetics that mimics the structure in the eyes of moths, also called moth-eye structures. The right side of Fig. 18 shows the transmittance performance of the SWS AR. From Fig. 18, we confirm that the SWS AR shows a high transmittance over a broad band. The SWS is fabricated using ultra-short-pulse laser machining [71]. The details of the fabrication methods are shown in R. Takaku et al. [71].

1.5.4 Cryogenic rotation mechanism

The LFT in LiteBIRD operates the PMU at cryogenic temperatures below 20K to reduce thermal noise. In addition, since the refrigeration capacity of the refrigerator in a satellite is limited, it is necessary to develop a cryogenic rotation mechanism with minimal heat dissipation. Fig. 19 shows the overview of a rotation mechanism of the PMU Bread Board Model (BBM). The rotation mechanism consists of a Superconducting Magnetic Bearing (SMB), a hollow-bore synchronous motor with an optical encoder, gripper mechanisms, and a launch lock. When a permanent magnet is placed on a Type II superconductor with a space, the position of the permanent magnet is fixed in a levitation state by the pinning effect of the magnetic field after the superconducting transition. The SMB is a contactless bearing that uses this effect and consists of a Type II superconductor ring and a permanent magnet ring. We use YBCO ($Y_{1.65}Ba_2Cu_3O_7$) as the superconductor ring and SmCo magnet as the magnet ring. For the SMB magnet ring, our current baseline uses SmCo

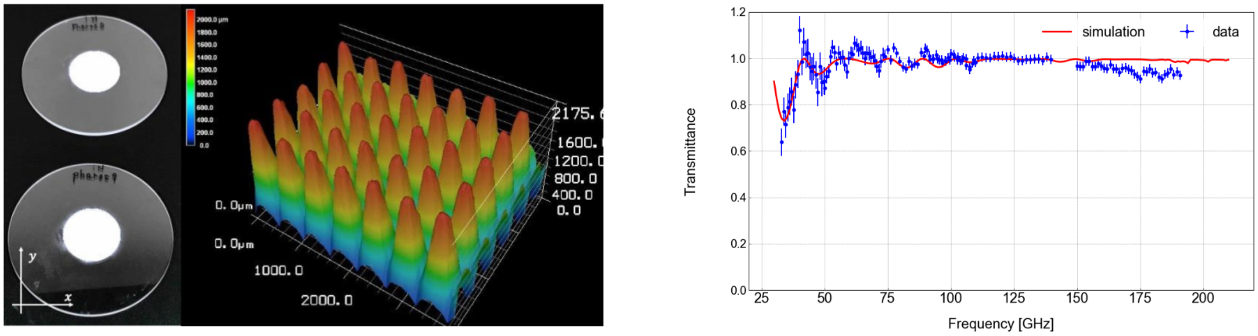

Figure 18: Picture and transmittance of Sub-Wavelength Structure (SWS). The left side shows pictures of two sapphire plates fabricated the with SWS and an image of a confocal microscopy of the SWS shape. The right side shows the transmittance performance of a plate constructed by stacking two sapphire plates, in the left, side back to back. Image from [63]

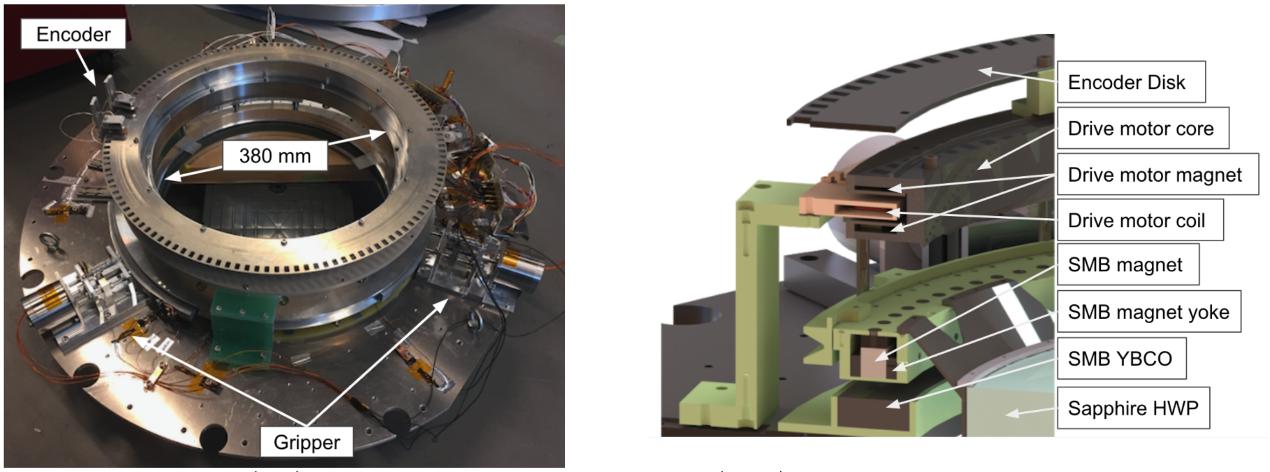

Figure 19: Cryogenic rotation mechanism overview. The left side shows a picture of the rotation mechanism of the PMU BBM. The left side shows a conceptual sketch of the rotation mechanism. Image from [63]

due to the small temperature dependence of the magnetic field, but early prototypes such as that used in Sec. 4.3 uses NdFeB magnet. Since the drive motor that rotates the rotating mechanism is also a hollow-bore synchronous motor, the rotor part rotates completely without contact and generates very low heat dissipation because there is no physical friction. Details of this work can be found in Y. Sakurai et al. [62, 63, 64].

In order to use a continuously rotating HWP as a PMU, it is necessary to know the rotation angle of the HWP accurately. In the LFT PMU, the angle is reconstructed from a signal from three optical encoders consisting of an encoder disk, silicon photodiode, and LED. The encoder disk has 128 slots (64 in subsec. 4.3) and is placed between a pair of silicon photodiode and LED. When the rotating mechanism rotates, the light from the LED is chopped by the slots, and the signal detected by the silicon photodiode becomes a square wave. Since one period of this square wave corresponds to the angle of one slot of the disk, the rotation angle of the HWP can be reconstructed. Details on the method and accuracy of this angle reconstruction can be found in S. Sugiyama et al. [69].

2 Half-wave plate design

2.1 Introduction

This section is based on K. Komatsu et al. [40, 39]. Images are taken from [40, 39]. While the AHWP achieves a broader band width of a polarization efficiency, one caveat is that it introduces a frequency dependence on the effective optic axis of the AHWP. This means that a polarimeter using an AHWP has a frequency dependent polarization angle sensitivity. The other way to phrase is that Q and U signals defined in a telescope coordinate is no longer defined by the physical orientation of a polarization sensitive axis, and it varies over the observing electromagnetic frequency. In principle, such this effect can be corrected with a perfect knowledge of a spectral response of an instrument and a source. Any limited knowledge of them can lead to the uncertainty of the polarization angle sensitive orientation. The detail of this systematics will be discussed in Sec. 3. In recent years, there are studies to investigate the impact of this effect in the context of the CMB polarization experiment. [11, 10, 19] The analysis based mitigation has been also proposed [7, 76]. The typical required accuracy of a polarization angle for future inflationary B-mode CMB polarization experiments probing the tensor-to-scalar ratio of 10^{-3} is in the range of $1-10$ arcmin for both absolute and relative angles [63, 15, 32, 13] This is a stringent calibration requirement, and it is desirable if we do not have to take into account the additional effect from the frequency dependent optic axis. In this section, we have studies the numerical optimization of the AHWP design to eliminate the spectral dependence of the effective optic axis of an AHWP.

2.2 HWP polarimetry

2.2.1 Formalism

We present the formalism of HWP polarimetry for our optimization study. Similar descriptions of the formalism can be found in K. Komatsu et al.[42, 40, 41, 39]. To reduce calculation time, we ignore the effect of reflection on any surface of a wave plate. The retardance for a single wave plate, which has refractive indices of n_o and n_e for ordinary and extraordinary rays and thickness of d, is defined as

$$\delta(\nu) = 2\pi\nu \, \frac{d|n_e - n_o|}{c}. \tag{28}$$

where ν is the frequency and c is the speed of light. A wave plate with the retardance $\delta(\nu)$ and rotation matrix with a rotation angle χ [67] are expressed in Mueller matrices as

$$\gamma(\nu) = \begin{pmatrix} 1 & 0 & 0 & 0 \\ 0 & 1 & 0 & 0 \\ 0 & 0 & \cos\delta(\nu) & -\sin\delta(\nu) \\ 0 & 0 & \sin\delta(\nu) & \cos\delta(\nu) \end{pmatrix}, \tag{29}$$

$$R(\chi) = \begin{pmatrix} 1 & 0 & 0 & 0 \\ 0 & \cos 2\chi & -\sin 2\chi & 0 \\ 0 & \sin 2\chi & \cos 2\chi & 0 \\ 0 & 0 & 0 & 1 \end{pmatrix}. \tag{30}$$

A Mueller matrix of N layers wave plates staked with relative angles χ_i for i^{th} layer can be written using rotation matrices as,

$$\Gamma(\nu) = \prod_i^N R(-\chi_i)\gamma(\nu)R(\chi_i). \tag{31}$$

Fig. 20 shows a conceptual sketch of the three layer AHWP polarimetry. Radiation passes through the AHWP and is detected by a linearly polarization-sensitive detector. When incident radiation has the Stokes parameters, $S_{\rm in}(\nu) = (I_{\rm in}(\nu), Q_{\rm in}(\nu), U_{\rm in}(\nu), V_{\rm in}(\nu))$ in unit of spectral radiance, propagates through the continuously-rotating N-layered wave plates with an rotation angle ρ, the output Stokes parameters, $S_{\rm out}(\nu) = (I_{\rm out}(\nu), Q_{\rm out}(\nu), U_{\rm out}(\nu), V_{\rm out}(\nu))$, are written as

$$S_{\rm out}(\nu) = R(-\rho)\Gamma(\nu)R(\rho)S_{\rm in}(\nu). \tag{32}$$

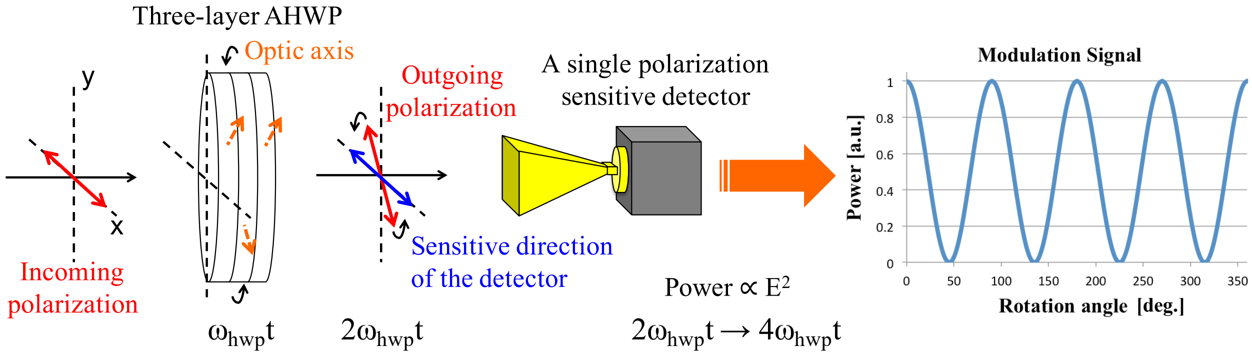

Figure 20: Conceptual sketch of the three-layer AHWP polarimetry. The linearly polarized plane waves propagate from left to right in this figure. An example of the modulated signal when the AHWP rotates once is shown in the most right hand side. The amplitude is related to the polarized intensity and the phase is related to the polarization angle of the incident radiation. Image from [42]

We define a perfect wire grid to get a measured signal of a linearly polarization-sensitive detector, and select the intensity component along the x-axis in Fig. 21 of measured Stokes parameters. As a result, the detected signal can be written as

$$I_{\rm det}(\nu) = (GS_{\rm out}(\nu))\Big|_I, \tag{33}$$

where G is a Mueller matrix of a perfect wire grid along the x-axis [67] expressed as,

$$G = \frac{1}{2}\begin{pmatrix} 1 & 1 & 0 & 0 \\ 1 & 1 & 0 & 0 \\ 0 & 0 & 0 & 0 \\ 0 & 0 & 0 & 0 \end{pmatrix}. \tag{34}$$

A Stokes parameter V is related to circular polarization. The circular polarization of the CMB is negligible. For the Galactic synchrotron emission, the circular polarization level is estimated to be about 10 nK at most for 10 GHz frequency [37] and about 4 pK at 100GHz assuming the frequency dependence of a power of -3.5 in the Rayleigh-Jeans units (a factor of 1.29 is different between Rayleigh-Jeans units and blackbody temperature at 100GHz). The circular polarization due to the dust is considered to be even lower [47]. In summary, the circular polarization from foreground components is negligible compared to the CMB B-mode polarization of about a few nK. Therefore, we set $V_{\mathrm{in}} = 0$ in this thesis.

The detected intensity $I_{det}(\nu)$ as a function of the HWP angle ρ can be written as

$$\begin{aligned} I_{\mathrm{det}}(\nu) =& D_{0\mathrm{I}}(\nu) I_{\mathrm{in}}(\nu) + D_{0\mathrm{Q}}(\nu) Q_{\mathrm{in}}(\nu) + D_{0\mathrm{U}}(\nu) U_{\mathrm{in}}(\nu) \\ &+ D_{2\mathrm{I}}(\nu) I_{\mathrm{in}}(\nu) \cos(2\rho - 2\phi_0(\nu)) + D_2(\nu)\sqrt{Q_{\mathrm{in}}(\nu)^2 + U_{\mathrm{in}}(\nu)^2} \cos(2\rho - 2\phi_2(\nu)) \\ &+ D_4(\nu)\sqrt{Q_{\mathrm{in}}(\nu)^2 + U_{\mathrm{in}}(\nu)^2} \cos(4\rho - 4\phi_4(\nu)). \end{aligned} \tag{35}$$

The polarization efficiency and phase are defined as $2D_4(\nu)$ and $\phi_4(\nu)$, respectively. This phase is corresponding to the effective optic axis angle of the AHWP. It is worth stressing that these polarization efficiency and phase depend on the incident radiation frequency for an AHWP while the phase is frequency independent for a single HWP. Each coefficient and phase can be written using Mueller matrix elements of $\Gamma(\nu)$ as

$$\begin{aligned} D_{0\mathrm{I}}(\nu) &= \frac{1}{2} M_{\mathrm{II}}(\nu), \\ D_{0\mathrm{Q}}(\nu) &= \frac{1}{4}(M_{\mathrm{QQ}}(\nu) + M_{\mathrm{UU}}(\nu)), \\ D_{0\mathrm{U}}(\nu) &= \frac{1}{4}(M_{\mathrm{QU}}(\nu) - M_{\mathrm{UQ}}(\nu)), \\ D_{2\mathrm{I}}(\nu) &= \frac{1}{2}\sqrt{M_{\mathrm{UI}}(\nu)^2 + M_{\mathrm{QI}}(\nu)^2}, \\ \phi_0(\nu) &= \frac{1}{2}\arctan\frac{M_{\mathrm{UI}}(\nu)}{M_{\mathrm{QI}}(\nu)}, \\ D_2(\nu) &= \frac{1}{2}\sqrt{M_{\mathrm{IQ}}(\nu)^2 + M_{\mathrm{IU}}(\nu)^2}, \\ \phi_2(\nu) &= \frac{1}{2}\arctan\frac{M_{\mathrm{IU}}(\nu)}{M_{\mathrm{IQ}}(\nu)} + \frac{1}{2}\arctan\frac{U_{\mathrm{in}}(\nu)}{Q_{\mathrm{in}}(\nu)}, \\ D_4(\nu) &= \frac{1}{4}\sqrt{(M_{\mathrm{QQ}}(\nu) - M_{\mathrm{UU}}(\nu))^2 + (M_{\mathrm{QU}}(\nu) + M_{\mathrm{UQ}}(\nu))^2}, \\ \phi_4(\nu) &= \frac{1}{4}\arctan\frac{M_{\mathrm{QU}}(\nu) + M_{\mathrm{UQ}}(\nu)}{M_{\mathrm{QQ}}(\nu) - M_{\mathrm{UU}}(\nu)} + \frac{1}{4}\arctan\frac{U_{\mathrm{in}}(\nu)}{Q_{\mathrm{in}}(\nu)}, \end{aligned} \tag{36}$$

where the element of $\Gamma(\nu)$ is generalized as

$$\Gamma(\nu) = \begin{pmatrix} M_{\mathrm{II}}(\nu) & M_{\mathrm{IQ}}(\nu) & M_{\mathrm{IU}}(\nu) & M_{\mathrm{IV}}(\nu) \\ M_{\mathrm{QI}}(\nu) & M_{\mathrm{QQ}}(\nu) & M_{\mathrm{QU}}(\nu) & M_{\mathrm{QV}}(\nu) \\ M_{\mathrm{UI}}(\nu) & M_{\mathrm{UQ}}(\nu) & M_{\mathrm{UU}}(\nu) & M_{\mathrm{UV}}(\nu) \\ M_{\mathrm{VI}}(\nu) & M_{\mathrm{VQ}}(\nu) & M_{\mathrm{VU}}(\nu) & M_{\mathrm{VV}}(\nu) \end{pmatrix}. \tag{37}$$

To account for the finite band width, we integrate the detected signal over the band width as

$$\langle I_{det} \rangle = \int_0^\infty w(\nu) I_{det}(\nu) d\nu, \tag{38}$$

where $w(\nu)$ is a weight function for taking into account each frequency dependence of a telescope (e.g. band shape, beam effect). When we pick up the part from Eq. 38 corresponding to the final term in Eq. 35, it can be written as

$$\int_0^\infty w(\nu)D_4(\nu)\sqrt{Q_{\text{in}}(\nu)^2+U_{\text{in}}(\nu)^2}\cos(4\rho-4\phi_4(\nu))d\nu = A_4\cos(4\rho-4\Phi_4). \tag{39}$$

The band averaged polarization efficiency and phase from $\langle I_{det}\rangle$ relate as $2A_4$ and Φ_4.Therefore, we use $2A_4$ as the figure of merit and the relative angles of the wave plates χ_i as optimization variables. The thickness of each plate can be used as another optimization parameter, but we did not find the use in our analysis as described in the later subsections.

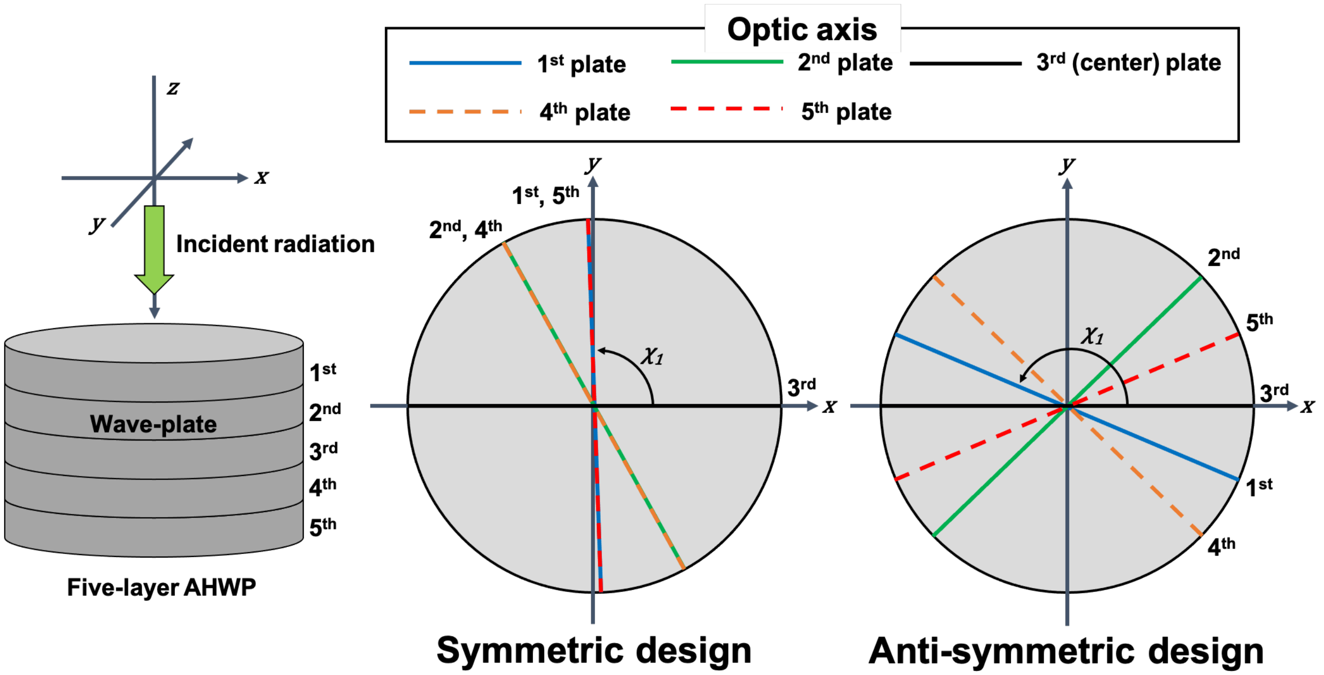

Figure 21: Conceptual sketch of the symmetric and anti-symmetric designs for the case of a five-layer AHWP. Image from [40, 39].

Table 1: A summary of the parameters used for the optimization process. Table from [40, 39].

Frequency range, ν	$34-161$ GHz
Center frequency, ν_0	97.5 GHz
Refractive indices, (n_o, n_e)	$(3.047, 3.361)$ [34]
Thickness of each plate, d	4.9 mm
Incident angle	0 degrees

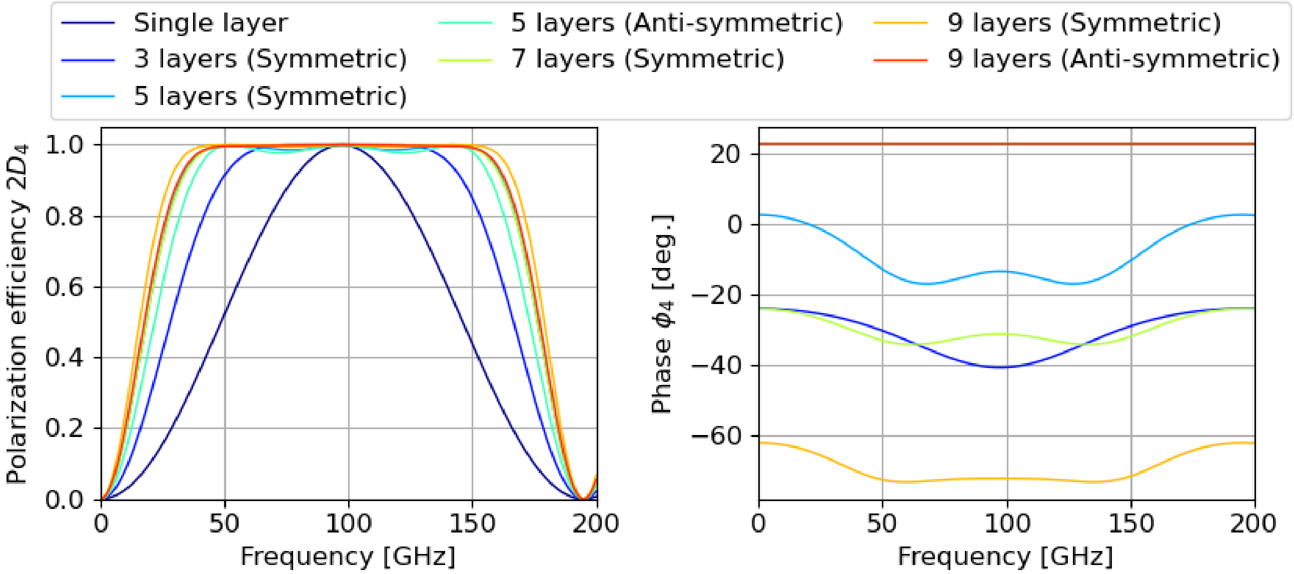

Figure 22: Comparison of polarization efficiency and phase of each design. In the phase plot, the line of the 5 layer anti-symmetric case is under the line of the 9 layer anti-symmetric case. Image from [39].

2.2.2 Optimization

To achieve the frequency-independent phase, we set the condition for angle set χ_i to be that each optic axis angle is oriented as anti-symmetric with respect to the angle of the center plate as shown in Fig. 21. Hereafter, we call this type of AHWP design as "anti-symmetric design". This condition is key to realize the frequency-independent optic axis over the broadband. We describe how the polarization angle rotates through an AHWP using a five layer anti-symmetric design as an example. In the anti-symmetric design, the first and fifth plates are rotated by the same angle in opposite directions about the orientation of the third axis. The fourth and second plates are rotated similarly, but at a different angle than the first and fifth plates. Namely, we impose the conditions of $\chi_4 = -\chi_2$ and $\chi_5 = -\chi_1$ in case of $N = 5$. In this way, any frequency dependence of phase introduced by the first 2.5 plates at each frequency is canceled by the second 2.5 plates. While we achieve the cancellation of the frequency dependent phase, we still achieve the rotation of the incoming linear polarization plane as the AHWP rotates. A similar concept can be found for the case which two sets of the AHWPs are employed to cancel the frequency dependent effective optic axis response [46]. With this condition, we do not randomize all the χ_i angles fully, but randomize only the $(N-1)/2$ plates of the N-layer AHWP. It leads to a reduction in computational power.

We demonstrate the optimization of the AHWP design under the anti-symmetric condition with a specific observational frequency range. LiteBIRD [28] is one of candidates to apply our AHWP designs. The LiteBIRD low frequency telescope [66] has the largest frequency coverage, 34-161 GHz, within a single telescope with a presence of a HWP to date. Thus, we use this range in our study as an example. In a real application, we should be able to derive the optimized recipe by taking into account a more detailed band shape, but this is beyond the scope of this section. So that we assume a top-hat band shape in this frequency range (i.e $w(\nu) = 1/N_f$ where N_f is number

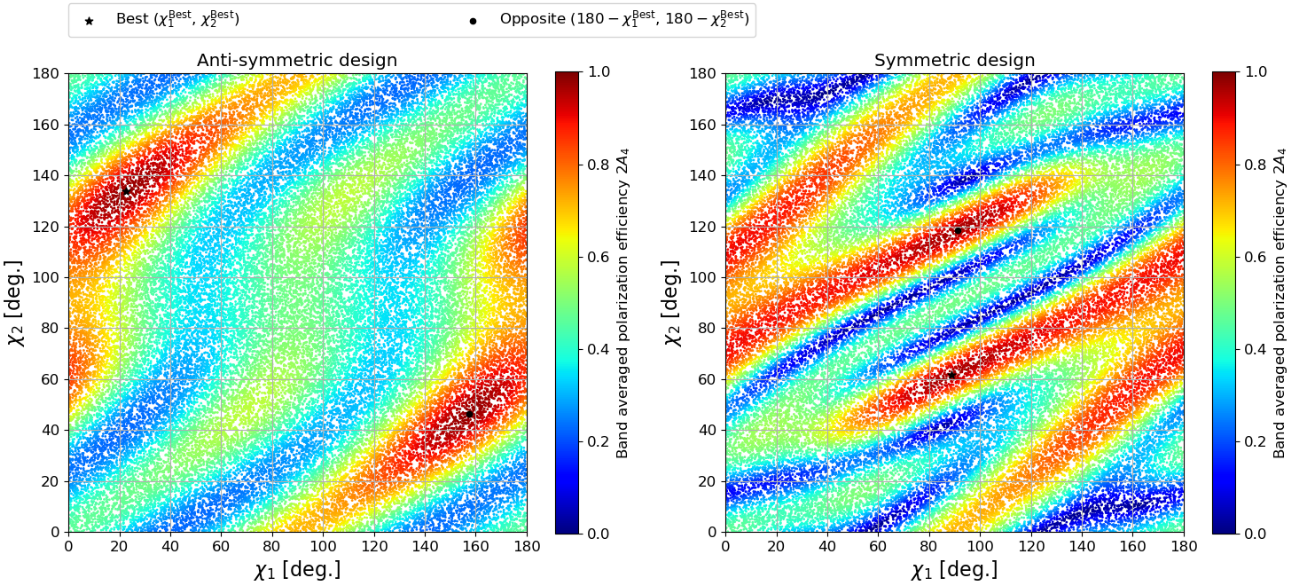

Figure 23: The color map of band averaged polarization efficiency $2A_4$ for $N = 5$ anti-symmetric design (left) and symmetric design (right). χ_1 and χ_2 are the angle of first and second layers. The optimized designs in Tab. 2 and Tab. 3 are shown as χ_1^{Best}, χ_2^{Best} and a black star. For comparison, we also show an angle set that has opposite sign to the optimized design.

of frequencies). In this work, we use A-cut sapphire as a wave plate. The set of the parameters used in this design work is summarized in Tab. 1.

In the optimization calculation, the integration of Eq. 40 is replaced by summation with the frequency resolution of 1 GHz as

$$\sum_{\nu=\nu_i}^{\nu_f} w(\nu) D_4(\nu) \sqrt{Q_{\rm in}(\nu)^2 + U_{\rm in}(\nu)^2} \cos(4\rho - 4\phi_4(\nu)) = A_4 \cos\left(4\rho - 4\Phi_4\right), \tag{40}$$

where ν_i and ν_f is an initial and final frequency of frequency band used to be optimized. We calculate $2A_4$ a total of 50,000 times with flat distribution of χ_i between 0 and 180 degrees for $S_{in} = (1, 0, 1, 0)$ and find the optimal AHWP designs for 3, 5, 7, 9 layers. From this calculation, we choose a set of χ_i angles that provide the largest $2A_4$ over the given frequency range. Note that the calculated $2A_4$ and Φ_4 does not depend on the detailed choice of $Q_{\rm in}$ and $U_{\rm in}$ except for an offset of Φ_4.

We have only explored the case with an odd number of wave plates because broadband AHWP designs are existed in past studies [42, 27, 65, 53]. It is worth pointing out that these existing designs tend to have relative optic axis angles oriented in symmetrically with respect to the angle of the center plate. In order to compare the results of our anti-symmetric design to conventional designs, we also compute the case in which the optic axis angles are oriented symmetrically with respect to the angle of the center plate as shown in Fig. 21. Hereafter, we call this type of conventional AHWP design as the “symmetric design”.

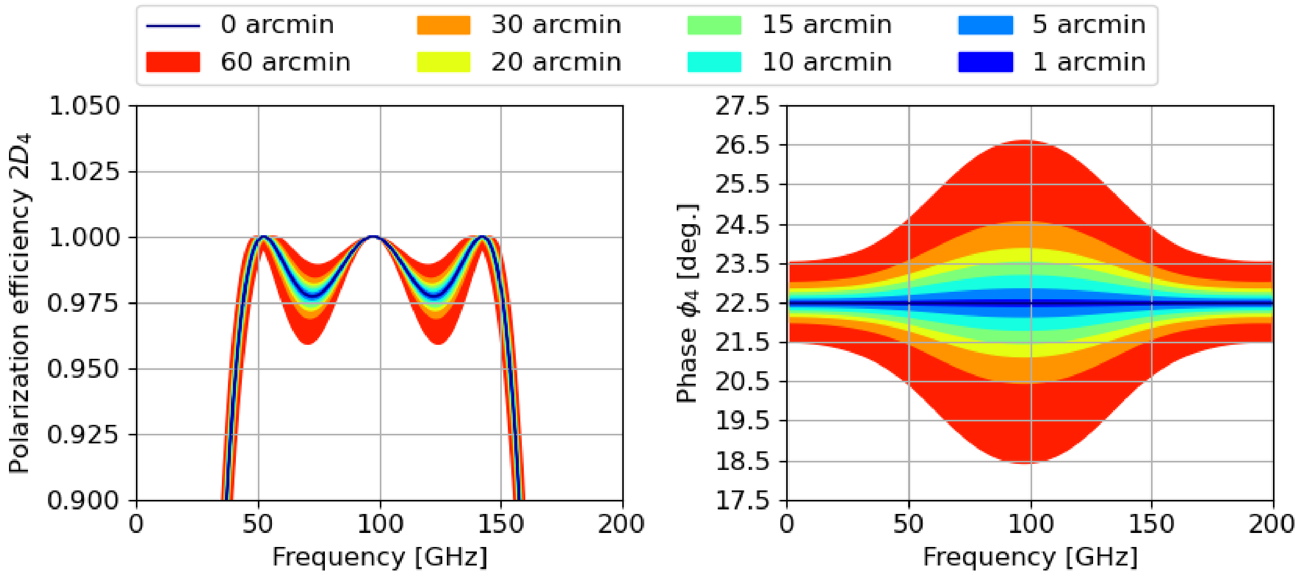

Figure 24: The relation between alignment accuracy of the optic axis angles of each plate and performances of the $N = 5$ anti-symmetric design. The left panel shows polarization efficiency and the right panel shows phase. Image from [39].

2.3 Results

Tab. 2 and 3 show the parameter search results. To see the frequency coverage, we list the fractional band width $\Delta\nu/\nu_0$ that is the ratio of the frequency range with polarization efficiency $2D_4$ greater than 0.9 to a center frequency of 97.5 GHz. The band-averaged polarization efficiency $2A_4$ and the maximum phase differences $\Delta\phi_4$ computed within the frequency range in Tab. 1 are also listed. As mentioned in above, in the case of $N = 5$, only two angles of the first and second plates are randomized, so the angle set and the band averaged polarization efficiency $2A_4$ can be represented as a color map. Fig. 23 shows two color maps for the $N = 5$ anti-symmetric and symmetric designs. Each color dot shows the searched angle set. The angle sets in Tab. 2 and 3 are shown as a black star and dot. From Fig. 23, we find that all the value ranges are searched almost uniformly and that the values of Tab. 2 and 3 are well optimized. Fig. 22 shows polarization efficiency and phase ϕ_4 as a function of the frequency calculated using the angle set listed in Tab. 2 and 3 for $S_{in} = (1, 0, 1, 0)$. The symmetric designs show a broad coverage of the polarization efficiency and non-flat phase response over frequency. On the other hand, the anti-symmetric designs of $N = 5$ and 9 can completely eliminate the phase variation over frequency while the polarization efficiency is maintained to be broad. The demonstrations of the $N = 5$ anti-symmetric design assembled with an optic axis alignment accuracy of 1 degree can be found in Komatsu et al. [41] and Sec. 4.3.

We also computed the $N = 3$ and 7 anti-symmetric designs. For $N = 3$, we found the solution to be $\chi_i = (90.00, 0.00, -90.00)$ degrees, which is essentially the same as a single layer HWP. For $N = 7$, we found the solution to be $\chi_i = (111.73, 43.70, 97.20, 0.00, -97.20, -43.70, -111.73)$ degrees but the calculated polarization efficiency and fractional band width are close to $N = 5$. Therefore, we omit to show these in the table and figure due to redundancy.

The solutions which we have shown in Tab. 2 and 3 are not unique. For example with the angle set for the $N = 5$ anti-symmetric design, the same performance can be obtained by the angle set of

$$\chi_1 = 22.67 \pm 180 \times j \tag{41}$$
$$\chi_2 = 133.63 \pm 180 \times j \tag{42}$$
$$\chi_3 = 0.00 \pm 180 \times j \tag{43}$$
$$\chi_4 = -133.63 \pm 180 \times j \tag{44}$$
$$\chi_5 = -22.67 \pm 180 \times j \tag{45}$$

in units of degrees, where j is an arbitrary integer because of the spin-2 nature of the wave plate. And from Fig. 23, we also confirm that the same performance can be obtained when all optic axis angles have opposite sign. Therefore, the set of angles may look different but multiple combinations of angles can produce the same performance. Needless to say, there are overall rotational degrees of freedom, thus any global rotation, i.e. $\chi_3 \neq 0$, added to all the angles χ_i still provides the same spectral performance except for the change of the global phase offset of ϕ_4.

The quoted band width of polarization efficiency in Tab. 2 and 3 should be treated as a representative value. From Fig 22, we find that in some designs, such as $N = 5$ anti-symmetric design, have oscillatory features around the polarization efficiency close to 1. Depending on the application, when we allow to have more large oscillatory features, we obtain the broader band width by trading the degradation of the overall averaged efficiency. In such case, we can increase the fractional band width. This point is addressed in Sec. 2.4.2.

Table 2: A summary of anti-symmetric designs. The the maximum phase difference, $\Delta\phi_4$, is completely zero. Table from [39].

The number of layers N	Fractional band width $\Delta\nu/\nu_0$	Pol. eff. $2A_4$	Phase diff. $\Delta\phi_4$[deg.]	Optic axis angles χ_i [deg.]
5	1.23	0.978	0.0	22.67 , 133.63 , 0.00 , -133.63 , -22.67
9	1.35	0.993	0.0	23.19 , 170.88 , 89.85 , 143.85 , 0.00 , -143.85 , -89.85 , -170.88 , -23.19

Table 3: Table of symmetric designs. Table from [39].

The number of layers N	Fractional band width $\Delta\nu/\nu_0$	Pol. eff. $2A_4$	Phase diff. $\Delta\phi_4$[deg.]	Optic axis angles χ_i [deg.]
3	1.00	0.894	13.9	58.35 , 0.00 , 58.35
5	1.33	0.965	11.9	88.65 , 61.68 , 0.00 , 61.68 , 88.65
7	1.32	0.989	5.1	49.76 , 99.86 , 23.20 , 0.00 , 23.20 , 99.86 , 49.76
9	1.42	0.993	4.8	1.83 , 66.92 , 15.36 , 132.66 , 0.00 , 132.66 , 15.36 , 66.92 , 1.83

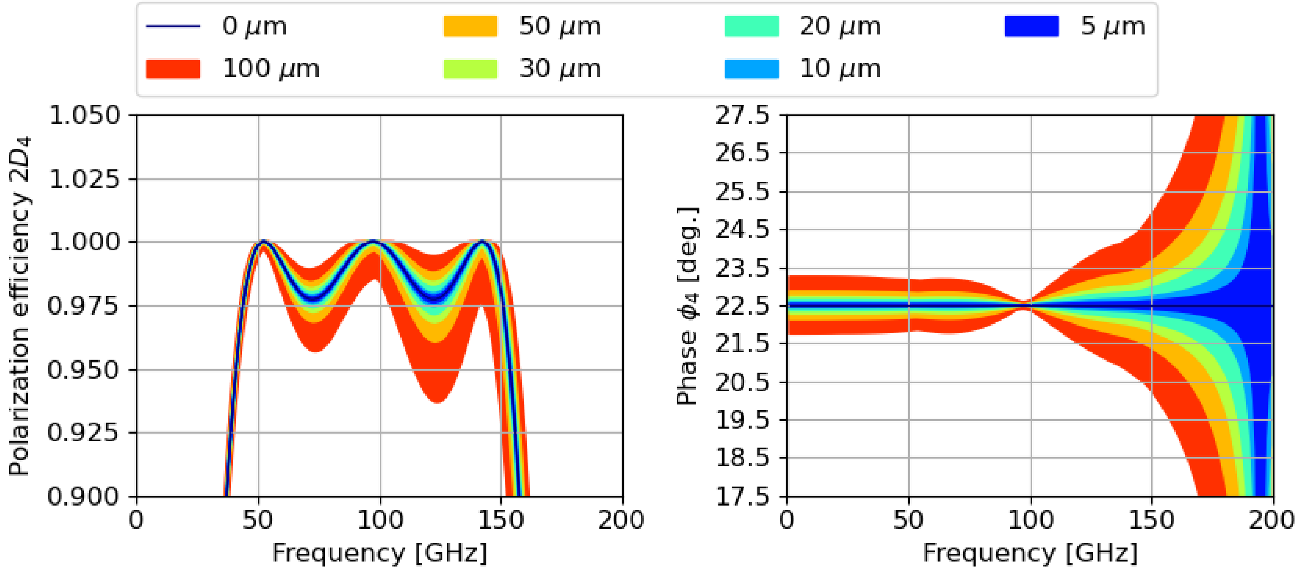

Figure 25: The relation between the variation of each wave plate thickness and performances of the $N = 5$ anti-symmetric design five-layer AHWP. Image from [39].

2.4 Discussions

2.4.1 Tolerance analysis

LiteBIRD plans to use a five layer AHWP instead of a nine layer AHWP due to the requirement for HWP weight and so on [63]. Therefore, we discuss tolerance analysis for the $N = 5$ anti-symmetric design as an example.

Optic axis angle alignment We evaluate the relation between the alignment accuracy of χ_i and AHWP performances, polarization efficiency and phase in the case of the $N = 5$ anti-symmetric design. We fix all the parameters except for the relative HWP angles χ_i, which are randomized with flat distributions for each plate in the range of 1, 5, 10, 15, 20, 30 and 60 arcmin centered at the nominal designed angles. Fig. 24 shows the susceptibility of the frequency dependence of the polarization efficiency and phase for the alignment accuracy of each optic axis angle. We perform this calculation 10,000 times for each case to obtain the range of the performances. From Fig. 24, for example, the alignment accuracy of the optic axis angle is required to be less than 15 arcmin to suppress the maximum deviation of the frequency dependent phase to be less than 1 degree.

The alignment accuracy of the rotational angle between the plates can be achieved to < 10 arcmin [42] by aligning the orientation flat between the plates using a properly designed alignment jig, e.g. a universal measurement machine. The orientation flat can be machined to each plate, and its accuracy can be about a degree without any effort and can be sub-degree level if the crystal orientation is determined by using X-ray diffraction.

Wave plate thickness We also perform the tolerance analysis to the accuracy of the wave plate thickness. Fig. 25 shows the polarization efficiency and phase when we add the flat distribution of the random thickness within the range of $5, 10, 20, 30, 50,$ and 100 μm to the nominal thickness for the $N = 5$ anti-symmetric design. Each plate thickness is varied independently without any correlation among the plates. We assume that the plates are always adjacent to each other without any gap. From these Fig. 25, we identify that the impact is prominent at the higher frequency for both of the polarization efficiency and phase. The reason is simply because the higher frequency is more susceptible to small changes of the thickness in order to maintain the same retardance as shown in Eq. 28. At 195 GHz, since the retardance with the nominal thickness is 2π, and thus $A_4 = 0$, no phase can be defined and its error becomes larger. The impact of the uncertainty to the phase is also propagated from the last equation in Eq. 36 because the element of the Mueller matrix Γ is a function of the retardance. From Fig. 25, for example, in order to minimize the maximum phase variation in the frequency range from 34 to 161 GHz to be less than 1 degree, thickness variation has to be controlled to be less than 20 μm.

Sapphire disk with a diameter of 50 mm or larger can be commercially available with an accuracy of 0.1 mm. The measurement accuracy can be higher to 10 μm without serious effort, and therefore the AHWP designer can account the thickness variation as a part of the input design parameters. The surface accuracy of a sapphire disk can be a few tens of μm for 50 mm size diameter but this can be challenging to maintain small as the diameter becomes larger, e.g. 300 mm. Komatsu et al. [42] found the surface accuracy of the sapphire for the diameter of 100 mm to be less than 8 μm. Toda et al. [74] shows the 7 μm surface accuracy for the diameter of 50 mm sapphire disk plate.

Table 4: Table of the $N = 5$ anti-symmetric designs optimized with the various frequency ranges. The polarization efficiencies for the top three frequencies deviate from 1 by orders of 10^{-6}, 10^{-5}, and 10^{-4}, respectively. We omit the phase difference since the phase is frequency independent for the anti-symmetric design. Table from [39].

Optimization freq. range $\Delta\nu_{opt}$ [GHz]	Optimization band width $\Delta\nu_{opt}/\nu_0$	Fractional band width $\Delta\nu/\nu_0$	Polarization efficiency $2A_4$	Optic axis angles χ_i [deg.]
84 – 111	0.28	1.02	1.000	23.28 , 128.13 , 0.00 , -128.13 , -23.28
74 – 121	0.48	1.04	1.000	157.34 , 51.92 , 0.00 , -51.92 , -157.34
64 – 131	0.69	1.09	1.000	23.11 , 129.59 , 0.00 , -129.59 , -23.11
54 – 141	0.89	1.12	0.998	23.55 , 130.70 , 0.00 , -130.70 , -23.55
44 – 151	1.10	1.17	0.993	156.95 , 48.05 , 0.00 , -48.05 , -156.95
34 – 161	1.30	1.23	0.978	22.67 , 133.63 , 0.00 , -133.63 , -22.67
24 – 171	1.51	1.28	0.945	157.83 , 45.21 , 0.00 , -45.21 , -157.83
14 – 181	1.71	1.31	0.886	157.98 , 44.07 , 0.00 , -44.07 , -157.98
4 – 191	1.92	1.33	0.806	21.51 , 136.51 , 0.00 , -136.51 , -21.51

2.4.2 Further optimization for broader frequency coverage

As mentioned in Sec. 2.3, when we allow an oscillatory features at the frequency of the polarization efficiency close to 1, we can broaden the band width. Conversely, when we do not allow the oscillatory features, the available band width becomes narrower. To confirm this effect, we optimize with nine frequency ranges for the $N = 5$ and 9 anti-symmetric design.. Specifically, we start with a frequency range of 34-161 GHz and add/subtract 10 GHz to widen/narrow the band width. Tab. 4 and 5 show the optimization results for each case. We define the optimization band width

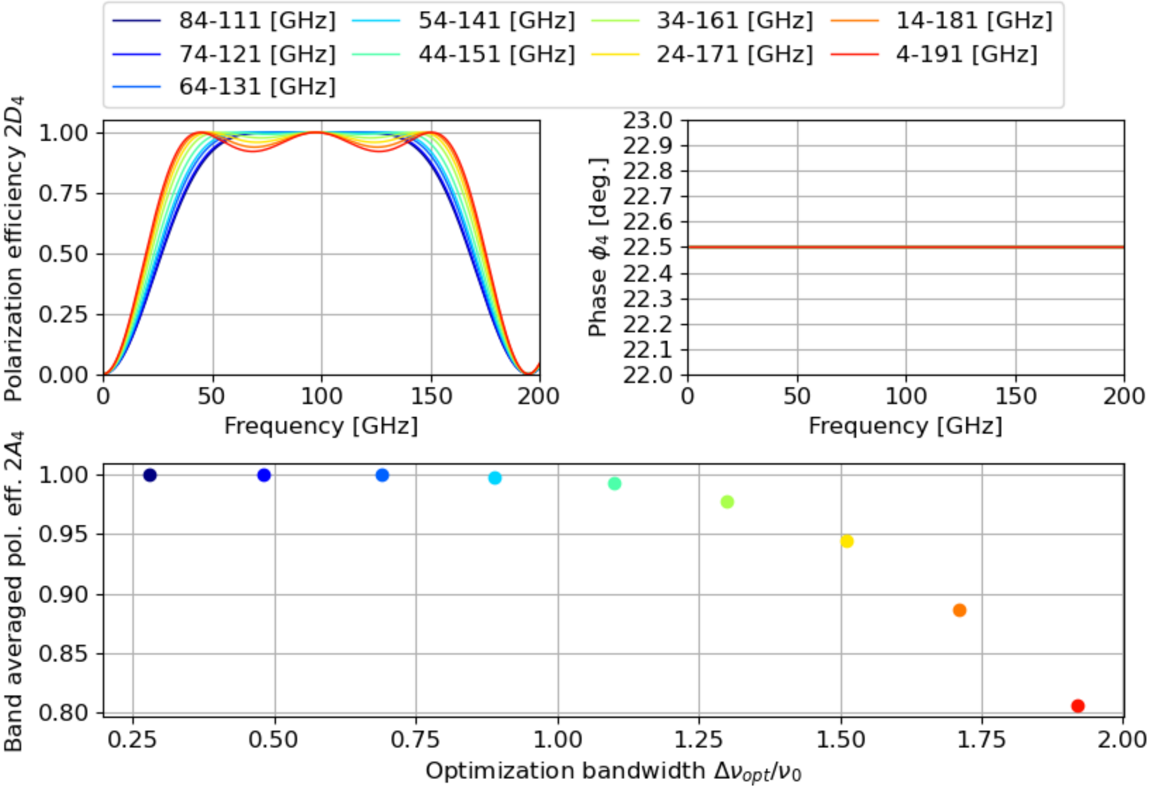

Figure 26: The comparison of the polarization efficiency and the effective optic axis angle of Tab. 4. The horizontal axis of the bottom plot is the ratio of the optimization frequency range to the canter frequency. In the phase plot, the all lines are overlap since the all design have same value. Image from [40, 39]

as $\Delta\nu_{opt}/\nu_0$, which is the ratio of the targeted optimization range, $\Delta\nu_{opt}$, to the center frequency of 97.5 GHz. Fig. 26 shows the polarization efficiency, phase, and band averaged polarization efficiency over the optimization band width for all the cases of $N = 5$. From the top-left panel of Fig. 26, we confirm that the optimized design has larger oscillatory features of polarization efficiency when we use optimization band width. An AHWP designer has to take into account the trade-off between the broadband availability and the overall averaged polarization efficiency based on each application. This consideration applies the same for both the symmetric and anti-symmetric designs.

2.4.3 Further design optimization with larger degree of freedoms

The optimizations done in this section were carried about by assuming the fixed thickness of each wave plate and by imposing the anti-symmetric condition so far. Here, we do not enforce these symmetric and anti-symmetric conditions. As a result, we take the thickness of all the wave plates and all the relative angles as the free parameters and carry out the optimization with the figure-of-metric of $2A_4$ for the frequency range of 34-161 GHz. We choose for $N = 9$, which gives $8+9$ extra free parameters. Because of this large number of free parameters, we use iminuit [16] to maximize A_4 after randomizing the parameters for the optimization in this subsection. Tab. 6 shows the

Table 5: Table of the $N = 9$ anti-symmetric designs optimized with the various frequency ranges. The polarization efficiencies for the top three frequencies deviate from 1 by orders of 10^{-6}, 10^{-5}, and 10^{-4}, respectively. We omit the phase difference since the phase is frequency independent for the anti-symmetric design. Table from [39].

Optimization freq. range ν_{opt} [GHz]	Optimization band width $\Delta\nu_{opt}/\nu_0$	Fractional band width $\Delta\nu/\nu_0$	Polarization efficiency $2A_4$	Optic axis angles χ_i [deg.]
84 – 111	0.28	0.96	1.000	11.71 , 154.96 , 56.67 , 66.41 , 0.00 , -66.41 , -56.67 , -154.96 , -11.71
74 – 121	0.48	1.07	1.000	50.10 , 142.71 , 19.65 , 124.47 , 0.00 , -124.47 , -19.65 , -142.71 , -50.10
64 – 131	0.69	1.08	1.000	145.87 , 52.56 , 17.93 , 122.93 , 0.00 , -122.93 , -17.93 , -52.56 , -145.87
54 – 141	0.89	1.21	0.999	0.73 , 139.90 , 42.67 , 60.88 , 0.00 , -60.88 , -42.67 , -139.90 , -0.73
44 – 151	1.10	1.35	0.998	23.19 , 170.88 , 89.85 , 143.85 , 0.00, -143.85 , -89.85 , -170.88 , -23.19
34 – 161	1.30		0.993	
24 – 171	1.51	1.50	0.984	158.36 , 166.52 , 65.73 , 35.57 , 0.00 , -35.57 , -65.73 , -166.52 , -158.36
14 – 181	1.71	1.55	0.957	20.64 , 4.72 , 108.96 , 150.26 , 0.00 , -150.26 , -108.96 , -4.72 , -20.64
4 – 191	1.92		0.886	

results of the optimization. All the thicknesses ended up converging to essentially the same value. Fig. 27 shows the polarization efficiency and phase as a function of the frequency calculated with

Table 6: Table of the another design has the smaller frequency dependent optic axis. Table from [39].

The number of layers N	Fractional band width $\Delta\nu/\nu_0$	Polarization efficiency $2A_4$	Phase difference $\Delta\phi_4$[deg.]		
9	1.48	0.998	0.17	χ_i [deg.]	-69.92, 5.13, -7.27, 44.90 , 0.00, 109.89, -18.27, -36.60 , 29.83
				d_i [mm]	4.694, 4.649, 4.755, 4.686, 4.747, 4.700, 4.743, 4.663, 4.713

the angles in Tab. 6 and the fixed thickness of 4.7 mm. We can not find the broader coverage within the range of our parameter searches by thickness while we had assumed that adding thickness as free parameters should increase the degrees of freedom to find a broader polarization efficiency with a flat phase response. Due to the large number of the free parameters, there may be room for improvement in the optimization process, but such an investigation is beyond the scope of this paper. However, one of the designs shown in Tab. 6 has a maximum phase difference of about 0.2 degrees over the targeted frequency range without imposing an anti-symmetric condition. This means that when we have a large number of free parameters, the anti-symmetric condition is not

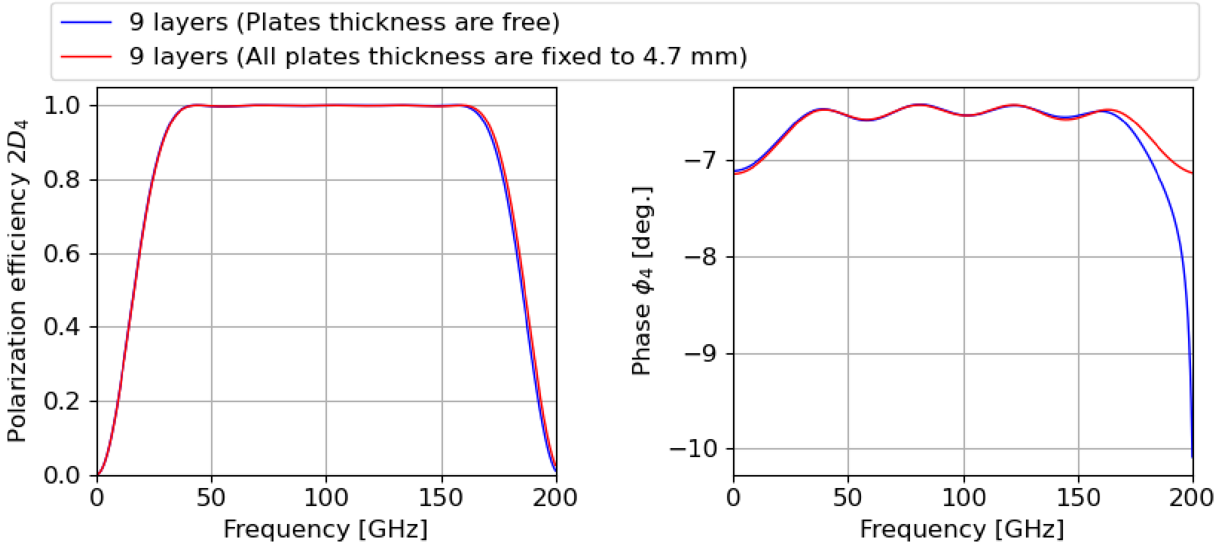

Figure 27: Polarization efficiency and effective optic axis angle of the design in Tab. 6. Image from [39].

the only way to reach a flat phase response.

2.5 Conclusions

In order to achieve high sensitivity to CMB radiation as well as foreground emissions in a single polarimeter, a HWP for current CMB polarization experiments is required to cover a broad band. While an AHWP is one of solution to broaden the band width, its frequency-dependent optic axis adds challenges to calibration and analysis complexity. We propose a novel AHWP design which eliminates this effect by imposing the anti-symmetric orientation to the relative wave plate angles. We obtain the examples of AHWP designs for five and nine layers. The optimized designs achieves the frequency-independent optic axis and covers a fractional band width of 1.3 and 1.5 for five and nine layer AHWPs, respectively. We also discuss about the tolerance of the design in relation to wave plate relative angles and thicknesses. In order to mitigate the maximum phase variation to be less than 1 degree over frequency, we need to assemble the AHWP within an accuracy for relative angles less than 15 arcmin and thickness less than 20 μm. This result can be applicable not to CMB polarimetry, but any other application which requires flat spectral response of the effective optic axis of an AHWP.

3 Systematics originated from half-wave plate

3.1 Introduction

When we use the HWP has the frequency dependent optic axis as the PMU, the polarization angles of each component of the sky (i.e. CMB, dust, synchrotron) have the different frequency dependence, respectively. This effect causes leakage from E-mode to B-mode, and there is a concern that more stringent requirements for calibration accuracy is needed to mitigate this leakage. Our new type of AHWP design shown in Sec. 2 has the potential to solve this concern. In this section, we discuss about the systematics caused by the frequency dependency of the HWP performance. We compare the two types of AHWP design that has frequency dependent optic axis or not (see Sec. 2) and decide a preferred design type for LiteBIRD.

3.2 Formalism

3.2.1 Spectrum of each sky component

When we assume that $V_{in}(\nu) = 0$, the total Stokes parameters of the incident polarization to the telescope for each frequency, can be written as,

$$\begin{aligned} Q_{\rm in}(\nu) &= Q_{\rm CMB}(\nu) + Q_{\rm dust}(\nu) + Q_{\rm sync.}(\nu), && (46)\\ U_{\rm in}(\nu) &= U_{\rm CMB}(\nu) + U_{\rm dust}(\nu) + U_{\rm sync.}(\nu), && (47)\end{aligned}$$

where, ν is the frequency. The frequency dependence of the polarization flux of each sky component can be written as [30],

$$\begin{aligned} F_c(\nu) &= B'(\nu)\Delta P_{\rm CMB}, && (48)\\ F_d(\nu) &= F_d(\nu_0)\left(\frac{\nu}{\nu_0}\right)^{\beta_d}\frac{B_\nu(\nu, T_{\rm dust})}{B_\nu(\nu_0, T_{\rm dust})}, && (49)\\ F_s(\nu) &= F_s(\nu_0)\left(\frac{\nu}{\nu_0}\right)^{\beta_s}, && (50)\\ & && (51)\end{aligned}$$

where $F_{c,d,s}(\nu)$ is the flux, the symbols c , d, and s mean CMB, dust, synchrotron, $\Delta P_{\rm CMB}$ is the fluctuation of the CMB polarization anisotropy. The functions, $B(\nu)$ and $B'(\nu)$, and the coefficients can be written as,

$$\begin{aligned}
B(\nu,T) &= \frac{2h\nu^3}{c^2}\frac{1}{\exp(\frac{h\nu}{k_B T})-1} && (52)\\
B'(\nu) &= \left.\frac{\partial B(\nu,T)}{\partial T}\right|_{T_{\rm CMB}} = \frac{2h^2\nu^4}{k_B c^2 T_{\rm CMB}^2}\frac{\exp(\frac{h\nu}{k_B T_{\rm CMB}})}{(\exp(\frac{h\nu}{k_B T_{\rm CMB}})-1)^2}\ [10^{26}\text{Jy sr}^{-1}\ \text{K}^{-1}], && (53)\\
h &= 6.62607015\times 10^{-34}\ [\text{W s}^2], && (54)\\
k_B &= 1.380649\times 10^{-23}\ [\text{W s K}^{-1}], && (55)\\
c &= 299792458\ [\text{m s}^{-1}], && (56)\\
T_{\rm CMB} &= 2.7255K, && (57)\\
T_{\rm dust} &= 19.6K, && (58)\\
\beta_d &= 1.55\ \text{(for polarization)}, && (59)\\
\beta_s &= -1.1. && (60)
\end{aligned}$$

3.2.2 Unit conversion

We use the CMB unit, $\mu\text{K}_{\rm CMB}$, to evaluate these systematic effects. However, in this section, we integrate the modulated signal to see the effect of the frequency dependence of the HWP performance in the unit of Jy/sr. Therefore, we need to considerate unit conversion.

Jansky unit In radio astronomy, the Jansky unit (Jy) is used as a unit of power. The Jansky unit can be expressed using SI units as,

$$1\text{Jy} = 10^{-26}\text{Wm}^{-2}\text{Hz}^{-1}. \quad (61)$$

CMB temperature unit The spectrum of the CMB anisotropies, I_c, can be written as,

$$I_c(\nu) = B'(\nu)\Delta T_{\rm CMB}\ [\text{Jy sr}^{-1}], \quad (62)$$

where $\Delta T_{\rm CMB}$ is the fluctuation of the CMB temperature from $T_{\rm CMB}$. The generic signal, $I_g(\nu)$, is converted to temperature T_g as,

$$T_g(\nu) = \frac{I_g}{B'(\nu)}\ [\text{K}_{\rm CMB}]. \quad (63)$$

This temperature, $\text{K}_{\rm CMB}$, is the CMB temperature unit.

Conversion factor For a single frequency, the conversion factor, $b(\nu)$, which convert $\text{K}_{\rm CMB}$ to Jy/sr is,

$$b(\nu) = B'(\nu). \quad (64)$$

$$(65)$$

When we integrate the signal $I_g(\nu)$ with the band shape of the detector $g(\nu)$, the effective antenna area $A_e(\nu)$, the solid angle of the telescope Ω_b, and the polarization efficiency $\epsilon(\nu)$, the integrated signal $I'_g(\nu)$ can be written in units of power (W) as,

$$I'_g(\nu) = \int_0^\infty d\nu \; A_e(\nu)\Omega_b(\nu)g(\nu)\epsilon(\nu)I_g(\nu) \text{ [W]}. \tag{66}$$

$$\tag{67}$$

When we observe the CMB monopole only, then Eq. 66 can be rewritten in $\mathrm{K_{CMB}}$ using the integrated conversion factor, b', as,

$$T_{\rm CMB} = b' \int_0^\infty d\nu \; A_e(\nu)\Omega_b(\nu)g(\nu)\epsilon(\nu)b(\nu)T_{\rm CMB} \text{ [K}_{\rm CMB}\text{]}. \tag{68}$$

$$\tag{69}$$

Since the right and left sides of the above equation need to be equal, the integrated conversion factor, b', which convert the unit of W to $\mathrm{K_{CMB}}$ is obtained as,

$$b' = \frac{1}{\int_0^\infty d\nu \; A_e(\nu)\Omega_b(\nu)g(\nu)\epsilon(\nu)B'(\nu)}. \tag{70}$$

$$\tag{71}$$

3.2.3 HWP modulation effect for observed polarization

We pick up the part of the modulated signal, $I^{4f}_{\rm det}(\nu,t)$, in Eq. 35 with adding the detector angle ψ_i and time t and removing 1/2, which is multiplied by all the terms as,

$$I^{4f}_{\rm det}(\nu,t) = \epsilon(\nu)[Q_{\rm in}(\nu)\cos(4\rho(t) - 4\phi_4(\nu) - 2\psi_i) + U_{\rm in}(\nu)\cos(4\rho(t) - 4\phi_4(\nu) - 2\psi_i)], \tag{72}$$

where $\epsilon(\nu)$ is polarization efficiency. Since the modulated signal is demodulated using the HWP rotation angle and the detector angle, we separate the term of the AHWP phase, $4\phi_4$, as,

$$I^{4f}_{\rm det}(\nu,t) = Q'(\nu)\cos(4\rho(t) - 2\psi_i) + U'(\nu)\sin(4\rho(t) - 2\psi_i), \tag{73}$$

where $Q'(\nu)$ and $U'(\nu)$ are

$$Q'(\nu) = \epsilon(\nu)\{Q_{\rm in}(\nu)\cos(4\phi_4(\nu)) - U_{\rm in}(\nu)\sin(4\phi_4(\nu))\}, \tag{74}$$
$$U'(\nu) = \epsilon(\nu)\{Q_{\rm in}(\nu)\sin(4\phi_4(\nu)) + U_{\rm in}(\nu)\cos(4\phi_4(\nu))\}. \tag{75}$$

To obtain $Q'(\nu)$ and $U'(\nu)$, we use the addition theorem of trigonometric functions as

$$\cos(a-b) = \cos(a)\cos(b) + \sin(a)\sin(b), \tag{76}$$
$$\sin(a-b) = \sin(a)\cos(b) - \cos(a)\sin(b). \tag{77}$$

Eq. 74 and 75 can be summarized to an equation using matrices as,

$$\begin{pmatrix} Q'(\nu) \\ U'(\nu) \end{pmatrix} = \epsilon(\nu) \begin{pmatrix} \cos(4\phi_4(\nu)) & -\sin(4\phi_4(\nu)) \\ \sin(4\phi_4(\nu)) & \cos(4\phi_4(\nu)) \end{pmatrix} \begin{pmatrix} Q_{\rm in}(\nu) \\ U_{\rm in}(\nu) \end{pmatrix}. \tag{78}$$

In the observation, the Stokes parameters $Q'(\nu)$ and $U'(\nu)$ are integrated in the detector bandwidth. In this section, we integrate these Stokes parameters with the band shape of the detector, the effective antenna area, solid angle of the telescope, the polarization efficiency, the HWP phase, ϕ_4. We express the observed stoked parameters, $Q_{\mathrm{obs.}}$ and $U_{\mathrm{obs.}}$, in the matrix as

$$\left(\begin{array}{c} Q_{\mathrm{obs.}} \\ U_{\mathrm{obs.}} \end{array}\right) = \eta^c \left(\begin{array}{c} Q_{\mathrm{CMB}}(\nu_0) \\ U_{\mathrm{CMB}}(\nu_0) \end{array}\right) + \eta^d \left(\begin{array}{c} Q_{\mathrm{dust}}(\nu_0) \\ U_{\mathrm{dust}}(\nu_0) \end{array}\right) + \eta^s \left(\begin{array}{c} Q_{\mathrm{sync.}}(\nu_0) \\ U_{\mathrm{sync.}}(\nu_0) \end{array}\right), \tag{79}$$

where ν_0 is the center frequency for each LFT band. The matrices, $\eta^{c,d,s}$ and $(\eta^{c,d,s})^{-1}$, can be written as

$$\eta^{c,d,s} = \kappa^{c,d,s} \left(\begin{array}{cc} \cos(\Phi^{c,d,s}) & -\sin(\Phi^{c,d,s}) \\ \sin(\Phi^{c,d,s}) & \cos(\Phi^{c,d,s}) \end{array}\right), \tag{80}$$

$$(\eta^{c,d,s})^{-1} = \frac{1}{\kappa^{c,d,s}} \left(\begin{array}{cc} \cos(\Phi^{c,d,s}) & \sin(\Phi^{c,d,s}) \\ -\sin(\Phi^{c,d,s}) & \cos(\Phi^{c,d,s}) \end{array}\right). \tag{81}$$

The coefficients and functions can be written as

$$\begin{aligned} \kappa^{c,d,s}\sin(\Phi^{c,d,s}) &= b(\nu_0)b' \int_0^\infty d\nu\ A_e(\nu)\Omega_b(\nu)g(\nu)\epsilon(\nu)\frac{F_{c,d,s}(\nu)}{F_{c,d,s}(\nu_0)}\sin(4\phi_4(\nu)), & (82)\\ \kappa^{c,d,s}\cos(\Phi^{c,d,s}) &= b(\nu_0)b' \int_0^\infty d\nu\ A_e(\nu)\Omega_b(\nu)g(\nu)\epsilon(\nu)\frac{F_{c,d,s}(\nu)}{F_{c,d,s}(\nu_0)}\cos(4\phi_4(\nu)). & (83)\end{aligned}$$

Since we use $\mu\mathrm{K}_{\mathrm{CMB}}$ as the unit of the input and output Stokes parameters, Eq. 82 and Eq. 83 contain a conversion factor, $b(\nu_0)b'$. To obtain the integrated cosine and sine, we use trigonometric composition (Eq.84 and 87).

$$\begin{aligned} A\cos(a-b) + B\cos(a-c) &= \cos(a)\{A\cos(b) + B\cos(c)\} + \sin(a)\{A\sin(b) + B\sin(c)\} \\ &= C\cos(a-d) & (84)\\ C &= \sqrt{\{A\cos(b) + B\cos(c)\}^2 + \{A\sin(b) + B\sin(c)\}^2} & (85)\\ d &= \left\{\begin{array}{ll} \arctan\frac{A\sin(b)+B\sin(c)}{A\cos(b)+B\cos(c)} & (A\cos(b) + B\cos(c) > 0) \\ \arctan\frac{A\sin(b)+B\sin(c)}{A\cos(b)+B\cos(c)} - \pi & (A\cos(b) + B\cos(c) < 0) \end{array}\right. & (86)\end{aligned}$$

$$\begin{aligned} A\sin(a-b) + B\sin(a-c) &= \sin(a)\{A\cos(b) + B\cos(c)\} - \cos(a)\{A\sin(b) + B\sin(c)\} \\ &= C\sin(a-d) & (87)\\ C &= \sqrt{\{A\cos(b) + B\cos(c)\}^2 + \{A\sin(b) + B\sin(c)\}^2} & (88)\\ d &= \left\{\begin{array}{ll} \arctan\frac{A\sin(b)+B\sin(c)}{A\cos(b)+B\cos(c)} & (A\cos(b) + B\cos(c) > 0) \\ \arctan\frac{A\sin(b)+B\sin(c)}{A\cos(b)+B\cos(c)} - \pi & (A\cos(b) + B\cos(c) < 0) \end{array}\right. & (89)\end{aligned}$$

Since the coefficient $\kappa^{c,d,s} \neq 1$ and the angle Φ_4 has the global offset determined from the initial angle of the HWP, we need to correct $\eta^{c,d,s}$ as,

$$\left(\begin{array}{c} Q_{\mathrm{obs.}}^{\mathrm{Corrected}} \\ U_{\mathrm{obs.}}^{\mathrm{Corrected}} \end{array}\right) = (\eta^{\mathrm{calib.}})^{-1}\left[\eta^c \left(\begin{array}{c} Q_{\mathrm{CMB}}(\nu_0) \\ U_{\mathrm{CMB}}(\nu_0) \end{array}\right) + \eta^d \left(\begin{array}{c} Q_{\mathrm{dust}}(\nu_0) \\ U_{\mathrm{dust}}(\nu_0) \end{array}\right) + \eta^s \left(\begin{array}{c} Q_{\mathrm{sync.}}(\nu_0) \\ U_{\mathrm{sync.}}(\nu_0) \end{array}\right)\right]. \tag{90}$$

The matrix, $\eta^{\mathrm{calib.}}$, is a matrix written as,

$$\eta^{\mathrm{calib.}} = \kappa^{\mathrm{calib.}} \begin{pmatrix} \cos(\Phi^{\mathrm{calib.}}) & -\sin(\Phi^{\mathrm{calib.}}) \\ \sin(\Phi^{\mathrm{calib.}}) & \cos(\Phi^{\mathrm{calib.}}) \end{pmatrix}, \tag{91}$$

where $\kappa^{\mathrm{calib.}}$ and $\Phi^{\mathrm{calib.}}$ are the coefficient and angle obtained from a blackbody light source in a ground calibration, η^{c} in a in-flight calibration, and so on. They are calculated using the spectrum of the calibration source, $F_{calib.}(\nu)$, as,

$$\kappa^{\mathrm{calib.}} \sin(\Phi^{\mathrm{calib.}}) = b(\nu_0)b' \int_0^\infty d\nu\ A_e(\nu)\Omega_b(\nu)g(\nu)\epsilon(\nu)\frac{F_{calib.}(\nu)}{F_{calib.}(\nu_0)}\sin(4\phi_4(\nu)), \tag{92}$$

$$\kappa^{\mathrm{calib.}} \cos(\Phi^{\mathrm{calib.}}) = b(\nu_0)b' \int_0^\infty d\nu\ A_e(\nu)\Omega_b(\nu)g(\nu)\epsilon(\nu)\frac{F_{calib.}(\nu)}{F_{calib.}(\nu_0)}\cos(4\phi_4(\nu)). \tag{93}$$

3.2.4 Model of observed power spectrum

If the telescope has the offset of the polarization angle, $\Delta\alpha$, for all pixels of the observed map, the power spectrum of the observed B-mode, $C_\ell^{BB,\ obs.}$, is obtained using the original E- and B-mode, C_ℓ^{EE} and C_ℓ^{BB}, as [38],

$$C_\ell^{BB,\ obs.} = C_\ell^{\mathrm{EE}} \sin^2(2\Delta\alpha) + C_\ell^{\mathrm{BB}} \cos^2(2\Delta\alpha) \tag{94}$$

This equation means that non-zero $2\Delta\alpha$ causes a leakage from E-mode to B-mode. The angle, $2\Delta\alpha$, is corresponding to $\Phi^{c,d,s}$ and the coefficient $\kappa^{c,d,s}$ affects to the power spectrum as a coefficient $(\kappa^{c,d,s})^2$. Therefore, the observed B-mode power spectrum of Eq. 79 can be rewritten as,

$$C_\ell^{BB,\ obs.} = \sum_{j=c,d,s} (\kappa^j)^2 [C_\ell^{EE,\ j} \sin^2(\Phi^j) + C_\ell^{BB,\ j} \cos^2(\Phi^j)], \tag{95}$$

where $C_\ell^{EE,\ j}$ and $C_\ell^{BB,\ j}$ are the original power spectrum for each component. When we correct the observed map as Eq. 90, then,

$$C_\ell^{BB,\ obs.} = \sum_{j=c,d,s} (\frac{\kappa^j}{\kappa^{\mathrm{calib.}}})^2 [C_\ell^{EE,\ j} \sin^2(\Phi^j - \Phi^{\mathrm{calib.}}) + C_\ell^{BB,\ j} \cos^2(\Phi^j - \Phi^{\mathrm{calib.}})], \tag{96}$$

3.3 Evaluation method

In this section, we evaluate these systematic effects from a map-based simulation. We compute the integrated Q and U map with the HWP effect using Eq. 79 or Eq. 79, and take a residual from a base map defined per situation. We obtain the power spectrum of the residual maps and compare it for the requirement or between the AHWP designs.

3.3.1 Analysis flowchart

Fig. 28 shows a flowchart of this analysis. There are three steps summarised below.

Step 1: Calculate η matrices In this step, we calculate the matrices, $\eta^{c,d,s}$, with the calibration error and the foreground parameters for the symmetric and anti-symmetric AHWP design. We

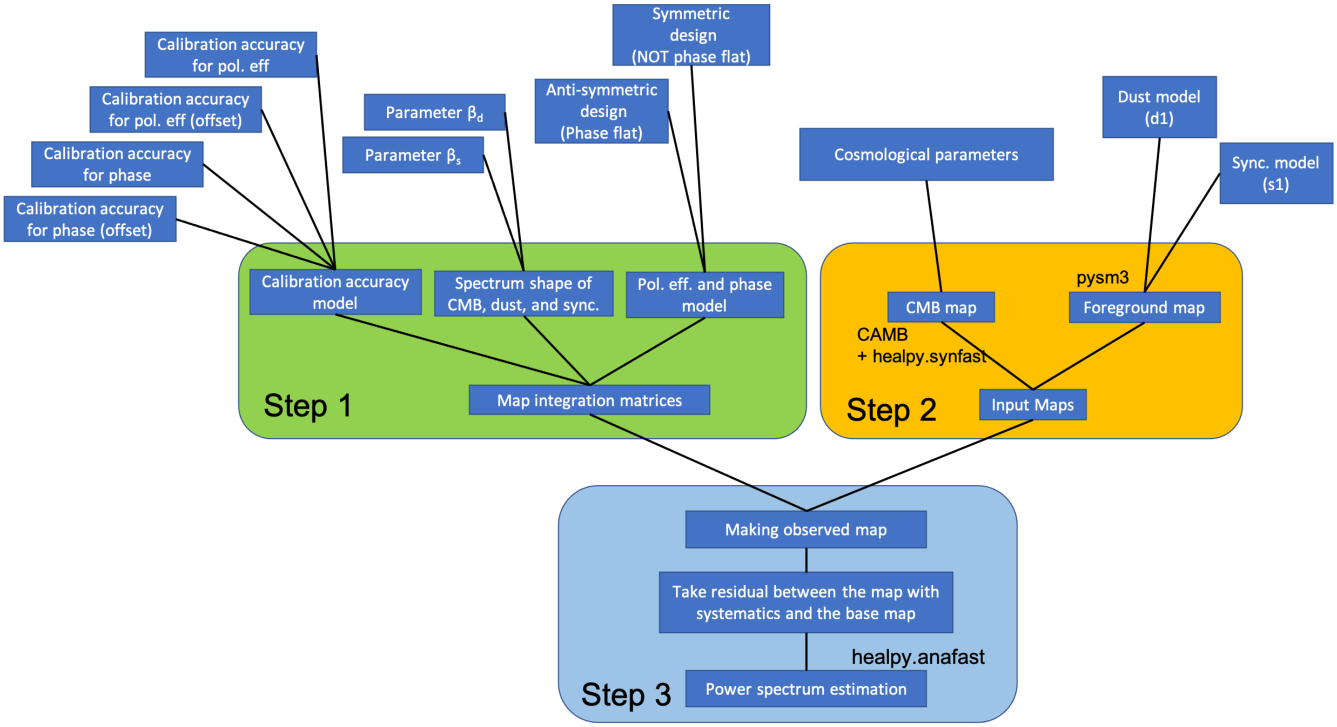

Figure 28: Flowchart of this analysis

consider the following calibration errors:

- Measurement error of the polarization efficiency, $\delta_\epsilon(\nu)$, has a normal distribution with standard deviation, σ_ϵ
- Measurement offset of the polarization efficiency, δ_ϵ^{off}
- Measurement error of the HWP phase, $\delta_p(\nu)$, has a normal distributions with standard deviation, σ_p
- Measurement offset of the HWP phase, δ_p^{off}

The two errors, $\delta_\epsilon(\nu)$ and $\delta_p(\nu)$, are obtained for each frequency as random numbers which have normal distributions with standard deviations σ_ϵ and σ_{phase}. The two offsets, δ_ϵ^{off} and δ_p^{off}, behave as constants over all frequencies. The integration in Eq. 82 and Eq. 83 are calculated as summation considering the above calibration errors as,

$$\kappa^{c,d,s}\sin(\Phi^{c,d,s}) = b(\nu_0)b'\sum_{\nu=\nu_i}^{\nu_f} d\nu\ G'(\nu)(\epsilon(\nu)+\delta_\epsilon(\nu)+\delta_\epsilon^{off})\frac{F_{c,d,s}(\nu)}{F_{c,d,s}(\nu_0)}\sin(4\phi_4(\nu)+\delta_p(\nu)+\delta_p^{off}), \quad (97)$$

$$\kappa^{c,d,s}\cos(\Phi^{c,d,s}) = b(\nu_0)b'\sum_{\nu=\nu_i}^{\nu_f} d\nu\ G'(\nu)(\epsilon(\nu)+\delta_\epsilon(\nu)+\delta_\epsilon^{off})\frac{F_{c,d,s}(\nu)}{F_{c,d,s}(\nu_0)}\cos(4\phi_4(\nu)+\delta_p(\nu)+\delta_p^{off}), \quad (98)$$

where ν_i and ν_f are the initial and final frequency of the band, $G'(\nu) = A_e(\nu)\Omega_b(\nu)g(\nu)$. In this calculation, the frequency step $d\nu$ is set to 1 GHz and the band shape, $g(\nu)$, is set to 1. We assume the effective antenna area as,

$$A_e(\nu) = \frac{\lambda^2}{\Omega_b(\nu)} = \frac{c^2}{\Omega_b(\nu)\nu^2}. \tag{99}$$

We also use the coefficients, $\beta^{d,s}$, in Eq. 49 and Eq. 50, as the input value to calculate these matrices. In practice, these coefficients have spatial variation, but in this section we apply the same value to the entire sky. We use the polarization efficiency and the phase of the five layers symmetric and anti-symmetric design shown in Tab. 3 and Tab. 2. The polarization efficiency and phase of both design is shown in Fig. 22, but all phases change 22.5 degree from the figure because we calculate these value for $S_{in} = (1, 1, 0, 0)$.

Step 2: Produce input maps In this step, we make the input maps of CMB and foreground for each LFT bands. Every map used in this section is smoothed using the beam size in Fig. 14 to consider the effect of the beam size of the telescope. We need to divide the celestial sphere into pixels in order to make the maps of the sky. The short description of them can be found in Appendix A.

CMB map A cosmology code *CAMB* [1] obtains the CMB power spectrum from the input cosmological parameters. We calculate the power spectrum and the cross-power spectrum, $C_\ell^{TT,EE,BB,TE,EB,TB}$, using *CAMB* and make a CMB map using *healpy* and *synfast*, which is a routine for calculating CMB maps from the power spectrum and the cross-power spectrum. An example of the generated Q and U map is in the top of Fig. 29.

Foreground map To obtain the foreground map, we use a python module *pysm* which simulate the galactic foregrounds in intensity and polarization for CMB experiments [4, 73, 79]. We use the foreground models named *d1* and *s1*. In the dust model *d1*, the thermal dust is modeled as a single-component modified blackbody. In the synchrotron model *d1*, a power law scaling is used with varying spectral index spatially. An example of the generated Q and U maps are in the middle and bottom of Fig. 29.

Step 3: Make observed map and power spectrum of systematic effects In this step, at first, we calculate an observed map with and without the correction of the coefficient and the global offset of the phase as Eq. 90 using the input map and matrices obtained in Steps 1 and 2. Secondly, we define the base map to compare with the observed map, for example, the map calculated for an ideal HWP (i.e. $\epsilon(\nu) = 1$ and $\phi_4(\nu) = 0$), the map calculated without calibration errors (i.e. $\delta_\epsilon(\nu) = \delta_\epsilon^{off} = \delta_p(\nu) = \delta_p^{off} = 0$), and so on. Finally, we make residual maps by subtracting the base map from the observed map as,

$$\begin{aligned}\begin{pmatrix} Q_{\text{res.}} \\ U_{\text{res.}} \end{pmatrix} = (\eta^{\text{calib.}})^{-1}\left[\eta^c \begin{pmatrix} Q_{\text{CMB}}(\nu_0) \\ U_{\text{CMB}}(\nu_0) \end{pmatrix} + \eta^d \begin{pmatrix} Q_{\text{dust}}(\nu_0) \\ U_{Dust}(\nu_0) \end{pmatrix} + \eta^s \begin{pmatrix} Q_{\text{sync.}}(\nu_0) \\ U_{\text{sync.}}(\nu_0) \end{pmatrix}\right] \\ - \begin{pmatrix} Q_{Base\ map} \\ U_{Base\ map} \end{pmatrix},\end{aligned} \tag{100}$$

where $Q_{\text{res.}}$ and $U_{\text{res.}}$ are the Stokes parameters of the residual map, $Q_{Base\ map}$ and $U_{Base\ map}$ are the Stokes parameters of the base map. We obtain the B-mode power spectrum of the residual map, $C_\ell^{\text{BB, res.}}$, using *healpy* and *anafast*.

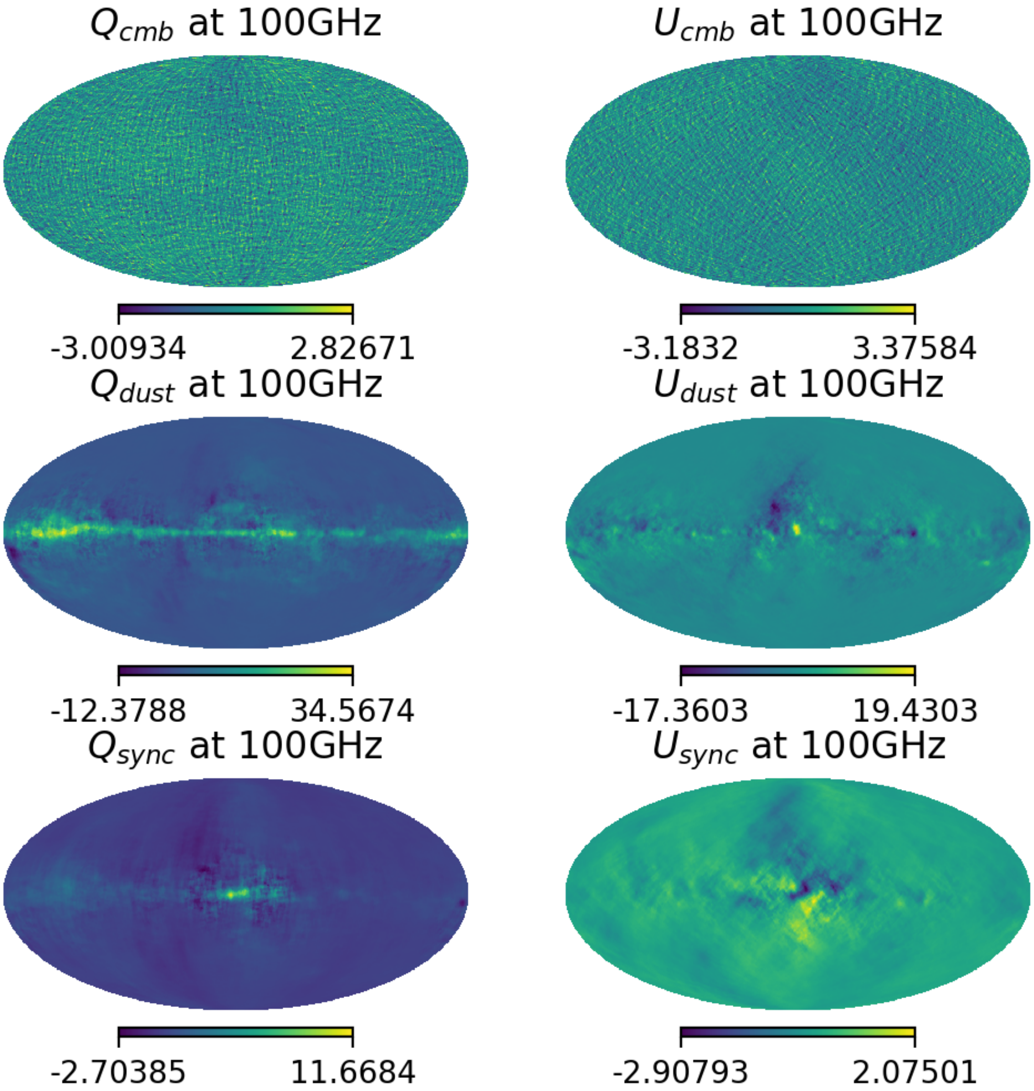

Q_{cmb} at 100GHz

U_{cmb} at 100GHz

Q_{dust} at 100GHz

U_{dust} at 100GHz

Q_{sync} at 100GHz

U_{sync} at 100GHz

Figure 29: Example of input Q and U maps at 100 GHz. The unit of the colorbar is $\mu\mathrm{K}_{\mathrm{CMB}}$

3.4 Results

3.4.1 Elements of matrices

Tab. 7 shows the calculation results of the coefficient $\kappa^{c,d,s}$ and the phase, $\Phi^{c,d,s}$, for each LFT frequency in the case of an ideal HWP (i.e. $\epsilon(\nu) = 1$, $\phi_4 = 0$). The numbers in parentheses show the comparison with the CMB. Tab. 8 and Tab. 9 show the same tables in the case of the five layers symmetric and anti-symmetric design AHWP. The change of $\kappa^{c,d,s}$ is percentage level in absolute value compared with the ideal HWP case. In the case of the relative value with respect to CMB, the change is sub-percentage level. For $\Phi^{c,d,s}$, we should see only the relative value with respect to CMB because the absolute value is changed by the initial angle setting of the AHWP. In the case of the anti-symmetric design, since it has frequency independent phase, there is no change compared to the case of an ideal HWP. In the case of the symmetric design, we find that there are degree-scale changes for both the dust and the synchrotron emissions.

Table 7: Table of $\kappa^{c,d,s}$ and $\Phi^{c,d,s}$ of an ideal HWP (i.e. $\epsilon(\nu) = 1$, $\phi_4 = 0$) for each LFT frequency band.

Center frequency [GHz]	band width	κ^c (κ^c/κ^c)	κ^d (κ^d/κ^c)	κ^s (κ^s/κ^c)	Φ^c [deg.] ($\Phi^c - \Phi^c$)	Φ^d [deg.] ($\Phi^d - \Phi^c$)	Φ^s [deg.] ($\Phi^s - \Phi^c$)
40	0.3	1.000 (1.000)	1.003 (1.003)	1.058 (1.058)	0.000 (0.000)	0.000 (0.000)	0.000 (0.000)
50	0.3	1.000 (1.000)	1.003 (1.003)	1.050 (1.050)	0.000 (0.000)	0.000 (0.000)	0.000 (0.000)
60	0.3	1.000 (1.000)	1.001 (1.001)	1.025 (1.025)	0.000 (0.000)	0.000 (0.000)	0.000 (0.000)
69	0.3	1.000 (1.000)	1.001 (1.001)	1.026 (1.026)	0.000 (0.000)	0.000 (0.000)	0.000 (0.000)
78	0.3	1.000 (1.000)	1.001 (1.001)	1.026 (1.026)	0.000 (0.000)	0.000 (0.000)	0.000 (0.000)
89	0.3	1.000 (1.000)	1.002 (1.002)	1.031 (1.031)	0.000 (0.000)	0.000 (0.000)	0.000 (0.000)
100	0.3	1.000 (1.000)	1.001 (1.001)	1.029 (1.029)	0.000 (0.000)	0.000 (0.000)	0.000 (0.000)
119	0.3	1.000 (1.000)	1.002 (1.002)	1.048 (1.048)	0.000 (0.000)	0.000 (0.000)	0.000 (0.000)
140	0.3	1.000 (1.000)	1.001 (1.001)	1.051 (1.051)	0.000 (0.000)	0.000 (0.000)	0.000 (0.000)

3.4.2 Validation of the methodlogy

To verify the methodlogy and the simulation code, we compare the B-mode power spectrum $C_\ell^{BB,\ obs.}$ obtained by the equation-based calculation using Eq. 96 with the map-based calculation using Eq. 90. In this comparison, we set $\eta^{\rm calib.}$ as a unit matrix (i.e. $\kappa^{\rm calib.} = 1$ and $\Phi^{\rm calib.} = 0$) and use only the CMB as the input. If our formalism and calculation code are correct, the result of these two cases must be same. Fig. 30 shows $C_\ell^{BB,\ obs.}$ of the CMB of the map-based simulation and the equation based calculation. We use the values in Tab. 8 and Tab. 9 to do this simulation and calculation. From Fig. 30, we confirm that the result of the map-based simulation and the equation based calculation are consistent. Therefore, we confirm that the methodology and the simulation code work correctly.

3.4.3 Comparison with an ideal HWP

To compare the two AHWP design types, we use the map calculated for an ideal HWP (i.e. $\epsilon(\nu) = 1$ and $\phi_4(\nu) = 0$) as the base map. In this calculation, all calibration errors set to 0. We use η^c as $\eta^{\text{calib.}}$ and Eq. 90 to calculate the observed maps. Fig. 31 shows the power spectrum of the CMB, the foregrounds, and the B-mode power spectrum of the residual map, $C_\ell^{\text{BB, res.}}$, for each AHWP design type. The power spectrum of the residual map is corresponding to the size of the effect, which is from the frequency dependency of the HWP performances. From Fig. 31, we confirm that the average of the power spectrum of the residual map for the symmetric design is larger than that of the anti-symmetric design by at least 10^1 orders and up to 10^3 orders for each LFT frequency band. The effect of the original C_ℓ^{EE} and C_ℓ^{BB} to the observed $C_\ell^{\text{BB, obs.}}$ is modeled in Eq. 96 as shown in Sec. 3.2. In the case of no effects from the frequency dependency of the HWP performances and the anti-symmetric design from Tab. 7 and Tab. 9, $\Phi^{c,d,s} - \Phi^c$ are zero, so there is no leakage from $C_\ell^{EE,\ ,c,d,s}$. On the other hand, in the case of symmetric design, from Tab. 8, there are leakages from $C_\ell^{EE,\ d,s}$ since $\Phi^{d,s} - \Phi^c$ are not equal to zero. This leakage causes the large difference of the B-mode power spectrum of the residual map between the two AHWP design types. Note that since the matrix η^c is canceled by $\eta^{\text{calib.}}$, $C_\ell^{\text{BB, res.}}$ is not got effects from the CMB power spectrum . This fact also suggests that the accuracy of the AHWP performance correction of the symmetric design has a greater impact than that of the anti-symmetric design on the results of the observational data analysis. Note that since we do not use any mask for the maps to avoid the masking effect in low-ℓ, the results in this section are dominated by the foregrounds around the galactic center. Therefore, the absolute values of the systematic effects will be decreased when we apply a mask after solving the masking effect in low-ℓ, since the galactic center is masked. However, the comparison results in this section are not changed since the relationship between the results for the two AHWP designs are not change.

Table 8: Table of $\kappa^{c,d,s}$ and $\Phi^{c,d,s}$ of five layers symmetric design for each LFT frequency band.

Center frequency [GHz]	band width	κ^c (κ^c/κ^c)	κ^d (κ^d/κ^c)	κ^s (κ^s/κ^c)	Φ^c [deg.] ($\Phi^c - \Phi^c$)	Φ^d [deg.] ($\Phi^d - \Phi^c$)	Φ^s [deg.] ($\Phi^s - \Phi^c$)
40	0.3	0.992 (1.000)	0.998 (1.007)	1.043 (1.052)	-122.608 (0.000)	-123.693 (-1.085)	-120.525 (2.083)
50	0.3	0.992 (1.000)	0.995 (1.004)	1.04 (1.049)	-141.22 (0.000)	-142.252 (-1.032)	-139.291 (1.929)
60	0.3	0.998 (1.000)	1.000 (1.001)	1.024 (1.026)	-154.448 (0.000)	-154.77 (-0.322)	-153.863 (0.584)
69	0.3	1.000 (1.000)	1.001 (1.001)	1.026 (1.026)	-157.565 (0.000)	-157.524 (0.041)	-157.614 (-0.05)
78	0.3	0.999 (1.000)	1.000 (1.002)	1.024 (1.026)	-154.052 (0.000)	-153.709 (0.344)	-154.591 (-0.539)
89	0.3	0.999 (1.000)	1.001 (1.002)	1.028 (1.029)	-147.624 (0.000)	-147.253 (0.371)	-148.195 (-0.571)
100	0.3	1.000 (1.000)	1.001 (1.001)	1.029 (1.029)	-145.903 (0.000)	-146.043 (-0.139)	-145.748 (0.155)
119	0.3	0.997 (1.000)	0.999 (1.002)	1.044 (1.048)	-153.263 (0.000)	-153.952 (-0.689)	-152.38 (0.883)
140	0.3	0.966 (1.000)	0.961 (0.995)	1.022 (1.058)	-144.809 (0.000)	-141.858 (2.952)	-147.366 (-2.556)

Table 9: Table of $\kappa^{c,d,s}$ and $\Phi^{c,d,s}$ of five layer anti-symmetric design for each LFT frequency band.

Center frequency [GHz]	band width	κ^c (κ^c/κ^c)	κ^d (κ^d/κ^c)	κ^s (κ^s/κ^c)	Φ^c [deg.] ($\Phi^c - \Phi^c$)	Φ^d [deg.] ($\Phi^d - \Phi^c$)	Φ^s [deg.] ($\Phi^s - \Phi^c$)
40	0.3	1.000 (1.000)	1.010 (1.010)	1.043 (1.043)	0.000 (0.000)	0.000 (0.000)	0.000 (0.000)
50	0.3	1.000 (1.000)	1.004 (1.004)	1.047 (1.047)	0.000 (0.000)	0.000 (0.000)	0.000 (0.000)
60	0.3	1.000 (1.000)	1.001 (1.001)	1.027 (1.027)	0.000 (0.000)	0.000 (0.000)	0.000 (0.000)
69	0.3	1.000 (1.000)	1.001 (1.001)	1.026 (1.026)	0.000 (0.000)	0.000 (0.000)	0.000 (0.000)
78	0.3	1.000 (1.000)	1.002 (1.002)	1.025 (1.025)	0.000 (0.000)	0.000 (0.000)	0.000 (0.000)
89	0.3	1.000 (1.000)	1.002 (1.002)	1.029 (1.029)	0.000 (0.000)	0.000 (0.000)	0.000 (0.000)
100	0.3	1.000 (1.000)	1.001 (1.001)	1.029 (1.029)	0.000 (0.000)	0.000 (0.000)	0.000 (0.000)
119	0.3	1.000 (1.000)	1.001 (1.001)	1.049 (1.049)	0.000 (0.000)	0.000 (0.000)	0.000 (0.000)
140	0.3	1.000 (1.000)	0.996 (0.996)	1.055 (1.055)	0.000 (0.000)	0.000 (0.000)	0.000 (0.000)

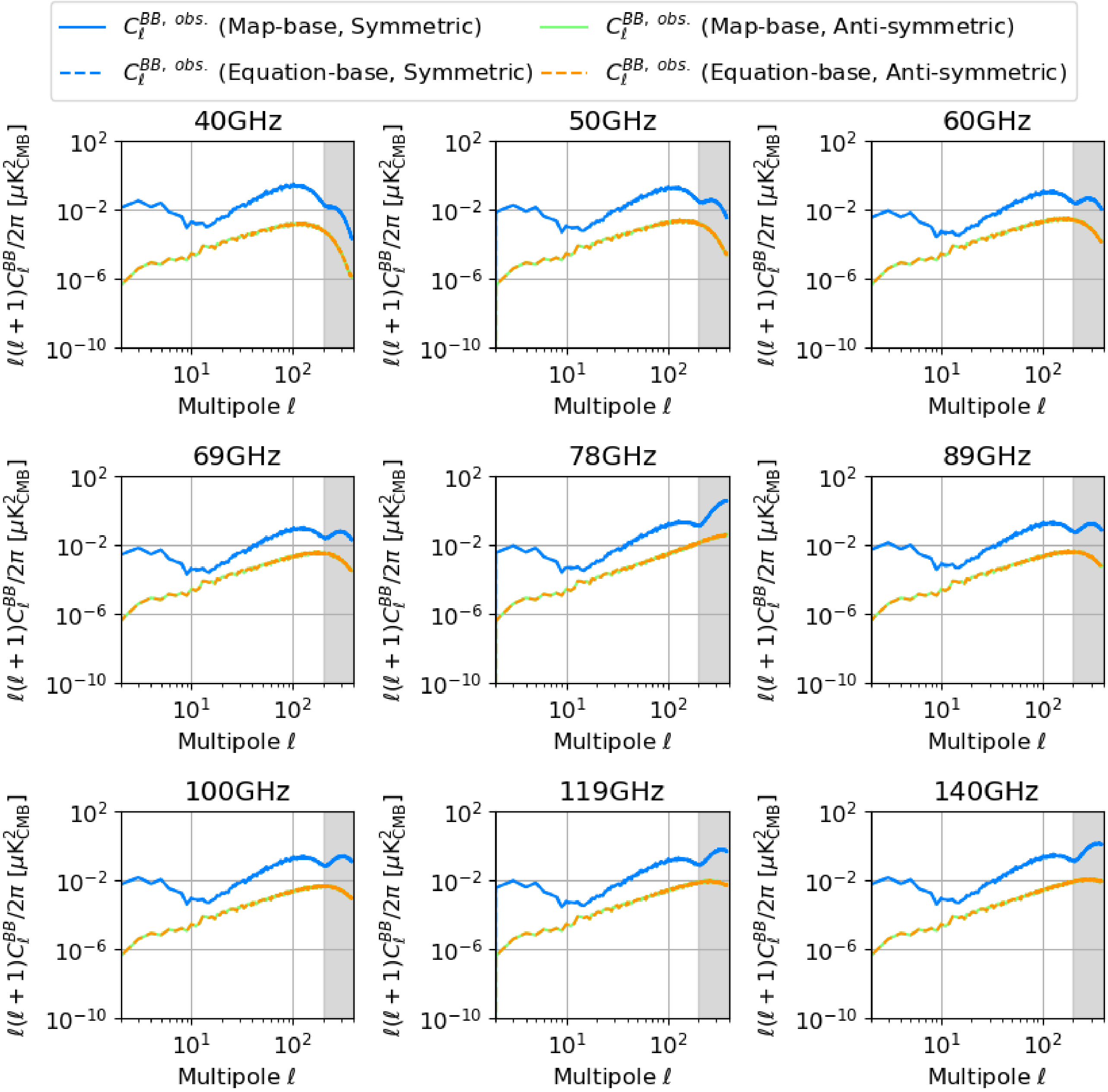

Figure 30: Power spectrum of the CMB from the map-based simulation and the equation-based calculation. The equation-based calculation using Eq. 95 and Tab. 8 and 8. The gray area is the area that is not observed by LiteBIRD.

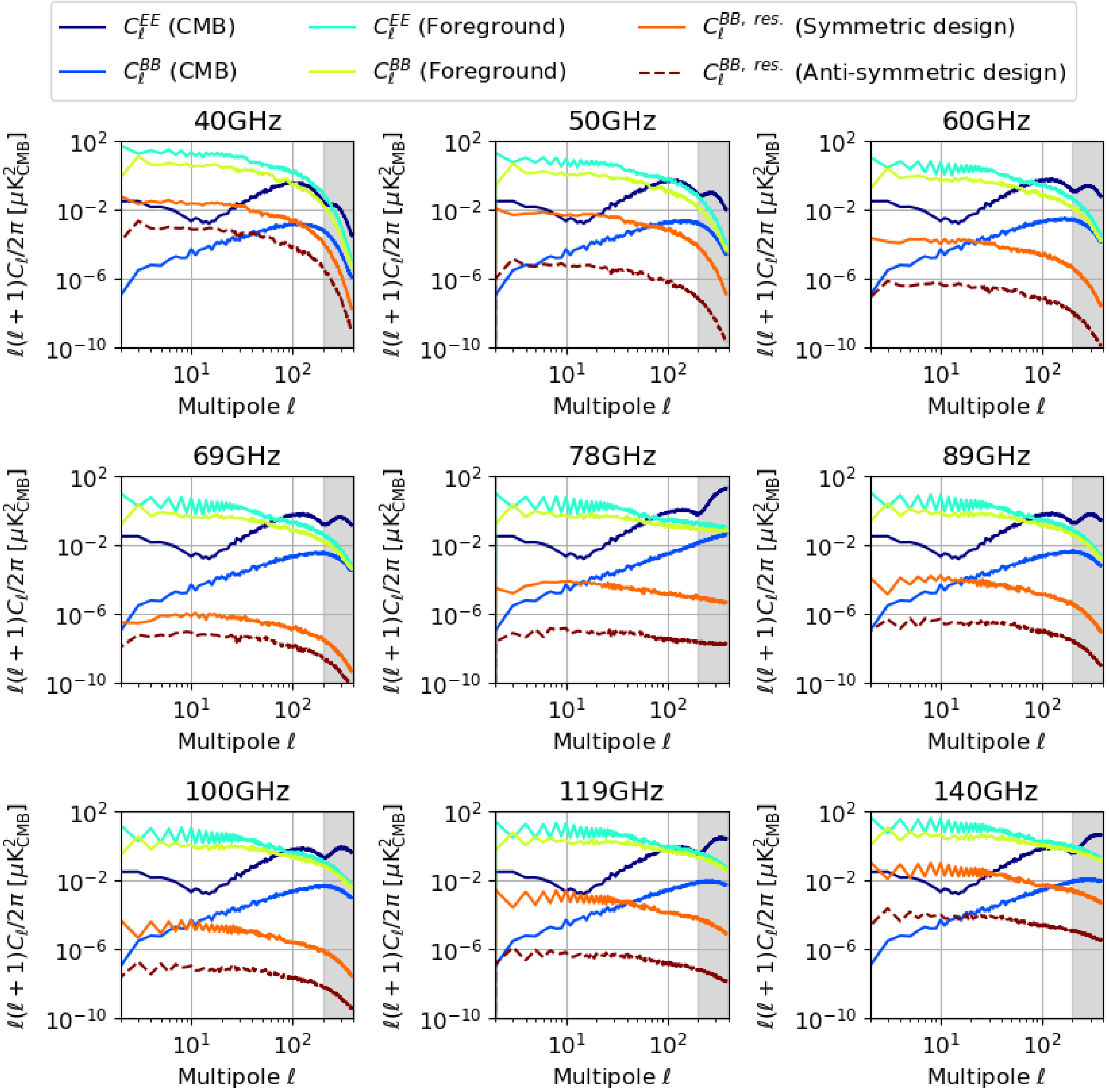

Figure 31: Power spectrum of the residual map for each AHWP design type. We also show the power spectrum of the CMB and the foregrounds for comparison. The gray area is the area which is not observed by LiteBIRD.

3.5 Discussion

3.5.1 Ground calibration

It is important for satellite experiments to verify the performance of the telescope from ground calibration. To solve the systematic effects presented in this section, we need to model the performance parameters of the telescope, such as $A_e(\nu)$, $\Omega_b(\nu)$, $g(\nu)$, $\epsilon(\nu)$, $\phi_4(\nu)$, and so on, based on the ground calibration, and correct $\eta^{c,d,s}$ in the analysis of observational data (e.g. foreground cleaning). Blackbody sources in the mm-wave band are often used in the ground calibration of CMB experiments. At this time, we calculate the matrix elements of $\eta^calib.$ when the blackbody spectra at temperatures of 300 K, 20 K, and 4 K used for $P_{\text{calib.}}$ as $\kappa^{300\text{K}}$, $\kappa^{20\text{K}}$, $\kappa^{4\text{K}}$, $\Phi^{300\text{K}}$, $\Phi^{20\text{K}}$, $\Phi^{4\text{K}}$, respectively. Fig. 32 shows the CMB polarization spectra and the blackbody spectra at temperatures of 300 K, 20 K, and 4 K. All spectrum are normalized by the value at 1 GHz. Tab. 10 and Tab. 11 show the calculation result of each matrix element for the symmetric and anti-symmetric design. The tables also show the comparison between the matrix elements of the CMB shown in Tab. 8 and Tab. 9, respectively. For $\Phi^{\text{calib.}}$, we can obtain the same value that of the CMB, the dust, and synchrotron for the anti-symmetric design. In the case of the symmetric design, the difference between Φ^c and Φ^c is less than 0.25 deg. except for 140 GHz at 300 K and 20 K. The 4 K case has the smallest maximum difference from Φ^c. From the comparison result, the 4 K blackbody source is considered to be useful for ground calibration when we use the symmetric design. For the anti-symmetric design, there is no significant change for all blackbody temperatures.

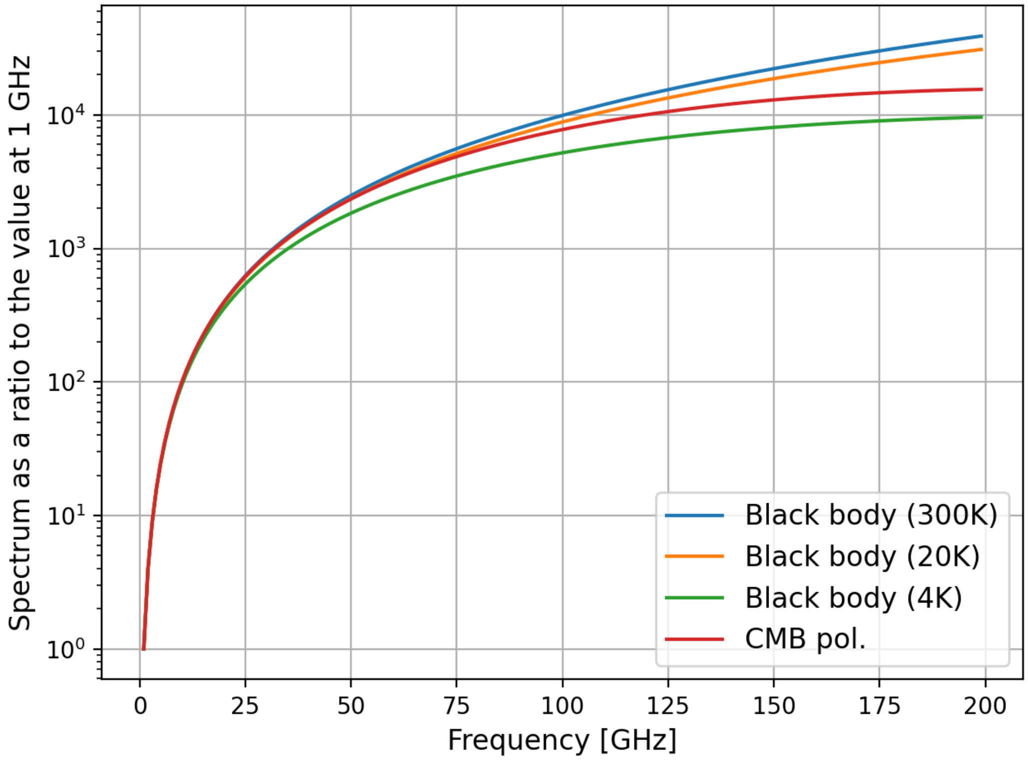

Figure 32: CMB polarization spectra and blackbody spectra at temperatures of 300 K, 20 K, and 4 K. All spectrum are normalized by the value at 1GHz.

Table 10: Table of $\kappa^{\text{calib.}}$ and $\Phi^{\text{calib.}}$ of five layers symmetric design for each LFT frequency band.

Center frequency [GHz]	$\kappa^{300\text{K}}$ ($\kappa^{300\text{K}}/\kappa^{c}$)	$\kappa^{20\text{K}}$ ($\kappa^{20\text{K}}/\kappa^{c}$)	$\kappa^{4\text{K}}$ ($\kappa^{4\text{K}}/\kappa^{c}$)	$\Phi^{300\text{K}}$ [deg.] ($\Phi^{300\text{K}}-\Phi^{c}$)	$\Phi^{20\text{K}}$ [deg.] ($\Phi^{20\text{K}}-\Phi^{c}$)	$\Phi^{4\text{K}}$ [deg.] ($\Phi^{4\text{K}}-\Phi^{c}$)
40	0.992 (1.000)	0.992 (1.000)	0.992 (1.000)	-122.662 (-0.054)	-122.631 (-0.023)	-122.486 (0.122)
50	0.992 (1.000)	0.992 (1.000)	0.992 (1.001)	-141.299 (-0.079)	-141.263 (-0.042)	-141.09 (0.13)
60	0.999 (1.000)	0.999 (1.000)	0.999 (1.001)	-154.482 (-0.035)	-154.469 (-0.021)	-154.404 (0.043)
69	1.000 (1.000)	1.000 (1.000)	1.001 (1.001)	-157.559 (0.006)	-157.561 (0.004)	-157.57 (-0.005)
78	0.999 (1.000)	0.999 (1.000)	0.999 (1.001)	-153.994 (0.059)	-154.011 (0.041)	-154.098 (-0.046)
89	0.999 (1.001)	0.999 (1.001)	1.000 (1.001)	-147.546 (0.078)	-147.567 (0.057)	-147.672 (-0.048)
100	1.000 (1.000)	1.000 (1.000)	1.001 (1.001)	-145.939 (-0.035)	-145.93 (-0.027)	-145.889 (0.015)
119	0.997 (1.001)	0.997 (1.001)	1.000 (1.003)	-153.487 (-0.223)	-153.44 (-0.177)	-153.193 (0.07)
140	0.963 (0.997)	0.964 (0.998)	0.97 (1.004)	-143.644 (1.166)	-143.857 (0.952)	-144.978 (-0.169)

Table 11: Table of $\kappa^{\text{calib.}}$ and $\Phi^{\text{calib.}}$ of 5 layer anti-symmetric design for each LFT frequency band.

Center frequency [GHz]	$\kappa^{300\text{K}}$ ($\kappa^{300\text{K}}/\kappa^{c}$)	$\kappa^{20\text{K}}$ ($\kappa^{20\text{K}}/\kappa^{c}$)	$\kappa^{4\text{K}}$ ($\kappa^{4\text{K}}/\kappa^{c}$)	$\Phi^{300\text{K}}$ [deg.] ($\Phi^{300\text{K}} - \Phi^{c}$)	$\Phi^{20\text{K}}$ [deg.] ($\Phi^{20\text{K}} - \Phi^{c}$)	$\Phi^{4\text{K}}$ [deg.] ($\Phi^{4\text{K}} - \Phi^{c}$)
40	1.001 (1.001)	1.000 (1.000)	1.000 (1.000)	0.000 (0.000)	0.000 (0.000)	0.000 (0.000)
50	1.000 (1.000)	1.000 (1.000)	1.001 (1.001)	0.000 (0.000)	0.000 (0.000)	0.000 (0.000)
60	1.000 (1.000)	1.000 (1.000)	1.001 (1.001)	0.000 (0.000)	0.000 (0.000)	0.000 (0.000)
69	1.000 (1.000)	1.000 (1.000)	1.001 (1.001)	0.000 (0.000)	0.000 (0.000)	0.000 (0.000)
78	1.000 (1.000)	1.000 (1.000)	1.001 (1.001)	0.000 (0.000)	0.000 (0.000)	0.000 (0.000)
89	1.001 (1.001)	1.001 (1.001)	1.001 (1.001)	0.000 (0.000)	0.000 (0.000)	0.000 (0.000)
100	1.000 (1.000)	1.000 (1.000)	1.001 (1.001)	0.000 (0.000)	0.000 (0.000)	0.000 (0.000)
119	1.000 (1.000)	1.000 (1.000)	1.003 (1.003)	0.000 (0.000)	0.000 (0.000)	0.000 (0.000)
140	0.998 (0.998)	0.998 (0.998)	1.004 (1.004)	0.000 (0.000)	0.000 (0.000)	0.000 (0.000)

3.5.2 Requirement for calibration of HWP performance

As explained in the previous section, the systematic effects of this section are solved by modeling the performance of the telescope and applying corrections in the data analysis. The corrections are made, for example, in the process of foreground cleaning, but it is outside the scope of this thesis to develop a tool for foreground cleaning that takes into account the HWP effects. Therefore, at this time, we use the maps which take into account the HWP effects with and without calibration errors as the observed map and the base map to make the residual map as,

$$\begin{aligned}\begin{pmatrix} Q_{\text{res.}} \\ U_{\text{res.}} \end{pmatrix} =& (\eta^{\text{calib.}})^{-1} \left[\eta_2^c \begin{pmatrix} Q_{\text{CMB}}(\nu_0) \\ U_{\text{CMB}}(\nu_0) \end{pmatrix} + \eta_2^d \begin{pmatrix} Q_{\text{dust}}(\nu_0) \\ U_{\text{dust}}(\nu_0) \end{pmatrix} + \eta_2^s \begin{pmatrix} Q_{\text{sync.}}(\nu_0) \\ U_{\text{sync.}}(\nu_0) \end{pmatrix} \right. \\ & \left. - \eta_1^c \begin{pmatrix} Q_{\text{CMB}}(\nu_0) \\ U_{\text{CMB}}(\nu_0) \end{pmatrix} - \eta_1^d \begin{pmatrix} Q_{\text{dust}}(\nu_0) \\ U_{\text{dust}}(\nu_0) \end{pmatrix} - \eta_1^s \begin{pmatrix} Q_{\text{sync.}}(\nu_0) \\ U_{\text{sync.}}(\nu_0) \end{pmatrix} \right],\end{aligned} \tag{101}$$

where $\eta_2^{c,d,s}$ and $\eta_1^{c,d,s}$ are the matrices calculated with and without calibration errors. We use η_1^c as $\eta^{\text{calib.}}$ at this time. This residual map corresponds to the systematic effects caused by the difference between the actual telescope and its model originated from the calibration error. From $Q_{\text{res.}}$ and $Q_{\text{res.}}$, we obtain the B-mode power spectrum of this residual map, $C_\ell^{\text{BB, res.}}$, for each AHWP design type.

In the case of $\Phi^{c,d,s} = 0$, the matrices $\eta^{c,d,s}$ can be reformed as coefficients $\kappa^{c,d,s}$. Since the coefficients do not equal 1 except for κ^c, we need to correct these coefficients in the data analysis. When we express coefficients after correction as $1 + \Delta_\gamma$, the observed map can be written as,

$$\begin{pmatrix} Q_{\text{obs.}} \\ U_{\text{obs.}} \end{pmatrix} = \begin{pmatrix} Q_{\text{CMB}}(\nu_0) \\ U_{\text{CMB}}(\nu_0) \end{pmatrix} + (1+\Delta_\gamma) \begin{pmatrix} Q_{\text{dust}}(\nu_0) \\ U_{\text{dust}}(\nu_0) \end{pmatrix} + (1+\Delta_\gamma) \begin{pmatrix} Q_{\text{sync.}}(\nu_0) \\ U_{\text{sync.}}(\nu_0) \end{pmatrix}. \tag{102}$$

The requirement of Δ_γ for each LiteBIRD observation band are obtained in T. Ghigna et al [26] as Tab. 12. To obtain this requirement, they performed component separation on maps with changing Δ_γ and obtained the degradation to the tensor-to-scalar ratio r of these systematic effects from the CMB maps after component separation. The requirements shown in the Table are obtained by choosing Δ_γ where r is smaller than 5.6×10^{-6}, which is 1% of the LiteBIRD requirements. When we take residual between the maps with and without Δ_γ, the requirement in Tab. 12 can be converted to the residual map we are discussing as,

$$\begin{pmatrix} Q_{\text{res.}}^{\text{req.}} \\ U_{\text{res.}}^{\text{req.}} \end{pmatrix} = \Delta_\gamma \left[\begin{pmatrix} Q_{\text{dust}}(\nu_0) \\ U_{\text{dust}}(\nu_0) \end{pmatrix} + \begin{pmatrix} Q_{\text{sync.}}(\nu_0) \\ U_{\text{sync.}}(\nu_0) \end{pmatrix} \right]. \tag{103}$$

From $Q_{\text{res.}}^{\text{req.}}$ and $U_{\text{res.}}^{\text{req.}}$, we calculate the requirement in the B-mode power spectrum as, $C_\ell^{\text{BB, req.}}$. This requirement does not include the effect of the HWP phase, but it is corresponding to a part of the systematic effects discussed in this section. Therefore, we assume that $C_\ell^{\text{BB, req.}}$ can be used as a tentative requirement to evaluate $C_\ell^{\text{BB, res.}}$.

To search for calibration accuracy requirements, we calculate $C_\ell^{\text{BB, res.}}$ with changing the measurement errors given in Sec. 3.3.1 and compared it with $C_\ell^{\text{BB, req.}}$. For $\sigma_\epsilon(\nu)$ and $\sigma_p(\nu)$, we use averaged values of $C_\ell^{\text{BB, res.}}$ calculated from 1000 sets of $\delta_\epsilon(\nu)$ and $\delta_p(\nu)$. When we calculate the residual map for one of the calibration errors, the other errors are fixed to zero. Tab. 13 shows the measurement errors we used and their values. Fig. 33 shows the B-mode power spectrum of the residual maps for each AHWP design type when we set $\sigma_\epsilon = 0.01$. In the calculations of Eq. 92 and Eq. 93, δ_ϵ changes $\Phi^{c,d,s}$ except in the case of $\phi_4(\nu) = 0$. From Eq. 96, this change produces

Table 12: Table of requirements for Δ_γ [26].

Frequency band [GHz]	Δ_γ
40	2.5×10^{-3}
50	7.5×10^{-3}
60	7.5×10^{-3}
68	7.5×10^{-3}
78	1.0×10^{-2}
89	5.0×10^{-3}
100	1.0×10^{-3}
119	1.0×10^{-3}
140	2.5×10^{-3}
166	7.5×10^{-4}
195	2.5×10^{-4}
235	5.0×10^{-4}
280	1.0×10^{-3}
337	1.0×10^{-4}
402	1.0×10^{-4}

Table 13: Table of calibration errors.

Calib. error	Values
σ_ϵ	0.001, 0.002, 0.003, 0.004, 0.005, 0.006, 0.007, 0.008, 0.009 0.01, 0.02, 0.03, 0.04, 0.05, 0.06, 0.07, 0.08, 0.09, 0.1, 0.2
δ_ϵ	-0.05, -0.06, -0.07, -0.08, -0.09, -0.1, -0.2
σ_p [arcmin]	1, 2, 3, 4, 5, 6, 7, 8, 9, 11, 12, 13, 14, 15, 16, 17, 18, 19, 20, 30, 60
δ_p [arcmin]	0.1, 0.2, 0.3, 0.4, 0.5, 0.6, 0.7, 0.8, 0.9, 1, 2, 3, 4, 5, 6, 7, 8, 9, 10

E-mode leakage, so $C_\ell^{\text{BB, res.}}$ is larger for symmetric design than for anti-symmetric design.

Fig. 34 shows the B-mode power spectrum of the residual maps for each AHWP design type when we set $\delta_\epsilon^{off} = 0.05$. Since $\Phi^{c,d,s}$ is only affected by the spectral shape of $\epsilon(\nu)$, δ_ϵ does not change $\Phi^{c,d,s}$ and does not create E-mode leakage. Of course, the offset affects the absolute value of $\kappa^{c,d,s}$, but $C_\ell^{\text{BB, res.}}$ is small since this change in absolute value is almost canceled in the correction using the CMB.

Fig. 35 shows the B-mode power spectrum of the residual maps for each AHWP design type when we set $\sigma_p = 10$ arcmin. When we correct the element of $\eta^{c,d,s}$ with respect to the CMB as shown in parentheses in Tab. 8 and Tab. 9, there is a large difference in $\phi_4(\nu)$ between the two designs (see Fig. 22), even though $\kappa^{c,d,s}/\kappa^c$ difference is at the sub-percent level. This suggests that the change in $\kappa^{c,d,s}/\kappa^c$ due to $\delta_p(\nu)$ is even smaller. In other words, the effect of $\delta_p(\nu)$ almost to add a small angle to $\Phi^{c,d,s}$ and is independent of the design. Since the $\delta_p(\nu)$ used in the calculation for each design is the same, the $C_\ell^{\text{BB, res.}}$ shown in Fig. 35 are same.

Fig. 36 shows the B-mode power spectrum of the residual maps for each AHWP design type when we set $\delta_p^{off} = 10$ arcmin. Since $\kappa^{c,d,s}$ is only affected by the spectral shape of $\phi_4(\nu)$, δ_p^{off} does not change $\kappa^{c,d,s}$ and just add ownself to $\Phi^{c,d,s}$. Therefore, $C_\ell^{\mathrm{BB,\ res.}}$ becomes lager than that of in the case of $\sigma_p = 10$arcmin.

To find the requirement for each calibration accuracy, we calculate the ratio, $C_\ell^{\mathrm{BB,\ res.}}/C_\ell^{\mathrm{BB,\ req.}}$, in $2 < \ell < 200$. Fig. 37 shows the one of example of the calculation results of $C_\ell^{\mathrm{BB,\ res.}}/C_\ell^{\mathrm{BB,\ req.}}$ for the symmetric design at 100GHz. We choose the calibration errors when $C_\ell^{\mathrm{BB,\ res.}}/C_\ell^{\mathrm{BB,\ req.}} < 1$ and summarize in Tab. 14 and Tab. 15 with the maximum value. If the maximum value of the ratio is much smaller than 1, it means that there is room to find a relaxed requirement. However, for δ_ϵ^{off}, the maximum value of $C_\ell^{\mathrm{BB,\ res.}}/C_\ell^{\mathrm{BB,\ req.}}$ is much smaller than 1 for both AHWP designs because the simulations in this section do not take into account any noise. Since, as mentioned in Sec. 1.4.2, the large $\delta_\epsilon^{\mathrm{off}}$ increases the NET, $\delta_\epsilon^{\mathrm{off}}$ should be limited from the noise (sencitivity) calculation. There was no difference in σ_p and δ_p^{off} between the designs. In the case of σ_ϵ, we confirm that the anti-symmetric design can relax the requirements compared to the symmetric design. The strict requirements are obtained at 100 and 119 GHz in all cases. This is due to the small requirements of Tab. 12 and the fact that CMB is dominant in these bands but the effect of CMB is not considered in Eq. 103, so the requirements may be relaxed in a future study.

Table 14: Table of calibration accuracy for symmetric design.

Center frequency [GHz]	Error of $\epsilon(\nu)$				Error of $4\phi_4(\nu)$			
	σ_ϵ		$\delta_\epsilon^{\mathrm{off}}$		σ_p		δ_p^{off}	
	Max. ratio	Req.	Max. ratio	Req.	Max. ratio	Req. [arcmin]	Max. ratio	Req. [arcmin]
40	0.72	< 0.003	0.84	< 0.07	0.49	< 2.0	0.96	< 0.9
50	0.96	< 0.009	0.02	< 0.20	0.93	< 13.0	0.57	< 2.0
60	0.59	< 0.020	0.00	< 0.20	0.99	< 9.0	0.53	< 2.0
69	0.86	< 0.070	0.00	< 0.20	0.99	< 19.0	0.47	< 2.0
78	0.80	< 0.030	0.00	< 0.20	0.78	< 30.0	0.92	< 4.0
89	0.34	< 0.010	0.01	< 0.20	0.72	< 20.0	0.81	< 2.0
100	0.81	< 0.007	0.06	< 0.20	0.90	< 3.0	0.76	< 0.4
119	0.76	< 0.003	0.03	< 0.20	0.88	< 16.0	0.73	< 0.4
140	0.65	< 0.030	0.80	< 0.07	0.56	< 20.0	0.73	< 1.0

Table 15: Table of calibration accuracy for anti-symmetric design.

	Error of $\epsilon(\nu)$				Error of $4\phi_4(\nu)$			
	σ_ϵ		$\delta_\epsilon^{\mathrm{off}}$		σ_p		δ_p^{off}	
Center frequency [GHz]	Max. ratio	Req.	Max. ratio	Req.	Max. ratio	Req. [arcmin]	Max. ratio	Req. [arcmin]
40	0.58	< 0.010	0.59	< 0.10	0.48	< 2.0	0.95	< 0.9
50	0.94	< 0.040	0.01	< 0.20	0.91	< 13.0	0.57	< 2.0
60	0.94	< 0.080	0.00	< 0.20	0.99	< 9.0	0.53	< 2.0
69	0.87	< 0.070	0.00	< 0.20	0.99	< 19.0	0.47	< 2.0
78	0.90	< 0.090	0.00	< 0.20	0.78	< 30.0	0.92	< 4.0
89	0.87	< 0.040	0.00	< 0.20	0.73	< 20.0	0.81	< 2.0
100	0.98	< 0.010	0.01	< 0.20	0.90	< 3.0	0.76	< 0.4
119	0.73	< 0.010	0.02	< 0.20	0.89	< 16.0	0.73	< 0.4
140	0.81	< 0.050	0.27	< 0.20	0.48	< 20.0	0.73	< 1.0

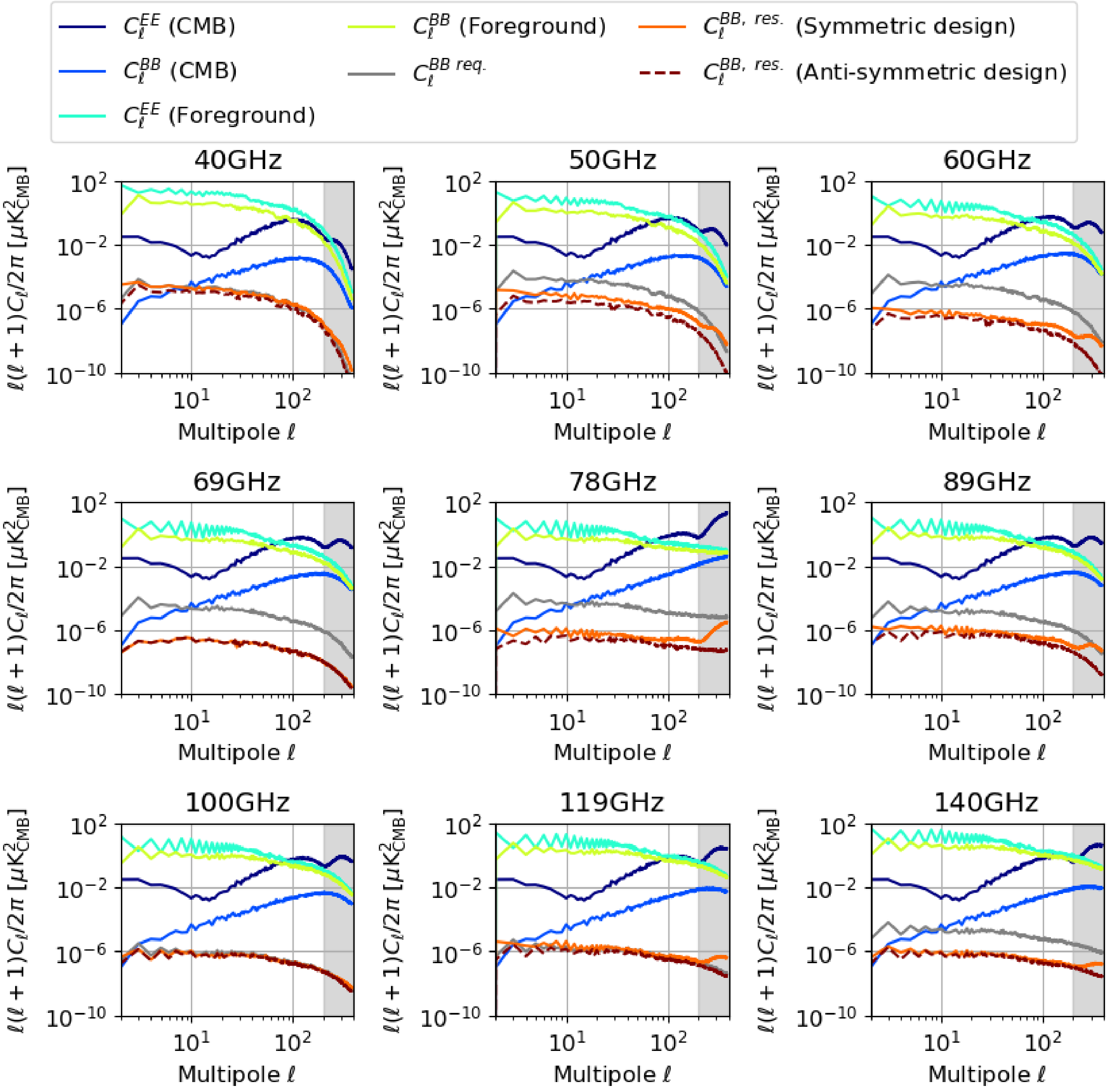

Figure 33: *B*-mode power spectrum of residual map in the case of $\sigma_\epsilon = 0.01$. We also show the power spectrum of the CMB and the foreground for comparison. The gray line shows the requirement calculated from Eq. 103. The gray area is the area that is not observed by LiteBIRD.

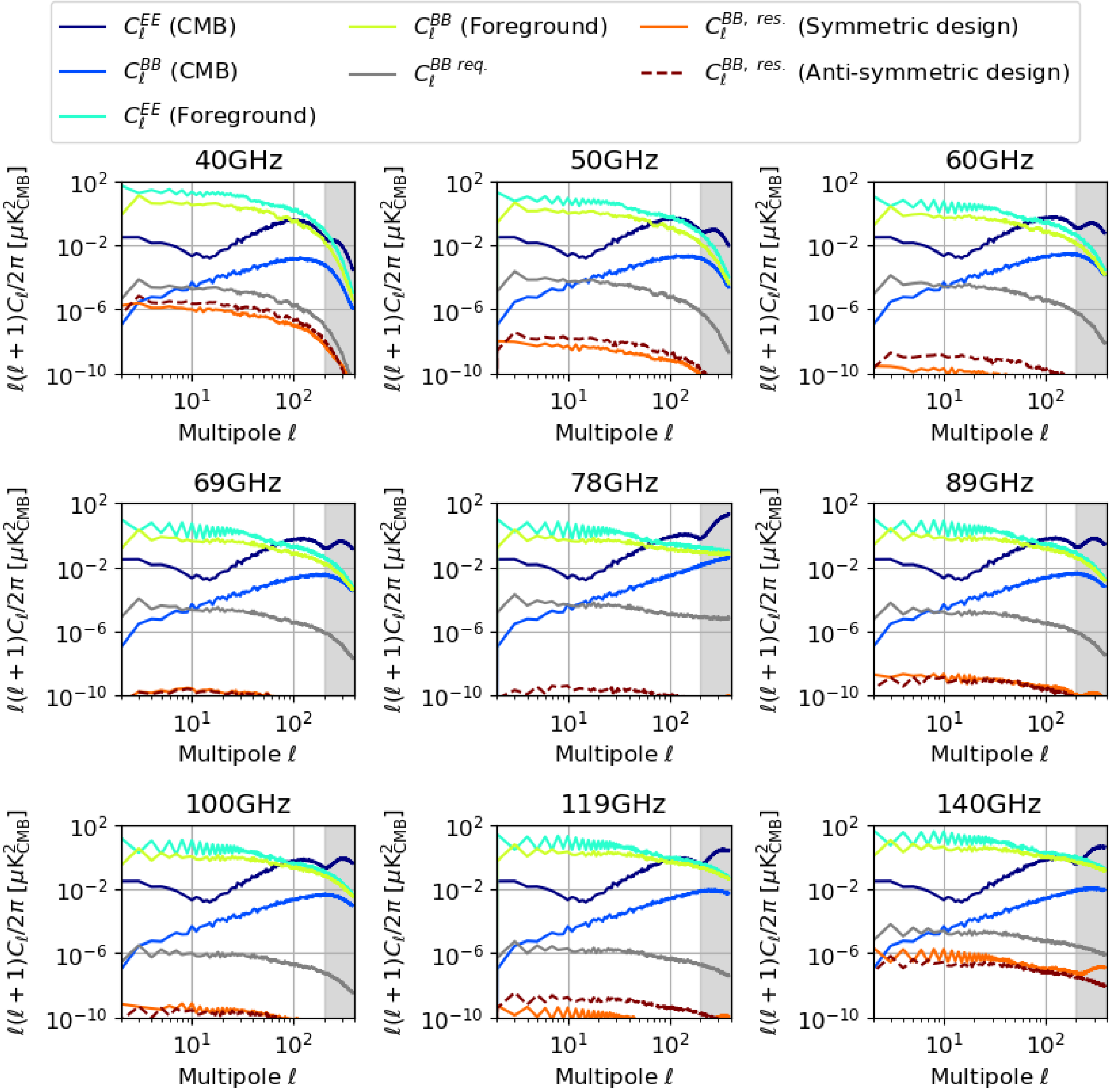

Figure 34: B-mode power spectrum of residual map in the case of $\delta_\epsilon^{off} = 0.05$. We also show the power spectrum of the CMB and the foreground for comparison. The gray line shows the requirement calculated from Eq. 103. The gray area is the area that is not observed by LiteBIRD.

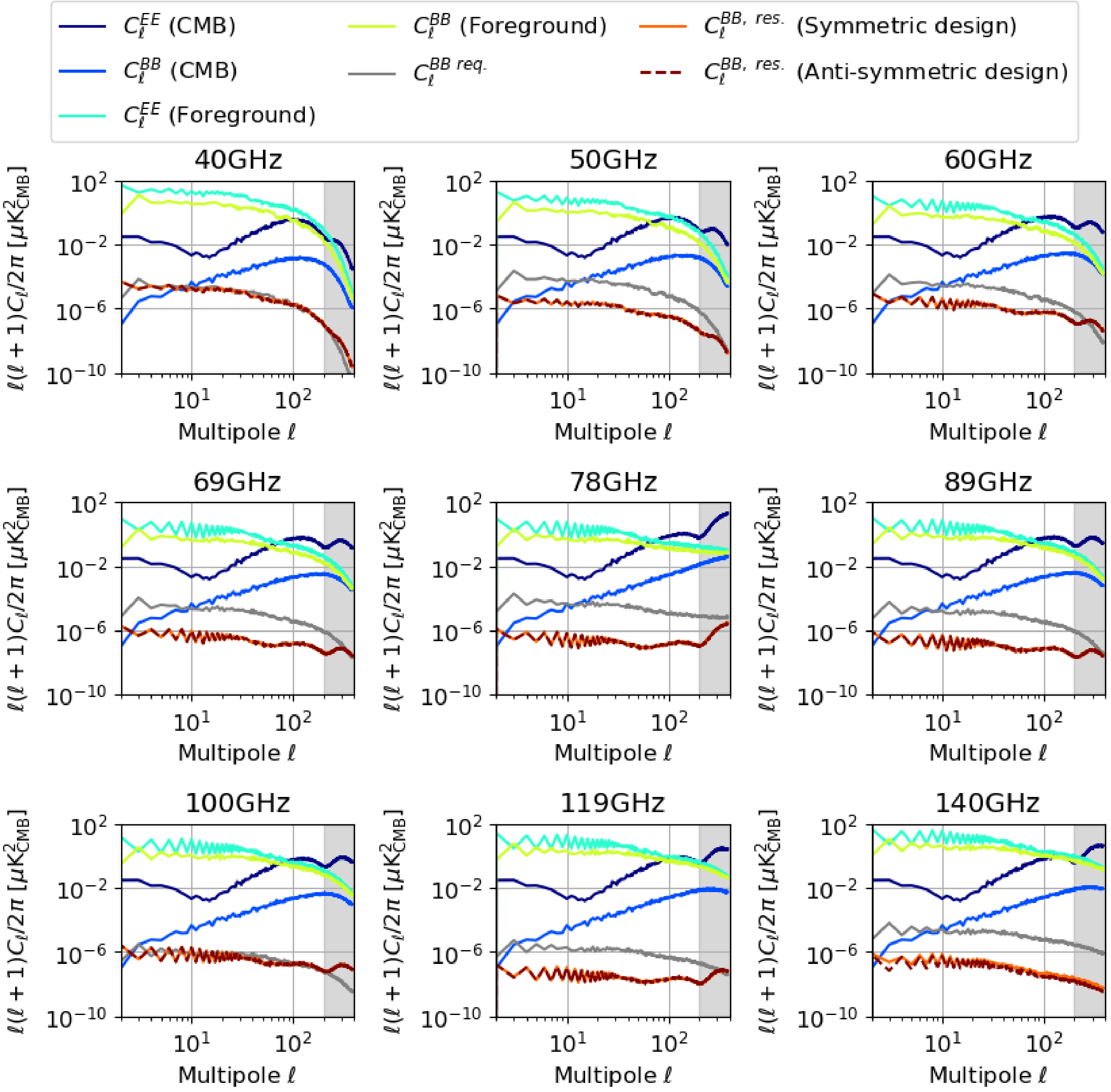

Figure 35: B-mode power spectrum of residual map in the case of $\sigma_p = 10$ arcmin. We also show the power spectrum of the CMB and the no HWP effect case for comparison. The gray line shows the requirement calculated from Eq. 103. The gray area is the area that is not observed by LiteBIRD.

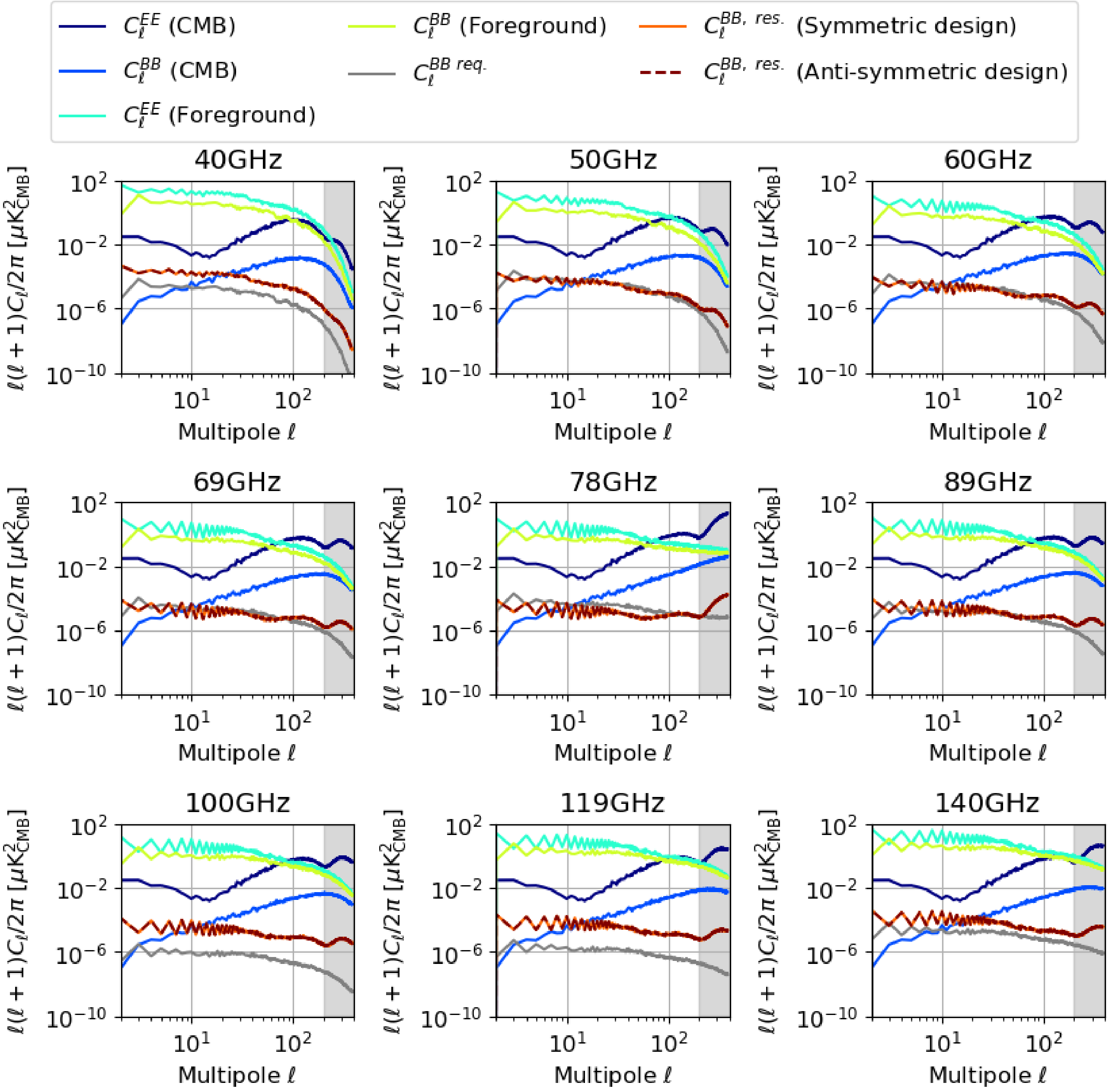

Figure 36: B-mode power spectrum of residual map in the case of $\delta_p^{off} = 10$ arcmin. We also show the power spectrum of the CMB and the no HWP effect case for comparison. The gray line shows the requirement calculated from Eq. 103. The gray area is the area that is not observed by LiteBIRD.

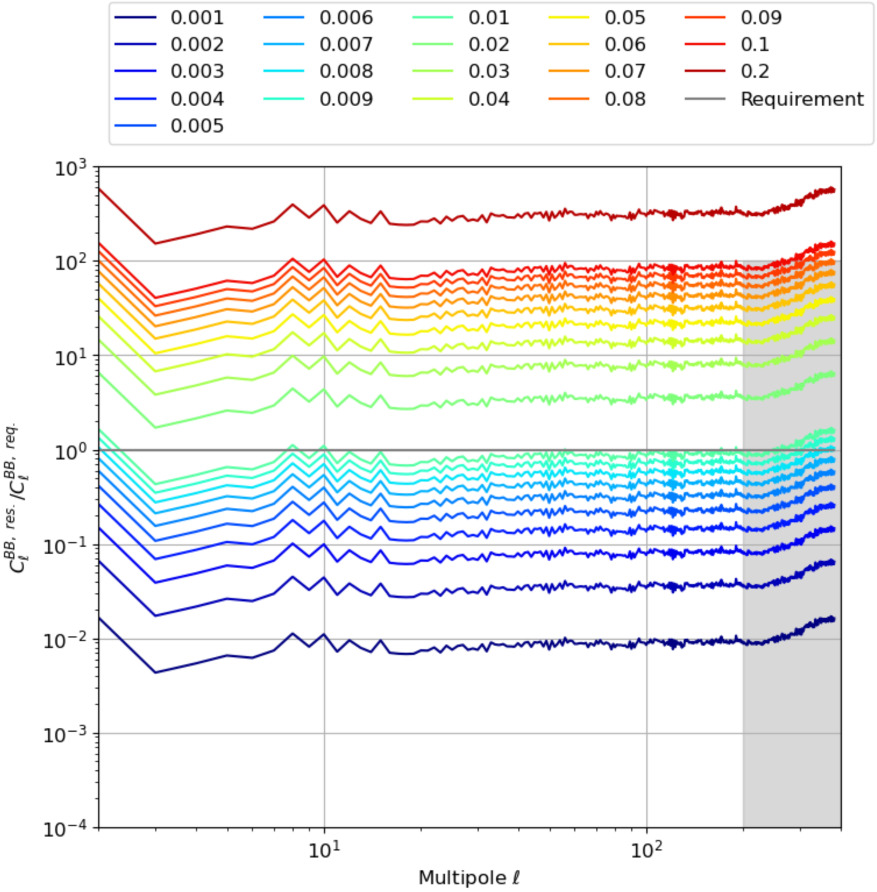

Figure 37: Ratio of power spectrum of residual map for symmetric design to requirement at 100 GHz. The values in the legend shows σ_ϵ. The gray area is the area that is not observed by LiteBIRD.

3.5.3 Effect of foreground spectrum change

We perform the same calculations for $\beta^{d,s}$ as are done in the previous subsection. From the Planck satellite observations, we know that $\beta^d = 1.55 \pm 0.05$ and $\beta^s = -1.1 \pm 0.1$. We calculate $C_\ell^{\mathrm{BB,\ res.}}$ for $\beta^d = 1.60,\ 1.50$ and $\beta^s = -1.0,\ -1.2$, respectively. Fig. 38 and Fig. 39 show the B-mode power spectrum of the residual map in the case of $\beta^d = 1.60$ and $\beta^s = -1.0$, respectively. In the case of $\beta^d = 1.50$ and $\beta^s = -1.2$, similar plots have appeared. We confirm that the anti-symmetric design is more robust to changes in the foreground spectrum than the symmetric design by the same reason for σ_ϵ in previous subsection.

3.5.4 Future works

In this section, we assume the frequency dependence of sensitive direction of a sinuous antenna ϕ_i is zero. However, in reality, it has frequency dependence and causes same effects of the frequency dependence of AHWP optic axis. The effects from the frequency dependence of AHWP optic axis and sinuous antennas should be consider together in the future works. In order to derive the requirement for calibration accuracy, we temporarily compare with T. Ghigna et al. [26] to obtain the requirements. In the future, it will be necessary to develop a foreground cleaning tool that includes AHWP performance, or apply the same method as T. Ghigna et al. [26] to $\kappa^{c,d,s}$ and $\Phi^{c,d,s}$ to estimate the requirements more precisely. In addition, the masking of the galactic center, foreground cleaning, or any noise effects, should be considered in future work.

3.6 Conclusions

In this section, we evaluate the systematic effects originated by the frequency dependence of the HWP performance on the observation results. We formulate the effect of the frequency dependence of the HWP performance on the observed results and simulate it for several cases. First, we estimate the effect of the HWP for the observed results, compared to the case without the HWP. We also discuss the light source used for the ground calibration. Next, we assume that the effects of the HWP are corrected in the data analysis. In this assumption, we simulate the systematic effects originated from some calibration error for the HWP, and obtain the requirements for the calibration errors from the comparison with the requirements of T. Ghigna et al. [26]. Each estimation and simulation are obtained for the five-layer case of the two AHWP designs presented in Sec. 2, and the comparison results of these two designs are summarized in Tab. 16. From Tab. 16, in some cases, we confirm that the anti-symmetric design is more useful for LiteBIRD observations than the symmetric design. Therefore, we conclude that we prefer to use the anti-symmetric design AHWP for LiteBIRD.

Table 16: Table of AHWP design comparison.

Item	Summary
AHWP effect in elements of $\eta^{c,d,s}$	The coefficients after the correction using CMB, $\kappa^{c,d,s}/\kappa^{c}$, are independent to the AHWP design at the sub-percent level. The angles $\Phi^{c,d,s}$ have the same value for all anti-symmetric designs, but have different value in a few degree scale in maximum for symmetric designs.
AHWP effect in C_ℓ	The average C_ℓ of the residual map for the symmetric design is larger than that of the anti-symmetric design by at least 10^1 orders and up to 10^3 orders for each LFT frequency band.
blackbody source for ground calibration	In the case of the anti-symmetric design, from the comparison with the in-flight calibration using the CMB, $\kappa^{\mathrm{calib.}}$ is equivalent at the sub-percent level and $\Phi^{\mathrm{calib.}}$ is completely equivalent. In the case of the symmetric design, from the comparison with the in-flight calibration using the CMB, $\kappa^{\mathrm{calib.}}$ is equivalent at the sub-percent level and $\Phi^{\mathrm{calib.}}$ is not equivalent in sub-degree scale difference. The 4 K blackbody gives the closest of $\Phi^{\mathrm{calib.}}$ to the in-flight calibration.
σ_ϵ	The anti-symmetric design relaxes the requirement four times than the symmetric design because there is no leakage from the E-mode caused by the frequency dependence of $\phi_4(\nu)$.
δ_ϵ	No useful requirements are found in this study. It should be obtained in future work considering with instrumental noises.
σ_p	There is no difference between the two AHWP designs.
δ_p	There is no difference between the two AHWP designs.
Change of β^d and β^s	From the same reason for σ_ϵ, the anti-symmetric design is more robust than the symmetric design to the change of $\beta^{d,s}$.

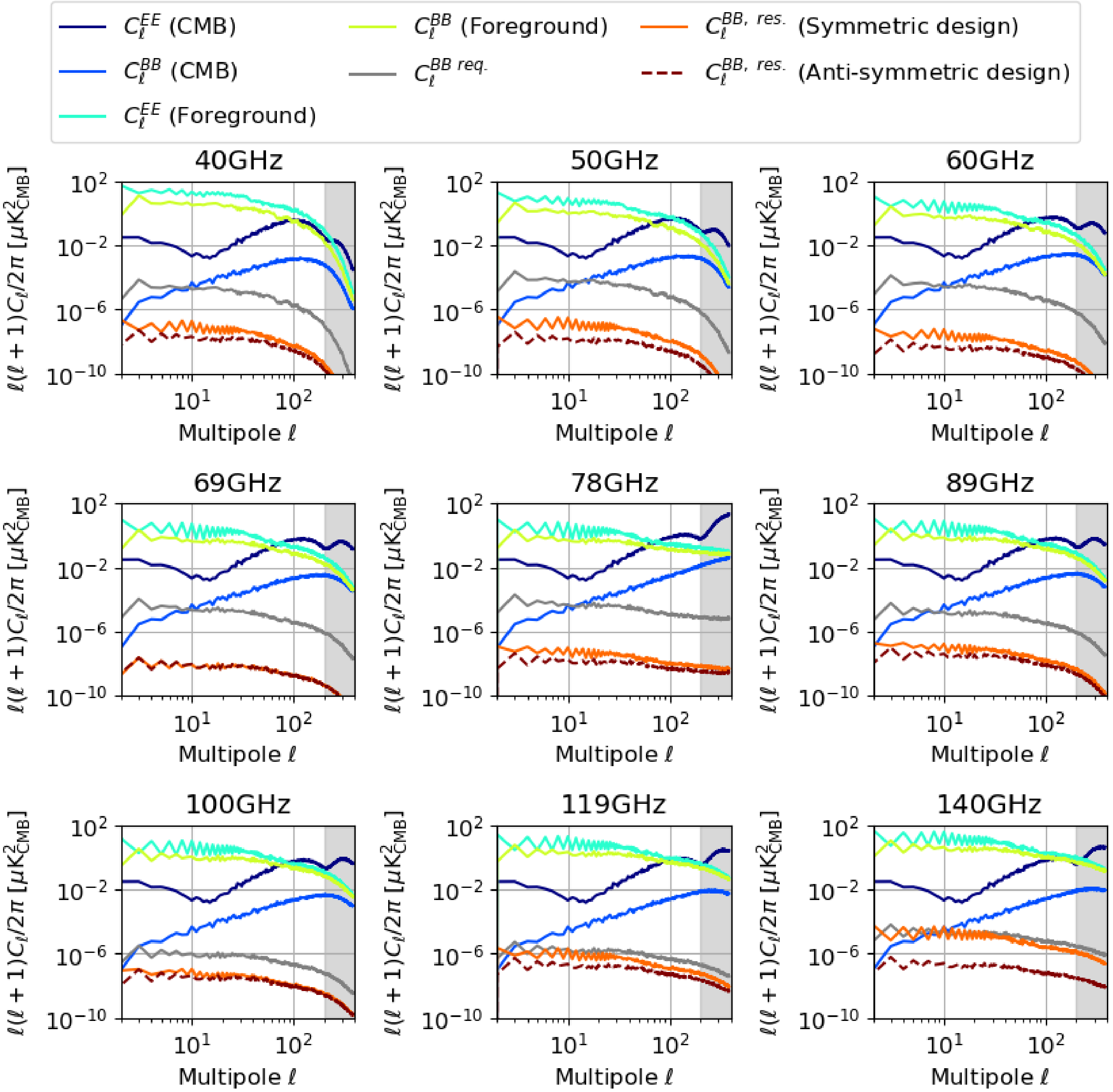

Figure 38: B-mode power spectrum of residual map in the case of $\beta^d = 1.60$. We also show the power spectrum of the CMB and the no HWP effect case for comparison. The gray line shows the requirement calculated from Eq. 103. The gray area is the area that is not observed by LiteBIRD.

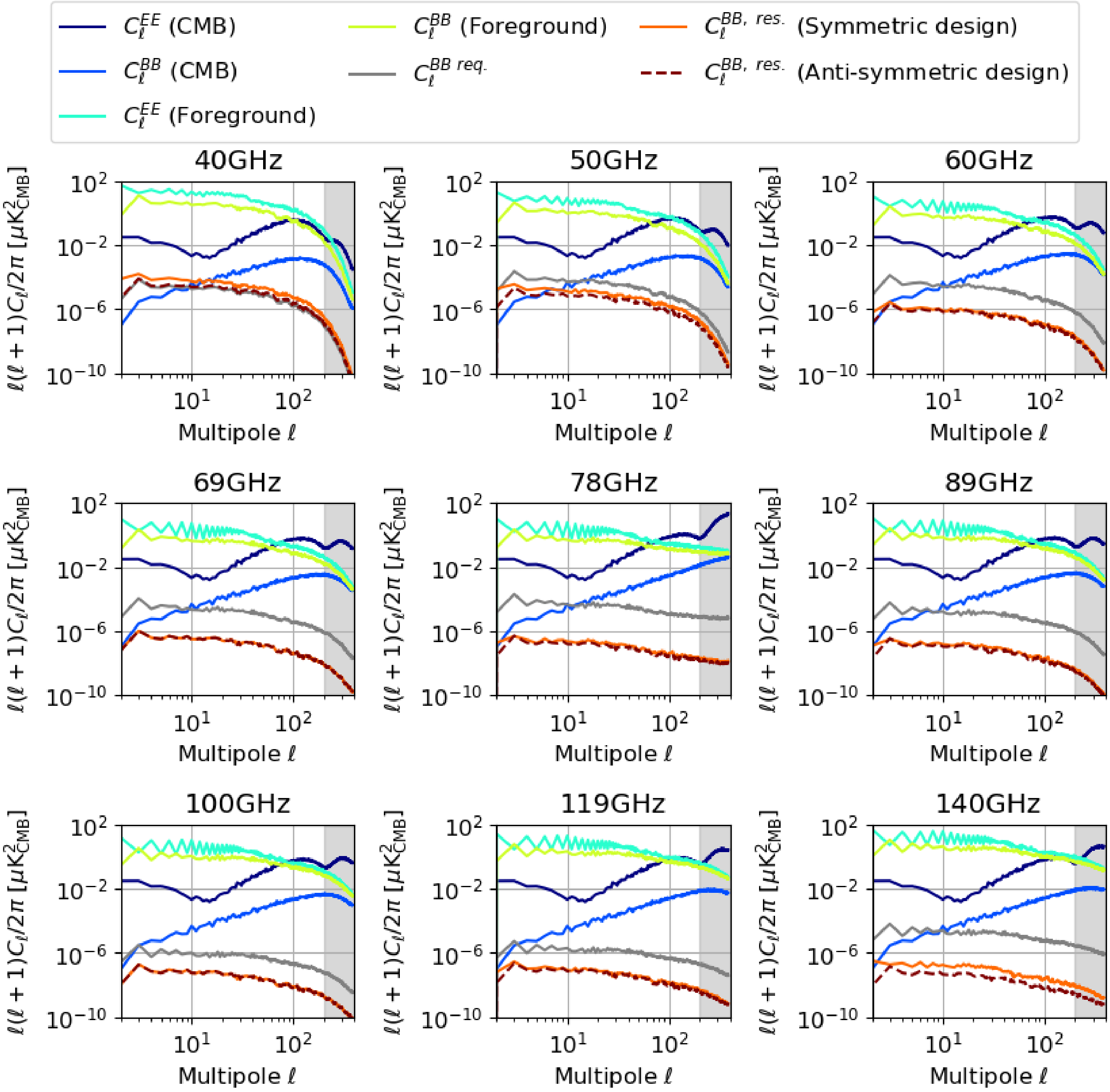

Figure 39: B-mode power spectrum of residual map in the case of $\beta^s = -1.0$ [57]. We also show the power spectrum of the CMB and the no HWP effect case for comparison. The gray line shows the requirement calculated from Eq. 103. The gray area is the area that is not observed by LiteBIRD.

4 Experimental demonstration

The following sections describe the AHWP design presented in Sec. 2, as well as some experimental demonstrations on PMUs. In the first half of this section, we report the results of an optical demonstration of the AHWP alone at room temperature. In the second half of this section, we report with the results of a cryogenic demonstration of a small 1/10 scale prototype PMU. All AHWPs demonstrated in this section consists of stacked A-cut sapphire plates. And we assume that the refractive indices of sapphire plates are constant in frequency range 34-270 GHz if there is no temperature change.

4.1 Modulation efficiency

The formalism of the HWP Polarimetry is previously shown in Sec. 2.2. In order to demonstrate the performance of the AHWP and to compare it with the model, we define the modulation efficiency $\epsilon'(\nu)$ as

$$\epsilon'(\nu) = \frac{D_4(\nu)\sqrt{Q_{\rm in}(\nu)^2 + U_{\rm in}(\nu)^2}}{D_{0\rm I}(\nu)I_{\rm in}(\nu) + D_{0\rm Q}(\nu)Q_{\rm in}(\nu) + D_{0\rm U}(\nu)U_{\rm in}(\nu)}. \tag{104}$$

The modulation efficiency is the ratio between the signal power that is modulated at 4 times frequency of the HWP rotational frequency and the detected power. There are two reasons why we defined the modulation efficiency in this way. First, we implicitly assume that the AHWP is going to be rotated continuously and thus, we only pick up the term which is relevant to the 4 times of the rotation frequency already. Secondly, we want to define the efficiency in such that we can make a comparison between the measured degree of polarization and the prediction. This is driven by the fact that it is easy to prepare the fully polarized incident source using a wire grid polarizer. Modulation efficiency is not exactly the same as polarization efficiency in previous sections, but they have a similar value. Therefore, temporary, we set the target values of band averaged modulation efficiencies for each LFT frequency band to 0.98. The connection between the lab measured efficiency and the CMB analysis is addressed in T. Matsumura et al. [45]. We also use the modulated signal phase ϕ_4 to compare the prediction with the measured data.

4.2 Demonstration at room temperature

4.2.1 Introduction

This subsection is based on K. Komatsu et al. [42]. Images are taken from [42]. In this section, we report the optical demonstration result for the nine layers AHWP at room temperature. The design of the AHWP is similar, but not same to, the symmetric design in Sec. 2. The initial design of the observational frequency band of the LFT was from 34 to 270 GHz, and thus we aim for this range as a development goal. We designed and constructed the prototype AHWP and evaluated it experimentally in the millimeter wave band, from 33 to 260 GHz, which is the widest demonstrated bandwidth at millimeter wave. We discussed the results including the features which we have observed in the measured modulation efficiency. After the latest design iteration, LiteBIRD LFT covers from 34 to 161 GHz [28]. As a result, the AHWP developed in this section covers the wider range as compared to the current LiteBIRD LFT frequency coverage. In this section, when referring to the frequency range or band of LiteBIRD, it refers to the old one, that is 34 to 270GHz.

4.2.2 Sample preparation

Design optimization As mentioned in above, the AHWP consists of stacked sapphire plates with specific set of optic axis angle. The design optimization of the AHWP demonstrated in section is carried out for a nine layers AHWP using a brute force method similar to that is shown in Sec. 2. In this optimization, we do not put any constraint on the optic axis angle of each sapphire plate (i.e. anti-symmetric and symmetric) as Sec. 2.4.3. Since we do not use thickness of each sapphire plates in this optimization, the optimized parameters are nine optic axis angle. For the frequency range of 34 - 270 GHz, the center frequency is given as $\nu_c = 152$ GHz, and its corresponding thickness is 3.14 mm, where we use $n_{\mathrm{o}} = 3.047$ and $n_{\mathrm{e}} = 3.361$ for the refractive indices at low temperature [34] and we assume lossless sapphire plates. We use the averaged modulation efficiency $2A_2$ in Eq. 40 as the figure-of-merit for this optimization. We generate random numbers for the relative optic axis angle to find an optimal optic axis angle set offering the high averaged modulation efficiency in the frequency range. We repeated the optimization using various initial starting value to search the wide range of the parameter space in the case of $S_{\mathrm{in}} = (1, 0, 1, 0)$. After the completion of the optimization, we considered the performance including the reflection using the calculation referring to T. Essinger-Hileman [22].

As a result of several times optimizations, we have concluded that the nine layers AHWP can cover almost all of the targeted bandwidth. Tab. 17 shows the optimized values of the relative angles in three and nine layers AHWP. The angles of 1^{st} and 9^{th} layers are not same due to the result of search to get higher 2_A4. Fig. 40 shows the modulation efficiency and phase as a function of frequency with the optimized design for a single plate, the three and nine layers.

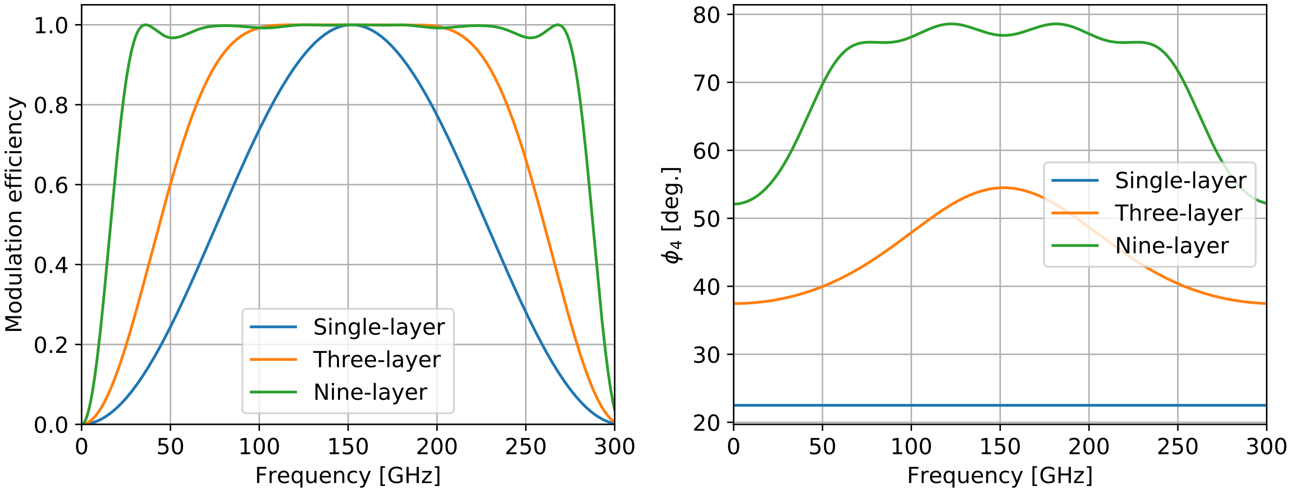

Figure 40: Calculated modulation efficiency and phase as a function of frequency for the optimized nine-layer AHWP design. For comparison, we also show the calculated result of a single HWP and three-layer AHWP. We calculate for $S_{\mathrm{in}} = (1, 0, 1, 0)$. Image from [42].

Fabrication We fabricated the nine layers AHWP based on the optimized parameters in Tab. 17. The sapphire plates used for the AHWP have a diameter of 100 mm and a thickness of 2.53 mm. Although the optimized thickness is 3.14 mm for the targeted frequency range, we have used sapphire plates with a thickness of 2.53 mm, which we had at the time for assembly. We believe that

Table 17: Designed values of the relative angles in the three- and nine-layer AHWP. The thickness of each plate is identical. χ_i is the optic axis angle of the i^{th} plate relative to the first layer. The design of the three-layer AHWP from T. Matsumura at al. [45]. Table from [42].

Number of plates	d_c [mm]	χ_i[deg.]
3	3.14	0, 58, 0
9	3.14	0, 18.5, 37.5, 73.9, 141.5, 73.9, 37.5, 18.5, 22.7

this slight difference in thickness is not critical for these demonstration purposes (e.g. comparison with the prediction and measured data). We measure the thickness of the sapphire plate cut from the same batch along the circumference of the disc, and the variation of the thickness within the sample is found to be less than 8 μm. The surface condition of all sapphire plates is unpolished. We have stacked the plates without glue at the interface of two plates, and fixed them with an aluminum holder as shown in Fig. 41. The SWS is not applied on any of the surfaces.

To stack the sapphire plates, we use a universal measurement machine (UMM). The UMM consists of a rotating table and a microscope. Each sapphire plate has an orientation flat (OF) at its side that is in perpendicular to the optic axis and can be used as the reference of the optic axis with the accuracy 3 degrees. This accuracy is coming from the uncertainty of the dicing capability in the manufacturing of the sapphire. The sapphire plates are stacked in the aluminum holder while adjusting with respect to OF to the designed orientation of the optic axis of each plate. Fig. 41 shows a picture of the assembled nine layers AHWP. The relative angular uncertainty between the OF of the plates is less than 10 arcmin. Sapphire plates are fixed in the holder with pressure applied by an aluminum ring. The implication of this uncertainty is addressed in subsection 4.2.5. After assembly, we investigate the thickness of the air gap by inserting several thin stainless steel plates with varying thickness ($\geq$50 μm), between layers of the AHWP. We identify that the air gap between the first and second layer is around 50 μm, and that air gaps between other layers are less than 50 μm. We take into account for the presence of the gap in the analysis.

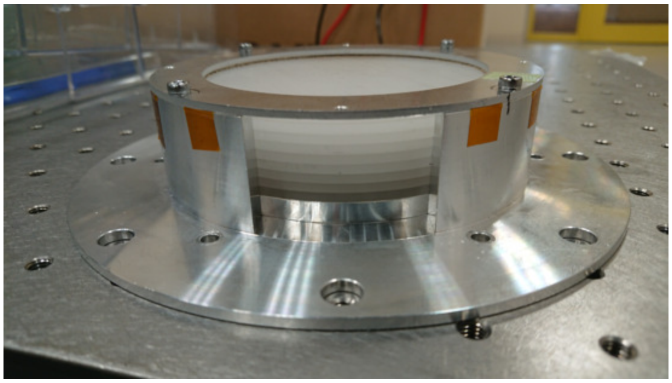

Figure 41: The assembled nine-layer AHWP. Image from [42].

4.2.3 Experiment

Experimental setup Fig. 42 shows a conceptual sketch of setup for measuring the modulation efficiency and transmittance of a sample in the sample holder in the frequency ranges of 33-140 GHz and 150-260 GHz. The millimeter waves are generated by a combination of a Continuous Wave (CW) generator and six active multipliers. The CW generator can output microwaves up to 20 GHz. Active multipliers up-convert the frequency of the signal from the CW generator with specific multiple factors, respectively. The multiple factors and band width of individual active multipliers are ×4 (33-50 GHz), ×4 (50-75 GHz), ×6 (75-110 GHz), ×8 (90-140 GHz), ×12 (150-220 GHz) and ×24 (210-260 GHz). The millimeter wave from the source is linearly polarized. We pair the active multiplier with a diode detector for the measurements of each band in above. The diode detectors are single polarization-sensitive detectors. Two feedhorns for the source (the active multiplier) and for the detector are placed at the foci of the off-axis parabolic mirrors. The millimeter waves emitted from the source horn are collimated by the first mirror. The plane waves propagate through the first attenuator, the first wire grid, the 70 mm diameter aperture, the measurement sample, the second attenuator, and the second wire grid. The plane waves are focused by the secondary mirror to be fed to the detector horn. We define the polarization angle of incident light to the sample using two free-standing wire grids. We set the transmission axis of the two wire grids in parallel. The transmittance of the wire grid for the radiation having the electric field perpendicular (parallel) to the wire orientation is 0.99 (0.01) in our frequency range. The signal is modulated by an optical chopper at 80 Hz and to be demodulated and amplified by a lock-in amplifier. The detector outputs voltage proportional to the detected power. All the measurements is performed at room temperature. About an optical measurement of AHWP at cryogenic temperatures is shown in Sec. 4.3.

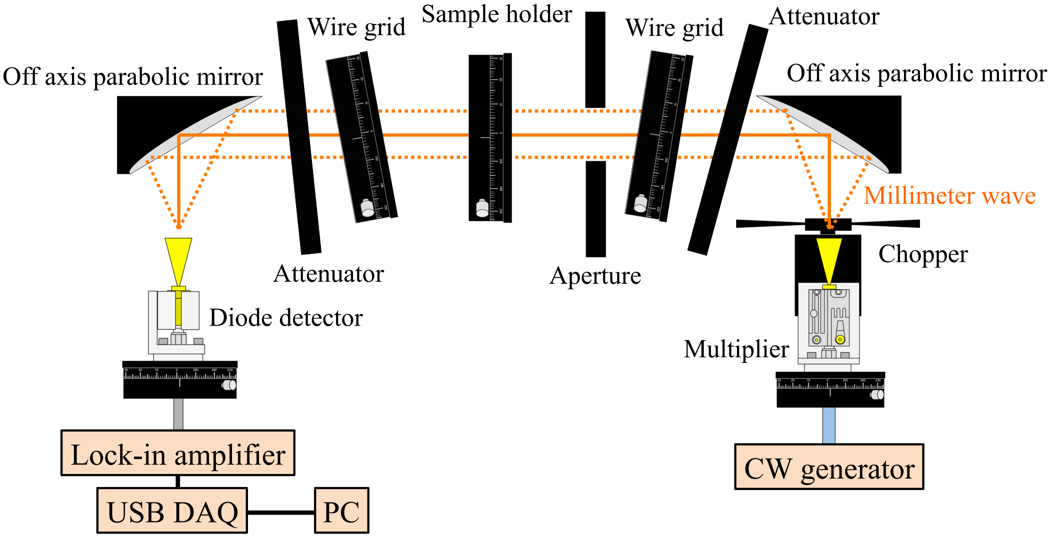

Figure 42: A sketch of the measurement system. The millimeter waves propagate along the orange lines from the right hand to the left hand side of the figure. The aperture size is approx. 70 mm in diameter. Image from [42].

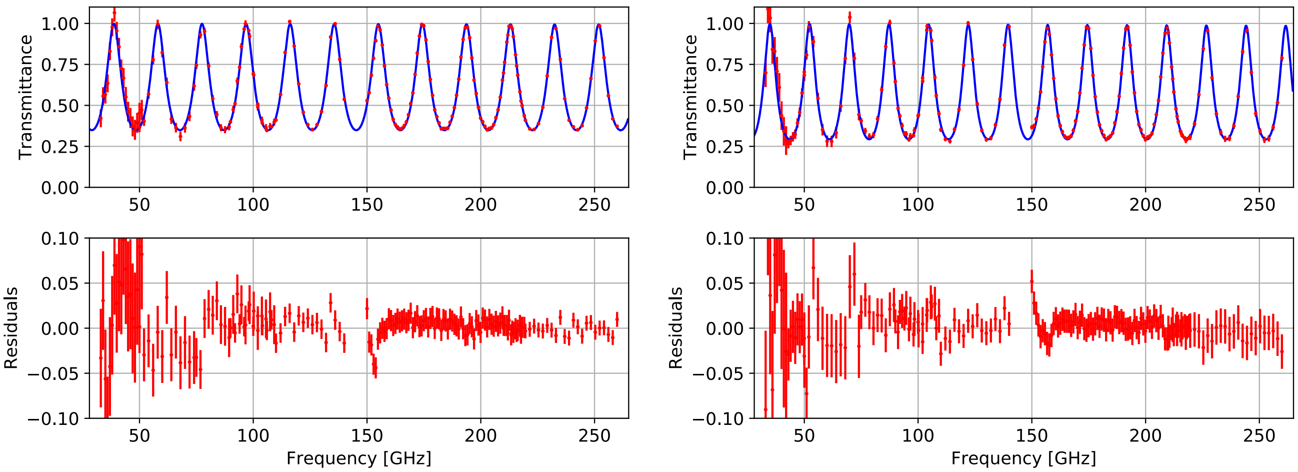

Figure 43: The transmittance for the ordinary ray (left) and the extraordinary ray (right) for a A-cut sapphire plate. The top plot shows the measurement (the red dots with error-bars) and fitted (the blue solid line) results. The bottom plot shows the residuals of the fitting. Image from [42].

Measurement of the refractive index To predict the modulation efficiency and phase of the assembled AHWP, we need to know the two refractive indices of an A-cut sapphire plate for ordinary and extraordinary rays at the room temperature. We obtain the indices by measuring transmittance, i.e. Fabry-Pérot interference, using the setup in Fig. 42. When the plane of incident polarization and the detector-sensitive direction are parallel to the optic axis, transmittance T and the complex refractive index $\tilde{n}$ for an extraordinary (ordinary) ray are simply related in the case of the normal incidence [29] as

$$T(\tilde{n}) \quad = \quad \left| \frac{2\tilde{n}}{2\tilde{n}\cos k_0\tilde{n}d + i(\tilde{n}^2+1)\sin k_0\tilde{n}d} \right|^2 , \tag{105}$$

$$\tilde{n} \quad \simeq \quad n\left(1 - \frac{i}{2}\tan\delta\right) , \tag{106}$$

where variable d is the thickness of the sapphire plate and k_0 is the wave number in the vacuum. Since the loss tangent of sapphire is small enough to use the approximation, $\tilde{n}$ is expressed using the refractive index n and the loss tangent $\tan\delta$ in Eq. 106. The spectral shape of transmittance for polarization parallel and perpendicular to the optic axis are computed by taking a ratio of the acquired data between the sapphire plate case and the air case. We measure the refractive indices of one sapphire plate, and assume the same indices for the rest, which is valid because all the samples are originated from the same batch. We put the sapphire plate to the sample holder in Fig. 42. We then measure output voltages of the lock-in amplifier at 33 to 140 GHz and 150 to 260 GHz every ~ 1 GHz. After removing the A-cut sapphire plate, we remeasure output voltages of the lock-in amplifier for the same frequency. The measurement system is susceptible to the effect of the standing wave due to that we use a coherent source. The period of standing wave is $\lambda/2$ where λ is a wavelength of incident radiation. So that when we take an average of the power measured at two points separated by a distance $\lambda/4$, the oscilation of the standing wave is canceled. In reality, the effect of the standing wave is not completlt canceled due to the effect of focusing by the mirror and so on. However, this method is one of useful way for mitigating the effects of standing waves, so we use this method in our measurements.

Measurement of modulation efficiency The nine layers AHWP is mounted on a sample holder which can be automatically rotated by a stepping motor. The sample holder continuously rotates around the optical axis of this system with a revolution rate of $\omega_{\mathrm{hwp}} = 2\pi f_{\mathrm{hwp}}$, where f_{hwp} is about 0.02 Hz. We measure the modulated signal as the output voltage of the lock-in amplifier. The measurement time at each frequency is 60 seconds, during which the AHWP rotates about 360 degrees. The frequency of the electromagnetic source is swept during the rotation. The measured frequency range is 33 to 140 GHz and 150 to 260 GHz in ~ 1 GHz interval. The sampling rate of the demodulated signal from the lock-in amplifier is 100 Hz. For each frequency, we fit the acquired data using

$$I(t,\nu) = a_0(\nu) + \sum_{m=1}^{8} a_m(\nu) \cos\left(m\omega_{\mathrm{hwp}}t + m\phi_m(\nu)\right). \tag{107}$$

Since the AHWP rotates continuously while acquiring data at all frequencies, the initial offset of ϕ_n is different by frequencies. This offset is recorded and subtracted for each ϕ_n at given frequency. The $m = 4$ component is the modulatied signal of the AHWP. The $m = 2$ component appears due to the refractive index difference which is results of the frequency dependent transmittance, reflectance, and emissivity between for the ordinary and extraordinary rays of the HWP. The other components are included to capture all features, although we do not expect the odd-m components within the framework of the formalism in this thesis. We address this point in Sec. 4.2.5. The modulation efficiency and phase are obtained as a_4/a_0 and ϕ_4, respectively. The global offset of ϕ_4 is determined by the initial rotation angle of the sample holder. We have repeated the measurements for incident angles relative to the AHWP of 0 and ±10° for p- and s-polarization, which corresponds to the field-of-view of LiteBIRD LFT and the CMB telescope which observes small angular scales.

In many CMB experiments, the intensity of the observation signal is integrated by the detector with a specific band width. Therefore, we introduce the band average modulation efficiency to evaluate the integrated modulation signal. We use the frequency bands centered at 40, 50, 60, 68, 78, 89, 100, 119, 140, 166, 195, and 235 GHz with the band width of about 30% (see Fig. 14), that are covered by the LiteBIRD LFT. We normalize $I(t,\nu)$ by a_0 for each frequency, and integrate this normalized modulated signals as

$$\int_{\nu_i}^{\nu_f} \frac{I(t,\nu)}{a_0(\nu)} d\nu = \sum_{\nu=\nu_i}^{\nu_f} \frac{I(t,\nu)}{a_0(\nu)} = A_0 + \sum_{m=1}^{8} A_m \cos\left(m\omega_{\mathrm{hwp}}t + m\phi_m\right), \tag{108}$$

where ν_i and ν_f are the lower and higher boundary in each frequency band, respectively. We define the band averaged modulation efficiency as A_4/A_0.

4.2.4 Results

Measurement of refractive index Fig. 43 shows the measured transmittance and its fitting curve by Eq. 105 of an A-cut sapphire plate. From the fitting, we obtain the refractive index and loss tangent of the A-cut sapphire plate at room temperature as Tab. 18. In Fig. 43, the residuals between the fit and the measured data becomes larger at the lower frequency. It is thought that the

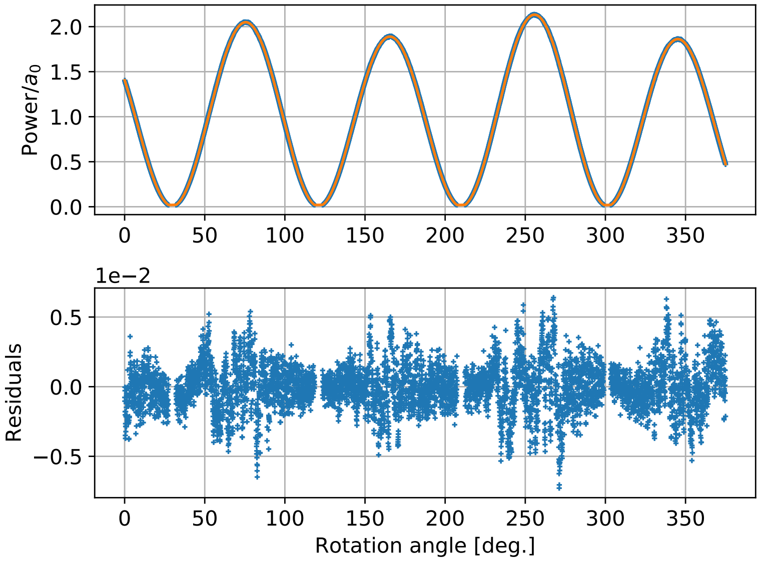

Figure 44: The output voltages of the lock-in amplifier, modulated signal, as a function of the AHWP rotation angle at 150 GHz for the normal incident angle. The output voltage is proportional to the millimeter wave power injected into the detector and normalized by a_0. The top plot shows the measurement (the blue crosses) and fitted (the orange solid line) results. The bottom plot shows the residuals of fitting. Image from [42].

differences are caused by the stability of the source or the effect of the diffraction at the aperture, which prevents the full cancellation of the standing effect.

Table 18: Fitted result to the refractive index and loss tangent for an A-cut sapphire plate at the room temperature. Table from [42].

Ordinary ray		Extraordinary ray	
Refractive index	Loss tangent ($\times 10^{-4}$)	Refractive index	Loss tangent ($\times 10^{-4}$)
3.059 ± 0.002	0.9 ± 0.3	3.397 ± 0.003	1.6 ± 0.5

Measurement of modulation efficiency Fig. 44 shows one example for the modulated signal and fitted result using Eq. 107 as a function of the rotation angle at 150 GHz. The modulated signal is normalized by the DC component, $m = 0$. Since the lock-in amplifier can not output a negative voltage, the sign of modulated signal is inverted where the signal becomes negative due to noise or offset. This effect decreases the amplitude of modulation signal and the modulation efficiency. Therefore, we removed the part of the modulated signal close to zero. For all frequencies and incident angles, we confirm that the residual is less than 3% (in RMS) of the $m = 0$ component. Fig. 45 shows the frequency dependence of the modulation efficiency and phase for each incident angle θ with p- and s-polarization. The prediction for the normal incidence takes into account the reflections between plates but does not consider the air gaps between them. In the prediction calculations, we use n_o and n_e at the room temperature in Tab. 18. We can see two features in

Fig. 45: the sharp dips that appear at about every 18 GHz, and the fast oscillatory features that fluctuate quickly and with a small amplitude. The dips originate from Fabry-Pérot interference within each plate that composes the AHWP. By contrast, the oscillatory feature is from the reflection at the boundaries between the first/last plate and air. Since these features originated from the reflection, they are mitigated the SWS is fabricated on the AHWP as anti-reflective structures, and that can be seen in Sec. 4.3.

Tab. 19 shows the measured band-averaged modulation efficiency and Tab. 20 shows the maximum difference of the phase variation within a band width, which is calculated for the LiteBIRD LFT frequency band. About the source of the modulation efficiency measurement errors is discussed in Sec. 4.2.5.

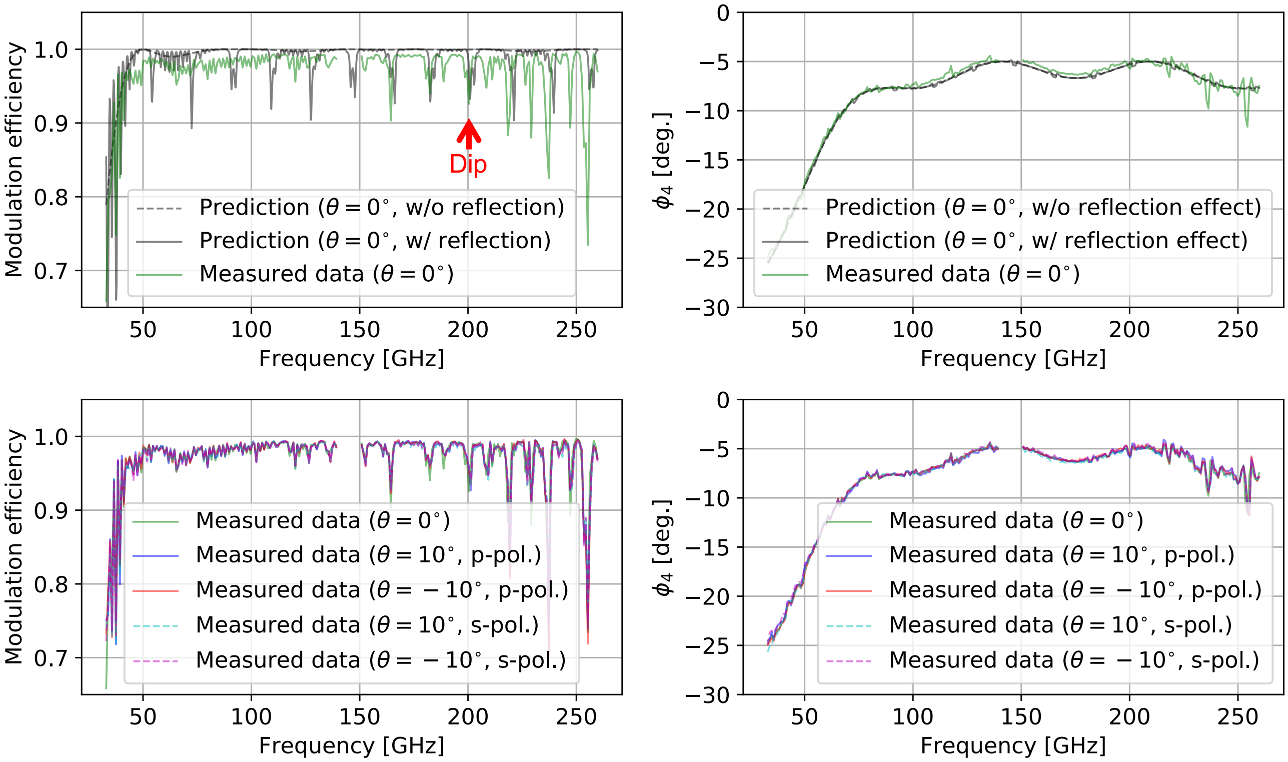

Figure 45: The modulation efficiency and the phase from 33 to 260 GHz are plotted in ~ 1 GHz interval, where θ is the incident angle of the millimeter waves for the AHWP. The predictions are plotted in in 0.2 GHz interval. The top side panels show the comparison of the measured data and the prediction for normal incidence. The bottom side panels show the comparison of normal and oblique incidence. Image from [42].

Table 19: The measured band-averaged modulation efficiency within the bandwidth for the nine-layer AHWP at each incident angle. Table from [42].

		band-averaged modulation efficiency				
		$\theta = 0^\circ$	$\theta = 10^\circ$	$\theta = 10^\circ$	$\theta = -10^\circ$	$\theta = -10^\circ$
band [GHz]	bandwidth [%]		(p-pol.)	(s-pol.)	(p-pol.)	(s-pol.)
40	30	0.902	0.895	0.892	0.897	0.900
50	30	0.961	0.960	0.959	0.961	0.960
60	23	0.971	0.970	0.970	0.970	0.971
68	23	0.969	0.969	0.969	0.969	0.970
78	23	0.976	0.975	0.976	0.976	0.977
89	23	0.981	0.981	0.981	0.982	0.982
100	23	0.985	0.985	0.986	0.985	0.986
119	30	0.984	0.983	0.983	0.983	0.984
140	30	0.984	0.984	0.984	0.984	0.984
166	30	0.983	0.984	0.983	0.984	0.983
195	30	0.979	0.979	0.978	0.979	0.979
235	30	0.959	0.955	0.955	0.954	0.954

Table 20: The maximum difference of the phase variation within the bandwidth for the nine-layer AHWP at each incident angle. Table from [42].

		$\Delta\phi_4$				
		$\theta = 0^\circ$	$\theta = 10^\circ$	$\theta = 10^\circ$	$\theta = -10^\circ$	$\theta = -10^\circ$
band [GHz]	bandwidth [%]		(p-pol.)	(s-pol.)	(p-pol.)	(s-pol.)
40	30	4.86°	5.11°	5.34°	5.05°	4.77°
50	30	6.86°	7.25°	6.78°	7.10°	6.64°
60	23	5.20°	5.41°	5.08°	5.56°	5.01°
68	23	3.90°	4.17°	3.82°	3.97°	3.86°
78	23	2.52°	2.86°	2.74°	2.65°	2.47°
89	23	0.82°	0.79°	0.68°	0.69°	0.74°
100	23	0.95°	0.94°	0.83°	0.89°	1.05°
119	30	3.15°	3.05°	3.25°	3.13°	3.22°
140	30	1.83°	1.83°	1.97°	1.86°	1.82°
166	30	1.49°	1.51°	1.41°	1.51°	1.74°
195	30	2.08°	2.31°	1.74°	1.98°	2.00°
235	30	7.12°	7.65°	6.63°	7.37°	6.84°

4.2.5 Discussion

Sources of measurement error Overall, Fig. 45 shows that the prediction and the measurement data are in good agreement for both modulation efficiency and phase. However, when we look detailed features, we identify some discrepancies between the measurement results and the predictions. In this section, we discuss possible sources of the the discrepancies between the measurement results and the predictions.

Relative angular uncertainties In our nine-layer AHWP fabrication using the UMM, the relative angle error of OF of each sapphire plate is less than 10 arcmin. The OF is used for the reference of the optic axis with an accuracy of 3 degrees (180 arcmin). Therefore the angular position uncertainty of the optic axis of the i^{th} plate is less than $(i-1) \times 190$ arcmin. To see the effect of this angular position uncertainty to the AHWP performances, we consider a conservative case; all the plates have angular position shifts of 190 arcmin relative to the former plate in the same direction. Fig. 46 shows the comparison of the predictions of the modulation efficiency and phase with and without this angular position shifts. The bottom plot shows the difference between them. In this prediction calculation, we ignore the air gaps and fix all the other parameters to their designed values in Tab. 17. From the comparison result, the differences between teo predictions are found to be less than 0.33 (0.06 in RMS) for the modulation efficiency and less than 17 degrees (14 degrees in RMS) for the phase. These large differences are obtained in a very conservative way. To avoid them, in the fabrication of the AHWP used for the LiteBIRD observation, we expect to use the sapphire plates produced from the same ingot and define each optic axis in higher accuracy without referring OF using optical measurement for mm-wave or X-ray. In this case, the position determination precision in stacking the plates is expected to be order of 10 arcmin with random variation. In addition to this, we can measure the modulation efficiency and phase as shown in this section and they can be used for calibrations.

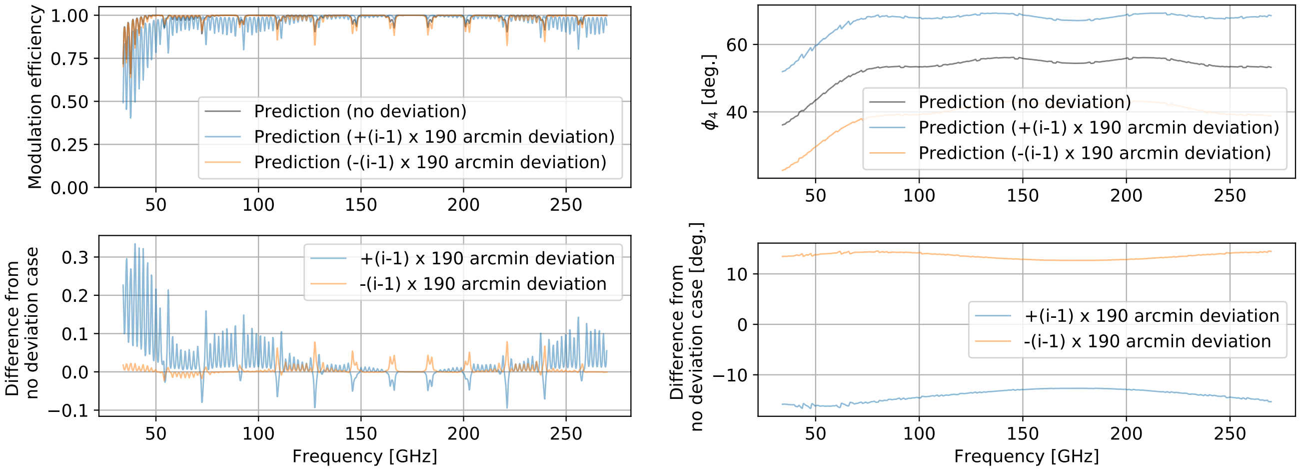

Figure 46: Calculated results of the modulation efficiency and the phase for the nine-layer AHWP with and without the angular position shifts. The bottom plots show the differences from the case with no uncertainty. Image from [42].

Thickness uncertainty of sapphire plates We estimate the uncertainty of the thickness of individual sapphire plates to be ±4 μm from measurements of thickness variation along the circumference of a sapphire plate from the same ingot. We calculate the modulation efficiency and phase with a plate thickness of 2.534 mm and 2.526 mm and compare them with the calculated result of the plate thickness of 2.530 mm as shown in Fig. 47. From the comparison, the uncertainties of the modulation efficiency and phase are estimated to be less than 0.05 (0.007 in RMS) and 0.4 degrees (0.06 degrees in RMS), respectively. To calculate these values, we again ignore the air gaps and set all the other parameters to designed values.

Note that the finite thickness of the AHWP can becomes a potential systematic effect source. For example, the total thickness of the assembled AHWP is ≈23 mm. It can be affected the focus position by refraction when such a thick AHWP is employed with a converging or a diverging optical system. In case of LiteBIRD, the AHWP is placed as a first optical element and its incident radiation is parallel wave. But the AHWP tilts 5 degrees and that causes the parallel displacement of ≈0.7 mm for the LFT optical axis when we assume the AHWP is a parallel plate has a refractive index of 3 and thickness of 23 mm. We also need to discuss about the effect for the focus position from the in-parallel plate in future work. Since the importance of the size of this effect depends on what optical system to use with the AHWP, we do not address further in this thesis.

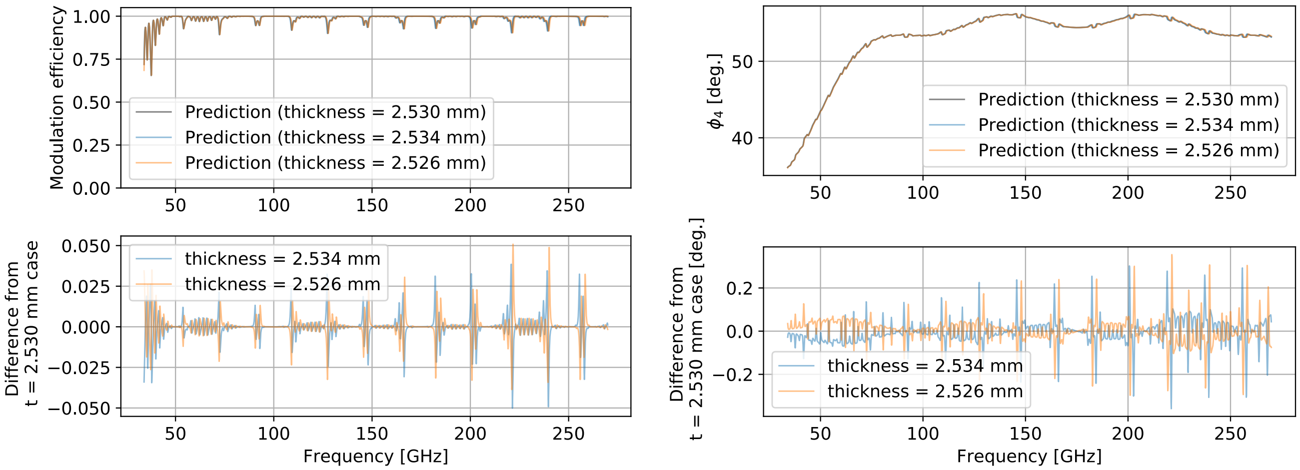

Figure 47: Calculated results of the modulation efficiency and the phase of the nine-layer AHWP for the plate thicknesses of 2.530 mm, 2.534 mm and 2.526 mm. The bottom plot shows the differences of those values from the ones with 2.530 mm. Image from [42].

Uncertainty of the refractive indices From Tab. 18, we estimate the difference between the two refractive indices for ordinary and extraordinary ray of the A-cut sapphire to be $\Delta n = 0.338 \pm 0.005$. We compare the prediction calculated with Δn set to 0.343, 0.333 and 0.338 as Fig. 48. We ignore the air gaps and set all the other parameters to the designed values. With the comparison, we find the uncertainties in the modulation efficiency and phase to be 0.03 (0.003 in RMS) and 0.4 degrees (0.2 degrees in RMS), respectively.

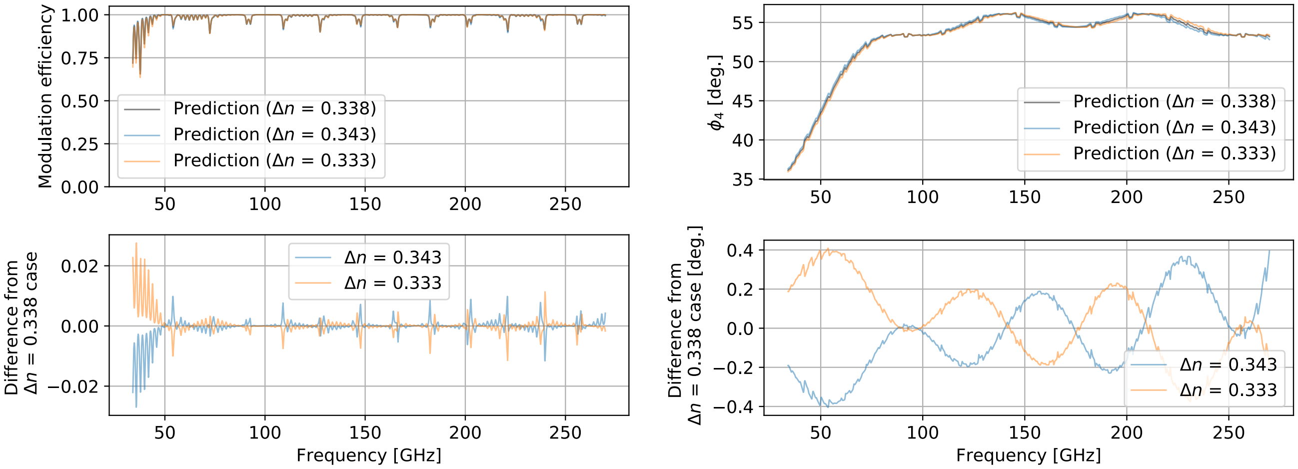

Figure 48: Calculated results of the modulation efficiency and the phase of the nine-layer AHWP for the refractive index differences of 0.338, 0.343 and 0.333. The bottom plot shows the difference of them from the ones with 0.338. Image from [42].

The effect of air gaps After the AHWP assembling, we identify the air gaps between the first and second layer to be around 50 μm and between other plates are found to be less than 50 μm. We compare the modulation efficiency and the phase of the nine-layer AHWP calculated with and without the 10 μm and 50 μm air gaps between all plates as Fig. 49. We find that there is no difference in the modulation efficiency and phase around 175.3 GHz. This is because the transmittance of all the sapphire plates is close to 1 at this frequency and the air gaps do not affect to the reflections at the boundaries of the plates. On the other hand, the dips and oscillatory features seem to depend on the magnitude of the air gap. The reason is that these two features originated from the reflections at the AHWP inside and the air gaps increase those reflections. For example, on the high frequency side, the depth of the dips and oscillatory features monotonically increases according to the thickness of the air gap. On the low frequency side, where the thickness of the air gap is small, the dip depth is decreased, and where the thickness becomes large, it starts to increase. This trend is consistent with the difference between the prediction and the measured data in Fig. 45. The reason of why the impact is prominent at the higher frequency is simply because the higher frequency is more susceptible to small changes of the thickness due to the small wavelength. The air gaps cause the changes in the modulation efficiency and phase to be 0.9 in maximum (0.1 in RMS) and 14 degrees at maximum (2 degrees in RMS), respectively.

From the comparison, we find that the air gaps affect the modulation efficiency and phase around the dips significantly.

Summary of error sources From the consideration in this section, we find that the air gaps dominate the change in the AHWP performance around the dips. Fig. 50 shows a comparison of the measured data and the prediction of the modulation efficiency and phase, that calculated with taking into account the measured air gaps thickness. The prediction with the air gaps reproduces the tendency of the depth of the dip and oscillatory feature better than Fig. 45. But the residuals between the prediction and the measured data is not reduced because of the frequency shift of the dips caused by the uncertainties of thickness and refractive indices.

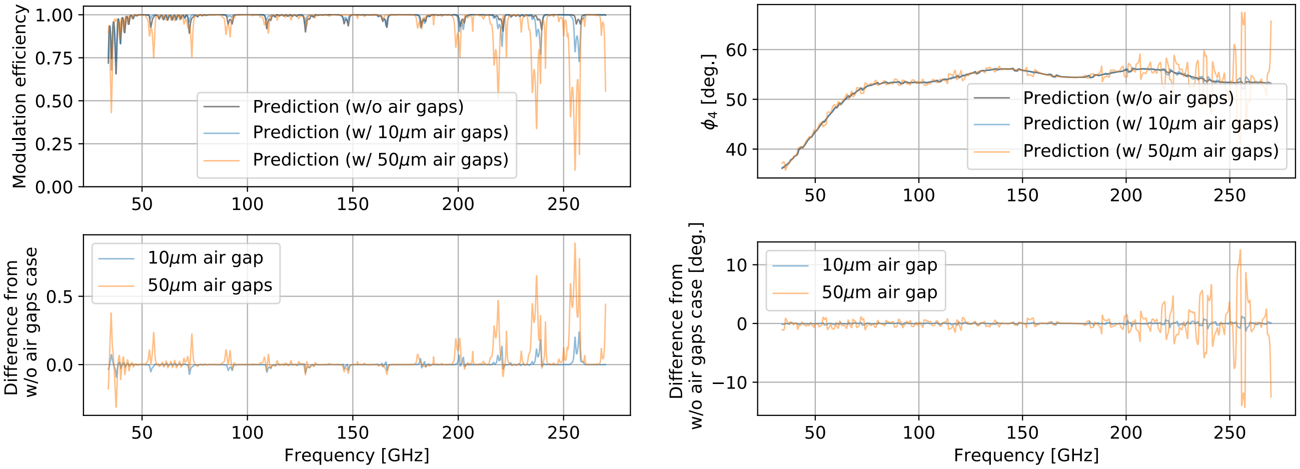

Figure 49: Dependence of the modulation efficiency and the phase on the air gaps. The bottom plot shows the difference of them from the ones without the air gap. Image from [42].

To calculate the prediction, the air gaps are inserted between each plate as a parallel flat plate which have a refractive index of 1. The thickness of the air gap between the first and the second plate is set to 50 μm and other gaps are set to 8 μm. Since the thickness of the air gaps except for that of between the first and second plates could not be measured directly, it is estimated from the thickness variation along the circumference of a sapphire plates.

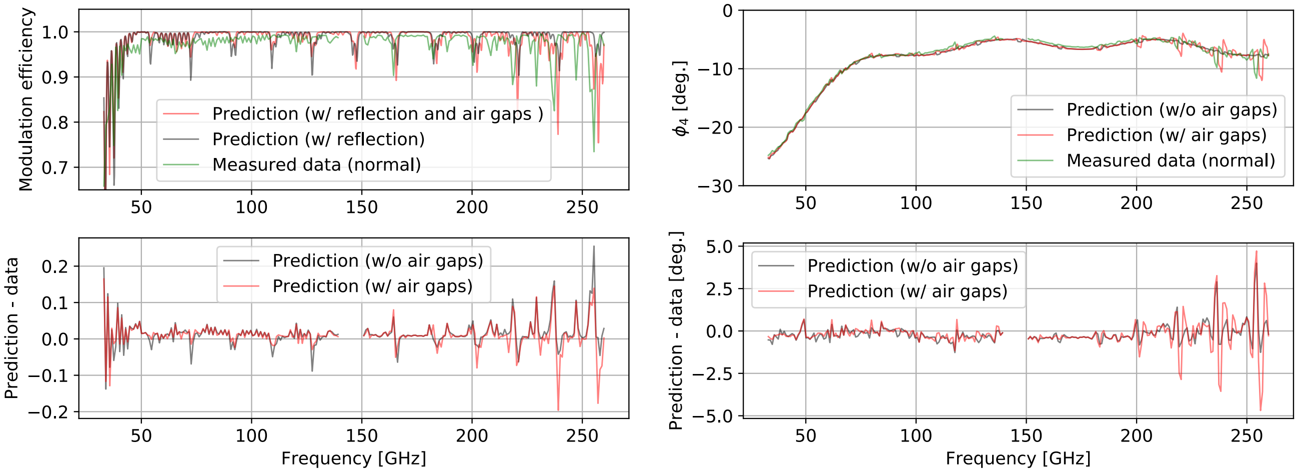

Figure 50: The modulation efficiency (left panels) and the phase (right panels) from 33 to 260 GHz are plotted in $\sim$ 1 GHz interval. The predictions take into account the air gaps based on the measurements and are plotted in 0.2 GHz interval. Image from [42].

Amplitude of modulated signal for each mode We use the nine amplitude and eight phases for the fitting of the modulated signal to obtain the modulation efficiency and phase. Here, we discuss the modes other than $m = 4$ in Eq. 107. The $m = 2$ mode appears due to the difference of the transmittance between the two refractive indices for ordinary and extraordinary rays, and this mode becomes larger by the absence of the anti-reflection coating. Fig. 51 shows a comparison of the measured data and the prediction for the $m = 2$ mode. We take into account the air gap effects to compute the prediction. Whilst the model of the air gap may not be complete, we qualitatively recover the consistency between the prediction and the measured data. The origin of other modes, $m = 1, 3, 5, 6, 7, 8$, is not physically motivated within the formalism described in Eq. 35. The potential contributors to the peaks at $m \neq 2, 4$ are from the imperfection of the assembly and measurement setup (e.g. in the case of there is a rotational asymmetry in the sapphires or sample holder), or simply electric noise. Hownever, the peak amplitudes of $m = 1, 3, 5, 6, 8$ modes are generally signal-to-noise above 100 in the range of above 40 GHz. This means that the identified peaks are not due to the noise. Fig. 52 shows the measured amplitude of the $m = 1, 3, 5, 6, 7, 8$ modes. The $m = 1, 3, 5$ modes have the general trend of its amplitude s as that the amplitude becomes large on the higher frequency. This is generally consistent with the effect of the air gap. On the other hand, the $m = 6, 7, 8$ modes have the different tendency. The $m = 6, 8$ modes originate from the incident angle dependency of the refractive index for extraordinary ray. When an incident wave enters with an incident angle θ and an azimuthal angle of ϕ with respect to the optic axis, the refractive index for extraordinary ray $n'_{\mathrm{e}}(\theta, \phi)$ is given by [49]

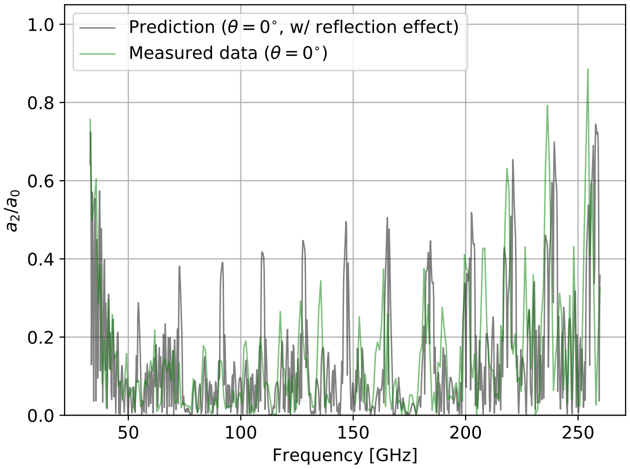

Figure 51: The amplitude of $m = 2$ mode from 33 to 260 GHz are plotted in ~ 1 GHz interval. The predictions takes into account the air gaps and are plotted in 0.2 GHz interval. Image from [42].

$$n'_{\mathrm{e}}(\theta, \phi) = n_{\mathrm{e}} \sqrt{1 - \left(\frac{1}{n_{\mathrm{o}}^2} - \frac{1}{n_{\mathrm{e}}^2} \right) n_1^2 \sin^2 \theta \cos^2 \phi}, \tag{109}$$

where n_1 is an index of the ambient space. The refractive index $n'_{\mathrm{e}}(\theta, \phi)$ includes higher order cosines of ϕ and cannot account for the odd order cosines of ϕ. This is the reason the $m = 6, 8$ modes have the different tendency. However, the origin of the $m = 7$ mode tendency is still unclear. As shown in Fig. 53, we also look at the correlation between $m = 1$ and $m = 3, 5$. From Fig. 53, we can see the positive correlation between the $m = 1$ mode and the $m = 3, 5$ If the majority of the source of the $m = 1$ mode is due to the air gap which has a wedge-like shape, we expect the rotational synchronous $m = 1$ mode and potentially higher harmonics. Fig. 53 supports the idea of the effect of the wedge shape air gap and its harmonics. Candidates for other sources of $m = 1, 3, 5$ modes are the rotational speed instability, the vibration and wobble in the rotation. Especially, the effect from the vibration and wobble are expected to be more pronounced at higher frequencies.

At the demodulation step, the $m \neq 4$ modes can be filtered out. There is a potential leakage from $m = 2$ to higher harmonics and this leakage is one of sources of the conversion from unpolarized light to polarized light. When the incident angle is not normal incident to the HWP, such a possibility can be addressed particularly. The result is highly dependent on the performance of the AR coating, which is not accounted for in this subsection. The study related on this topic can be found in T. Essinger–Hileman et al. [20] and H. Imada et al. [33] Therefore, we do not to explore beyond the identification of the existence of $m \neq 4$ mode.

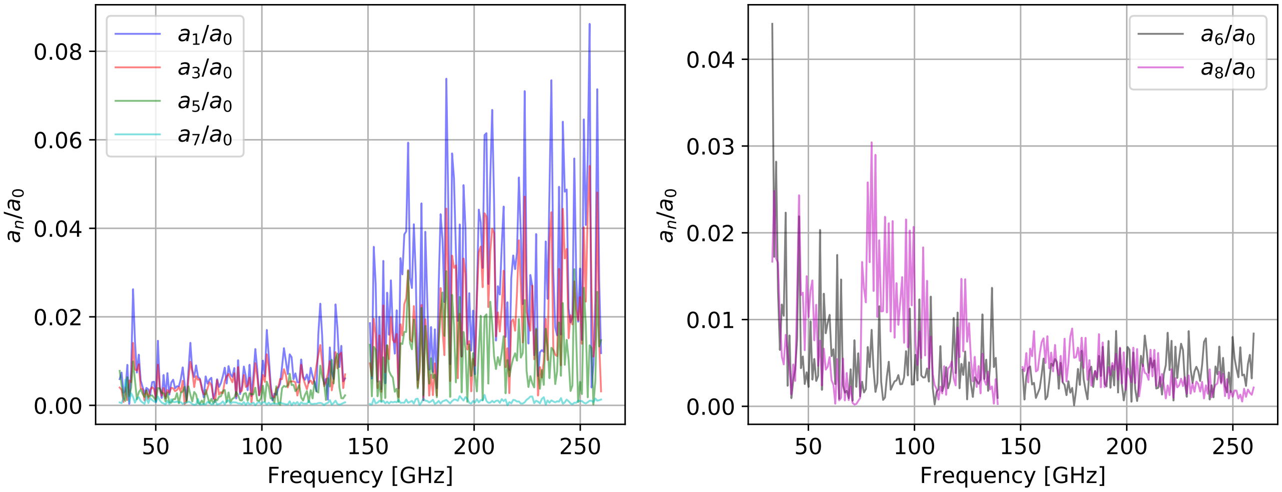

Figure 52: The $m = 1, 3, 5, 6, 7, 8$ modes from 33 to 260 GHz are plotted in every 0.9 GHz. Image from [42].

Dependency for incident angle Tab. 19 shows the band-averaged modulation efficiencies with the incident angle of 10 degrees. The differences of the efficiencies between normal and the 10 degree oblique incidence are less than 0.005 (0.01) for the highest (lowest) bands. The differences of the other bands are less than 0.001. The bottom panels of Fig. 45 show the modulation efficiency and phase for the two incident angles and suggest there is no significant difference between them.

We repeat the measurement with a finer frequency step of 0.15 GHz between 230 and 240 GHz with incident angle of ±5 degrees to understand the incident angle dependence more precisely. From Fig. 54, we find that there is a frequency shift of the dip. When the incident angle is 5 degrees (10 degrees), the refraction angle at the first plate of the AHWP is calculated to be about 1.5 degrees (3 degrees) for both of ordinary and extraordinary ray. Since the difference in the refractive indices is small at the boundary between each sapphire plate of the AHWP, the refraction angles within each plate are similar to the first plate. When the incident angle $\theta \neq 0$, frequencies of Fabry-Pérot interference spectrum scaled by $(\cos\theta)^{-1}$ compared with the normal incidence ($\theta = 0$). This means the frequency shift to the higher side. For the refraction angle of 1.5 degrees (3 degrees), the frequency shift is calculated to be about 0.08 (0.33) GHz. The

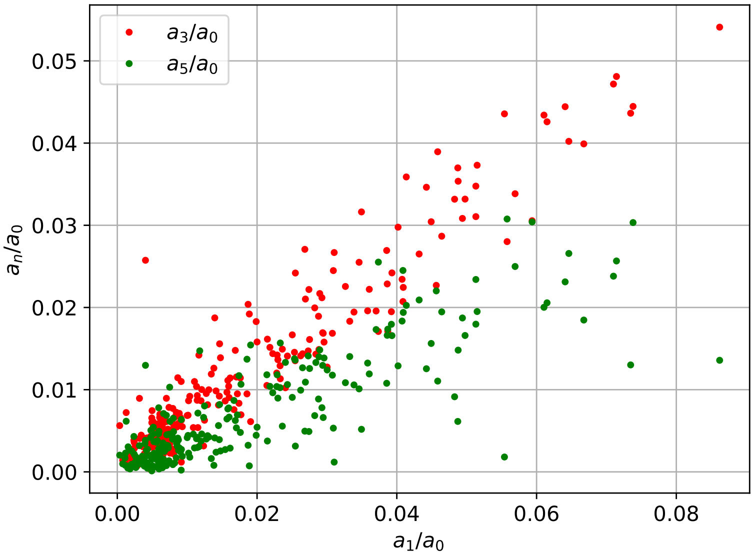

Figure 53: The correlation of a_1/a_0 and a_3/a_0, a_5/a_0 from 33 to 260 GHz. The data is every 0.9 GHz. Image from [42].

estimation of the frequency shift is in good agreement to the frequency shift shown in Fig. 54. It suggest that the observed frequency shift can be explained by the incident angle dependence.

The incident angle dependency of AHWP performances is also related to the potential leakage from the incident unpolarized light to the polarized light. This is one of the important effects which needs to be addressed in CMB experiments. H. Imada et al. [33] addressed this effect, and the further study to propagate this effect to quantify the impact to the cosmology is in progress.

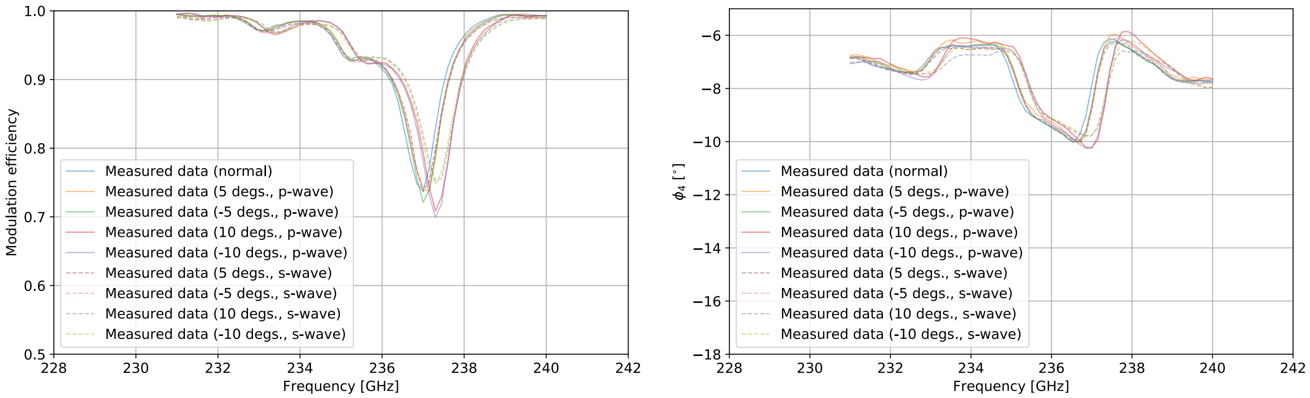

Figure 54: Frequency dependence of the modulation efficiency and the phase for 230 to 240 GHz. The data points of the measurement result are plotted for every 0.15 GHz. Image from [42].

Comparison with target value In spite of the fact that the assembled nine layer AHWP becomes broadband as expected, the band averaged modulation efficiency is not reach 0.98 in some bands. There are three reasons why the band averaged modulation efficiency is lower than

0.98. The first and second reasons are due to the hardware preparation, and the third one arises from the AHWP design. The first reason is the fact that the thickness of the sapphire plates used for the assembled AHWP is slightly thinner than the optimized thickness. This causes an overall frequency shift to higher frequency of the modulation efficiency and phase. The second reason is the large dips and oscillatory features in the modulation efficiency and phase caused by the air gaps, which also decreases the band averaged modulation efficiency. Particularly, this influence is large on the higher frequency bands where the effects of the air gaps become large. The third reason is the large phase variation on the higher and lower frequency bands (Tab. 20). The prediction of the averaged modulation efficiencies and the maximum phase variation with reflection effects, no air gaps and the optimized thickness are shown in Tab. 21. The band averaged modulation efficiencies at the highest and lower frequency band are less than 0.98 even though we use a correct thickness. This exception is due to the large phase variation in the frequency band. Currently, we set a same target value of 0.98 for the band averaged modulation efficiency for all bands. To achieve this target from the hardware side, we need to add the extra layers to the AHWP but it causes the mass increasing. From the analysis side, for example, we need to confirm whether the requirements of the two bands can be relaxed by considering the modulation efficiency requirement per band from the simulation.

Table 21: The prediction of the averaged modulation efficiency and the maximum phase variation of the nine-layer AHWP with reflection effects, no air gaps, and optimized thickness. Table from [42].

band [GHz]	bandwidth [%]	band averaged modulation efficiency	$\Delta\phi_4$
40	30	0.969	6.26°
50	30	0.977	7.49°
60	23	0.982	3.87°
68	23	0.991	2.07°
78	23	0.995	0.55°
89	23	0.995	0.85°
100	23	0.989	2.41°
119	30	0.990	1.87°
140	30	0.993	1.98°
166	30	0.993	2.01°
195	30	0.990	3.08°
235	30	0.938	16.46°

4.2.6 Conclusions

For CMB polarization experiments, we design and evaluate the prototype of the nine-layer AHWP. The measured modulation efficiency and phase at room temperature are in good agreement with their predictions. That means we demonstrate our nine-layer AHWP to be broadband. On the other hand, we find small discrepancies between the measurements and the predictions. The primary contribution around the dips is due to the existence of air gaps between each layer of the AHWP. The agreement between the measurements and the predictions is improved when this effect is considered. We also measure the incident angle dependency of the modulation efficiency and phase in a range of about 10 degrees comparable to the field of view of LiteBIRD and the

CMB telescope that observes small angle scales. We find that this incident angle dependence can be explained by the internal refraction and reflections in individual plates.

The intensity of the observation signal is integrated by the detector in a specific bandwidth in many CMB experiments. Therefore, we calculate the band averaged modulation efficiency over the bandwidth to obtain the value usable for the experiments. From the evaluation in the band averaged modulation efficiency, we find that the smaller the phase variation improves the averaged modulation efficiency. Therefore, the optimization to obtain higher modulation efficiency requires us to have uniform phase values in the bandwidth, the solution of which is presented in Sec. 2.

In our development, we set a same target value of 0.98 for the band averaged modulation efficiency for all bands. From comparison between the prediction calculated with designed values and the target value, the band averaged modulation efficiencies at the highest and lower frequency band are less than 0.98. To achieve this target value from the hardware side, for example, we need to add the extra layers to the AHWP but it increases the HWP weight. From the analysis side, for example, we need to confirm whether the requirements of the two bands can be relaxed by considering the modulation efficiency requirement per band from the simulation. Either way, we need to continue the efforts to improve the modulation efficiency on the highest and lowest bands.

4.3 Demonstration at cryogenic temperatures

4.3.1 Introduction

This subsection is based on K. Komatsu et al. [41]. Images are taken from [41]. In this subsection, we go into further detail and report the demonstration result of the small prototype PMU at cryogenic temperature. We have constructed a 1/10 scaled prototype PMU for LiteBIRD LFT. This prototype consists of an achromatic HWP (AHWP) and the cryogenic rotation mechanism using a superconducting magnetic bearing. We employ five layers Pancharatnam-based AHWP with a moth-eye anti-reflective (AR) sub-wavelength structure (SWS) to achieve broadband transmittance and modulation efficiency [50, 51, 42]. The AHWP has a diameter of 50 mm, which corresponds 1/10 scale of the flight size PMU. The SWS is a robust solution for achieving broadband transmittance at cryogenic temperatures [71]. The AHWP is mounted on a rotor levitated by a ring magnet, placed above the an array of high temperature superconductor, YBCO tiles. The rotor is driven by the AC drive system with contact-free from the stator to minimize the heat dissipation from the physical contact. The rotation angle of the AHWP is monitored by an optical encoder, i.e. LED/photodiode and optical chopper [70]. The combination of the AHWP with the broadband AR using SWS mounted on the SMB that operates below 20 K is unique set. The entire system is placed in a cryostat which is cooled to ≈20 K by a 4 K Gifford-McMahon (GM) cooler. In order to implement such a newer system for a space mission, it is necessary to test key functionalities during the early stages of the mission preparation and identify possible problems that may appear in the entire system is assembly and testing. In this subsection, we focus on the optical characterization of the PMU at millimeter wave (mm-wave) range. We also construct a low temperature optical measurement setup for this purpose. In this subsection, we address the following features by using the prototype scaled PMU and the constructed measurement setup:

- Frequency components included in a modulated signal
- Performance of the AHWP at low temperatures
- Cooling tolerance of the AHWP and the SWS

4.3.2 Formalism

The formalism of the HWP Polarimetry is already shown in Sec. 2.2. In this subsection, as in the previous subsection, we continue to use the modulation efficiency defined in Eq. 104 instead of the polarization efficiency to compare the measurement results with the model. Same as previous section, we set a target value of 0.98 for the band averaged modulation efficiency.

4.3.3 Sample preparation

Design of AHWP The AHWP used in this subsection is based on the five layers anti-symmetric design in Sec. 2. We assemble a five sapphire plates with the design parameters shown in Tab. 22. The thickness is chosen in order to set the central frequency of the broadband coverage to be at 97.5 GHz. To obtain thickness, we used the refractive indices of the A-cut sapphire as $n_o = 3.047$ and $n_e = 3.361$, where n_o and n_e for the ordinary and extraordinary rays [34]. We used these indices only for design purposes. On the other parts of this subsection, we use the refractive indices as $n_o = 3.035 \pm 0.003$ and $n_e = 3.359 \pm 0.003$ that are measured from the transmittance between 150 and 220 GHz at $\sim$ 25 K using the setup shown in Sec. 4.3.4. The detail of this refractive indices measurement is shown in Appendix B.

Table 22: The AHWP design parameters and measured parameters. The thickness of the first and the fifth plates does not include the thickness of the SWS AR. Table from [41].

Plate number	1	2	3	4	5
Designed thickness [mm]	4.9	4.9	4.9	4.9	4.9
Optic axis angle [deg.]	157.31	47.66	0.00	-47.66	-157.31
Measured thickness [mm]	4.929 ± 0.003	4.929 ± 0.002	4.920 ± 0.002	4.926 ± 0.001	4.931 ± 0.002
Assembled angle [deg.]	157 ± 1	47 ± 1	0 ± 1	-47 ± 1	-157 ± 1

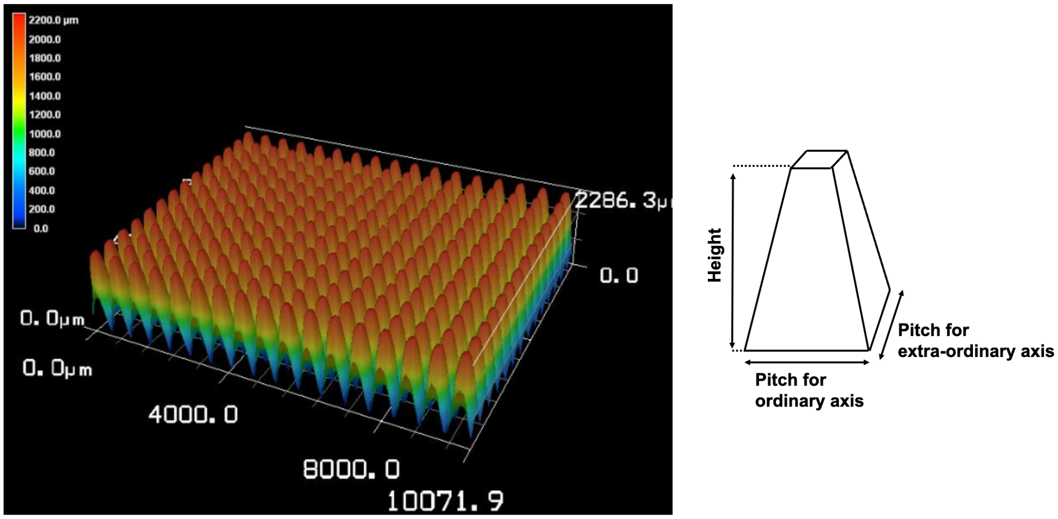

Figure 55: The fabricated AR structure and the sketch of a structure. Left panel shows the image of fabricated SWS at the center of the sample taken by the laser con-focal microscopy. Right sketch shows the definition of the fabricated shape. Image from [41].

Anti-reflective structures We fabricate the SWS on one side of the first and fifth sapphire plate surfaces of the AHWP as a broadband AR. We use ultra short pulse laser machining to fabricate the SWS to the sapphire plates. The detail of the fabrication can be found in [71]. We measured 230 structures using a confocal microscope at the center of fabricated area as shown in Fig.55. The relevant geometrical parameter of the fabricated SWS, i.e. the height, pitch for ordinary axis, and pitch for extraordinary axis as defined on the right side of Fig.55, are summarized in Tab. 23.

Effective thickness of the anti-reflective structure As mentioned in the previous subsection, we directly dabricate the SWS on an A-cut sapphire as the AR. In order to obtain a prediction of the assembled AHWP performances with the SWS, we need to take into account the retardance of the electromagnetic wave at the SWS. The resultant AR part of the A-cut sapphire has a retardance partly because of the birefringence of the material itself and the asymmetry of the SWS shape. Here, we conceptually split the single HWP with the SWS on both sides into two parts as the left side of Fig. 56: the SWS part on both ends and the a sapphire wave plate (plate part) in the

Table 23: The geometrical parameters of the fabricated SWS. Table from [41].

Plate number	1	5
Height [mm]	2.187 ± 0.002	2.178 ± 0.002
Pitch for ordinary axis [mm]	0.598 ± 0.011	0.598 ± 0.008
Pitch for extraordinary axis [mm]	0.537 ± 0.010	0.537 ± 0.009

middle without the SWS. We define the retardances created from each part, $2\delta_{\mathrm{sws}}(\nu)$ and $\delta_{\mathrm{wp}}(\nu)$. Using rigorous coupled-wave analysis (RCWA), we calculate the total retardance, $\delta_{\mathrm{sws-wp}}(\nu)$, from a single HWP with the SWS on both sides. From this we can compute the retardence from the SWS part as $\delta_{\mathrm{sws}}(\nu) = (\delta_{\mathrm{sws-wp}}(\nu) - \delta_{\mathrm{wp}}(\nu))/2$. When we assume the refractive indices of the SWS part are the same of sapphire and the wavelength are known, then we can compute the effective thickness of the SWS, t_{AR}, as a parallel plate thickness as shown in Fig. 56. The calculated effective thickness is not constant is because the phase difference from the SWS depends on the incident wavelength. The height of the SWS is about 2.2 mm as Tab. 23 to achieve the frequency coverage of 34 to 161 GHz. When we fabricate the SWS on a sapphire plate, we need to adjust the total of an effective thickness of the SWS and a sapphire plate to be 4.9 mm. Therefore, we need to subtract the difference between t_{AR} and the height of the SWS from 4.9 mm and fabricate the SWS AR to a sapphire has this thickness. In this time, due to the proximity of the height of the SWS and its effective thickness, we fabricate a 2.2 mm thick SWS to a 4.9 mm sapphire plate.

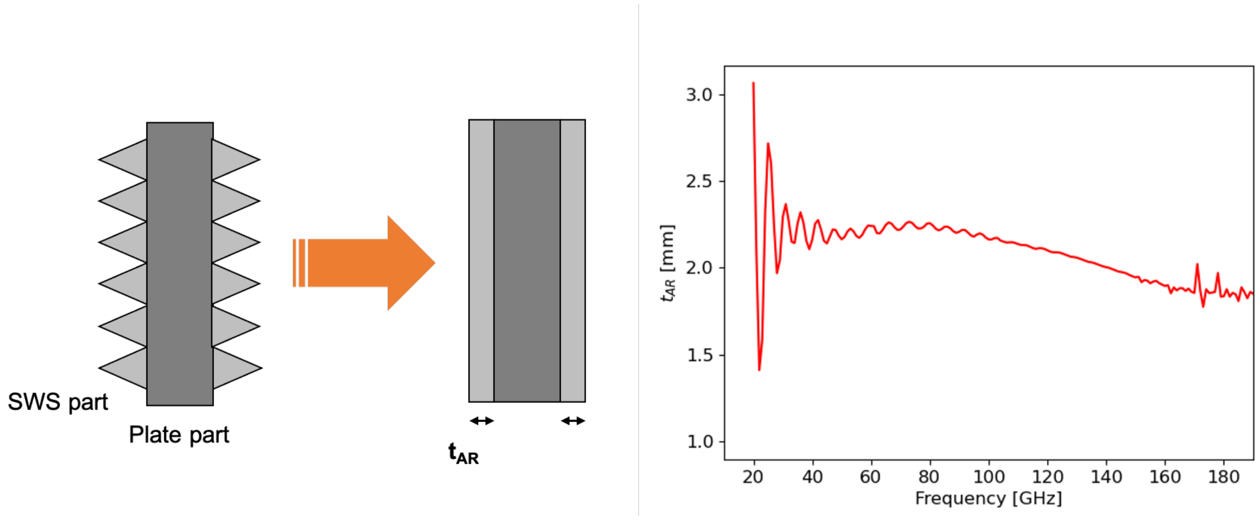

Figure 56: Left: A conceptual sketch of the correspondence between the SWS AR and the equivalent single layer AR. Right: The effective thickness as a function of the electromagnetic frequency. Image from [41].

Assembly We prepare five A-cut sapphire plates with a thickness of 4.9 mm and diameter of 50 mm. The surfaces of all plates are polished. Tab 22 summarize the measured thickness for each plate. The thickness and its error are obtained as the average and the standard deviation of the 20 times measurement around the plate center. We measure the modulated signal for each plate using the setup shown in Sec. 4.2. Before fabricating the SWS, we define the plate optic axis by finding the rotation angle that take a local maximum of the modulated signal at room temperature. We mark the angle with a line at the side of the sapphire plate in such that the five plates line up at the desired angles as Fig. 57. The width of the alignment line is 1 mm, which corresponds to about 2 degrees at the circumference of the wave plate with a diameter of 50 mm. Therefore, we obtain the alignment accuracy of the optic axis angle assembly within 1 degree. Fig 57 shows the assembled five layer AHWP and it is not glued between the plates.

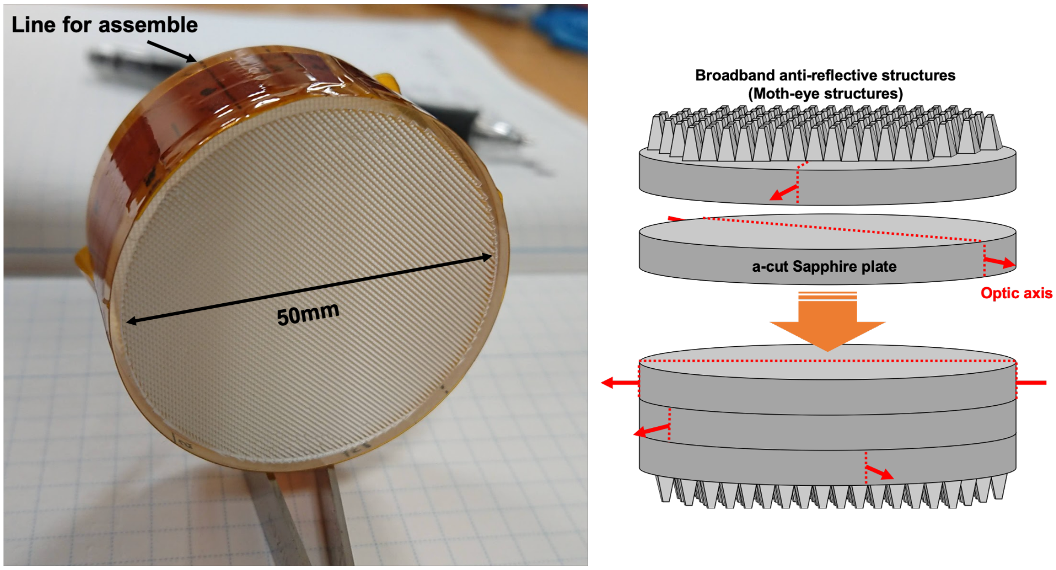

Figure 57: The assembled five-layer AHWP and the conceptual sketch of the AHWP. The white area is AR structure. Image from [41].

4.3.4 Experiment

Experimental setup Figure 58 shows a 3D CAD model of the experimental setup. We measure the power transmitted through the small PMU prototype at around 20 K using this setup. Both the mm-wave source and the diode detector are placed outside of the 4 K GM cryostat that means their temperature is the same of room. Although the mm-wave is polarized and the detector is sensitive to a single polarization, we use two wire grids to obtain a better definition of the polarization angle. We modulate the mm-wave emitted from the source at 200 Hz with a mechanical chopper and isolate the power measured by the detector from external signals using a lock-in amplifier. We use the six pairs of the coherent source and the diode detector to cover the frequency range of our interest: V band (50-75 GHz), W band (75-110 GHz), F band (90-140 GHz), and G band (150-220 GHz). In order to carry out the optical characterization at mm-wave range with the coherent source and the diode detector that are only functional at room temperature, each cryostat shell has have a 100 mm diameter opening hole and the prototype scaled PMU is installed in a cryostat as shown in Fig. 58 and 59. Two acrylonitrile butadiene styrene (ABS) plates with a thickness of 2 mm are placed at both windows of the 3$^{\text{rd}}$ shell as IR filters. The optical windows are made of UHMWPE (Ultra High Molecular Weight Polyethylene) plates and its inside surface has thin HR-10 layer in order to control the total signal power as well as to mitigate reflections and reduce the optical loading.

Figure 59 shows the details of the innermost cryostat shell containing the small PMU. The small PMU prototype consists of the assembled five layer AHWP, the optical encoder, the drive motor, the cryogenic holder mechanism, and the SMB. The drive motor is a contact-free three-phase synchronous motor and used for rotate the rotor. The optical encoder consists of an encoder disk, a LED, and a silicon photodiode. The encoder disk has 64 slots along the edge and one reference slot on the inner side for absolute calibration of the rotation angle. Three cryogenic holders set the levitation height at 5 mm between the rotor magnet and the YBCO and keep the rotor in the position during cool-down. The mounting position of the AHWP is shown as a red rectangular area in Fig. 59. We put a thermometer and a Hall sensor with a sensitivity axis along z in order to monitor the temperature and vertical displacement (wobble) of the rotor and HWP as shown in Fig. 59. When the cryogenic holders are retracted after the cool down, the rotor levitates and can be rotate by the drive motor.

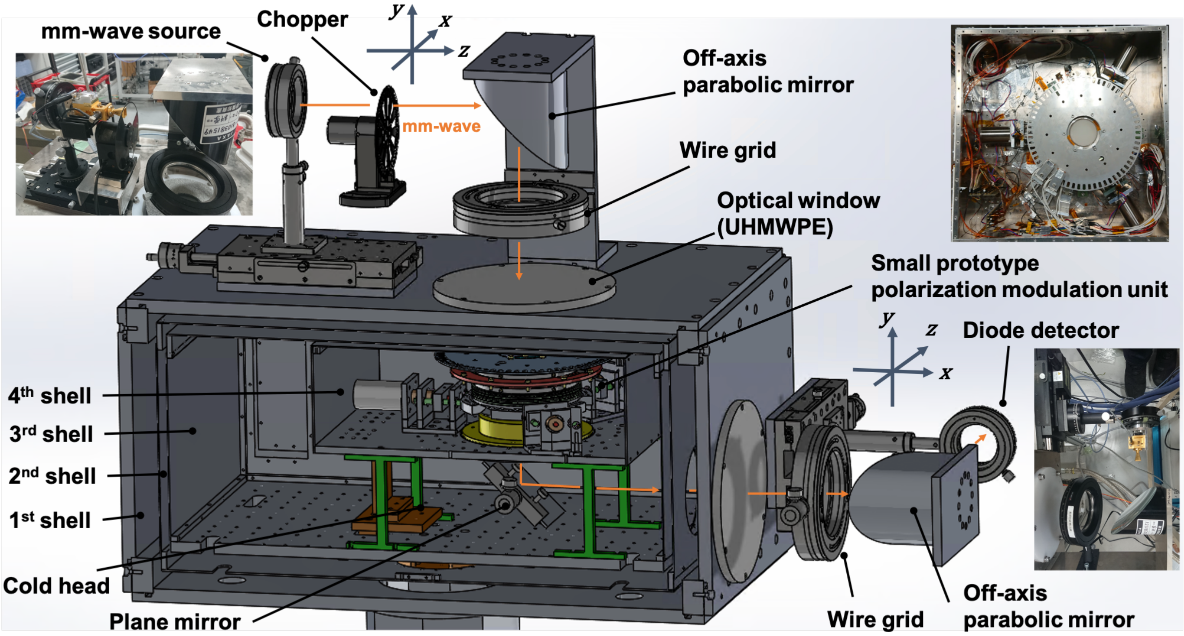

Figure 58: The sketch of measurement setup. Image from [41].

Measurement The modulated signal of the small PMU is measured in the frequency range 50 to 190 GHz at 0.6 GHz steps for $S_{in} = (1, 1, 0, 0)$. The rotor is rotated at 24 rpm (0.4 Hz). The total of the measurement time for each band is ≈one hour, during which time the rotor temperature increases from around 20 K to 33 K. The reason for this temperature increase is that there is no heat path from the rotor to the other part since it is levitated but there is heat inflow from the windows itself. In order to resolve this, we need to improve the filtering scheme near the infrared and mm-wave regime, which we will carry out in future work. For each frequency, we measure the modulated signal of 4 full rotations of the AHWP in ≈10 seconds. Theoretically, the HWP rotation should appear in the time-stream of the modulated signal in the form of second and fourth order harmonics as shown in Sec. 2.2. However, in reality, other harmonics appear due to either imperfect parallelism of the sapphire plates, misalignment between the optic axis, the wobbling (unstable rotation) of the rotation mechanism, and the plate surface, or other possible

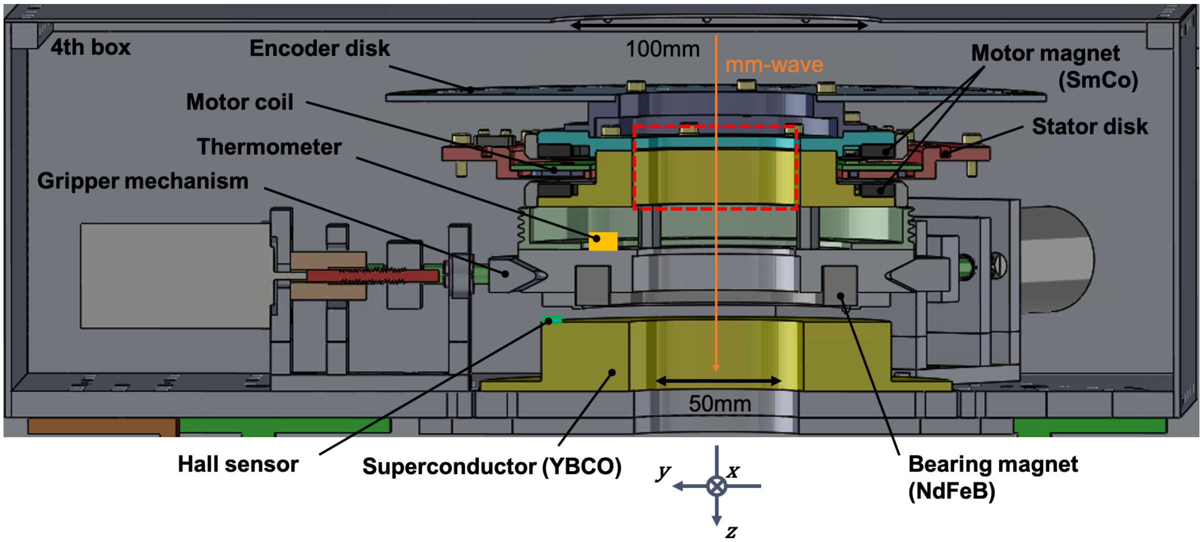

Figure 59: The sketch of 4th shell and the small prototype PMU. The HWP is placed at the red square area. Image from [41].

non-idealities. Therefore, we fit the modulated signal at each frequency with a model equation as

$$I(t,\nu) = a_0(\nu) + \sum_{m=1}^{8} a_m(\nu)\cos\left(m\omega_{\mathrm{hwp}}t + m\phi_m(\nu)\right). \tag{110}$$

In principle, there is no reason to limit the order up to 8 but the modulated signal can be fitted enough by this order. We will address the rotational synchronous peaks in the later subsection. Same as Sec. 4.2, in order to mitigate the effect of standing waves between various components in the measurement setup, we measure the modulated signal at two detector positions along the direction of the light path and take the average of a_m and ϕ_m. The distance between the two positions as 1/4 of the signal wavelength, which corresponds to the period of the standing wave.

4.3.5 Results

Figure 60 shows examples of the measured modulated signal at 90 GHz and the magnetic field variation near the SMB. The modulated signal is over-plotted with the data that correspond to four complete rotations. We subtract the offset from the modulated signal by estimating the offset using the data taken when the mm-wave source is off. We only use the blue part of the data in Fig. 60 when the modulated signal is fitted by using Eq. 110. This choice is due to the lock-in amplifier dynamic range that causes negative values to be inverted. The observed dips in the measured magnetic field appear twice during one full rotation, and are caused by the physical contact between the rotor and the gripper mechanism or the rotation wobbling. The reason of that this dips are not from the magnetic field of the bearing magnet is found in Appendix B. The points scattered in the magnetic field data are due to electrical noise.

Power spectral density The power spectral density (PSD) of the optical signal and the magnetic field variation for four cases at 90 GHz is shown in Fig. 61. As mentioned in above, we

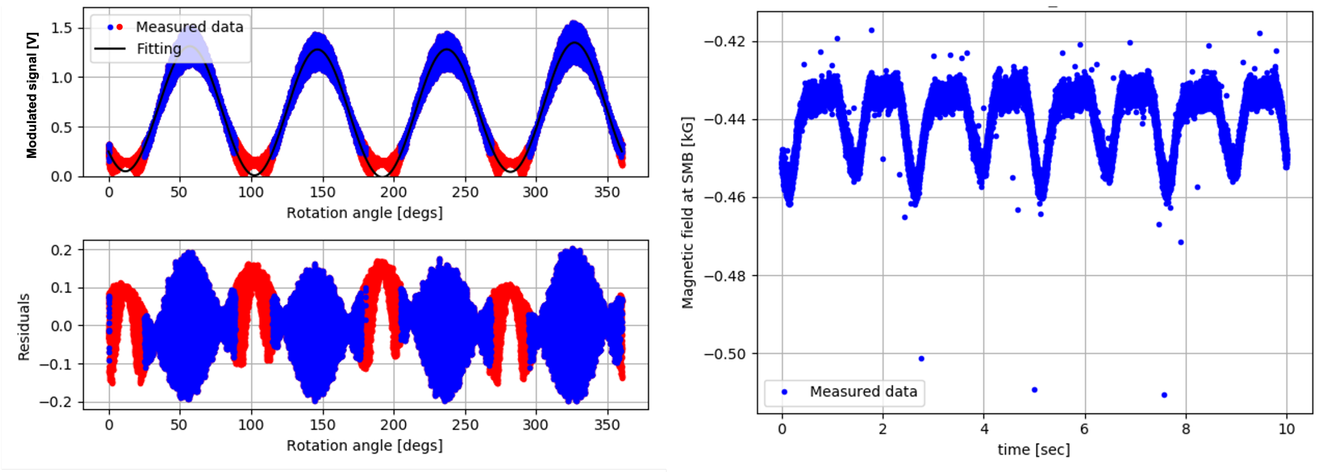

Figure 60: The modulated signal at 90 GHz and the magnetic field variation. The left panels show the modulated signal. Top panel shows the measured data and fitting. The bottom panel shows the residual between the measured data and the fitting. Since signal inversion happens because of the lock-in amplifier dynamic range, the data in red are not used for the fitting. The right panel shows the magnetic field variation during four full rotations. Since the rotation rate is 24 rpm (0.4 Hz), one rotation takes 2.5 seconds. The scattered data are due to residual electrical noise. Image from [41].

measured each data at two positions of the diode detector but we only use one of them to compute the PSDs. The top panels (case-1) show the PSD of the modulated signal acquired during the PMU rotation shown in Fig. 60. To compute the PSD, the data shown in red in Fig. 60 are included. The second row (case-2) shows the data that are taken in the same condition as the top row except that the AHWP is not mounted on the PMU that means the rotor has an empty hole. The third row (case-3) shows again the same data in the case of the levitating rotor but it is not rotated without the AHWP. Lastly, the bottom panels (case-4) show the data in the case of the rotor held by the cryogenic holder mechanism without the AHWP. The red and blue vertical lines show the position of the harmonics of the rotational frequency. The red lines show the multiples of the modulation frequency (fourth harmonic). So that there is a blue line hidden under every red line. The peaks present in the bottom panels are due to noise in the measurement setup, with the exception of the one at 200 Hz and its harmonics that are due to the optical chopper that was not completely removed by the low-pass filter (LPF) of the lock-in amplifier. The signal of 200 Hz is a main reason of why the modulated signal in Fig. 60 becomes wider than that of Fig. 44.

Rotation-synchronous optical signal Figure 62 shows the fitted amplitudes a_m, which is normalized by the DC level a_0, in the modulated signal. We also plot the data taken without the AHWP mounted on the rotor for a comparison. As written in Sec. 4.3.4, we take data during four full rotations of the PMU per the frequencies and the detector positions for each measurement set. Each point in Fig. 62 is the average over four times measurement sets and its error is half of the maximum variation. The relative amplitude of the fourth harmonic a_4/a_0 is the modulation efficiency. The relative amplitude of the second harmonic a_2/a_0 mainly originates from the transmittance difference between the ordinary and extraordinary ray.

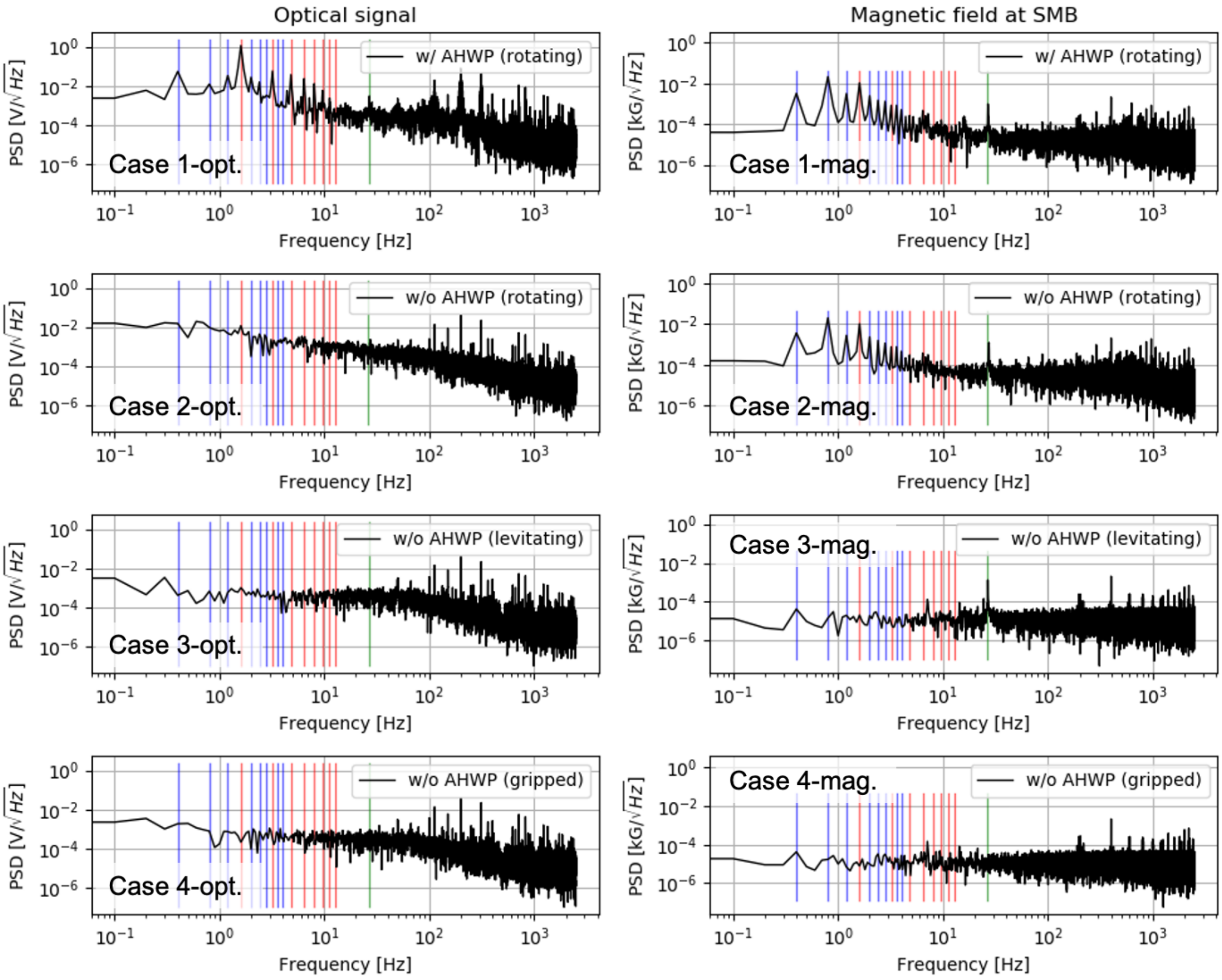

Figure 61: The power spectral density of the modulated signal and the magnetic field at SMB. The top panels show the PSD of the modulated signal acquired during HWP rotation shown in Fig. 60. The second row shows the same pair in the case of no AHWP present. The third row shows the pair in the case of levitating rotor (not rotating) without the AHWP present. The bottom row shows the pair when we hold the rotor without the AHWP present. The red and blue lines show the harmonics due to the rotation. The red lines show the multiple harmonics of the fourth harmonic. The green line show the resonance of the SMB. Image from [41].

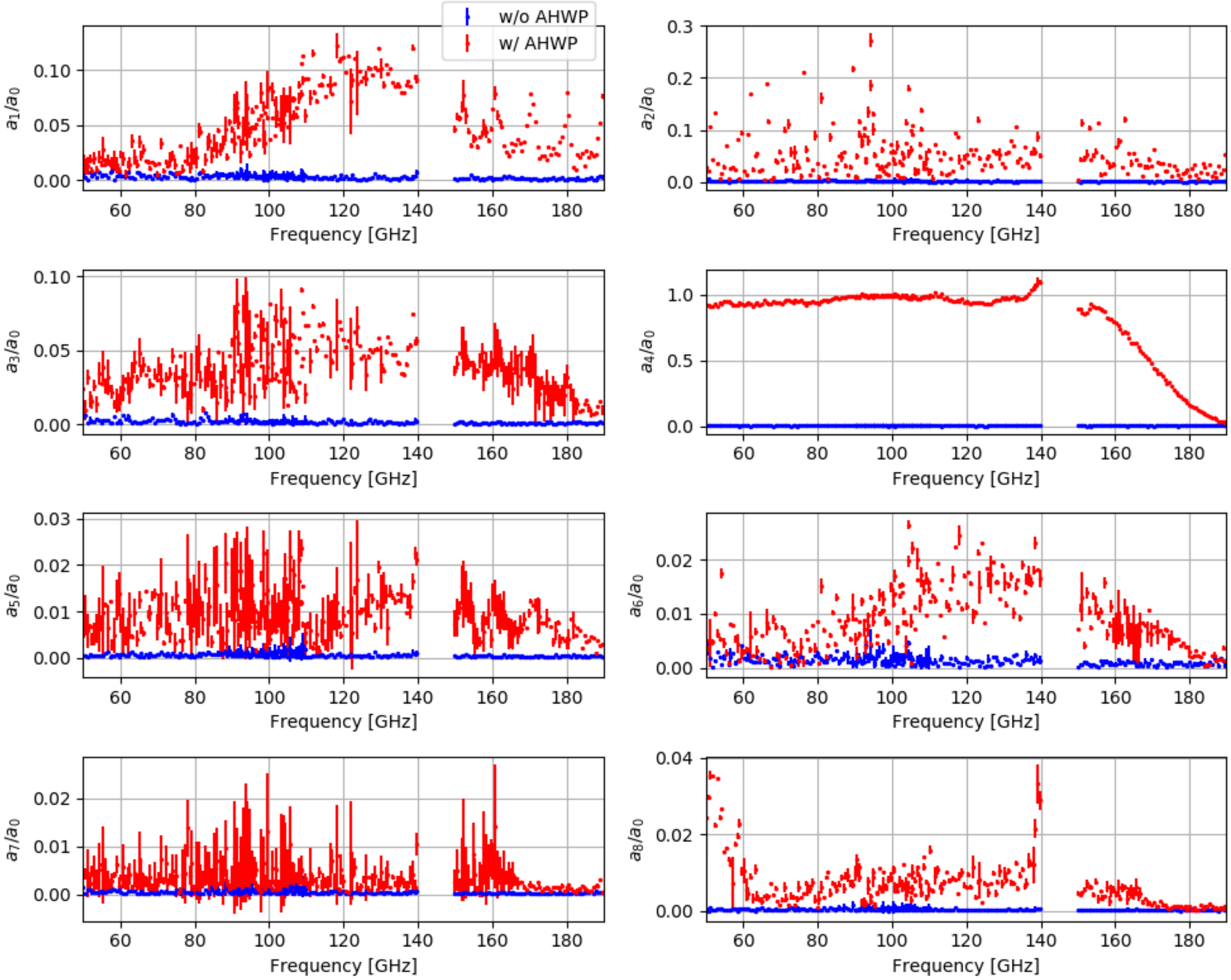

Figure 62: The fitted amplitudes divided by a_0 (DC component). Image from [41].

4.3.6 Discussion

Frequency content in modulated signal We identified the origins of the peaks seen in the modulated signal in the power spectral domain in Fig 61 by sorting them out by comparing the four cases. The origins of the peaks are largely composed of three categories: the rotational synchronous frequency and its harmonics (blue lines), the optically modulated frequency and its harmonics (red lines), and the resonance frequency of the SMB (green line). Only in the case 1-opt., we observed a number of rotational synchronous peaks but not in other cases. The area of the beam entering the HWP is larger than the size of the hole on the small PMU. It is not surprising to see a large rotational synchronous signal at the rotational frequency and its harmonics since we have not defined an aperture clearly in the system at around the rotation mechanism due to the current space constraint. The series of peaks in the magnetic field measurements at the SMB during its rotation are expected due to the physical contact between the rotor and the gripper mechanism, or due to the rotation wobbling. Figure 62 shows the amplitudes a_m ($m = 1-8$) which are normalized by a_0. We find the similar spectrum in the case of $m = 1, 3, 5, 6$. In addition, we found a strong correlation between the amplitudes of $m = 3, 5$ and $m = 1$ in the case of sample without the SWS as shown in Fig. 53. But in this time, we did not find a strong correlation between these amplitudes and a_1. It is suggests that the SWS have affect to the odd number component amplitudes. Only when the rotor is levitating (see Case 1, 2, 3-mag), we observe the small peak which appears at 27 Hz in the magnetic field data (green vertical line). The rotor is levitated by the SMB, and thus the rotor is pinned in all directions except the axis of rotation due to the symmetry of the magnetic field. The ring magnet of the rotor is pinned in all directions except the axis of rotation due to the symmetry of the magnetic field when the rotor levitates. For the SMB, we can define a stiffness in all degrees of freedom. Correspondingly, an associated effective spring constant is there for each mode. The levitating rotor is always susceptible to the small vibration with an external excitation in this spring system. Given the resonance frequency at 27 Hz corresponds the effective spring constant is $k_r \sim 6. \times 10^4$ N/m based on $f_r = 1/(2\pi)\sqrt{k_r/m}$ where $m \sim 2$ kg is the rotor weight. The amplitude of the peak in the magnetic field data depends on the orientation of the rotor vibration and magnetic field at a Hall sensor. The peak observed in this time originates from the combination of vertical and horizontal vibration. We also searched the peaks in the optical data, which corresponds to the micro-vibration of the rotor. As the result, we identified a peak when the rotor is rotating and its amplitude is at least two order of magnitudes lower than the peak of the modulated signal. We should make a close attention to the presence of such this signature in the future measurement. It should be noted that the amplitude of this peak relates to the amount of the displacement by the micro-vibration, which is inversely proportional to the moment of inertia of the rotor. The target size of the PMU is ten times larger in diameter than that of the small prototype PMU demonstrated in this subsection. When we make the rotor in the target size, it becomes larger (heavier) than that of the small prototype PMU, thus the micro-vibration will be small.

Performance of AHWP at low temperature Figure 63 shows the comparison of the modulation efficiency a_4/a_0 and phase ϕ_4 between the measured data and the prediction. We can predict the modulation efficiency, a_4/a_0, and the phase ϕ_4 using the equations in Sec. 4.3.2, the effective thickness of the SWS t_{AR} shown in Fig 56, and the measured thickness and the assembled angles in Tab. 22. The prediction of a blue line does not include the effects from the measurement errors of each values. The yellow area shows the error expected for the prediction by propagating the uncertainty of the parameters used in the calculation (e.g. the refractive index, the thickness of the plates, the optic axis angle). In order to obtain this area, we perform 50,000 calculations which randomized all parameters within their respective error ranges. We do not account for the effect of multiple reflections between the AHWP layers in this prediction calculations. However, because the reflection effects, which are like the dips and the oscillatory features in Fig. 45, is suppressed to less than a few percent by the SWS, the predictions from a model without taking into account the effect of reflection are in good agreement with the measured data. For the prediction of ϕ_4, the error in the estimation of the initial rotation angle offset (about 3 degrees) when we mount the AHWP to the rotation mechanism, is also included. We expect t_{AR} to change depending on the refractive index, however here it is fixed the values in Fig. 56. Since the almost part of the measured data are within the yellow area, we can confirm that the AHWP and the SWS performance are in good agreement with the expectations. The same measurement result for a five layers anti-symmetric design AHWP with out the SWS can be found in Appendix B.

In Tab. 24, we also show the band averaged modulation efficiency and maximum phase difference for each LFT band. The values of the prediction is calculated from the blue line in Fig. 63. We do not given values for the measured data of the first two band because there is no data in half or full of the bandwidth. Although the prediction is calculated without the optic axis angle error, the phase difference for each band is not equals zero due to the thickness asymmetry of the sapphire plates except for the center plate. For the measured data, the band averaged modulation efficiency does not achieve the target value of 0.98 except for 89 and 100 GHz bands. For the prediction, the band averaged modulation efficiency also does not achieve the target value for the half number of the bands, i.e. 40, 69, 78, 119, and 140 GHz. The reason except for 40 and 140 GHz is that we use an AHWP design optimized without considering t_{AR} which causes the oscillatory features in the modulation efficiency around 70 and 120 GHz becomes deep. Especially in the measurement data, this effect is large because the oscillatory features become deeper than the prediction due to the thickness of each sapphire plate and the accuracy of the optical axis angle. These problems may be improved by optimizing the AHWP design by considering t_{AR}. For 40GHz and 140GHz, the problem is caused by the frequency coverage of the five layers AHWP. It is necessary to continue efforts to improve by increasing the number of layers of the AHWP or studying the possibility of relaxing requirements by simulation.

We find some deviations between the measured data and the prediction particularly at around 50 and 140 GHz. Figure 64 shows the measured DC level a_0. At around 50 GHz the mm-wave source output is larger than other frequencies. There is a possibility that the diode detector performance becomes non-linear in this range and it affects the amplitude of the modulated signal. From Fig. 64, we find that the DC level becomes very low at around 140 GHz. Therefore, the modulation efficiency a_4/a_0 is boosted due to the noise component from the division with very small number. Similar behaviour can be found at around 110 GHz. Therefore, these are considered to be the systematic effects of this measurement setup.

Cooling tolerance of the AHWP and the SWS It is necessary to check the cooling tolerance for the AHWP and the SWS since the PMU is operated at a temperature of ~ 20 K. The sample has been cooled to around 20 K twice to take data presented in this subsection. The issues like cracks, deformations, or breaks were not observed in the plates or the SWS. As mentioned in above, the sample size of the AHWP demonstrated in this subsection is 1/10 scale of the target size. The thermal contraction effects may become larger with a larger sample or if the plates are glued together. Therefore, we will evaluate the cooling tolerance again with a bigger HWP or if glue is applied between the plates.

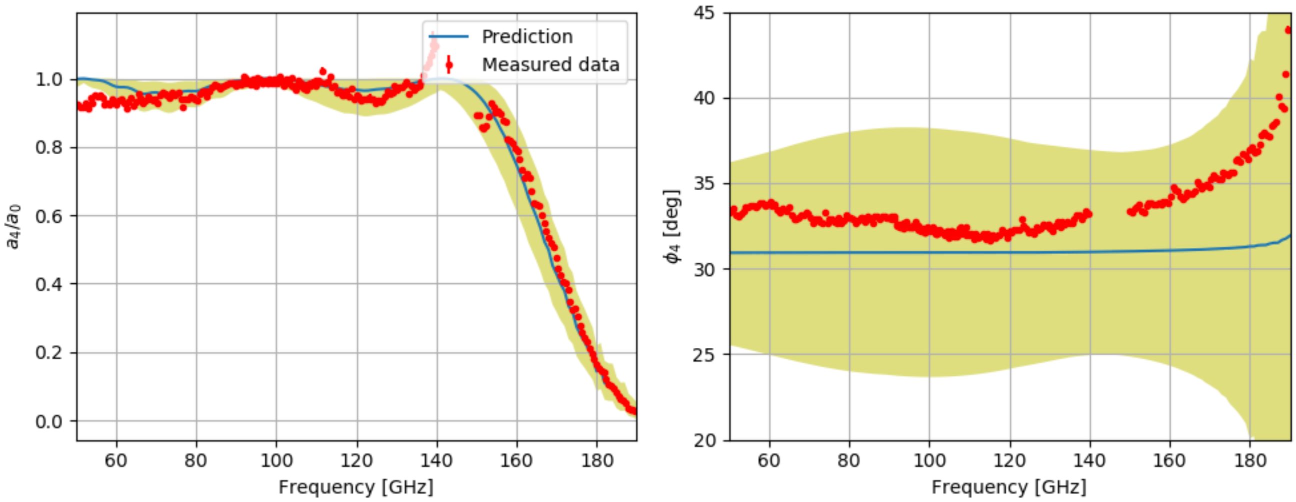

Figure 63: The measured and predicted modulation efficiency a_4/a_0 and phase ϕ_4. The yellow region indicates the error given the uncertainties of the input parameters to the model. Image from [41].

Expectations for a HWP with larger diameter Since the PMU flight model is about 10 times larger than the small PMU in diameter, its moment of inertia is about 1000 times the one of the small PMU presented here even only from the difference in radius. As mentioned in Sec. 4.3.6, the amplitude of the wobble is inversely proportional to the moment of inertia, and thus we expect that this effect of the wobble will be suppressed by a factor of the order 1000.

We have reported an orientation accuracy of the optic axis angle of 1 degree in Tab. 22 , which is the main reason why the phase ϕ_4 has the oscillatory features. This accuracy is determined by the finite width of the line used for assembling the AHWP. When we assume that the assembly lines are drawn in the same way for the large diameter sample, the accuracy improves linearly with diameter. In this assumption, when we make the AHWP in 500 mm diameter, the alignment accuracy improves to 0.2 degrees (14 arcmin). A comparison between the predictions for an error of the optic axis angle of 1 degree and 0.2 degrees is shown in Fig. 65. We have fixed the amplitude of the error in other parameters and can observe a significant improvement around the center of the band. However, the uncertainty of the rotation angle offset is not included in Fig. 65. On the other hand, the growth of the uncertainty toward the higher frequency is due to the error of the thickness and the refractive index of each plate that composes the AHWP. The required assembly accuracy to achieve the frequency independent phase of AHWP is discussed in K. Komatsu et al.[40, 39] and Sec. 2.

AHWP design optimization considering the effective thickness of the SWS In Sec. 2, we did not consider a frequency dependent effective thickness of the SWS. As shown in Fig. 56, the effective thickness of the SWS is large/small at the low/high frequency side, respectively. That causes the modulation efficiency to become broadband to the low/high frequency side because the thickness of the wave plates that have the SWS become thicker/thinner at the low/high frequency side. But the oscillatory features in the modulation efficiency at around 70 and 120 GHz becomes deeper. The effective thickness is uniquely determined by the SWS shape. There is a possibility to find a more suitable design by optimizing the optic axis angle and the thickness of the plate

Table 24: Table of band averaged modulation efficiency and maximum phase difference for each LFT band. The values of prediction are calculated from the blue line in Fig. 63. For the first two bands, the values of measured data are not given because there is no data in half or full of the bandwidth.

Frequency band [GHz]	Band averaged modulation efficiency		Phase difference	
	Prediction	Measured data	Prediction	Measured data
40	0.888	-	0.01	-
50	0.988	-	0.01	-
60	0.980	0.935	0.01	0.94
69	0.960	0.941	0.01	1.12
78	0.964	0.952	0.00	0.65
89	0.986	0.982	0.01	1.01
100	0.994	0.987	0.01	1.33
119	0.978	0.972	0.03	1.44
140	0.946	0.933	0.13	2.95

after defining the effective thickness by tuning the SWS shape. We access to this improvement in Sec. 6.

4.3.7 Conclusions

We have reported on the results of the optical demonstration of the small PMU prototype in this subsection. The motivation of this work is to study potential system-wide challenges that we may encounter at the later integrated phase LiteBIRD. We have prepared a five layers AHWP with a diameter of 50 mm with fabricating the SWS, and mount it on the SMB driven by the AC motor. We measured the AHWP performance in a cryogenic setup at ~ 20 K. We measured the modulated signal of a continuously rotating AHWP in the frequency range of 50 to 190 GHz. We confirm that the produced AHWP largely performs as expected from this demonstration. The SMB-originated resonance peak is expected in the magnetic field data. We have identified the origins of the frequency contents in the modulated signal by correlating the magnetic field of the SMB at the same time. We also identified the peak at the corresponding frequency in the optical data at the sub-percent level of with respect to the polarized amplitude at the 4^{th} harmonics of the rotation. In addition to the theoretically predicted harmonics in the modulated optical signal, we also identified harmonics at the percent level synchronized to the HWP rotation. Lastly, we discussed these effects from the micro-vibration of the rotor for the larger diameter AHWP, and which should suppress due to the larger inertia.

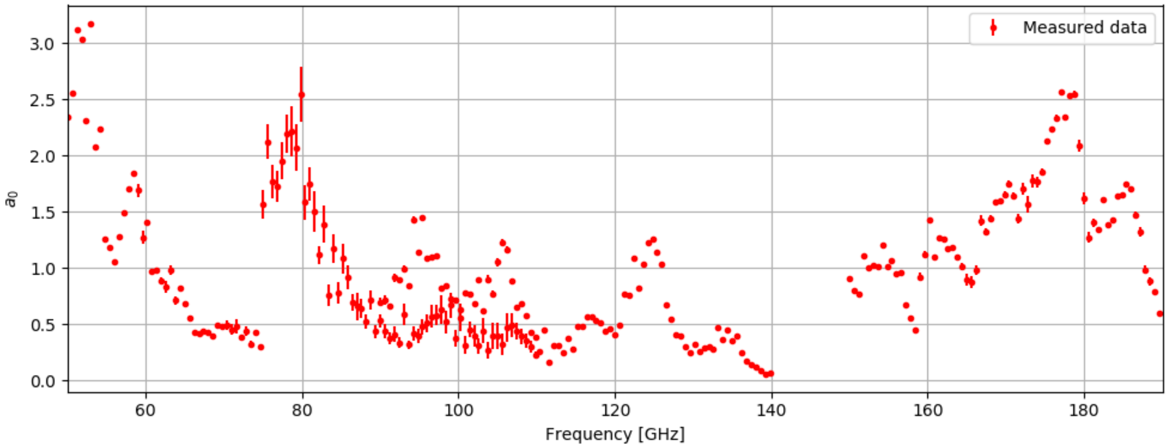

Figure 64: The fitted DC level a_0 as a function of frequency. Image from [41].

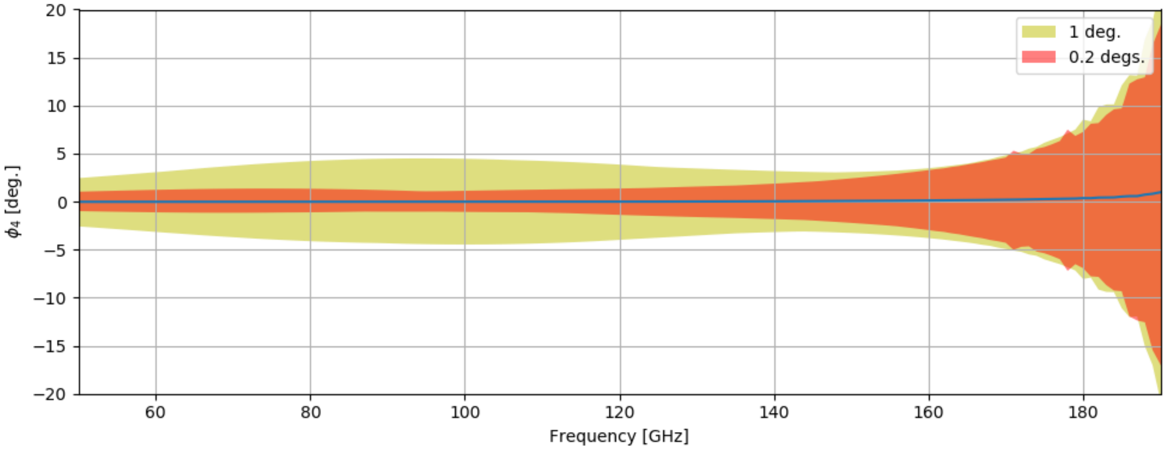

Figure 65: Comparison between the prediction with optic axis angle uncertainty of 1 degree and 0.2 degrees. Image from [41].

5 Conclusion

We report development efforts for the Polarization Modulator Unit (PMU) of the low-frequency telescope (LFT) on the LiteBIRD satellite.

In Sec. 2, we obtain the formalism of the HWP polarimetry that is useful for designing AHWP and considering systematic effects originating from HWP performance. While an AHWP can broaden the bandwidth, the frequency-dependent fast axis of the AHWP can create challenges in terms of calibration and add complexity in analysis. Using the formalism, we propose to eliminate this effect with a specific angular orientation of a novel AHWP by imposing anti-symmetric orientation to the relative wave plate angles. We derived the examples of the wave plate relative angles for the number of plates of $N = 5$ and $N = 9$. The optimized set of relative angles achieves the frequency-independent optic axis and covers the fractional bandwidth of 1.3 and 1.5 for five and nine layer AHWP, respectively. We also discussed the tolerance of the design in the wave plate relative angles and thicknesses. In order to suppress the maximum variation of the phase response to be less than 1 degree in 34 to 161 GHz, we need to assemble the AHWP within relative angles of 15 arcmin with a thickness accuracy less than 20 μm. This result can be applicable not only to CMB polarimetry, but any other applications that require a flat spectral response of the effective fast axis of a AHWP. We also present the design of the AHWP for several bandwidths, which will help CMB polarization experiments that plan to use the AHWP for millimeter-wave applications.

In Sec. 3, we evaluate the systematic effects originating from the frequency dependence of the HWP performance on observation results, simulating it for several cases. First, we estimate the effect of the HWP on the observed results, compared with the case of an ideal HWP. We also discuss the light source used for the ground calibration. Next, we assume that the effects of the HWP are corrected in the data analysis. In this assumption, we simulate the systematic effects originated from some calibration error of the HWP, and obtain the requirements for the calibration errors from the comparison with the requirements of T. Ghina et al. [26]. Each estimate and simulation is obtained for the five-layer case of the two AHWP designs presented in Sec. 2, and the comparison results of these two designs are summarized in a table. In some cases, we confirm that the anti-symmetric design is more useful for LiteBIRD observations than the symmetric design. Therefore, we conclude that we prefer to use the anti-symmetric design AHWP for LiteBIRD. The results in this paper do not include masking of the galactic center, the foreground cleaning via component separation, or any noise effects, which should be considered in future work.

The AHWP design methods and formalism and the discussion of systematic effects due to the frequency dependence of HWP performance shown in Sec. 2 and Sec. 3 are applicable not only for LiteBIRD but also CMB polarization experiments planned for the future. Therefore, these findings should prove useful for those who will do such studies in the future.

In Sec. 4.2, we report the results of an optical demonstration at room temperature for a 9-layer AHWP intended for use in the old LFT band with a design which is similar to the symmetric design presented in Sec. 2. We measure the modulation efficiency and phase in the range of 33 to 260 GHz and found good agreement between experiment and prediction. This result confirms the feasibility of the AHWP, which covers an unprecedentedly wide bandwidth. The effects of the assumed ±10 degree incident angle of LiteBIRD, the air gap between the plates of the AHWP, and the non-theoretical component of the modulated signal are also discussed.

In Sec. 4.3, we report on the results of the optical demonstration of the small PMU prototype. This work is intended to study potential system-wide challenges that we may encounter at the later integrated phase of the LiteBIRD space mission. We have prepared a 5-layer AHWP with a diameter of 50 mm with machined SWS AR, which is mounted on the SMB driven by an AC motor.

We measured the AHWP performance in a cryogenic setup at ~ 20 K. By continuously rotating the AHWP, we measured the modulated signal in the frequency range of 50 to 190 GHz. From this demonstration prototype, we confirm that the produced AHWP largely performs as expected. We have identified the origins of the frequency contents in the modulated signal by correlating the magnetic field of the SMB at the same time. The SMB-originated resonance peak is expected in the magnetic field data. We also identified the peak at the corresponding frequency in the optical data at the sub-percent level of with respect to the polarized amplitude at the 4^{th} harmonics of the rotation. In addition to the theoretically-predicted harmonics in the modulated optical signal, we also identified harmonics at the percent-level synchronized to the HWP rotation. Lastly, we discussed these effects for the larger diameter AHWP, which should suppress the amplitude of the micro-vibration even further due to the larger inertia.

Experimental demonstrations such as those presented in Sec. 4 and the discussion provide important considerations in employing a PMU in the satellite. The demonstrations are performed on small scales such as 1/10 and 1/5 scale. It is not realistic to conduct a large-scale demonstration without tests in a smaller scale in terms of cost and iteration speed. The measurement and discussion on the small scale, as well as the verification method used, will be of great help to large-scale development in the future.

6 Future works

Whilst we report results summarized in Sec. 5 in this thesis, we also find several issues that need to be addressed in the future. In this section, we summarize these issues.

6.1 Band-specific requirements

The current requirements for transmittance and polarization efficiency of the LFT PMU are larger than 0.97 and 0.98 for all frequency bands, respectively (see Tab. 17). These values come from sensitivity (noise) calculations like Sec. 1.4.2, but the requirements for each band are not evaluated. For Tab. 2 in Sec. 2, we calculated the band-averaged polarization efficiency for the whole LFT frequency range 34-161 GHz and obtained a value of 0.978. When we calculate it for each LFT frequency band, the band-averaged polarization efficiencies are over 0.98 except for the lowest and highest frequency bands. The band-averaged polarization efficiencies for the lowest and highest frequency bands are 0.930 and 0.971, slightly smaller than the requirement. In the case of transmittance, the band-averaged transmittance are 0.91 and over 0.97 for the lowest frequency and other frequency bands [71]. If we continue to impose the same requirements for all bands, for transmittance, we need to fabricate deeper SWS using higher-energy lasers than the current one, but it is challenging. In terms of polarization efficiency, we need to change the number of AHWP layers from 5 to 9, which increases the HWP weight from 17 kg to 32 kg and conflicts with the mass requirement of the PMU. If the requirement for polarization efficiency of the lowest frequency band is relaxed, we can continue to use a five layer AHWP since the polarization efficiency at the highest frequency band is satisfies 0.98 by adjusting the thickness of all the plates of the AHWP by the same amount, instead of decreasing the polarization efficiency at the lowest frequency band, and vice versa. It means that there is a trade-off between polarization efficiencies at the highest and lowest frequency bands when we use a five layer AHWP. From these facts, it is important to define band-specific requirements for optical performances of the PMU. There are nine frequency bands for LFT and most of them are mainly used for foreground cleaning, except for the CMB bands. Foreground is separated from the observed map by fitting a spectrum for each sky component. As discussing in Sec 3, if there are no HWP phase effects, this fitting in foreground cleaning is done individually for Q and U. In the presence of phase effects, this must be done taking into account the mixing of Q and U. One way to obtain band-specific requirements would be making a simulation of r calculation for CMB maps separated by foreground cleaning from observed maps which include noise shown in Sec. 1.4.2 and the HWP effects shown in Sec 3.

6.2 Predicting anti-symmetric design performance with reflection effects

Since methods to predict AHWP performances used in Sec. 4 is only for plates, we cannot predict performances of a HWP with SWS in the same way. For a symmetric design AHWP and a single layer HWP, we use RCWA calculation to predict performances of an AHWP with SWS [71, 72]. RCWA calculations require that the input AHWP model has a periodic structure. However, when SWS is applied to both surfaces of an anti-symmetrically designed AHWP, we cannot find a unit structure period satisfying the condition. In Sec. 4.3, since the reflections are reduced by SWS, we ignore the reflections and only focus on the retardance generated by SWS to calculate the prediction. However, it is necessary to include the effect of reflection in the calculation to more accurately predict AHWP performance. The terms have two times the frequency of rotation in

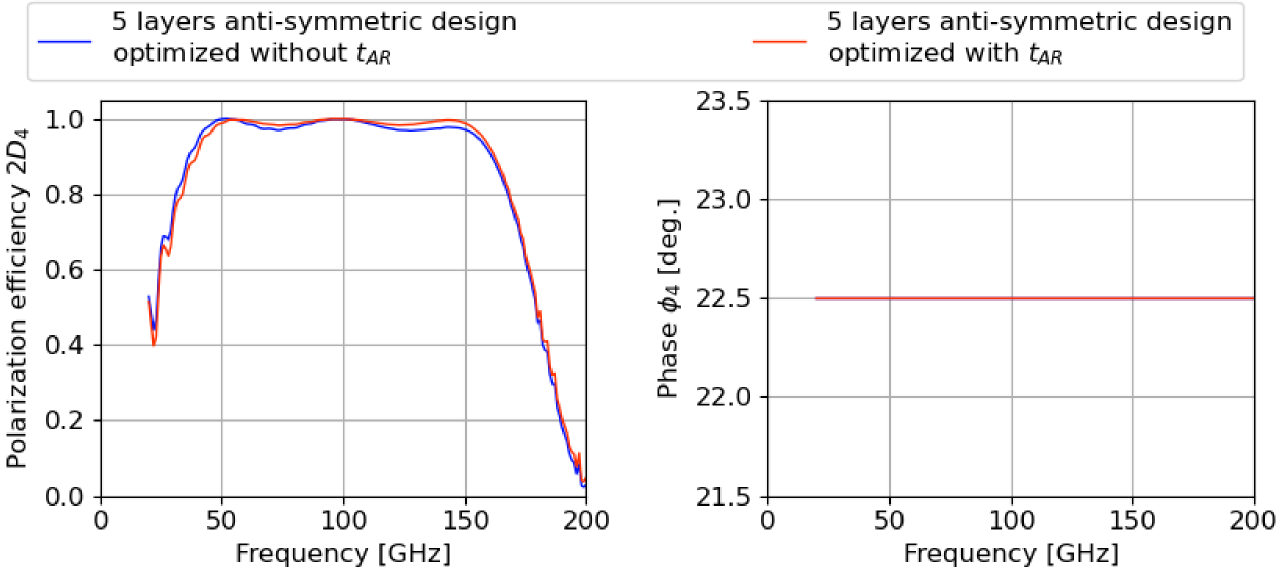

Figure 66: Polarization efficiency and phase of an $N = 5$ anti-symmetric design AHWP. The red and blue line show the designs optimized with and without t_{AR}. To calculate both lines, we ignore reflection effects and use first and fifth layer thickness of $2.7 + t_{AR}(\nu)$ mm. The blue line of the right panel is behind the red line.

the second line of Eq. 35 is caused by the transmittance difference of the HWP between ordinary and extra-ordinary rays originated from birefringence of wave plates or SWS. These terms can not be obtained from calculations which ignore reflection effects. In CMB observations, the power from the sky is dominated by the unpolarized component, meaning $I_{in} >> \sqrt{Q_{in}^2 + U_{in}^2}$. Since the the transmittance difference between two rays causes the power difference between orthogonal detectors, there could possibility be a leakage from the unpolarized component to the polarized component. This leakage is called instrumental polarization, and is one of the candidates of systemetic effects arising from the PMU. Therefore, to estimate instrumental polarization, it is important to find a way to perform optical simulations for aperiodic structures that take reflections into account.

6.3 AHWP design optimization specialized for LiteBIRD

AHWP designs in Sec. 2 are obtained for the LFT frequency range but the other situations are not specialized for a specific application. This frequency range can be shifted by changing the thickness of the plates.

One of the ways to make more specialized design for a specific application is to put a weight for each frequency as $w(\nu)$ in Eq. 38 or Eq. 40 (set to unity in Sec. 2). The candidates for setting weights are CMB and foreground spectra, detector bandpass shape, antenna beam effects, and so on. Another way is to use a sum of band-averaged polarization efficiencies for each FT band with weights as a figure of merit in the optimization. In addition, for applications using an AHWP with SWS such as LiteBIRD, it is necessary to consider the frequency dependence of the SWS effective thickness in the design optimization.

In this thesis, an example of the optimization method of AHWP design and SWS effective thickness by RCWA calculation is given in Sec. 2 and Sec. 4.3, respectively. Since it is a good chance, we perform an optimization for a five layers anti-symmetric design with taking into account the effective thickness of the SWS for a frequency range 34 to 161 GHz. We assume that the SWS has a physical thickness of 2.2 mm and an effective thickness $t_{AR}(\nu)$ shown in Fig. 56 is fabricated on the first and fifth layer of five layer anti-symmetric design AHWP where each layer has a thickness of 4.9 mm. Other fixed parameters are same as Tab. 1. At this time, the thickness of first and fifth layers are $4.9 - 2.2 + t_{AR}(\nu) = 2.7 + t_{AR}(\nu)$ mm. We randomize the optic axis angles of first and second layer under the anti-symmetric condition and obtain an AHWP design optimized by considering the SWS effective thickness. Tab. 25 shows the optimization results with and without $t_{AR}(\nu)$. The fractional bandwidth, band-averaged polarization efficiency, and phase difference are calculated in the case of the AHWP with SWS has the effective thickness $t_{AR}(\nu)$. The top line is the same design in Tab. 2 but since $t_{AR}(\nu)$ has larger and smaller value at lower and higher frequency, a frequency shift occurs which expands the fractional bandwidth. Comparing the top and bottom line of Tab. 25, we find a design has a higher polarization efficiency from the design optimization with $t_{AR}(\nu)$ but the fractional band width is a little narrower. Fig. 66 shows the polarization efficiency and phase of $N = 5$ anti-symmetric design AHWP optimized with and without $t_{AR}(\nu)$. From Fig. 66, we confirm that the design, optimized with $t_{AR}(\nu)$, has a slightly narrower bandwidth at lower frequency edge, but a higher polarization efficiency after about 50 GHz. Such a optimization needs to be done with other specializations referred to above when the design of SWS and other specifications of the telescope are fixed.

Table 25: A summary of anti-symmetric designs. The top and bottom lines show designs optimized without and with $t_{AR}(\nu)$, respectively. The fractional bandwidth, band-averaged polarization efficiency, and phase difference are calculated for each optic axis angle set in the case of the AHWP with SWS. In this calculation, we ignore reflection effects. The maximum phase difference $\Delta\phi_4$ is completely zero.

The number of layers N	Fractional bandwidth $\Delta\nu/\nu_0$	Pol. eff. $2A_4$	Phase diff. $\Delta\phi_4$[deg.]	Optic axis angles χ_i [deg.]
5 (opt. w/o $t_{AR}(\nu)$)	1.27	0.976	0.0	22.67 , 133.63 , 0.00 , -133.63 , -22.67
5 (opt. w/ $t_{AR}(\nu)$)	1.25	0.981	0.0	19.01, 129.81, 0., -129.81, -19.01

6.4 Upscaling of measurement setup and PMU

The final target of optical area size of the LFT PMU is 500 mm in diameter. In our current development, the optical demonstration is done at a sample size of < 200 mm and 50 mm diameter for room and cryogenic temperature. The mechanical and thermal demonstration of the cryogenic rotation mechanism is 380 mm in diameter. In order to realise a demonstration with a diameter of 500 mm, we need to upscale the measurement setup, rotation mechanism, and AHWP. The experimental setup can be upscaled by installing a mm-wave source, a detector, and an optical window on a large 4K GM cryostat with an inner diameter of ∼1 m at Kavli IPMU, which is used for the demonstration of the rotation mechanism, and is a similar concept to the setup shown in Sec. 4.3. In addition, by changing the mm-wave source and detector from the pair of a multiplier and diode detector to a vector network analyzer, we will improve the measurement accuracy for transmittance, polarization efficiency, and so on by measuring the electromagnetic wave phase after though a sample. The rotating mechanism is already close to 500 mm in diameter, so its scaling up is minimal. However, improvements are needed in terms of heat generation and weight. A new version of the rotation mechanism uses a glass epoxy material instead of metal to reduce weight and heat generation, has already been made, and will be tested in the next few months. On the other hand, there are many challenges involved with upscaling the AHWP. As mentioned in above, optical demonstrations of HWP have been done with diameters < 200 mm. When sapphire plates are made with a large diameter, there is concern that the uniformity of the crystals becomes poor (e.g., bubbles will be mixed in from the center to the periphery). The bubbles affect visible light, but we confirm that the bubbles do not change the refractive index in the millimeter waveband. It is necessary to check whether the bubbles change the mechanical strength of sapphire plates. Furthermore. the impact of the bubbles to the SWS fabrication must also be checked. Another is the deteriorating on the parallelism of the plates and the accuracy of the surface polishing, causing the air gap effect as shown in Sec. 4.2. When we fabricate SWS by laser machining, the area that can be fabricated at one time is limited, so it is necessary to consider the fabricating method. We are planning to fabricate these over a large area using the stitching method, and related studies are found in [72]. We also need to consider the assembling method of AHWP and the methods for mounting it on the rotating mechanism. Each 500 mm diameter, 5 mm thick sapphire weighs about 4 kg, and in addition, the SWS on both sides of the AHWP are easily damaged by physical contact, so we need to handle it whilst avoiding contact by hand. In order to avoid damage caused by vibration during launch, we plan to glue each sapphire plate which composes the AHWP. A sodium silicate solution is to be used for bonding, and sufficient bonding strength of 20 MPa has been obtained for a requirement of 5.5 MPa gave from a finite element method [74]. On the other hand, this demonstration of bond strength is done on a small area of 4×4 mm^2, and the bounding strength decreases more quickly than on polished surfaces (Ra$\leq$ 1 nm where Ra is arithmetic-mean-roughness) when the surface condition of the sapphire is unpolished (Ra$\leq$ 1μm). The bonding strength has not been evaluated, but samples of 50 mm in diameter have been successfully bonded and the optical effect of a bounding layer of ~ 7 mm is less than 0.02 in transmittance [74]. When bonding a sapphire plate as large as 500 mm in diameter, there are two options: full bonding or partial bonding (e.g. only rim, a few points). In either case, it is necessary to verify whether it is possible to bond a large area first. In addition, the larger the plate, the more difficult it is to ensure surface accuracy, and there is a concern that sufficient bonding strength will not be obtained. Since the required bonding strength varies depending on the holding method and bonding pattern of the AHWP, the bonding method should be determined based on a strength estimation by a finite element method calculation, and finally, a vibration test should be done on sapphire plates with a diameter of 500 mm. One of the other challenges is to devise a method of bonding while keeping the assembly accuracy.

We also need to perform integration tests with all LFT elements, including the PMU. This integration test of LFT is planned at KEK (High Energy Accelerator Research Organization).

A Appendix for Sec. 3

A.1 Drawing sky maps with *healpy*

In order to make the maps of the sky, we need to divide the celestial sphere into pixels as Fig. 67. In the python framework *healpy* used in the analysis and simulation of CMB experiments [3], the number of sky divisions is controlled by the value, *nside*, and the number of pixels is $12 nside^2$. In this thesis, we set *nside* to 128.

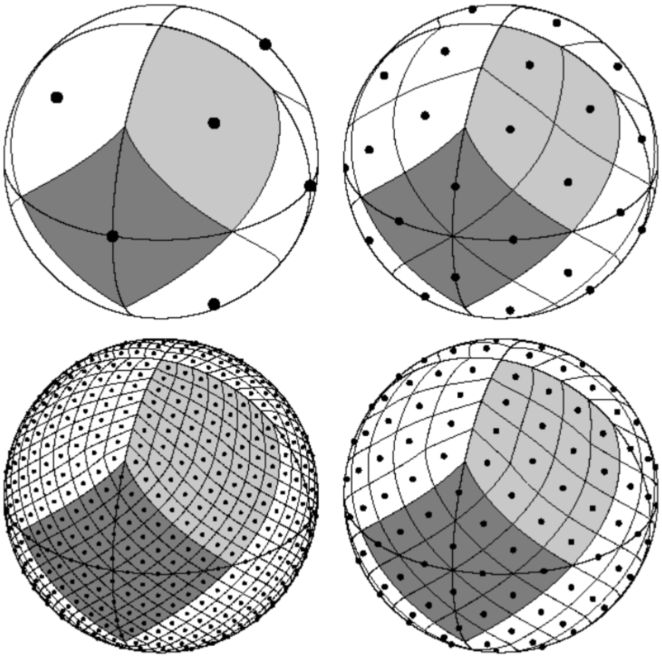

Figure 67: Image of pixelization of a sky map. [2]

A.2 Smoothing

To consider the effect of the beam size of the telescope, every map used in this section is smoothed using the beam size in Fig. 14. Fig. 69 shows the E and B-mode power spectrum, C_ℓ^{EE} and C_ℓ^{BB} before and after smoothing for each LFT band. The structures on the map smaller than the beam size are suppressed, so there is a decrease in intensity above ℓ, which corresponds to the beam size.

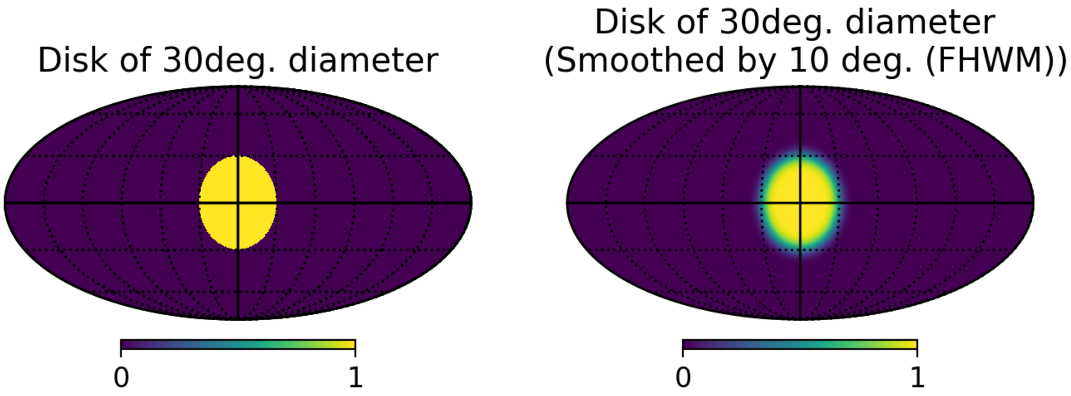
Disk of 30deg. diameter

Disk of 30deg. diameter
(Smoothed by 10 deg. (FHWM))

Figure 68: Disk of 30 deg. diameter on sky with and without smoothing by 10 deg. beam. The beam size is in full half width maximum (FHWM).

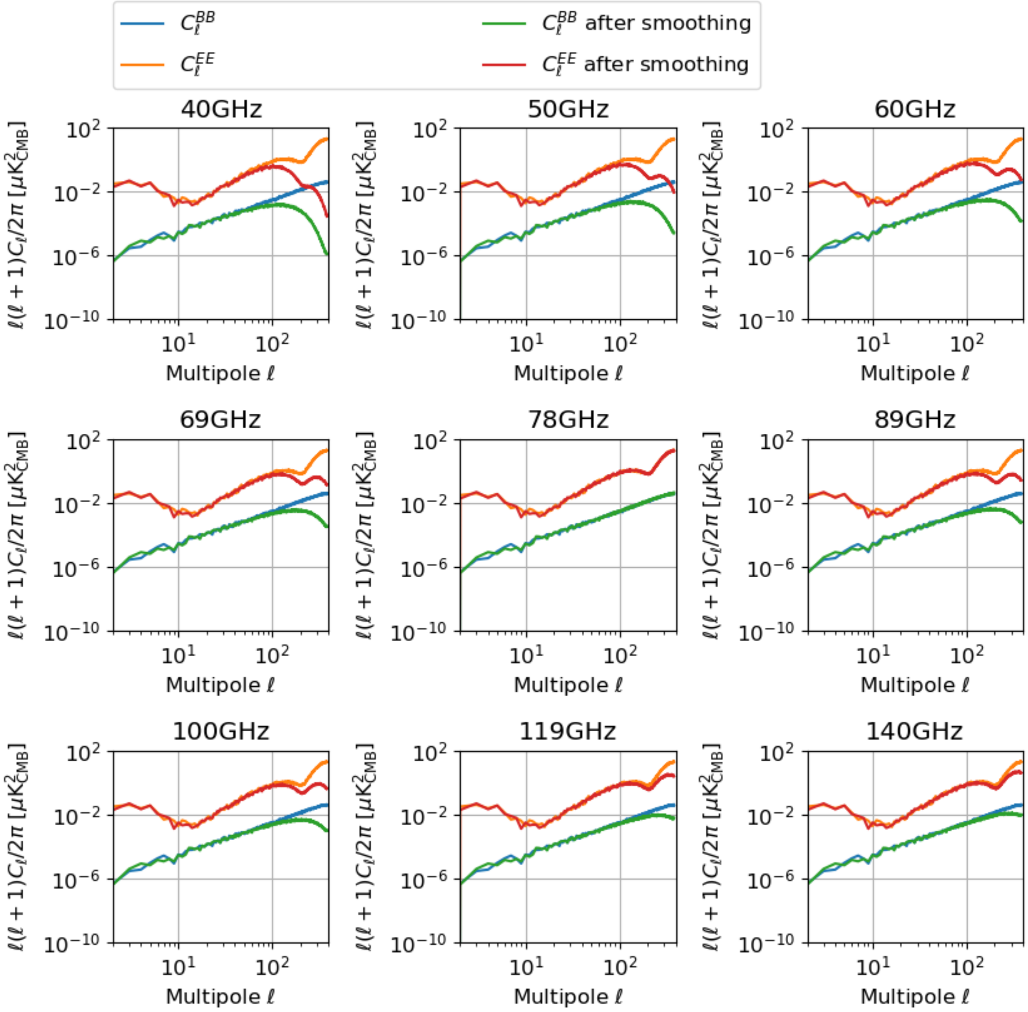
40GHz, 50GHz, 60GHz, 69GHz, 78GHz, 89GHz, 100GHz, 119GHz, 140GHz

Figure 69: Power spectrum of the CMB polarization before and after smoothing.

B Appendix for Sec. 4.3

B.1 Transmittance measurement for a sapphire plate

The modulation signal of a single A-cut sapphire plate is measured with the same setup as in Sec. 4.3 and fitted with Eq. 110. The sample thickness is 2.926 ± 0.005 mm. Since the maxima of the modulation signal correspond to each optical axis of the plate, the transmittance for ordinary and extraordinary ray is obtained by dividing the value of the maxima gave from the fit curve of the modulation signal by the intensity of without sample, as shown in Fig. 70. The transmittance in Fig. 70 is fitted using Eq. 106 to obtain the refractive index and absorption at low temperature as shown in Tab. 26. Although the temperature increases from 17 K to 33 K during the measurement, the same refractive index can be fitted, suggesting that the refractive index change in this temperature range is small.

Table 26: Fitted result to the refractive index and loss tangent for an A-cut sapphire plate at the room temperature.

Ordinary ray		Extraordinary ray	
Refractive index	Loss tangent ($\times 10^{-4}$)	Refractive index	Loss tangent ($\times 10^{-4}$)
3.035 ± 0.003	< 7.9	3.358 ± 0.003	< 5.2

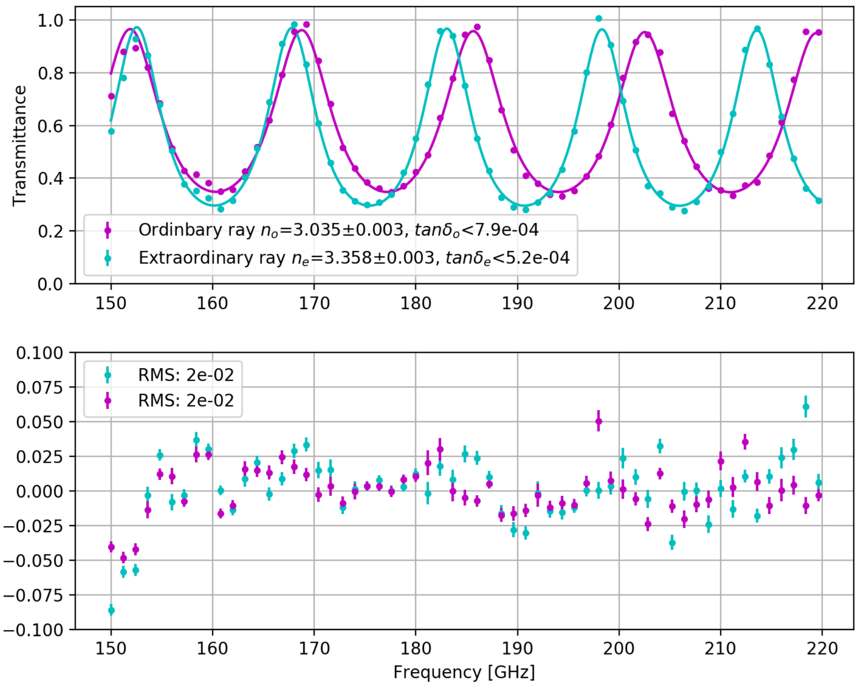

Figure 70: The measured and predicted modulation efficiency a_4/a_0 and phase ϕ_4. The yellow region indicates the error given the uncertainties of the input parameters to the model.

B.2 Modulation efficiency of a five layer anti-symmetric design AHWP without SWS

Before the measurements for the AHWP with SWS in Sec. 4.3, we also measured the modulation efficiency and phase of a sample without SWS. The measurement is done at 90-140 GHz and 150-220 GHz. The experimental setup, the AHWP design, and used sapphire plates are the same as in Sec. 4.3. Fig. 71 shows the measurement result of modulation efficiency and phase. The yellow region indicates the error given the uncertainties of the input parameters in the model. To predict the modulation efficiency and phase of the sample without SWS, we need to consider the reflection effects. Since this calculation is for a flat plate, it is done by converting the Jones matrix, calculated by the method shown in T. Essinger-Hileman [22], to the Mueller matrix. From the comparison between Fig. 71 and Fig. 63, we confirm that the dips and oscillatory features in modulation efficiency originating from reflection at the boundary surfaces of sapphire plates are mitigated by SWS.

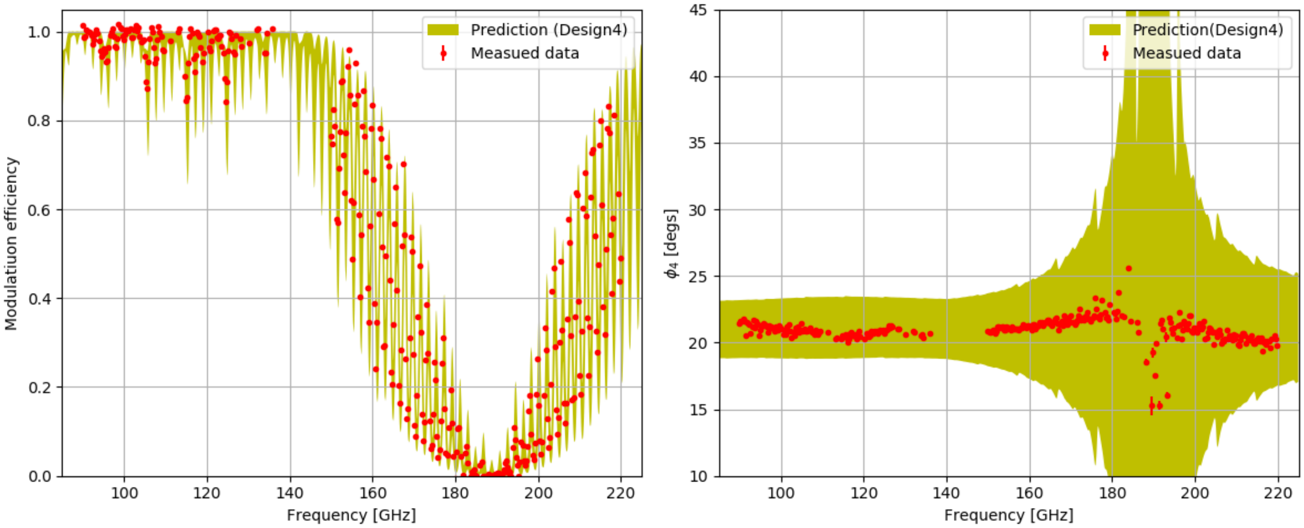

Figure 71: The measured and predicted modulation efficiency a_4/a_0 and phase ϕ_4. The yellow region indicates the error given the uncertainties of the input parameters to the model.

B.3 Magnetic field measurements of the magnet ring

To probe the origin of the dips of magnetic field measurement in Fig. 60, we measure the magnetic field using a 2D stage at a height of 5 mm from the magnet ring, which is the same height as the levitation height. Fig 72 and Fig 73 show the measurement setup and measurement results. In Fig 73, the black dot and rings are the center of magnet ring and the inner and outer diameter of magnet ring and holder. The dips are shown as yellow lines. The Hall sensor used for measuring the magnetic field of Fig. 60 is placed between the two outermost black rings. To emphasize the magnitude of the magnetic field at the radius of the Hall sensor placed, the right panel uses a different range than the left panel. In Fig. 60, there is a variation of around 10% in the magnetic field at the dips, but no such variation can be found in the right panel, although a gradient is there due to the inclination of the setup. This suggests that the dip in Fig. 60 is not caused by the magnet ring but by physical contact, such as between the rotor and gripper.

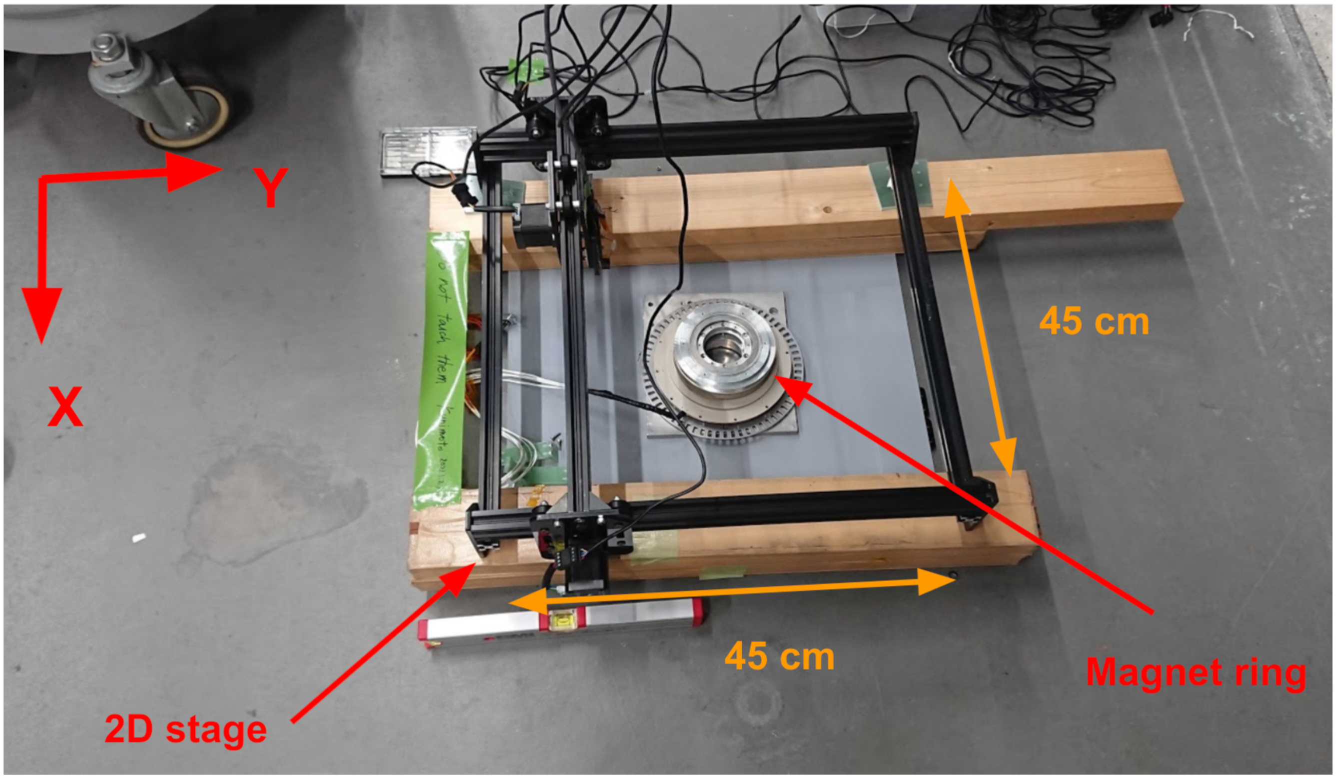

Figure 72: A setup for magnetic field measurement.

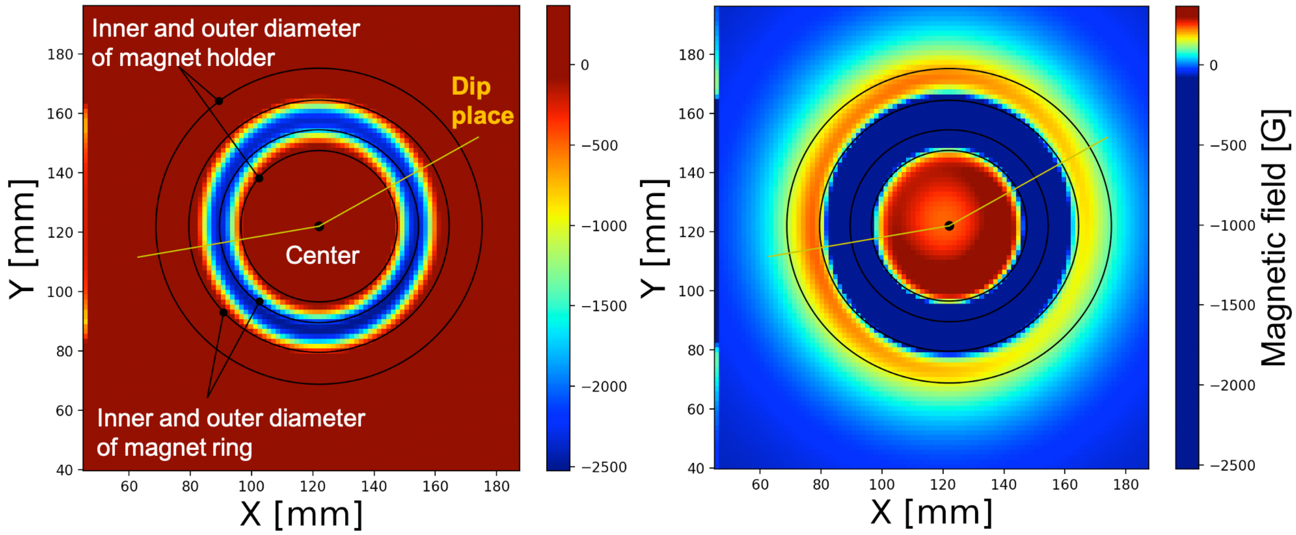

Figure 73: Color map of magnetic field of magnet ring with two colorbar ranges. The left and right panels have ranges of -76 to -2500 G and -76 to 300 G. The black dot is the center of magnet ring. The black rings are inner and outer diameters of the magnet ring and holder. The places of dips in Fig. 60 are shown as yellow lines. The Hall sensor is placed between the two outermost black rings.

References

[1] Camb. http://camb.info.

[2] Healpix. https://healpix.jpl.nasa.gov/pdf/intro.pdf.

[3] healpy. https://healpy.readthedocs.io/en/latest/.

[4] pysm. https://pysm3.readthedocs.io/en/latest/index.html.

[5] *Cosmic Microwave Background Ratiation*. Nippon Hyoron sha, 2019.

[6] Kevork N. Abazajian et al. Cmb-s4 science book. *arXiv preprint arXiv:1610.02743*, 2016.

[7] Maximilian H. Abitbol, David Alonso, Sara M. Simon, Jack Lashner, Kevin T. Crowley, Aamir M. Ali, Susanna Azzoni, Carlo Baccigalupi, Darcy Barron, Michael L. Brown, Erminia Calabrese, Julien Carron, Yuji Chinone, Jens Chluba, Gabriele Coppi, Kevin D. Crowley, Mark Devlin, Jo Dunkley, Josquin Errard, Valentina Fanfani, Nicholas Galitzki, Martina Gerbino, J. Colin Hill, Bradley R. Johnson, Baptiste Jost, Brian Keating, Nicoletta Krachmalnicoff, Akito Kusaka, Adrian T. Lee, Thibaut Louis, Mathew S. Madhavacheril, Heather McCarrick, Jeffrey McMahon, P. Daniel Meerburg, Federico Nati, Haruki Nishino, Lyman A. Page, Davide Poletti, Giuseppe Puglisi, Michael J. Randall, Aditya Rotti, Jacob Spisak, Aritoki Suzuki, Grant P. Teply, Clara Vergès, Edward J. Wollack, Zhilei Xu, and Mario Zannoni. The simons observatory: Bandpass and polarization-angle calibration requirements for b-mode searches. https://arxiv.org/abs/2011.02449, 2020.

[8] M. N. Afsar. Precision millimeter-wave dielectric measurements of birefringent crystalline sapphire and ceramic alumina. *IEEE Transactions on Instrumentation and Measurement*, IM-36(2):554–559, June 1987.

[9] Kam Stahly Arnold. *Design and Deployment of the Polarbear Cosmic Microwave Background Polarization Experiment*. PhD thesis, University of California, Berkeley, December 2010.

[10] C. Bao, C. Baccigalupi, B. Gold, S. Hanany, A. Jaffe, and R. Stompor. MAXIMUM LIKELIHOOD FOREGROUND CLEANING FOR COSMIC MICROWAVE BACKGROUND POLARIMETERS IN THE PRESENCE OF SYSTEMATIC EFFECTS. *The Astrophysical Journal*, 819(1):12, feb 2016.

[11] C. Bao, B. Gold, C. Baccigalupi, J. Didier, S. Hanany, A. Jaffe, B. R. Johnson, S. Leach, T. Matsumura, A. Miller, and et al. The impact of the spectral response of an achromatic half-wave plate on the measurement of the cosmic microwave background polarization. *The Astrophysical Journal*, 747(2):97, Feb 2012.

[12] C. L. Bennett et al. Nine-Year Wilkinson Microwave Anisotropy Probe (WMAP) Observations: Final Maps and Results. *Astrophys. J. Suppl.*, 208:20, 2013.

[13] Sean A. Bryan, Sara M. Simon, Martina Gerbino, Grant Teply, Amir Ali, Yuji Chinone, Kevin Crowley, Giulio Fabbian, Patricio A. Gallardo, Neil Goeckner-Wald, Brian Keating, Brian Koopman, Akito Kusaka, Frederick Matsuda, Philip Mauskopf, Jeff McMahon, Federico Nati, Giuseppe Puglisi, Christian L. Reichardt, Maria Salatino, Zhilei Xu, and Ningfeng

Zhu. Development of calibration strategies for the Simons Observatory. In Jonas Zmuidzinas and Jian-Rong Gao, editors, *Millimeter, Submillimeter, and Far-Infrared Detectors and Instrumentation for Astronomy IX*, volume 10708, pages 685 – 697. International Society for Optics and Photonics, SPIE, 2018.

[14] Buzzelli, A., de Bernardis, P., Masi, S., Vittorio, N., and de Gasperis, G. Optimal strategy for polarization modulation in the lspe-swipe experiment. *A&A*, 609:A52, 2018.

[15] Fabio Columbro, Paolo de Bernardis, Luca Lamagna, Silvia Masi, Alessandro Paiella, Francesco Piacentini, and Giampaolo Pisano. A polarization modulator unit for the mid- and high-frequency telescopes of the LiteBIRD mission. In Makenzie Lystrup, Marshall D. Perrin, Natalie Batalha, Nicholas Siegler, and Edward C. Tong, editors, *Space Telescopes and Instrumentation 2020: Optical, Infrared, and Millimeter Wave*, volume 11443, pages 1113 – 1128. International Society for Optics and Photonics, SPIE, 2020.

[16] Hans Dembinski and Piti Ongmongkolkul et al. scikit-hep/iminuit. Dec 2020.

[17] R. H. Dicke, P. J. E. Peebles, P. G. Roll, and D. T. Wilkinson. Cosmic Black-Body Radiation. *Astrophysical Journal*, 142:414–419, July 1965.

[18] Elena R Dobrovinskaya, Leonid A Lytvynov, and Valerian Pishchik. *Sapphire: material, manufacturing, applications*. Springer Science & Business Media, 2009.

[19] Adriaan J Duivenvoorden, Alexandre E Adler, Matteo Billi, Nadia Dachlythra, and Jon E Gudmundsson. Probing frequency-dependent half-wave plate systematics for CMB experiments with full-sky beam convolution simulations. *Monthly Notices of the Royal Astronomical Society*, 502(3):4526–4539, 02 2021.

[20] T. Essinger-Hileman et al. Systematics of an ambient-temperature, rapidly-rotating half-wave plate. In *Millimeter, Submillimeter, and Far-Infrared Detectors and Instrumentation for Astronomy VIII*, volume 9914 of *Proc. SPIE*, 2016.

[21] T. Essinger-Hileman, A. Kusaka, J. W. Appel, S. K. Choi, K. Crowley, S. P. Ho, N. Jarosik, L. A. Page, L. P. Parker, S. Raghunathan, S. M. Simon, S. T. Staggs, and K. Visnjic. Systematic effects from an ambient-temperature, continuously rotating half-wave plate. *Review of Scientific Instruments*, 87(9):094503, 2016.

[22] Thomas Essinger-Hileman. Transfer matrix for treating stratified media including birefringent crystals. *Applied Optics*, 53:4264–4265, 2014.

[23] D. J. Fixsen. THE TEMPERATURE OF THE COSMIC MICROWAVE BACKGROUND. *The Astrophysical Journal*, 707(2):916–920, nov 2009.

[24] N. Galitzki et al. The simons observatory: instrument overview. In *Millimeter, Submillimeter, and Far-Infrared Detectors and Instrumentation for Astronomy IX*, volume 10708 of *Proc. SPIE*, 2018.

[25] T Ghigna. *Development of new generation receivers for experimental cosmology with the cosmic microwave background and systematic effect studies*. PhD thesis, University of Oxford, 2020.

[26] T. Ghigna, T. Matsumura, G. Patanchon, H. Ishino, and M. Hazumi. Requirements for future cmb satellite missions: photometric and band-pass response calibration. *Journal of Cosmology and Astroparticle Physics*, 2020(11):030–030, Nov 2020.

[27] S. Hanany et al. Millimeter-wave achromatic half-wave plate. *Applied Optics*, 44:4666–4670, 2005.

[28] Masashi Hazumi, Peter A.R. Ade, Alexandre Adler, Erwan Allys, David Alonso, Kam Arnold, Didier Auguste, Jonathan Aumont, Ragnhild Aurlien, Jason Austermann, Carlo Baccigalupi, Anthony J. Banday, Ranajoy Banerji, Rita B. Barreiro, Soumen Basak, Jim Beall, Dominic Beck, Shawn Beckman, Juan Bermejo, Paolo de Bernardis, Marco Bersanelli, and Julien Bonis. LiteBIRD satellite: JAXA's new strategic L-class mission for all-sky surveys of cosmic microwave background polarization. In Makenzie Lystrup, Marshall D. Perrin, Natalie Batalha, Nicholas Siegler, and Edward C. Tong, editors, *Space Telescopes and Instrumentation 2020: Optical, Infrared, and Millimeter Wave*, volume 11443. International Society for Optics and Photonics, SPIE, 2020.

[29] E. Hecht. *Optics, 4th Edition*. Addison-Wesley, 2001.

[30] Brandon Hensley and Philip Bull. Mitigating complex dust foregrounds in future cosmic microwave background polarization experiments. *The Astrophysical Journal*, 853:127, 01 2018.

[31] Charles A. Hill, Sarah Marie M. Bruno, Sara M. Simon, Aamir Ali, Kam S. Arnold, Peter C. Ashton, Darcy Barron, Sean Bryan, Yuji Chinone, Gabriele Coppi, Kevin T. Crowley, Ari Cukierman, Simon Dicker, Jo Dunkley, Giulio Fabbian, Nicholas Galitzki, Patricio A. Gallardo, Jon E. Gudmundsson, Johannes Hubmayr, Brian Keating, Akito Kusaka, Adrian T. Lee, Frederick Matsuda, Philip D. Mauskopf, Jeffrey McMahon, Michael D. Niemack, Giuseppe Puglisi, Mayuri Sathyanarayana Rao, Maria Salatino, Carlos Sierra, Suzanne Staggs, Aritoki Suzuki, Grant Teply, Joel N. Ullom, Benjamin Westbrook, Zhilei Xu, and Ningfeng Zhu. BoloCalc: a sensitivity calculator for the design of Simons Observatory. In Jonas Zmuidzinas and Jian-Rong Gao, editors, *Millimeter, Submillimeter, and Far-Infrared Detectors and Instrumentation for Astronomy IX*, volume 10708, pages 698 – 718. International Society for Optics and Photonics, SPIE, 2018.

[32] Charles A. Hill et al. Design and development of an ambient-temperature continuously-rotating achromatic half-wave plate for cmb polarization modulation on the polarbear-2 experiment. In *Millimeter, Submillimeter, and Far-Infrared Detectors and Instrumentation for Astronomy VIII*, volume 9914 of *Proc. SPIE*, 2016.

[33] H. Imada et al. Instrumentally induced spurious polarization of a multi-layer half wave plate for a cmb polarization observation. *Proceedings for TWENTY-NINTH INTERNATIONAL SYMPOSIUM ON SPACE TERAHERTZ TECHNOLOGY*, 2018.

[34] Bradley R. Johnson. *MAXIPOL: A Bolometric, Balloon-Borne Experiment for Measuring the Polarization Anisotropy of the Cosmic Microwave Background Radiation.* Ph.d. thesis, University of Minnesota, Twin Cities, 2004.

[35] William C. Jones et al. A Measurement of the angular power spectrum of the CMB temperature anisotropy from the 2003 flight of BOOMERANG. *Astrophys. J.*, 647:823–832, 2006.

[36] Marc Kamionkowski and Ely D. Kovetz. The quest for b modes from inflationary gravitational waves. *Annual Review of Astronomy and Astrophysics*, 54(1):227–269, 2016.

[37] Soma King and Philip Lubin. Circular polarization of the cmb: Foregrounds and detection prospects. *Phys. Rev. D*, 94:023501, 2016.

[38] Eiichiro Komatsu, K. Smith, J. Dunkley, C. Bennett, Ben Gold, G. Hinshaw, N. Jarosik, D. Larson, M. Nolta, Lyman Page, D. Spergel, M. Halpern, R. Hill, A. Kogut, Stephan Meyer, N. Odegard, G. Tucker, J. Weiland, and and Wright. Seven-year wilkinson microwave anisotropy probe (wmap) observations: Cosmological interpretation. *The Astrophysical Journal Supplement Series*, 192:18, 01 2011.

[39] Kunimoto Komatsu, Hirokazu Ishino, Nobuhiko Katayama, Tomotake Matsumura, and Yuki Sakurai. Design of a frequency-independent optic axis Pancharatnam-based achromatic half-wave plate. *Journal of Astronomical Telescopes, Instruments, and Systems*, 7(3):1 – 13, 2021.

[40] Kunimoto Komatsu, Hirokazu Ishino, Nobuhiko Katayama, Tomotake Matsumura, Yuki Sakurai, and Ryota Takaku. Design the frequency independent fast axis of the pancharatnam base multi-layer half-wave plate for cmb polarization experiment. Proc. SPIE, 2020. in preparation.

[41] Kunimoto Komatsu, Hirokazu Ishino, Hirokazu Kataza, Kuniaki Konishi, Makoto Kuwata-Gonokami, Nobuhiko Katayama, Shinya Sugiyama, Tomotake Matsumura, Haruyuki Sakurai, Yuki Sakurai, Ryota Takaku, and Junji Yumoto. Demonstration of five-layer phase-flat achromatic half-wave plate with anti-reflective structures and superconducting magnetic bearing for CMB polarization experiments. In Jonas Zmuidzinas and Jian-Rong Gao, editors, *Millimeter, Submillimeter, and Far-Infrared Detectors and Instrumentation for Astronomy X*, volume 11453, pages 779 – 794. International Society for Optics and Photonics, SPIE, 2020.

[42] Kunimoto Komatsu, Tomotake Matsumura, Hiroaki Imada, Hirokazu Ishino, Nobuhiko Katayama, and Yuki Sakurai. Demonstration of the broadband half-wave plate using the nine-layer sapphire for the cosmic microwave background polarization experiment. *Journal of Astronomical Telescopes, Instruments, and Systems*, 5(4):1 – 14, 2019.

[43] A. Kusaka et al. Modulation of cosmic microwave background polarization with a warm rapidly rotating half-wave plate on the Atacama B-Mode Search instrument. *Rev. Sci. Instrum.*, 85:024501, 2014.

[44] J. C. Mather, E. S. Cheng, D. A. Cottingham, Jr. Eplee, R. E., D. J. Fixsen, T. Hewagama, R. B. Isaacman, K. A. Jensen, S. S. Meyer, P. D. Noerdlinger, S. M. Read, L. P. Rosen, R. A. Shafer, E. L. Wright, C. L. Bennett, N. W. Boggess, M. G. Hauser, T. Kelsall, Jr. Moseley, S. H., R. F. Silverberg, G. F. Smoot, R. Weiss, and D. T. Wilkinson. Measurement of the Cosmic Microwave Background Spectrum by the COBE FIRAS Instrument. *Astrophysical Journal*, 420:439, January 1994.

[45] T. Matsumura et al. Analysis of performance of three- and five-stack achromatic half-wave plates at millimeter wavelengths. *Applied Optics*, 48:3614–3625, 2009.

[46] Tomotake Matsumura. Mitigation of the spectral dependent polarization angle response for achromatic half-wave plate. `https://arxiv.org/abs/1404.5795`, 2014.

[47] Paulo Montero-Camacho and Christopher M. Hirata. Exploring circular polarization in the CMB due to conventional sources of cosmic birefringence. *Journal of Cosmology and Astroparticle Physics*, 2018(08):040–040, 2018.

[48] L. Montier, B. Mot, P. de Bernardis, B. Maffei, G. Pisano, F. Columbro, J. E. Gudmundsson, S. Henrot-Versillé, L. Lamagna, J. Montgomery, T. Prouvé, M. Russell, G. Savini, S. Stever, K. L. Thompson, M. Tsujimoto, C. Tucker, B. Westbrook, P. A. R. Ade, A. Adler, E. Allys, K. Arnold, D. Auguste, J. Aumont, R. Aurlien, J. Austermann, C. Baccigalupi, A. J. Banday, R. Banerji, R. B. Barreiro, S. Basak, J. Beall, D. Beck, S. Beckman, J. Bermejo, M. Bersanelli, J. Bonis, J. Borrill, F. Boulanger, S. Bounissou, M. Brilenkov, M. Brown, M. Bucher, E. Calabrese, P. Campeti, A. Carones, F. J. Casas, A. Challinor, V. Chan, K. Cheung, Y. Chinone, J. F. Cliche, L. Colombo, J. Cubas, A. Cukierman, D. Curtis, G. D'Alessandro, N. Dachlythra, M. De Petris, C. Dickinson, P. Diego-Palazuelos, M. Dobbs, T. Dotani, L. Duband, S. Duff, J. M. Duval, K. Ebisawa, T. Elleflot, H. K. Eriksen, J. Errard, T. Essinger-Hileman, F. Finelli, R. Flauger, C. Franceschet, U. Fuskeland, M. Galloway, K. Ganga, J. R. Gao, R. Genova-Santos, M. Gerbino, M. Gervasi, T. Ghigna, E. Gjerløw, M. L. Gradziel, J. Grain, F. Grupp, A. Gruppuso, T. de Haan, N. W. Halverson, P. Hargrave, T. Hasebe, M. Hasegawa, M. Hattori, M. Hazumi, D. Herman, D. Herranz, C. A. Hill, G. Hilton, Y. Hirota, E. Hivon, R. A. Hlozek, Y. Hoshino, E. de la Hoz, J. Hubmayr, K. Ichiki, T. Iida, H. Imada, K. Ishimura, H. Ishino, G. Jaehnig, T. Kaga, S. Kashima, N. Katayama, A. Kato, T. Kawasaki, R. Keskitalo, T. Kisner, Y. Kobayashi, N. Kogiso, A. Kogut, K. Kohri, E. Komatsu, K. Komatsu, K. Konishi, N. Krachmalnicoff, I. Kreykenbohm, C. L. Kuo, A. Kushino, J. V. Lanen, M. Lattanzi, A. T. Lee, C. Leloup, F. Levrier, E. Linder, T. Louis, G. Luzzi, T. Maciaszek, D. Maino, M. Maki, S. Mandelli, E. Martinez-Gonzalez, S. Masi, T. Matsumura, A. Mennella, M. Migliaccio, Y. Minami, K. Mitsuda, G. Morgante, Y. Murata, J. A. Murphy, M. Nagai, Y. Nagano, T. Nagasaki, R. Nagata, S. Nakamura, T. Namikawa, P. Natoli, S. Nerval, T. Nishibori, H. Nishino, C. O'Sullivan, H. Ogawa, H. Ogawa, S. Oguri, H. Ohsaki, I. S. Ohta, N. Okada, N. Okada, L. Pagano, A. Paiella, D. Paoletti, G. Patanchon, J. Peloton, F. Piacentini, G. Polenta, D. Poletti, G. Puglisi, D. Rambaud, C. Raum, S. Realini, M. Reinecke, M. Remazeilles, A. Ritacco, G. Roudil, J. A. Rubino-Martin, H. Sakurai, Y. Sakurai, M. Sandri, M. Sasaki, D. Scott, J. Seibert, Y. Sekimoto, B. Sherwin, K. Shinozaki, M. Shiraishi, P. Shirron, G. Signorelli, G. Smecher, R. Stompor, H. Sugai, S. Sugiyama, A. Suzuki, J. Suzuki, T. L. Svalheim, E. Switzer, R. Takaku, H. Takakura, S. Takakura, Y. Takase, Y. Takeda, A. Tartari, E. Taylor, Y. Terao, H. Thommesen, B. Thorne, T. Toda, M. Tomasi, M. Tominaga, N. Trappe, M. Tristram, M. Tsuji, J. Ullom, G. Vermeulen, P. Vielva, F. Villa, M. Vissers, N. Vittorio, I. Wehus, J. Weller, J. Wilms, B. Winter, E. J. Wollack, N. Y. Yamasaki, T. Yoshida, J. Yumoto, M. Zannoni, and A. Zonca. Overview of the medium and high frequency telescopes of the LiteBIRD space mission. In Makenzie Lystrup, Marshall D. Perrin, Natalie Batalha, Nicholas Siegler, and Edward C. Tong, editors, *Space Telescopes and Instrumentation 2020: Optical, Infrared, and Millimeter Wave*, volume 11443, pages 451 – 471. International Society for Optics and Photonics, SPIE, 2020.

[49] S. Orfanidis. *Electromagnetic Waves and Antennas*. 2016. `http://eceweb1.rutgers.edu/~orfanidi/ewa/`.

[50] S. Pancharatnam. Achromatic combinations of birefringent plates part i. an achromatic circular polarizer. *Proc. of Indian Acad. Sci.-Sect. A*, 41:130–136, 1955.

[51] S. Pancharatnam. Achromatic combinations of birefringent plates part ii. an achromatic quarter-wave plate. *Proc. of Indian Acad. Sci.-Sect. A*, 41:137–144, 1955.

[52] A. A. Penzias and R. W. Wilson. A Measurement of Excess Antenna Temperature at 4080 Mc/s. *Astrophysical Journal*, 142:419–421, July 1965.

[53] G. Pisano et al. Achromatic half-wave plate for submillimeter instruments in cosmic microwave background astronomy: experimental characterization. *Applied Optics*, 45:6982–6989, 2006.

[54] Planck Collaboration, Ade, P. A. R., Aghanim, N., Armitage-Caplan, C., Arnaud, M., Ashdown, M., Atrio-Barandela, F., Aumont, J., Baccigalupi, C., Banday, A. J., Barreiro, R. B., Bartlett, J. G., Bartolo, N., Battaner, E., Benabed, K., Benoît, A., Benoit-Lévy, A., Bernard, J.-P., Bersanelli, M., Bielewicz, P., Bobin, J., Bock, J. J., Bonaldi, A., Bond, J. R., Borrill, J., Bouchet, F. R., Bridges, M., Bucher, M., Burigana, C., Butler, R. C., Calabrese, E., Cardoso, J.-F., Catalano, A., Challinor, A., Chamballu, A., Chiang, H. C., Chiang, L.-Y., Christensen, P. R., Church, S., Clements, D. L., Colombi, S., Colombo, L. P. L., Couchot, F., Coulais, A., Crill, B. P., Curto, A., Cuttaia, F., Danese, L., Davies, R. D., Davis, R. J., de Bernardis, P., de Rosa, A., de Zotti, G., Delabrouille, J., Delouis, J.-M., Désert, F.-X., Dickinson, C., Diego, J. M., Dole, H., Donzelli, S., Doré, O., Douspis, M., Dunkley, J., Dupac, X., Efstathiou, G., Enßlin, T. A., Eriksen, H. K., Finelli, F., Forni, O., Frailis, M., Franceschi, E., Galeotta, S., Ganga, K., Gauthier, C., Giard, M., Giardino, G., Giraud-Héraud, Y., González-Nuevo, J., Górski, K. M., Gratton, S., Gregorio, A., Gruppuso, A., Hamann, J., Hansen, F. K., Hanson, D., Harrison, D., Henrot-Versillé, S., Hernández-Monteagudo, C., Herranz, D., Hildebrandt, S. R., Hivon, E., Hobson, M., Holmes, W. A., Hornstrup, A., Hovest, W., Huffenberger, K. M., Jaffe, A. H., Jaffe, T. R., Jones, W. C., Juvela, M., Keihänen, E., Keskitalo, R., Kisner, T. S., Kneissl, R., Knoche, J., Knox, L., Kunz, M., Kurki-Suonio, H., Lagache, G., Lähteenmäki, A., Lamarre, J.-M., Lasenby, A., Laureijs, R. J., Lawrence, C. R., Leach, S., Leahy, J. P., Leonardi, R., Lesgourgues, J., Lewis, A., Liguori, M., Lilje, P. B., Linden-Vørnle, M., López-Caniego, M., Lubin, P. M., Macías-Pérez, J. F., Maffei, B., Maino, D., Mandolesi, N., Maris, M., Marshall, D. J., Martin, P. G., Martínez-González, E., Masi, S., Massardi, M., Matarrese, S., Matthai, F., Mazzotta, P., Meinhold, P. R., Melchiorri, A., Mendes, L., Mennella, A., Migliaccio, M., Mitra, S., Miville-Deschênes, M.-A., Moneti, A., Montier, L., Morgante, G., Mortlock, D., Moss, A., Munshi, D., Murphy, J. A., Naselsky, P., Nati, F., Natoli, P., Netterfield, C. B., Nørgaard-Nielsen, H. U., Noviello, F., Novikov, D., Novikov, I., O´Dwyer, I. J., Osborne, S., Oxborrow, C. A., Paci, F., Pagano, L., Pajot, F., Paladini, R., Pandolfi, S., Paoletti, D., Partridge, B., Pasian, F., Patanchon, G., Peiris, H. V., Perdereau, O., Perotto, L., Perrotta, F., Piacentini, F., Piat, M., Pierpaoli, E., Pietrobon, D., Plaszczynski, S., Pointecouteau, E., Polenta, G., Ponthieu, N., Popa, L., Poutanen, T., Pratt, G. W., Prézeau, G., Prunet, S., Puget, J.-L., Rachen, J. P., Rebolo, R., Reinecke, M., Remazeilles, M., Renault, C., Ricciardi, S., Riller, T., Ristorcelli, I., Rocha, G., Rosset, C., Roudier, G., Rowan-Robinson, M., Rubiño-Martín, J. A., Rusholme, B., Sandri, M., Santos, D., Savelainen, M., Savini, G., Scott, D., Seiffert, M. D., Shellard, E. P. S., Spencer, L. D., Starck, J.-L., Stolyarov, V., Stompor, R., Sudiwala, R., Sunyaev, R., Sureau, F., Sutton, D., Suur-Uski, A.-S., Sygnet, J.-F., Tauber, J. A., Tavagnacco, D., Terenzi, L., Toffolatti, L., Tomasi, M., Tréguer-Goudineau, J., Tristram, M., Tucci, M., Tuovinen, J., Valenziano, L., Valiviita, J., Van Tent, B., Varis, J., Vielva, P., Villa, F., Vittorio, N., Wade, L. A., Wandelt, B. D., White, M., Wilkinson, A., Yvon, D., Zacchei, A., Zibin, J. P., and Zonca, A. Planck 2013 results. xxii. constraints on inflation. *A&A*, 571:A22, 2014.

[55] Planck Collaboration, Aghanim, N., Akrami, Y., Arroja, F., Ashdown, M., Aumont, J., Baccigalupi, C., Ballardini, M., Banday, A. J., Barreiro, R. B., Bartolo, N., Basak, S., Battye, R., Benabed, K., Bernard, J.-P., Bersanelli, M., Bielewicz, P., Bock, J. J., Bond, J. R., Borrill, J., Bouchet, F. R., Boulanger, F., Bucher, M., Burigana, C., Butler, R. C., Calabrese, E., Cardoso, J.-F., Carron, J., Casaponsa, B., Challinor, A., Chiang, H. C., Colombo, L. P. L., Combet, C., Contreras, D., Crill, B. P., Cuttaia, F., de Bernardis, P., de Zotti, G., Delabrouille, J., Delouis, J.-M., Désert, F.-X., Di Valentino, E., Dickinson, C., Diego, J. M., Donzelli, S., Doré, O., Douspis, M., Ducout, A., Dupac, X., Efstathiou, G., Elsner, F., Enßlin, T. A., Eriksen, H. K., Falgarone, E., Fantaye, Y., Fergusson, J., Fernandez-Cobos, R., Finelli, F., Forastieri, F., Frailis, M., Franceschi, E., Frolov, A., Galeotta, S., Galli, S., Ganga, K., Génova-Santos, R. T., Gerbino, M., Ghosh, T., González-Nuevo, J., Górski, K. M., Gratton, S., Gruppuso, A., Gudmundsson, J. E., Hamann, J., Handley, W., Hansen, F. K., Helou, G., Herranz, D., Hildebrandt, S. R., Hivon, E., Huang, Z., Jaffe, A. H., Jones, W. C., Karakci, A., Keihänen, E., Keskitalo, R., Kiiveri, K., Kim, J., Kisner, T. S., Knox, L., Krachmalnicoff, N., Kunz, M., Kurki-Suonio, H., Lagache, G., Lamarre, J.-M., Langer, M., Lasenby, A., Lattanzi, M., Lawrence, C. R., Le Jeune, M., Leahy, J. P., Lesgourgues, J., Levrier, F., Lewis, A., Liguori, M., Lilje, P. B., Lilley, M., Lindholm, V., López-Caniego, M., Lubin, P. M., Ma, Y.-Z., Macías-Pérez, J. F., Maggio, G., Maino, D., Mandolesi, N., Mangilli, A., Marcos-Caballero, A., Maris, M., Martin, P. G., Martinelli, M., Martínez-González, E., Matarrese, S., Mauri, N., McEwen, J. D., Meerburg, P. D., Meinhold, P. R., Melchiorri, A., Mennella, A., Migliaccio, M., Millea, M., Mitra, S., Miville-Deschênes, M.-A., Molinari, D., Moneti, A., Montier, L., Morgante, G., Moss, A., Mottet, S., Münchmeyer, M., Natoli, P., Nørgaard-Nielsen, H. U., Oxborrow, C. A., Pagano, L., Paoletti, D., Partridge, B., Patanchon, G., Pearson, T. J., Peel, M., Peiris, H. V., Perrotta, F., Pettorino, V., Piacentini, F., Polastri, L., Polenta, G., Puget, J.-L., Rachen, J. P., Reinecke, M., Remazeilles, M., Renault, C., Renzi, A., Rocha, G., Rosset, C., Roudier, G., Rubiño-Martín, J. A., Ruiz-Granados, B., Salvati, L., Sandri, M., Savelainen, M., Scott, D., Shellard, E. P. S., Shiraishi, M., Sirignano, C., Sirri, G., Spencer, L. D., Sunyaev, R., Suur-Uski, A.-S., Tauber, J. A., Tavagnacco, D., Tenti, M., Terenzi, L., Toffolatti, L., Tomasi, M., Trombetti, T., Valiviita, J., Van Tent, B., Vibert, L., Vielva, P., Villa, F., Vittorio, N., Wandelt, B. D., Wehus, I. K., White, M., White, S. D. M., Zacchei, A., and Zonca, A. Planck 2018 results - i. overview and the cosmological legacy of planck. *A&A*, 641:A1, 2020.

[56] Planck Collaboration, Akrami, Y., Arroja, F., Ashdown, M., Aumont, J., Baccigalupi, C., Ballardini, M., Banday, A. J., Barreiro, R. B., Bartolo, N., Basak, S., Benabed, K., Bernard, J.-P., Bersanelli, M., Bielewicz, P., Bock, J. J., Bond, J. R., Borrill, J., Bouchet, F. R., Boulanger, F., Bucher, M., Burigana, C., Butler, R. C., Calabrese, E., Cardoso, J.-F., Carron, J., Challinor, A., Chiang, H. C., Colombo, L. P. L., Combet, C., Contreras, D., Crill, B. P., Cuttaia, F., de Bernardis, P., de Zotti, G., Delabrouille, J., Delouis, J.-M., Di Valentino, E., Diego, J. M., Donzelli, S., Doré, O., Douspis, M., Ducout, A., Dupac, X., Dusini, S., Efstathiou, G., Elsner, F., Enßlin, T. A., Eriksen, H. K., Fantaye, Y., Fergusson, J., Fernandez-Cobos, R., Finelli, F., Forastieri, F., Frailis, M., Franceschi, E., Frolov, A., Galeotta, S., Galli, S., Ganga, K., Gauthier, C., Génova-Santos, R. T., Gerbino, M., Ghosh, T., González-Nuevo, J., Górski, K. M., Gratton, S., Gruppuso, A., Gudmundsson, J. E., Hamann, J., Handley, W., Hansen, F. K., Herranz, D., Hivon, E., Hooper, D. C., Huang, Z., Jaffe, A. H., Jones, W. C., Keihänen, E., Keskitalo, R., Kiiveri, K., Kim, J., Kisner, T. S., Krachmalnicoff, N., Kunz, M., Kurki-Suonio, H., Lagache, G., Lamarre, J.-M., Lasenby, A., Lattanzi, M.,

Lawrence, C. R., Le Jeune, M., Lesgourgues, J., Levrier, F., Lewis, A., Liguori, M., Lilje, P. B., Lindholm, V., López-Caniego, M., Lubin, P. M., Ma, Y.-Z., Macías-Pérez, J. F., Maggio, G., Maino, D., Mandolesi, N., Mangilli, A., Marcos-Caballero, A., Maris, M., Martin, P. G., Martínez-González, E., Matarrese, S., Mauri, N., McEwen, J. D., Meerburg, P. D., Meinhold, P. R., Melchiorri, A., Mennella, A., Migliaccio, M., Mitra, S., Miville-Deschênes, M.-A., Molinari, D., Moneti, A., Montier, L., Morgante, G., Moss, A., Münchmeyer, M., Natoli, P., Nørgaard-Nielsen, H. U., Pagano, L., Paoletti, D., Partridge, B., Patanchon, G., Peiris, H. V., Perrotta, F., Pettorino, V., Piacentini, F., Polastri, L., Polenta, G., Puget, J.-L., Rachen, J. P., Reinecke, M., Remazeilles, M., Renzi, A., Rocha, G., Rosset, C., Roudier, G., Rubiño-Martín, J. A., Ruiz-Granados, B., Salvati, L., Sandri, M., Savelainen, M., Scott, D., Shellard, E. P. S., Shiraishi, M., Sirignano, C., Sirri, G., Spencer, L. D., Sunyaev, R., Suur-Uski, A.-S., Tauber, J. A., Tavagnacco, D., Tenti, M., Toffolatti, L., Tomasi, M., Trombetti, T., Valiviita, J., Van Tent, B., Vielva, P., Villa, F., Vittorio, N., Wandelt, B. D., Wehus, I. K., White, S. D. M., Zacchei, A., Zibin, J. P., and Zonca, A. Planck 2018 results - x. constraints on inflation. *A&A*, 641:A10, 2020.

[57] Planck Collaboration, Akrami, Y., Ashdown, M., Aumont, J., Baccigalupi, C., Ballardini, M., Banday, A. J., Barreiro, R. B., Bartolo, N., Basak, S., Benabed, K., Bersanelli, M., Bielewicz, P., Bond, J. R., Borrill, J., Bouchet, F. R., Boulanger, F., Bucher, M., Burigana, C., Calabrese, E., Cardoso, J.-F., Carron, J., Casaponsa, B., Challinor, A., Colombo, L. P. L., Combet, C., Crill, B. P., Cuttaia, F., de Bernardis, P., de Rosa, A., de Zotti, G., Delabrouille, J., Delouis, J.-M., Di Valentino, E., Dickinson, C., Diego, J. M., Donzelli, S., Doré, O., Ducout, A., Dupac, X., Efstathiou, G., Elsner, F., Enßlin, T. A., Eriksen, H. K., Falgarone, E., Fernandez-Cobos, R., Finelli, F., Forastieri, F., Frailis, M., Fraisse, A. A., Franceschi, E., Frolov, A., Galeotta, S., Galli, S., Ganga, K., Génova-Santos, R. T., Gerbino, M., Ghosh, T., González-Nuevo, J., Górski, K. M., Gratton, S., Gruppuso, A., Gudmundsson, J. E., Handley, W., Hansen, F. K., Helou, G., Herranz, D., Hildebrandt, S. R., Huang, Z., Jaffe, A. H., Karakci, A., Keihänen, E., Keskitalo, R., Kiiveri, K., Kim, J., Kisner, T. S., Krachmalnicoff, N., Kunz, M., Kurki-Suonio, H., Lagache, G., Lamarre, J.-M., Lasenby, A., Lattanzi, M., Lawrence, C. R., Le Jeune, M., Levrier, F., Liguori, M., Lilje, P. B., Lindholm, V., López-Caniego, M., Lubin, P. M., Ma, Y.-Z., Macías-Pérez, J. F., Maggio, G., Maino, D., Mandolesi, N., Mangilli, A., Marcos-Caballero, A., Maris, M., Martin, P. G., Martínez-González, E., Matarrese, S., Mauri, N., McEwen, J. D., Meinhold, P. R., Melchiorri, A., Mennella, A., Migliaccio, M., Miville-Deschênes, M.-A., Molinari, D., Moneti, A., Montier, L., Morgante, G., Natoli, P., Oppizzi, F., Pagano, L., Paoletti, D., Partridge, B., Peel, M., Pettorino, V., Piacentini, F., Polenta, G., Puget, J.-L., Rachen, J. P., Reinecke, M., Remazeilles, M., Renzi, A., Rocha, G., Roudier, G., Rubiño-Martín, J. A., Ruiz-Granados, B., Salvati, L., Sandri, M., Savelainen, M., Scott, D., Seljebotn, D. S., Sirignano, C., Spencer, L. D., Suur-Uski, A.-S., Tauber, J. A., Tavagnacco, D., Tenti, M., Thommesen, H., Toffolatti, L., Tomasi, M., Trombetti, T., Valiviita, J., Van Tent, B., Vielva, P., Villa, F., Vittorio, N., Wandelt, B. D., Wehus, I. K., Zacchei, A., and Zonca, A. Planck 2018 results - iv. diffuse component separation. *A&A*, 641:A4, 2020.

[58] Frank Pobell. *Matter and Methods at Low Temperaturesv(Third Edition).* Springer, 2007.

[59] POLARBEAR Collaboration. A measurement of the cosmic microwave background b-mode polarization power spectrum at sub-degree scales with polarbear. *Astrophysical Journal*, 794:171, 2014.

[60] Britt Reichborn-Kjennerud et al. Ebex: a balloon-borne cmb polarization experiment. volume 7741 of *Proc. SPIE*, 2010.

[61] J. E. Ruhl et al. Improved measurement of the angular power spectrum of temperature anisotropy in the CMB from two new analyses of BOOMERANG observations. *Astrophys. J.*, 599:786–805, 2003.

[62] Y. Sakurai et al. Design and development of a polarization modulator unit based on a continuous rotating half-wave plate for litebird. In *Millimeter, Submillimeter, and Far-Infrared Detectors and Instrumentation for Astronomy IX*, volume 10708 of *Proc. SPIE*, 2018.

[63] Yuki Sakurai, Tomotake Matsumura, Nobuhiko Katayama, Kunimoto Komatsu, Ryota Takaku, Shinya Sugiyama, Yoshiki Nomura, Takayuki Toda, Tommaso Ghigna, Teruhito Iida, Hajime Sugai, Hiroaki Imada, Masashi Hazumi, Hirokazu Ishino, Hiroyuki Ohsaki, Yutaka Terao, Hisashi Enokida, Yusuke Ishida, Yosuke Iwata, Doa Ahmad, Kuniaki Konishi, Haruyuki Sakurai, Junji Yumoto, Makoto Kuwata-Gonokami, Akito Kusaka, and Charles Hill. Breadboard model of the polarization modulator unit based on a continuously rotating half-wave plate for the low-frequency telescope of the LiteBIRD space mission. In Jonas Zmuidzinas and Jian-Rong Gao, editors, *Millimeter, Submillimeter, and Far-Infrared Detectors and Instrumentation for Astronomy X*, volume 11453, pages 743 – 762. International Society for Optics and Photonics, SPIE, 2020.

[64] Yuki Sakurai, Tomotake Matsumura, Hajime Sugai, Nobuhiko Katayama, Hiroyuki Ohsaki, Yutaka Terao, Yusuke Terachi, Hirokazu Kataza, Shin Utsunomiya, and Ryo Yamamoto. Vibrational characteristics of a superconducting magnetic bearing employed for a prototype polarization modulator. *Journal of Physics: Conference Series*, 871:012091, jul 2017.

[65] G. Savini et al. Achromatic half-wave plate for submillimeter instruments in cosmic microwave background astronomy: modeling and simulation. *Applied Optics*, 45:8907–8915, 2006.

[66] Y. Sekimoto, P. A. R. Ade, A. Adler, E. Allys, K. Arnold, D. Auguste, J. Aumont, R. Aurlien, J. Austermann, C. Baccigalupi, A. J. Banday, R. Banerji, R. B. Barreiro, S. Basak, J. Beall, D. Beck, S. Beckman, J. Bermejo, Paolo de Bernardis, Marco Bersanelli, Julien Bonis, Julian Borrill, F. Boulanger, Sophie Bounissou, M. Brilenkov, Michael Brown, Martin Bucher, Erminia Calabrese, Paolo Campeti, Alessandro Carones, Francisco Casas, Anthony Challinor, Victor Chan, Kolen Cheung, Yuji Chinone, Jean Cliche, Loris Colombo, Fabio Columbro, Javier Cubas, Ari Cukierman, David Curtis, Giuseppe D'Alessandro, Nadia Dachlythra, Marco De Petris, Clive Dickinson, Patricia Diego-Palazuelos, Matt Dobbs, Tadayasu Dotani, Lionel Duband, Shannon Duff, Jean Duval, Ken Ebisawa, Tucker Elleflot, H. Eriksen, Josquin Errard, Thomas Essinger-Hileman, Fabio Finelli, Raphael Flauger, Cristian Franceschet, U. Fuskeland, M. Galloway, Ken Ganga, Jian Gao, Ricardo Genova-Santos, Martina Gerbino, Massimo Gervasi, Tommaso Ghigna, E. Gjerløw, Marcin Gradziel, Julien Grain, Frank Grupp, Alessandro Gruppuso, Jon Gudmundsson, Tijmen de Haan, Nils Halverson, Peter Hargrave, Takashi Hasebe, Masaya Hasegawa, Makoto Hattori, Masashi Hazumi, Sophie Henrot-Versillé, D. Herman, Diego Herranz, Charles Hill, Gene Hilton, Yukimasa Hirota, Eric hivon, Renee Hlozek, Yurika Hoshino, Elena de la Hoz, Johannes Hubmayr, Kiyotomo Ichiki, Teruhito iida, Hiroaki Imada, Kosei Ishimura, Hirokazu Ishino, Greg Jaehnig, Tooru Kaga, Shingo Kashima, Nobuhiko Katayama, Akihiro Kato, Takeo Kawasaki, Reijo Keskitalo, Theodore Kisner, Yohei Kobayashi, Nozomu Kogiso, Alan Kogut, Kazunori

Kohri, Eiichiro Komatsu, Kunimoto Komatsu, Kuniaki Konishi, Nicoletta Krachmalnicoff, Ingo Kreykenbohm, Chao-Lin Kuo, Akihiro Kushino, Luca Lamagna, Jeff Lanen, Massimiliano Lattanzi, Adrien Lee, Clément Leloup, François Levrier, Eric Linder, Thibaut Louis, Gemma Luzzi, Thierry Maciaszek, Bruno Maffei, Davide Maino, Muneyoshi Maki, Stefano Mandelli, Enrique Martinez-Gonzalez, Silvia Masi, Tomotake Matsumura, Aniello Mennella, Marina Migliaccio, Yuto Minanmi, Kazuhisa Mitsuda, Josua Montgomery, Ludovic Montier, Gianluca Morgante, Baptise Mot, Yasuhiro Murata, John Murphy, Makoto Nagai, Yuya Nagano, Takeo Nagasaki, Ryo Nagata, Shogo Nakamura, Toshiya Namikawa, Paolo Natoli, Simran Nerval, Toshiyuki Nishibori, Haruki Nishino, Créidhe O'Sullivan, Hideo Ogawa, Hiroyuki Ogawa, Shogo Oguri, Hiroyuki Osaki, Izumi Ohta, Norio Okada, Nozomi Okada, Luca Pagano, Alessandro Paiella, Daniela Paoletti, Guillaume Patanchon, Julien Peloton, Francesco Piacentini, Giampaolo Pisano, Gianluca Polenta, Davide Poletti, Thomas Prouvé, Giuseppe Puglisi, Damien Tambaud, Christopher Raum, Sabrina Realini, Martin Reinecke, Mathieu Remazeilles, Alessa Ritacco, Gilles Roudil, Jose Rubino-Martin, Megan Russell, Haruyuki Sakurai, Yuki Sakurai, Maura Sandri, Manami Sasaki, Giorgio Savini, Douglas Scott, Joseph Seibert, Blake Sherwin, Keisuke Shinozaki, Maresuke Shiraishi, Peter Shirron, Giovanni Signorelli, Graeme Smecher, S. Stever, Radek Stompor, Hajime Sugai, Shinya Sugiyama, aritoki Suzuki, Junichi Suzuki, T. L. Svalheim, Eric Switzer, Ryota Takaku, hayato Takakura, satoru Takakura, Yusuke Takase, Youichi Takeda, Andrea Tartari, Ellen Taylor, Yutaka Terao, H. Thommesen, Keith L Thompson, Ben Thorne, Takayuki Toda, Maurizio Tomasi, Mayu Tominaga, Neil Trappe, Matthieu Tristram, Masatoshi Tsuji, Masahiro Tsujimoto, Carole Tucker, Joe Ullom, Gerard Vermeulen, Patricio Vielva, Fabrizio Villa, Michael Vissers, Nicola Vittorio, I. Wehus, Jochen Weller, Benjamin Westbrook, Joern Wilms, Berend Winter, Edward Wollack, Noriko Y. Yamasaki, Tetsuya Yoshida, Junji Yumoto, Mario Zannoni, and Andrea Zonca. Concept design of low frequency telescope for CMB B-mode polarization satellite LiteBIRD. In Jonas Zmuidzinas and Jian-Rong Gao, editors, *Millimeter, Submillimeter, and Far-Infrared Detectors and Instrumentation for Astronomy X*, volume 11453. International Society for Optics and Photonics, SPIE, 2020.

[67] William A. Shurcliff. *Polarized Light.* Harvard University Press, 2013.

[68] Samantha Lynn Stever. *Characterisation and modelling of the interaction between sub-Kelvin bolometric detectors and cosmic rays: Caractérisation et modélisation de l'interaction entre les détecteurs bolométriques sub-Kelvin et les rayons cosmiques.* PhD thesis, Université Paris-Saclay (ComUE), 2019.

[69] Shinya Sugiyama, Tomotake Matsumura, Yuki Sakurai, Nobuhiko Katayama, Satoru Takakura, Makoto Tashiro, Yukikatsu Terada, Kosuke Sato, Satoru Katsuda, Yurika Hoshino, Ryota Takaku, and Kunimoto Komatsu. Evaluation of reconstructed angular error of a continuous rotating HWP for LiteBIRD. In Makenzie Lystrup, Marshall D. Perrin, Natalie Batalha, Nicholas Siegler, and Edward C. Tong, editors, *Space Telescopes and Instrumentation 2020: Optical, Infrared, and Millimeter Wave*, volume 11443, pages 1099 – 1112. International Society for Optics and Photonics, SPIE, 2020.

[70] Shinya Sugiyama, Tomotake Matsumura, Yuki Sakurai, Nobuhiko Katayama, Satoru Takakura, Makoto Tashiro, Yukikatsu Terada, Kosuke Sato, Satoru Katsuda, Yurika Hoshino, Ryota Takaku, and Kunimoto Komatsu. Evaluation of reconstructed angular error of a continuous rotating HWP for LiteBIRD. In Makenzie Lystrup, Marshall D. Perrin, Natalie Batalha,

Nicholas Siegler, and Edward C. Tong, editors, *Space Telescopes and Instrumentation 2020: Optical, Infrared, and Millimeter Wave*, volume 11443. International Society for Optics and Photonics, SPIE, 2020.

[71] R. Takaku, S. Hanany, H. Imada, H. Ishino, N. Katayama, K. Komatsu, K. Konishi, M. Kuwata-Gonokami, T. Matsumura, K. Mitsuda, H. Sakurai, Y. Sakurai, Q. Wen, N. Y. Yamasaki, K. Young, and J. Yumoto. Broadband, millimeter-wave anti-reflective structures on sapphire ablated with femto-second laser. *Journal of Applied Physics*, 128(22):225302, 2020.

[72] Ryota Takaku, Shaul Hanany, Yurika Hoshino, Hiroaki Imada, Hirokazu Ishino, Nobuhiko Katayama, Kunimoto Komatsu, Kuniaki Konishi, Makoto Kuwata Gonokami, Tomotake Matsumura, Kazuhisa Mitsuda, Haruyuki Sakurai, Yuki Sakurai, Qi Wen, Noriko Y. Yamasaki, Karl Young, and Junji Yumoto. Demonstration of anti-reflective structures over a large area for CMB polarization experiments. In Jonas Zmuidzinas and Jian-Rong Gao, editors, *Millimeter, Submillimeter, and Far-Infrared Detectors and Instrumentation for Astronomy X*, volume 11453, pages 236 – 247. International Society for Optics and Photonics, SPIE, 2020.

[73] Ben Thorne, Jo Dunkley, David Alonso, and Sigurd Naess. The python sky model: software for simulating the galactic microwave sky. *Monthly Notices of the Royal Astronomical Society*, 469:2821–2833, 08 2017.

[74] Takayuki Toda, Hirokazu Ishino, Kunimoto Komatsu, Tomotake Matsumura, Yuki Sakurai, and Nobuhiko Katayama. Mechanical strength and millimeter-wave transmission spectrum of stacked sapphire plates bonded by sodium silicate solution. In Jonas Zmuidzinas and Jian-Rong Gao, editors, *Millimeter, Submillimeter, and Far-Infrared Detectors and Instrumentation for Astronomy X*, volume 11453, pages 788 – 799. International Society for Optics and Photonics, SPIE, 2020.

[75] Tristram, M., Banday, A. J., Górski, K. M., Keskitalo, R., Lawrence, C. R., Andersen, K. J., Barreiro, R. B., Borrill, J., Eriksen, H. K., Fernandez-Cobos, R., Kisner, T. S., Martínez-González, E., Partridge, B., Scott, D., Svalheim, T. L., Thommesen, H., and Wehus, I. K. Planck constraints on the tensor-to-scalar ratio. *A&A*, 647:A128, 2021.

[76] Clara Vergès, Josquin Errard, and Radek Stompor. Framework for analysis of next generation, polarized cmb data sets in the presence of galactic foregrounds and systematic effects. *Phys. Rev. D*, 103:063507, Mar 2021.

[77] B. Westbrook, C. Raum, S. Beckman, A. T. Lee, N. Farias, T. Sasse, A. Suzuki, E. Kane, J. E. Austermann, J. A. Beall, S. M. Duff, J. Hubmayr, G. C. Hilton, J. Van Lanen, M. R. Vissers, M. R. Link, N. Halverson, G. Jaehnig, T. Ghinga, S. Stever, Y. Minami, K. L. Thompson, M. Russell, K. Arnold, J. Seibert, and M. Silva-Feaver. Detector fabrication development for the LiteBIRD satellite mission. In Makenzie Lystrup, Marshall D. Perrin, Natalie Batalha, Nicholas Siegler, and Edward C. Tong, editors, *Space Telescopes and Instrumentation 2020: Optical, Infrared, and Millimeter Wave*, volume 11443, pages 915 – 936. International Society for Optics and Photonics, SPIE, 2020.

[78] M. Zaldarriaga and U. Seljak. An all sky analysis of polarization in the microwave background. *Physical Review D*, 55:1830–1840, 1997.

[79] Andrea Zonca, Ben Thorne, Nicoletta Krachmalnicoff, and Julian Borrill. The python sky model 3 software, 2021.